Multiplicity and energy dependence of $\Lambda(1520)$ production in pp collisions at $\sqrt{s} = 5.02$ and 13 TeV with ALICE at the LHC

Thesis

submitted in the partial fulfilment of the requirements

of the degree of

Doctor of Philosophy

by

Sonali Padhan

(184123009)

Supervisor

Prof. Sadhana Dash

Department of Physics

INDIAN INSTITUTE OF TECHNOLOGY BOMBAY

(October - 2024)

Dedicated to My Parents...

Approval Sheet

This thesis report entitled "**Multiplicity and energy dependence of $\Lambda(1520)$ production in pp collisions at $\sqrt{s} = 5.02$ and 13 TeV with ALICE at the LHC**" by **Sonali Padhan** is approved for the degree of Doctor of Philosophy.

Examiners

.....

.....

.....

Supervisors

.....

.....

.....

Chairman

.....

Date: 29/01/2025

Place: Department of physics
IIT Bombay

Declaration

I declare that this written submission represents my ideas in my own words and where others' ideas or words have been included, I have adequately cited and referenced the original sources. I also declare that I have adhered to all principles of academic honesty and integrity and have not misrepresented or fabricated or falsified any idea/data/fact/source in my submission. I understand that any violation of the above will be cause for disciplinary action by the Institute and can also evoke penal action from the sources which have thus not been properly cited or from whom proper permission has not been taken when needed.

Sonali Padhan

Sonali Padhan

(184123009)

Date: 29/01/2025

Place: IIT Bombay

Acknowledgment

First and foremost, I would like to thank Lord Krishna and Lord Hanuman for their blessings and for guiding me through the challenges of my Ph.D. journey.

As I look back on my Ph.D. journey, I feel deeply grateful to all who have been part of it. First, I want to thank my parents and teachers, who motivated me to pursue a Ph.D. My parents have always supported me with their love and blessings, and I am deeply grateful for their encouragement throughout this journey.

I would like to extend my heartfelt gratitude to my supervisor, Prof. Sadhana Dash. Her constant support has allowed me the freedom to explore my interests, while her guidance has profoundly shaped my research journey. Our discussions have motivated me to aim higher, and I am truly grateful for the opportunity to work on exciting ideas under her mentorship. Her expertise and encouragement have been invaluable throughout this journey.

I would also like to express special thanks to Prof. Basanta Kumar Nandi. The physics discussions during our journal club sessions have significantly enhanced my understanding of high-energy physics, and his profound knowledge of the subject has been instrumental in my learning.

Additionally, I am grateful to both Prof. Dash and Prof. Nandi for their kindness and support with various projects and financial matters during collaborations, especially during my visits to CERN, which were essential for continuing my research and completing my ALICE shift duties.

I extend my heartfelt gratitude to the esteemed faculty members of the Department of Physics at IIT Bombay. I am especially thankful to my RPC members, Prof. Asmita Mukherji and Prof. Pradeep Sarin, for their invaluable feedback during each APS meeting. I am deeply grateful for the support and guidance provided by all the faculty members, which has been instrumental in shaping my journey.

I would also like to acknowledge the assistance and encouragement of the department's administrative staff, particularly Nilesh and Ashok Sir. Their support, suggestions, and willingness to help have been invaluable in navigating both the academic and administrative aspects of my research journey.

I extend my gratitude to the DST-sponsored ALICE India Project, funded by the Government of India, and to IIT Bombay for facilitating my participation in experimental analysis and data-taking operations at ALICE, CERN. I am sincerely appreciative of the guidance provided by the Resonance and PWGLF conveners—Enrico Fragiacomo, Jihye Song, Alberto Caliva, Ramona Lea, Livio Bianchi, Nicolo Jacazio, Sourav Kundu, Bong-Hwi, and Adrian Nassirpour. Their invaluable suggestions and assistance greatly enhanced the quality of my analysis, and I am truly grateful for their support.

I would like to express my special thanks to Pragati Di for her crucial guidance on resonance analysis, which significantly enhanced my understanding of the subject. Your patience and willingness to help have made a remarkable difference in my research journey. I also extend my heartfelt gratitude to Bharati Di, Baidya Bhai, and Ranjit Bhai for their invaluable support and suggestions throughout my research. Their insights have greatly contributed to my work, and their assistance during challenging times, both academically and personally, has been immensely appreciated.

I extend my heartfelt gratitude to my amazing lab mates—Tulika, Dibakar, Pritam, Subhadeep, Deependra, Tanu, Rahul, Yash, Swadhin, Pravat, Balaram, Debershi and Sayan for their unwavering support throughout my Ph.D. journey. I am especially grateful to Pritam, Dibakar, and Rahul for their invaluable assistance in resolving technical errors and engaging in stimulating discussions about physics. The friendly and collaborative environment you all fostered in the lab greatly motivated me throughout this journey. Thank you all for being such wonderful colleagues and friends. I extend my heartfelt thanks to Deependra and Sweta for their care and companionship during our travels to CERN, making the experience truly enjoyable and memorable.

I would like to acknowledge my friends, whose emotional support has been a source of strength during challenging times. A special thanks to Subhalaxmi Di, Sourav, Bhabani, Samikshya, Swadhin, and Milan for always being there for me through both good times and challenges. Your unwavering support and care have been invaluable throughout my journey. I am truly grateful for your friendship and encouragement in my life. I would like to extend my sincere thanks to my dear friends Nihar, Bikash, Prasad Raju, and Manas Bhai.

A special thanks to Sourav Bakshi, whose unwavering support and exceptional problem-solving skills have been a guiding light in my life. Your knack for finding solutions, combined with your great sense of humour, has not only made challenging times easier but has also filled my journey with laughter and joy. Your constant care and gentle reminders about important matters have made a significant difference in my path. I am truly grateful to have you by my side as I pursue my Ph.D. I would also like to extend my heartfelt gratitude to your family—Rupali Di, Debasish Jiju, and Siddhiksha—for their kindness, warmth, and thoughtful care. Their support has meant the world to me, and I feel incredibly fortunate to be surrounded by such a caring person.

I want to express my deepest gratitude to my parents and my little brother Aman and sister Tina for their unwavering support and understanding. Your sacrifices have inspired me every step of the way, and your love has been my guiding light throughout this scientific journey. From humble beginnings in a small village to pursuing my Ph.D. at IIT Bombay, I owe it all to you. Your happiness has always been my priority, and without your support, I am nothing. Dedicating my Ph.D. to you honours the sacrifices you've made and the dreams you've nurtured in me. Thank you for believing in me and for everything you have done to make this dream a reality. Your love and support have been the foundation of my achievements, and I will carry your hopes and dreams with me as I continue on this path.

Sonali Padhan

IIT Bombay

(October 2024)

Abstract

Quark Gluon Plasma (QGP), is believed to have existed just a few microseconds after the Big Bang, when the temperature of the universe was found to be 2000 billion degrees Celsius. The Large Hadron Collider (LHC) recreates the conditions necessary for studying QGP by colliding heavy ions at ultra-relativistic speeds, allowing scientists to explore nuclear matter under extreme conditions of high temperature and density. In these relativistic heavy-ion collisions, the intense energy melts the nuclear boundaries of the colliding ultrarelativistic nuclei, leading to the deconfinement of quarks and gluons. This results in the formation of QGP, where quarks and gluons are no longer bound within individual hadrons, enabling them to move freely and interact, thereby mimicking the conditions of the early universe.

As the pressure gradient increases, the system expands and cools down, resulting in a phase transition from the partonic phase to the hadronic phase. At the chemical freeze-out temperature, inelastic processes cease, stabilizing the chemical composition with no further particle production. Following this, hadrons interact elastically, allowing their momenta to evolve until reaching the kinetic freeze-out temperature. At this point, elastic collisions also cease, and hadrons with fixed momentum stream toward the detectors.

Hadronic resonances serve as valuable probes of the hadronic phase created between the two freeze-out stages in ultrarelativistic heavy-ion collisions. By studying these resonances, researchers can gain insights into the properties and dynamics of the medium formed during these high-energy collisions, as their lifetimes are comparable to that of the hadronic phase. As the collision system evolves, resonances may decay within the medium before thermal freeze-out, leading to a reduction in their yield due to the rescattering of their daughter particles. This effect alters the momenta of the daughter particles, affecting the reconstructed resonance signal. The interplay between medium effects such as rescattering and regeneration is investigated by comparing the ratios of resonance to stable hadron yields with similar quark content.

The $\Lambda(1520)$ resonance is significant due to its lifetime of approximately 12.6 fm/c, which lies between the shorter lifetime of the $K^{*0}(892)$ (4 fm/c) and the longer lifetime of the $\phi(1020)$ (42 fm/c) resonances. The yield of the $K^{*0}(892)$ resonance is gradually sup-

pressed as centrality increases in A–A collisions, with slight suppression also observed for high multiplicity pp collisions. The absence of such suppression for the $\phi(1020)$ resonance can be attributed to its longer lifetime, which allows it to decay outside the hadronic phase. In contrast, central Pb–Pb collisions show a clear suppression of the $\Lambda(1520)/\Lambda$ ratio, attributed to possible rescattering effects in the hadronic phase. However, the behavior of the $\Lambda(1520)$ resonance differs in p–Pb collisions, where the $\Lambda(1520)/\Lambda$ ratio remains constant as a function of $\langle dN_{\rm ch}/d\eta\rangle|_{|\eta|<0.5}$.

This thesis presents the first measurements of the production yields of the baryonic resonance $\Lambda(1520)$ at mid-rapidity ($|y| < 0.5$) in pp collisions at $\sqrt{s} = 5.02$ and 13 TeV as a function of charged-particle multiplicity. Additionally, the study extends to the production of $\Lambda(1520)$ and $\mathrm{K}^{*0}(892)$ resonances in high multiplicity pp collisions at $\sqrt{s} = 13, \mathrm{TeV}$. The $\Lambda(1520)$ resonance is reconstructed using the invariant mass reconstruction technique via its hadronic decay channel $\Lambda(1520) \rightarrow pK^-$, with a branching ratio of $22.5 \pm 0.5\%$. The $\mathrm{K}^{*0}(892)$ resonance is reconstructed through its hadronic decay channel $\mathrm{K}^{*0}(892) \rightarrow \mathrm{K}^{\mp}\pi^{\pm}$, with a branching ratio of $66 \pm 5\%$.

The resonance signal is reconstructed using the invariant mass technique and the raw yield is extracted using the bin counting method followed by applying various correction factors to obtain the corrected $p_{\rm T}$-spectra. The corrected transverse momentum ($p_{\rm T}$) spectra reveal a clear trend of hardening with increasing multiplicity. The $p_{\rm T}$-integrated yield ($\langle \mathrm{d}N/\mathrm{d}y\rangle$) increases with $\langle dN_{\rm ch}/d\eta\rangle|_{|\eta|<0.5}$ across the considered multiplicity classes, remaining consistent across collision systems and energies. This indicates that the production rate of $\Lambda(1520)$ is largely driven by multiplicity (or event activity) rather than the specific collision system or energy.

The mean transverse momentum ($\langle p_{\rm T}\rangle$) across different multiplicity classes shows an increase with multiplicity with no significant energy dependence. The slope of the $\langle p_{\rm T}\rangle$ trend in pp collisions is observed to be steeper than p–Pb collisions and considerably greater than the Pb–Pb collisions. Further, the $\langle p_{\rm T}\rangle$ values for $\Lambda(1520)$ is compared with other particle species and no mass ordering is observed for pp collisions at $\sqrt{s} = 13$ TeV. However, notable differences in the $\langle p_{\rm T}\rangle$ of baryons and mesons are observed.

The $\Lambda(1520)/\mathrm{K}^{\pm}$ ratio is measured as a function of $p_{\rm T}$ across various multiplicity

classes, revealing a consistent increase with p_{T}, followed by a plateau, without distinct peaks associated with radial flow effects in larger systems. The yield ratio of $\Lambda(1520)/\Lambda$ is estimated for different multiplicity classes in pp collisions at $\sqrt{s} = 5.02$ and 13 TeV and appears to be constant within the uncertainties.

The study of the $\Lambda(1520)$ and $\mathrm{K}^{*0}(892)$ resonances in high-multiplicity pp collisions is crucial for deepening our understanding of the properties of the hadronic phase and the production mechanisms of resonances in high multiplicity. This highlights the importance of resonances like $\Lambda(1520)$ and $\mathrm{K}^{*0}(892)$ as probes of the hadronic phase, which might be created in small systems, while also serving as a baseline for exploring such phenomena in high-energy heavy-ion collisions.

Contents

List of Publications

Data paper and Analysis Notes:

The ALICE data paper on "Multiplicity dependence of $\Lambda(1520)$ resonance production in pp collisions at $\sqrt{s} = 5.02$ and 13 TeV" is submitted to the ALICE website and is under IRC review. To be published in the European Physical Journal C (EPJC). Planning for paper proposal on "Measurement of $K^{*0}(892)$ and $\Lambda(1520)$ production in high multiplicity proton-proton collisions at $\sqrt{s} = 13$ TeV with ALICE at LHC"

- Measurement of $\Lambda(1520)$ baryons at mid-rapidity in pp collisions at $\sqrt{s} = 5.02$ TeV as a function of charged-particle multiplicity (alice-notes.web.cern.ch/node/1234)
- Measurement of $\Lambda(1520)$ resonance production in pp collisions at $\sqrt{s} = 13$ TeV as a function of charged-particle multiplicity. (alice-notes.web.cern.ch/node/1235)
- Measurement of $K^{*0}(892)$ resonance production in high-multiplicity pp collisions at $\sqrt{s} = 13$ TeV with ALICE (alice-notes.web.cern.ch/node/1448)
- Measurement of $\Lambda(1520)$ resonance production in high-multiplicity pp collisions at $\sqrt{s} = 13$ TeV with ALICE (alice-notes.web.cern.ch/node/1447)

Service Work and ALICE Shifts

I participated in the QC shift during the ALICE experiment. Additionally, I was involved in Train Operations as one of three regional shift-like operators (Hyperloop Operator). As part of fulfilling the Ph.D. requirements within the ALICE collaboration, I completed six months of service work.

Conference Publications:

- **Padhan S.**, *"Multiplicity-dependent study of* $\Lambda(1520)$ *resonance production in pp collisions at* $\sqrt{s} = 5.02$ *and 13 TeV with ALICE"*, presented at the ICHEP 2022 conference in Bologna, Italy, 6-13 July 2022, published in PoS(ICHEP2022)1186.

- Das, Santosh K., **Padhan S.**, and others, *"Dynamics of Hot QCD Matter – Current Status and Developments"*, presented at the Hot QCD Matter 2022 conference at IIT GOA, 12-14 May 2022, published in Int.J.Mod.Phys. E 31 (2022) 12.

- **Padhan S.**, *"Understanding the rescattering effect on* $\Lambda(1520)$ *resonance production in different systems and collision energies with ALICE at LHC"*, presented at the LHCP 2023 conference in Belgrade, Serbia, 22-26 May 2023, published in PoS LHCP2023 (2024) 269.

- **Padhan S.**, *"Studying the internal structure of exotic hadrons and bound states using spectroscopy and complementary techniques with ALICE"*, presented at the 16th International Conference on Heavy Quarks and Leptons (HQL2023) in TIFR, Mumbai, Maharashtra, India, 28 November-2 December 2023, published in PoS HQL2023 (2024) 042.

- **Padhan S.**, *"Insights into the internal structure of exotic resonances with ALICE"*, presented at the DAE NPSYMP 2023, IIT Indore, Simrol, Madhya Pradesh, India, 9-13 December 2023, published in DAE Symp.Nucl. Phys. 67 (2024) 1005-1006.

- **Padhan S.**, *"Exploring the internal structure of exotic resonances with ALICE"*, presented at Quark Matter 2023 in Houston, Texas, USA, 3-9 September 2023, published in EPJ Web Conf. 296 (2024) 12008.

- **Padhan S.**, *"Measurement of the Production of Hadronic Resonances in Small Systems with ALICE at LHC"*, presented at the XV DAE-BRNS High Energy Physics Symposium 2022, IISER Mohali, India, 12–16 December 2022, published in Springer Proc.Phys. 304 (2024) 183-186.

- **Padhan S.**, *" Exploring the* $\Lambda(1520)$ *resonance in high-multiplicity proton-proton collisions at LHC energies with ALICE"*, presented at 42nd International Conference on High Energy Physics, 18-24 July 2024, Prague, Czech Republic, to be published in PoS(ICHEP2024)570. (submitted in PoS, not yet published)

Refereed Journal Publications:

- Acharya S...**Padhan S.** et. al. [ALICE collaboration], *"$K^{*0}(892)$ and $\phi(1020)$ production in p–Pb collisions at $\sqrt{s_{\rm NN}} = 8.16$ TeV"*, Phys. Rev. C 107 (2023) 5, 055201

- Acharya S...**Padhan S.** et. al. [ALICE collaboration], *"Multiplicity and rapidity dependence of $K^{*0}(892)$ and $\phi(1020)$ production in p–Pb collisions at $\sqrt{s_{\rm NN}} = 5.02$ TeV"*, Eur. Phys. J. C 83, 540 (2023)

- Acharya S...**Padhan S.** et. al. [ALICE collaboration], *"$\Sigma(1385)^{\pm}$ resonance production in Pb–Pb collisions at $\sqrt{s_{\rm NN}} = 5.02$ TeV"*, Eur. Phys. J. C 83, 351 (2023)

- Acharya S...**Padhan S.** et. al. [ALICE collaboration], *"Direct observation of the dead-cone effect in quantum chromodynamics"*,Nature Phys. 605 (2022) 440–446

- Acharya S...**Padhan S.** et. al. [ALICE collaboration], *"Production of pions, kaons, (anti-)protons and ϕ mesons in Xe–Xe collisions at $\sqrt{s_{\rm NN}} = 5.44$ TeV"*, Eur. Phys. J. C 81 (2021) 7, 584

- Acharya S...**Padhan S.** et. al. [ALICE collaboration], *"Underlying-event properties in pp and p–Pb collisions at $\sqrt{s_{\rm NN}} = 5.02$ TeV"*,JHEP 06 (2023) 023

Conference and Workshop

- Poster - *"Exploring the $\Lambda(1520)$ resonance in high-multiplicity proton-proton collisions at LHC energies with ALICE"*, **42nd International Conference on High Energy Physics**, 18-24 July 2024, Prague, Czech Republic

- Oral - *"Insights into the internal structure of exotic resonances with ALICE"*, **67th DAE Symposium on Nuclear Physics**, 9-13 December 2023, IIT Indore, India

- Plenary Talk - *"Studying the internal structure of exotic hadrons and bound states using spectroscopy and complementary techniques with ALICE"*, **16th International Conference on Heavy Quarks and Leptons (HQL2023)**, 28 November - 2 December 2023, TIFR, Mumbai, India

- Oral - *"Exploring the internal structure of exotic resonances with ALICE"*, **Quark Matter 2023**, 3-9 September 2023, Houston, Texas, USA

- Poster - *"Understanding the rescattering effect on* $\Lambda(1520)$ *resonance production in different systems and collision energies with ALICE"*, **LHCP 2023 - 11th Large Hadron Collider Physics Conference**, 22–26 May 2023, Belgrade, Serbia

- Oral - *"Probing the hadronic phase with resonance production in pp, p-Pb, and Pb-Pb collisions with ALICE at LHC"*, **The 9th Asian Triangle Heavy-Ion Conference (ATHIC 2023)**, 23–27 April 2023, JMS Aster Plaza, Hiroshima, Japan

- Oral - *"Latest results on hadronic resonance production in small systems with ALICE"*, **International Conference on Physics and Astrophysics of Quark Gluon Plasma (ICPAQGP-2023)**, 7-10 February 2023, Puri, Odisha, India

- Oral - *"Measurement of hadronic resonance production in small systems with ALICE"*, **XV DAE-BRNS High Energy Physics Symposium 2022**, 12–16 December 2022, IISER Mohali, India

- Poster - *"Multiplicity-dependent study of* $\Lambda(1520)$ *resonance production in pp collisions at* $\sqrt{s} = 5.02$ *and 13 TeV with ALICE"*, **ICHEP 2022 - XLI International Conference on High Energy Physics**, 6-13 July 2022, Bologna, Italy

- Poster - *"Multiplicity-dependent study of* $\Lambda(1520)$ *resonance production in pp collisions at* $\sqrt{s} = 5.02$ *and 13 TeV with ALICE"*, **International Conference on Strangeness in Quark Matter (SQM 2022)**, 13-17 June 2022, Busan, Republic of Korea

- Poster - *"Multiplicity-dependent study of* $\Lambda(1520)$ *resonance production in pp collisions at* $\sqrt{s} = 5.02$ *and 13 TeV with ALICE"*, **Large Hadron Collider Physics (LHCP) 2022**, 16-20 May 2022, Taiwan

- Oral - *"Multiplicity-dependent study of* $\Lambda(1520)$ *resonance production in pp collisions at* $\sqrt{s} = 5.02$ *and 13 TeV with ALICE"*, **Hot QCD Matter 2022**, 12-14 May 2022, IIT GOA, India

- Poster - *"Multiplicity-dependent study of* $\Lambda(1520)$ *resonance production in pp collisions at* $\sqrt{s} = 5.02$ *and 13 TeV with ALICE"*, **Quark Matter 2022**, 4-10 April 2022, Krakow, Poland

List of Figures

List of Tables

Chapter 1

Introduction

The study of physics seeks to unravel the fundamental principles that govern the natural world. It aims to explain the underlying mechanisms behind everything one observes and experiences. It is all about understanding how the universe operates and what its constituents are made up of. Physics delves into the fundamental components of matter, seeking to understand the intricacies of particles, forces, and interactions that shape the universe. Physicists investigate the basic building blocks of matter and examine their behaviour under various conditions. For centuries, they have been posing questions like "What is everything made up of?". This enduring curiosity has driven countless explorations and research efforts, significantly expanding our understanding of the universe.

In the early 20th century, groundbreaking discoveries revolutionized our understanding of the microscopic world. The finding of the electron by J.J. Thomson in 1897 was a breakthrough, providing a glimpse into the realm of subatomic particles. In 1917, Ernest Rutherford's experiments provided compelling evidence for the existence of the proton, which he identified as the positively charged particle residing in the nucleus of atoms[1]. This discovery, along with Thomson's findings, significantly contributed to our understanding of the structure of atoms and the fundamental constituents of matter. Further contributions from pioneers such as Max Planck, Albert Einstein, and Niels Bohr in quantum mechanics and special relativity reshaped our understanding of particle behaviour at the smallest scales[2–5].

As physicists investigated deeper into the mysteries of the universe, cosmic ray exper-

iments conducted in the early 20th century unveiled the existence of previously unknown particles such as muons and pions. These discoveries provided valuable insights into the structure of matter [6–8]. Moreover, these experiments laid the foundation for the development of particle accelerators. These powerful machines enabled scientists to probe matter at higher energies, leading to a more profound understanding of particle behaviour and interactions [9].

In 1968, the quest for unravelling the fundamental nature of matter took a transformative leap with the deep inelastic scattering experiment conducted at the Stanford Linear Accelerator Center (SLAC) [10]. This groundbreaking experiment challenged existing notions and revealed important details about the inner workings of subatomic particles. It provided substantial evidence that protons and neutrons, previously considered elementary particles, possess a substructure composed of fundamental particles known as quarks and gluons. Quarks are the fundamental constituents of hadrons. The deep inelastic scattering (DIS) process allowed us to observe the interactions between the high-energy electrons and quarks within nucleons, providing crucial insights into the internal dynamics of subatomic particles. Quarks, bound together by the strong force mediated by particles called gluons, form the basis of the Standard Model of particle physics.

1.1 Standard Model

The Standard Model[11], developed through decades of experimental observations and theoretical advancements, provides a comprehensive framework for understanding the fundamental particles of matter and their interactions. It describes three of the four fundamental forces of nature – the electromagnetic, weak, and strong forces – and has led to remarkable discoveries, such as the prediction and subsequent discovery of the Higgs boson at the Large Hadron Collider (LHC) in 2012.

All constituents in the universe are composed of these fundamental particles, which interact through the fundamental interactions: Electromagnetic, Weak, and Strong interactions between elementary particles. While the Standard Model elucidates these forces, it does not encompass the most familiar force, the gravitational force. The Standard

Model describes the interactions among these essential building blocks. Its mathematical foundation lies in Quantum Field Theory (QFT).

The particles described by the Standard Model are shown in Figure 1.1, showing the diverse array of fundamental constituents and their interactions. The four fundamental in-

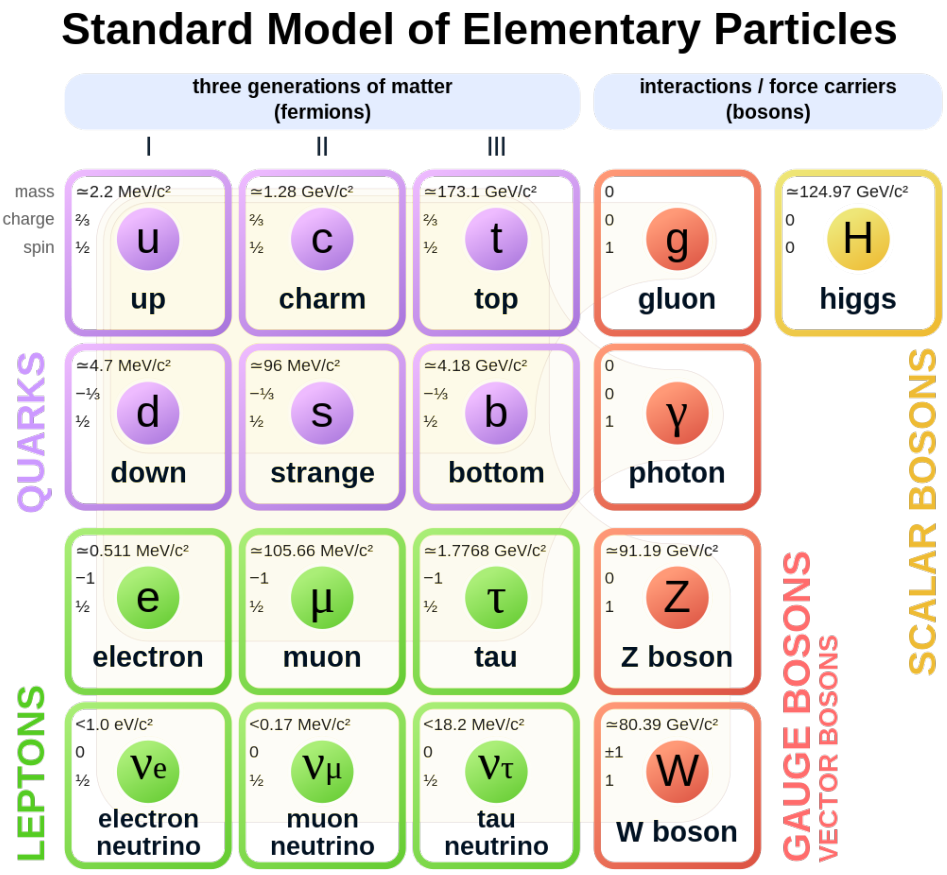

Figure 1.1: The standard model of particle physics

teractions [12] governing the physical forces in our universe exhibit distinct characteristics in terms of range and strength.

Gravitational Force:

- **Mediator (Hypothetical Graviton):** The gravitational force, as described by Einstein's theory of general relativity, is mediated by the hypothetical particle called the graviton. However, the graviton has not been experimentally detected.

- **Range and Strength:** It acts over infinite distances and is universally attractive, yet it is the weakest of the fundamental forces, by many orders of magnitude compared to the others.

- **Role:** Gravity governs the motion of massive objects in the universe and determines the structure of large-scale cosmic systems such as galaxies and clusters.

Electromagnetic Force:

- **Mediator (Photon):** The electromagnetic force is mediated by photons, which are massless particles.

- **Range and Strength:** Like gravity, it also acts over infinite distances, but it is significantly stronger, being approximately 10^{36} times stronger than gravity.

- **Role:** This force governs the interactions between electrically charged particles, including atoms and molecules, and is responsible for light, electricity, and magnetism.

Weak Force:

- **Mediators ($W^{\pm}$ and Z^0):** The weak force is mediated by the $W^{\pm}$ and Z^0, which are massive particles.

- **Range and Strength:** It operates at subatomic scales, with a very short range due to the large masses of the bosons. It is much weaker than the electromagnetic and strong forces but stronger than gravity.

- **Role:** The weak force is responsible for processes such as beta decay, neutrino interactions, and the transformation of one type of quark into another.

Strong Force:

- **Mediator (Gluon):** The strong force is mediated by gluons, which are massless particles.

- **Range and Strength:** It operates over extremely short distances, within the scale of atomic nuclei. It is the strongest fundamental force, approximately 100 times stronger than the electromagnetic force and 10^{38} times stronger than gravity.

- **Role:** Binds quarks together to form composite particles such as protons, neutrons, and hadrons, the strong force plays a pivotal role in understanding the structure and stability of atomic nuclei, overcoming the electromagnetic repulsion between positively charged protons.

The fundamental particles, serving as the basic constituents of the theory, are classified into various categories. According to their spin, particles are divided into two main groups: fermions and bosons. Fermions, characterized by half-integral spin are further divided into two distinct groups: quarks and leptons.

Quarks:

Quarks are fundamental particles with fractional electric charges. They come in six flavours, organized into three generations:

- First Generation: Up (u) and Down (d) quarks, which combine to form protons and neutrons.

- Second Generation: Charm (c) and Strange (s) quarks, which are heavier counterparts of the first generation quarks.

- Third Generation: Top (t) and Bottom (b) quarks, the heaviest and most massive quarks, with the top quark being the most massive known elementary particle.

All quarks are spin 1/2 fermions and come in three distinct colours: red, green, and blue. Each quark has an antiparticle counterpart with an opposite charge. The combination of quarks and anti-quarks form colour-neutral composite particles known as hadrons. Baryons, such as protons and neutrons, consist of three quarks, while mesons comprise a quark and an anti-quark pair. Quarks can interact among themselves via strong, weak, and electromagnetic interactions.

Leptons:

Leptons are another class of fundamental particles, which include:

- First Generation: Electron (e^-) and Electron Neutrino (ν_e).
- Second Generation: Muon (μ^-) and Muon Neutrino (ν_μ).
- Third Generation: Tau (τ^-) and Tau Neutrino (ν_τ).

Each generation contains particles that are similar in their properties but differ in their masses, with particles in higher generations being more massive than those in lower generations. It is important to note that while the electrons, muons, and taus can interact via both electromagnetic and weak forces, the neutrinos which are nearly massless, can interact via the weak force only.

Scalar Boson (Higgs Boson):

The Higgs boson, a scalar particle with spin 0, plays an important role in the mechanism of electroweak symmetry breaking, providing mass to other particles. The discovery of the Higgs boson in 2012 at CERN's Large Hadron Collider (LHC) by experiments conducted by ATLAS and CMS confirmed a key prediction made by Peter Higgs in 1964 [13, 14]. For this groundbreaking theoretical work, Higgs, along with François Englert, were jointly awarded the Nobel Prize in Physics in 2013 [15].

The Higgs mechanism explains how elementary particles acquire mass. According to this mechanism, particles interact with the Higgs field, and the strength of this interaction determines the mass of the particle. Particles that interact more strongly with the Higgs field acquire greater mass, while those with weaker interactions have lower masses. In essence, the Higgs boson acts as the mediator of this interaction, providing a mechanism for particles to acquire mass in the universe. This concept is central to our understanding of the fundamental forces and particles that govern the structure and behaviour of the universe.

Vector Bosons:

The fundamental vector bosons are particles with non-zero integral spin and serve as the mediators of fundamental forces within the Standard Model. These are also known as gauge bosons. They include:

- Photon (γ): Responsible for mediating the electromagnetic force, facilitating interactions between charged particles.
- $W^{\pm}$ and Z^0 Bosons: Mediate the weak nuclear force, governing processes like beta decay and neutrino interactions. Unlike photons, they possess mass. The $W^{\pm}$ bosons (with a mass of approximately 80.3 GeV) and the Z^0 boson (with a mass of around 91.1 GeV) play crucial roles in weak interactions.
- Gluon (g): Acts as the force carrier for the strong force, binding quarks together within protons, neutrons, and other hadrons. Gluons are massless and bi-coloured particles exhibiting self-interaction. It is essential for asymptotic freedom and confinement of quark.

1.2 Quantum Chromodynamics

Quantum Chromodynamics (QCD) is a fundamental theory in particle physics that describes the interactions between quarks and gluons, the fundamental constituents of matter. This theory governs the binding of quarks which form hadrons, including familiar particles like protons and neutrons. QCD differs significantly from QED because it involves three types of colour charges, unlike QED, which has just one type of conserved charge. This distinction highlights the complex nature of quantum chromodynamics. Additionally, QCD is characterized by the phenomenon of gluon self-interaction, where gluons, the force carriers of the strong interaction, can interact with each other due to their colour charge. This self-interaction adds to the complexity and richness of quantum chromodynamics, distinguishing it further from other quantum field theories.

The Quantum Chromodynamics Lagrangian density, expressed as the sum of the gluon ($\mathcal{L}_{\text{gluon}}$) and quark ($\mathcal{L}_{\text{quark}}$) Lagrangians is given by:

$$\mathcal{L}_{\text{QCD}} = \mathcal{L}_{\text{gluon}} + \mathcal{L}_{\text{quark}} = -\frac{1}{4} G^a_{\mu\nu} G^{\mu\nu}_a + \sum_f \bar{\psi}_f (i\gamma^\mu D_\mu - m_f)\psi_f \tag{1.1}$$

where:

- $\mathcal{L}_{\text{QCD}}$ is the QCD Lagrangian density,
- $\mathcal{L}_{\text{gluon}} = -\frac{1}{4} G^a_{\mu\nu} G^{\mu\nu}_a$ is the gluon Lagrangian,
- $\mathcal{L}_{\text{quark}} = \sum_f \bar{\psi}_f (i\gamma^\mu D_\mu - m_f)\psi_f$ is the quark Lagrangian,
- $G^a_{\mu\nu}$ is the field strength tensors for the gluon field,
- ψ_f represents the quark field for each quark flavor f,
- m_f denotes the mass of the quark,
- γ^μ is the Dirac gamma matrix, and
- D_μ is the covariant derivative, incorporating the gluon field.

This Lagrangian consists of two terms: the first term describes the kinetic energy of the gluon field, while the second term describes the kinetic energy and mass of the quark fields.

$$D_\mu = \partial_\mu - ig\frac{\lambda^a}{2} A^a_\mu(x), \tag{1.2}$$

$$G^a_{\mu\nu}(x) = \partial_\mu A^a_\nu(x) - \partial_\nu A^a_\mu(x) + g f^{abc} A^b_\mu(x) A^c_\nu(x), \tag{1.3}$$

where:

- f^{abc}: Represents the structure constant of the SU(3) group.
- λ^a: Represents the Gell-Mann matrix, which is a mathematical object used to describe the properties of quarks within the framework of QCD. These are also the generators of SU(3) representation.

- $A^a_{(x)}$: The eight vector gauge fields associated with QCD and represent the gluon fields.

The concept of "colour charge" arises within QCD, with quarks carrying colour charge (red, green, or blue) and gluons serving as carriers of the strong force, also possessing colour charge. The notion of colour in QCD emerged from the necessity to explain observations in strong force interactions, initially proposed by physicists Murray Gell-Mann and George Zweig in the 1960s. In QCD, quarks combine in such a way that their overall combination forms a colour singlet state of observed hadrons. This concept, known as colour singlet states, is crucial in understanding the confinement of quarks within hadrons. Any attempt to isolate a single quark would result in a violation of colour neutrality, necessitating the formation of bound states where quarks combine to form colour singlet combinations within hadrons.

Colour Confinement

Gluons, unlike photons, exhibit self-interaction due to their colour charge. Despite being massless, gluons exert their influence over very short distances, leading to the emergence of a short-range colour force. In the context of quark-antiquark interactions, this force is described by the Cornell potential, which comprises two terms. The expression for the Cornell potential is given by:

$$V(r) = -\frac{4}{3}\frac{\alpha_s}{r} + kr \tag{1.4}$$

where α_s represents the strong coupling constant, and the term kr accounts for linear confinement at large distances, with k being a constant related to the string tension. The Coulomb potential term ($\propto \frac{1}{r}$) dominates at small distances r, indicating the behaviour of the strong force between quarks at short distances. In contrast, the linear term is responsible for the confinement of quarks at larger distances. The force between quarks increases linearly with distance, preventing quarks from being isolated.

Asymptotic Freedom

The properties of Quantum Chromodynamics, particularly the behaviour of the strong interaction, can be understood by studying the strong interaction coupling constant denoted by α_s. This coupling constant describes the strength of the strong force between quarks and gluons, analogous to the electromagnetic coupling constant in Quantum Electrodynamics. Understanding the behaviour of α_s at different energy scales is essential for unravelling the dynamics of QCD and the phenomenon it governs. The α_s is expressed as

$$\alpha_s(Q^2) = \frac{4\pi}{11 - \frac{2n_f}{3}} \ln \frac{Q^2}{\Lambda^2} \tag{1.5}$$

where:

$\alpha_s(Q^2)$ represents the QCD running coupling constant n_f is the number of active quark flavours, Λ represents the QCD scale parameter, and Q^2 is the momentum transfer.

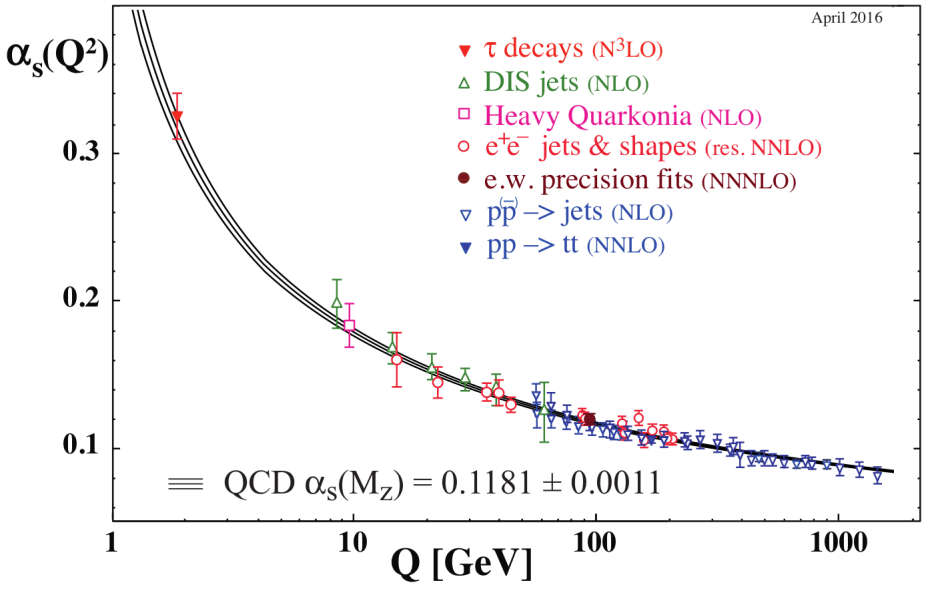

Figure 1.2: QCD running coupling constant $\alpha_s(Q^2)$ with momentum transfer Q^2 [16].

Figure 1.2 shows the variation of $\alpha_s(Q^2)$ with Q^2. The equation indicates that as momentum transfer increases, the strong interaction coupling constant decreases, eventually approaching zero for large values of Q^2.

This behaviour, is known as " asymptotic freedom" [17, 18]. Conversely, $\alpha_s(Q^2)$ increases at low momentum transfers and significant distances, preventing colour-charged particles from existing independently—a phenomenon termed as colour confinement. Consequently, under extreme conditions of temperature and energy density, the QCD medium is expected to transition into a deconfined state, allowing quarks and gluons to interact freely via colour charge.

1.3 Phase Transition in QCD

The QCD phase diagram provides a comprehensive view of the different phases of nuclear matter as a function of temperature (T) and baryon chemical potential (μ_B), where μ_B is related to the net baryon density of the matter. The μ_B is a crucial parameter in the QCD phase diagram, representing the energy required to remove or add a baryon at fixed temperature and pressure.

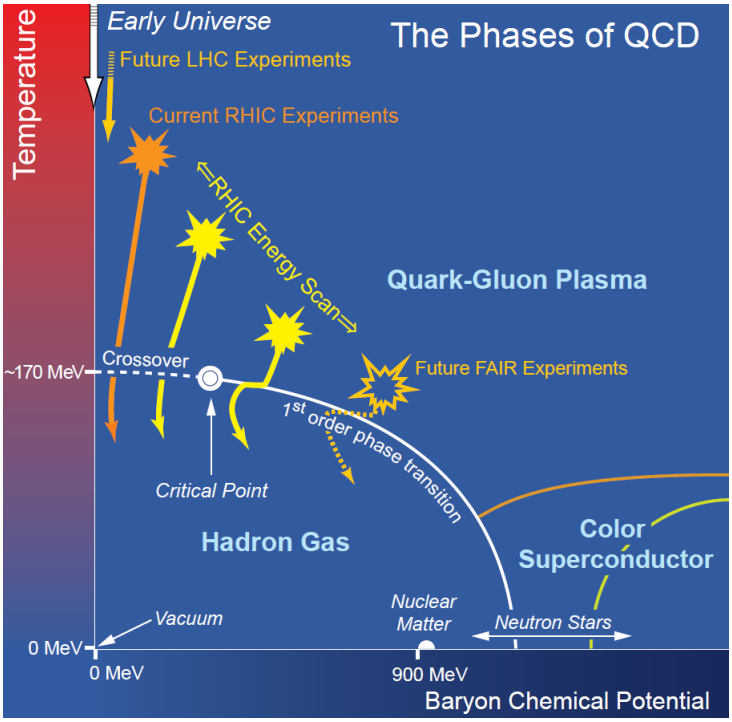

Figure 1.3: QCD phase diagram illustrating different states of matter under varying temperature and baryon chemical potential [19].

The QCD phase diagram as shown in Figure 1.3 provides valuable insights into the

behaviour of nuclear matter under extreme conditions, such as those encountered in high-energy collisions and astrophysical environments. Understanding the different phases in the phase diagram is essential to comprehend the origin of the early universe, neutron stars. The different phases are briefly outlined below [19].

Ordinary Nuclear Matter

At low temperatures ($T \sim 0$), ordinary nuclear matter exists with non-zero net baryon density ($\mu_B \approx 1$ GeV). This region of the phase diagram indicate the presence of atomic nuclei with stable configurations.

Cold Dense Matter

In the region corresponding to cold, dense matter, such as neutron stars, the temperature becomes very low while the baryon chemical potential is typically higher. The density of baryons is significantly higher compared to ordinary nuclear matter.

Color Superconductor Phase

At higher densities and slightly higher temperatures, the color superconducting phase occurs. In this phase, the formation of Cooper pairs by quarks leads to the breaking of chiral symmetry, indicating a transition to a new state of matter.

Hadron Gas Phase

In the region corresponding to the hadron gas phase, the temperature is relatively high, while the baryon chemical potential remains significant. In this phase, nucleons interact with each other to form hadrons, resonances, and pions. The presence of baryons is substantial, contributing to the overall baryon density of the system.

Quark-Gluon Plasma (QGP)

At high temperatures and densities, where the QGP phase exists, both the temperature and the baryon chemical potential can vary. The system reaches temperatures where the

binding between quarks and gluons becomes weak, leading to the deconfinement of quarks and gluons.

Critical Point and Crossover

The critical point marks the endpoint of the first-order phase transition between the hadron gas phase and the QGP phase. At this point, the temperature and the baryon chemical potential reach critical values where the nature of the phase transition changes. The critical point represents a unique region of the phase diagram where fluctuations in temperature and baryon chemical potential play a crucial role in the behaviour of the system.

In heavy-ion collisions studied by ALICE, the crossover between the hadron gas phase and the Quark-Gluon Plasma (QGP) phase occurs at $T \sim 156$ MeV. This crossover is characterized by a smooth transition between the two phases, without any abrupt change in the thermodynamic properties of the system.

In the QCD phase diagram, LHC experiments would typically fall into the region characterized by high-temperature and low-baryon chemical potential, which is close to the QGP phase. Collisions predominantly involving ultra-relativistic heavy-ion collisions result in the formation of a medium with extremely high temperature and low net baryon numbers, close to zero. Therefore these experiments are essential for studying the properties of the QGP phase and gaining insights into the behaviour of nuclear matter under extreme temperatures and densities.

1.4 Heavy-ion Collision and Space-time Evolution

Quark-Gluon Plasma (QGP), believed to have formed a few microseconds after the Big Bang, existed for a fleeting moment in an intensely hot universe, reaching temperatures of about 2000 billion degrees Celsius. It is also believed that QGP might exist within the core of neutron stars due to the extreme density of nuclear matter. Since we cannot travel back in time or explore the interior of neutron stars to directly study QGP, scientists recreate these conditions in the laboratory by colliding heavy ions at ultra-relativistic speeds. These collisions allow researchers to investigate the QGP and matter under extreme conditions. The Relativistic Heavy Ion Collider (RHIC) was established in 2000 at Brookhaven National Laboratory. Later, the Large Hadron Collider at CERN, operational since 2008, surpassed RHIC in energy capabilities, reaching TeV scales. Through these collisions, researchers seek to recreate early universe conditions, enabling a profound investigation into the properties of QGP and the fundamental nature of matter.

In Quantum Chromodynamics, quarks are confined within hadrons—such as protons and neutrons—by the strong force, mediated by the exchange of gluons. This phenomenon is called confinement, where quarks cannot move freely outside their bound states. However, at extremely high energies, the strong force weakens due to the decrease in the coupling constant, allowing quarks and gluons, known collectively as partons, to move freely in a process called deconfinement. This state is central to the formation of QGP, a phase of matter where quarks and gluons are no longer bound within hadrons.

In ultra-relativistic heavy-ion collisions, such as those conducted at LHC, nuclei made up of protons and neutrons collide at very high speeds. These collisions create conditions of extremely high nuclear density, causing hadrons to overlap and the quarks within them to lose their individual identities. Colour screening, a phenomenon that occurs when the density becomes so high that the strong force is screened, allows quarks to move freely beyond their typical confinement. This leads to a deconfinement of quarks, where the internal structure of hadrons breaks down.

As the kinetic energy from the colliding nuclei is converted into intense heat, hadrons melt due to the inelastic collisions, and a hot, dense soup of free quarks and gluons is formed known as QGP. This state of matter closely resembles the conditions of the early

universe just after the Big Bang, enabling scientists to study the properties of matter under extreme temperatures and densities and to better understand the fundamental nature of the strong interaction.

During heavy-ion collisions, various stages occur, including the initial collision leading to the formation of a fireball. This fireball evolves through stages depicted in Figure 1.4 [20, 21].

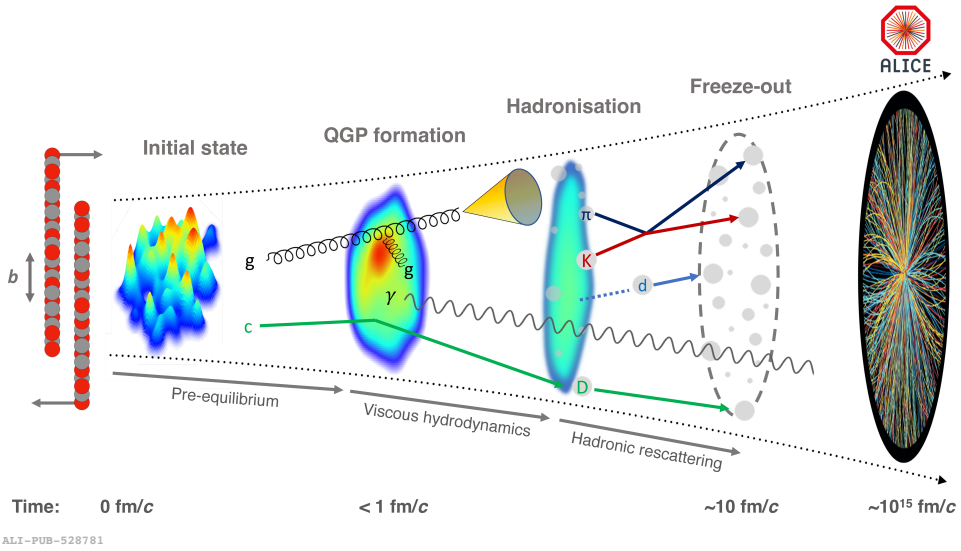

Figure 1.4: Different stages of a heavy-ion collision at LHC energies[21].

Bjorken proposed a model for the space-time evolution of fireballs in heavy-ion collisions[22]. According to this model, the fireball rapidly expands along the beam axis with a boost-invariant flow profile, making system properties independent of the longitudinal coordinate (z) and dependent only on the proper time (τ). Therefore, the proper time (τ) of evolution is calculated using $\tau = \sqrt{t^2 - z^2}$ from the space-time hyperbola, as depicted in Figure 1.5.

In the initial stage of heavy-ion collisions, ultra-relativistic nuclei collide head-on, resulting in a sudden release of energy due to hard scatterings between constituent partons. This intense energy release marks the beginning of the collision process, depicted by the system's evolution in space-time coordinates (z, t).

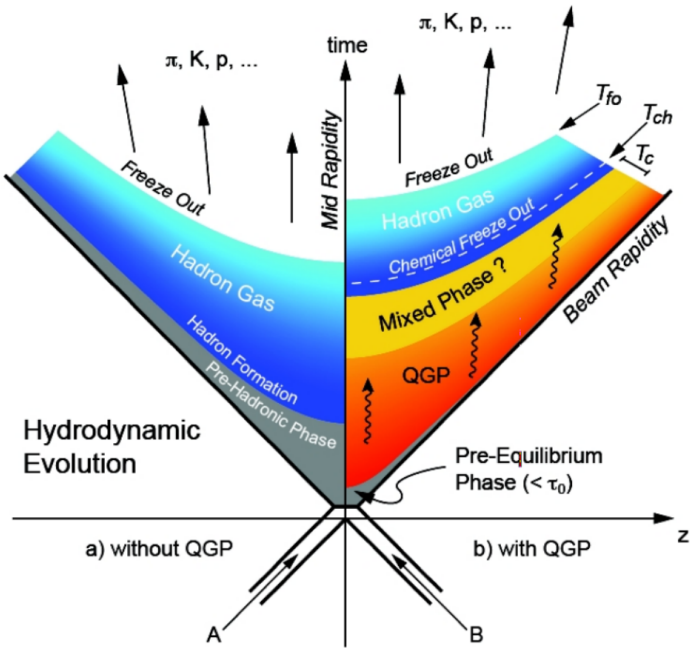

Figure 1.5: The schematic diagram of space-time evolution of relativistic heavy-ion collision [23].

1. **Pre-Equilibrium Stage:**

   Transitioning from the initial stage, the system undergoes the pre-equilibrium phase, characterized by the deconfinement of quarks and gluons through interactions among the colliding nucleons. This process leads to the generation of high-momentum partons, which undergo hard scatterings, producing jets or heavy quarks, along with the emission of prompt photons.

2. **Thermal Equilibrium Stage:**

   Following the pre-equilibrium phase, the system transitions into a state known as QGP due to multiple partonic interactions. This phase is characterized by its hot and dense thermally equilibrated nature, exhibiting almost perfect fluid behaviour and allowing for the application of hydrodynamic descriptions. During this stage, as a result of the pressure gradient within the medium, the system collectively expands and undergoes cooling.

3. **Hadronization Stage:**

   Hadronization occurs as the system cools to its critical temperature ($T = T_c$), resulting in a mixed phase of QGP and hadrons. At RHIC and LHC energies, this phase transition is known as a crossover, resembling a smooth transition from the QGP phase to the hadronic phase.

4. **Chemical Freeze-Out:**

   Collective expansion in the hadronic phase is sustained by ongoing interactions among hadrons until chemical freeze-out when the temperature drops to $T = T_{\mathrm{Ch}}$. All inelastic processes cease, and the chemical composition of the system remains unchanged, with no new particle production.

5. **Kinetic Freeze-Out:**

   After chemical freeze-out, hadrons continue to interact elastically, allowing their momenta to evolve until the system reaches the kinetic freeze-out temperature, T_{kin}. This temperature is achieved at approximately $\tau \sim 10$ fm/c. At this point, the particle momenta are fixed. The particles then travel towards the ALICE detector, where they are measured at $\tau \sim 10^{15}$ fm/c after the initial collision. At the kinetic freeze-out stage, the mean free path of the hadrons exceeds the size of the system, meaning that particles are no longer subject to significant interactions and can travel freely to the detector.

1.5 Quark-Gluon Plasma (QGP): Characteristics and Signatures

Quark-Gluon Plasma is a unique and transient state of matter that offers crucial insights into the early universe and the fundamental properties of nuclear matter. Its formation requires extreme conditions such as high temperature and density, resembling the state that was formed a few microseconds after the Big Bang.

Characteristics of QGP

One of the defining characteristics of QGP is its behaviour as a perfect liquid. This refers to its exceptionally low viscosity and high thermal conductivity, akin to that of an ideal fluid with minimal internal friction. Experimental observations, particularly those related to the collective flow of particles produced in heavy-ion collisions, support this behaviour. The near-perfect fluidity of QGP suggests that it behaves as a highly interactive medium with strong interactions among its constituent quarks and gluons, resulting in a state of almost frictionless flow.

Signatures of QGP

Direct observation of QGP is not possible due to its extremely short lifetime, spanning just 10^{-23} seconds. QGP undergoes dynamic evolution, expanding and cooling before finally forming hadrons. Detectors can only detect the final products. Therefore, scientists use experimental probes like charged particle multiplicities, photon counts, and momentum spectra to study their properties. These probes provide valuable insights into the behaviour of QGP.

1.5.1 Strangeness Enhancement

Strangeness enhancement is a prominent signature of QGP in heavy-ion collisions, initially proposed by Rafelski and Muller[24]. It arises from the dominance of $s\bar{s}$ production within QGP through the gluonic ($gg \rightarrow s\bar{s}$) channel, facilitated by the high gluon density at RHIC and LHC energies. The mass of the strange quark ($\sim$ 150 MeV) closely matches the critical temperature ($T \sim 170$ MeV) for the QCD phase transition, leading it to reach equilibrium before the QGP undergoes a phase change. Moreover, Pauli blocking of light quarks (u, d) contributes to the increased formation of strange quark pairs, as the filling of lower Fermi energy levels by up and down quarks renders $s\bar{s}$ pair production more favourable.

In Figures 1.6, measurements of strangeness enhancements in ALICE are compared with data from SPS and RHIC. The strangeness enhancement, defined as the ratio of

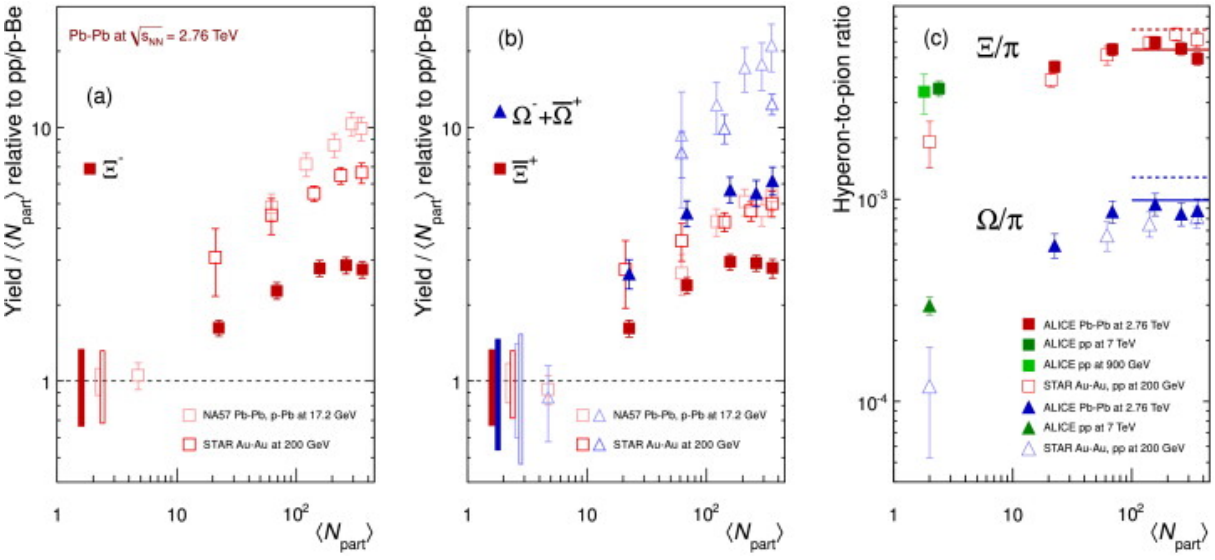

Figure 1.6: Yield of multi-strange hadrons as a function of $\langle N_{\text{part}} \rangle$ measured in ALICE, NA57 and STAR [25].

yields in Pb–Pb collisions to those in pp interactions and normalized to the mean number of participants $\langle N_{\text{part}} \rangle$, exhibits an increase with centrality and the strangeness content of the particle but decreases with higher center-of-mass energies. Production of strangeness in pp collisions is greater at the LHC compared to RHIC, while it remains consistent for heavy-ion collisions at both energy levels. This decrease in enhancement with increasing energy is primarily attributed to modifications in pp collisions. The rising trend seen in the hyperon to pion ratio as we move from pp collisions to heavy-ion collisions indicates an increase in the production of strange particles[25].

In Figure 1.7, the hadron to pion ratios as a function of $< dN_{\text{ch}}/d\eta >$ are shown across different collision systems and energies. Notably, the ratios in pp collisions at $\sqrt{s} = 13$ TeV closely resemble those at $\sqrt{s} = 7$ TeV, indicating a consistent enhancement of strange to non-strange hadron production with increasing particle multiplicity. At LHC energies, strangeness production in different collisions is observed to be influenced by final-state characteristics rather than collision species, with minimal energy dependence. Additionally, at higher multiplicities, these ratios resemble to those observed in Pb–Pb collisions [26, 27].

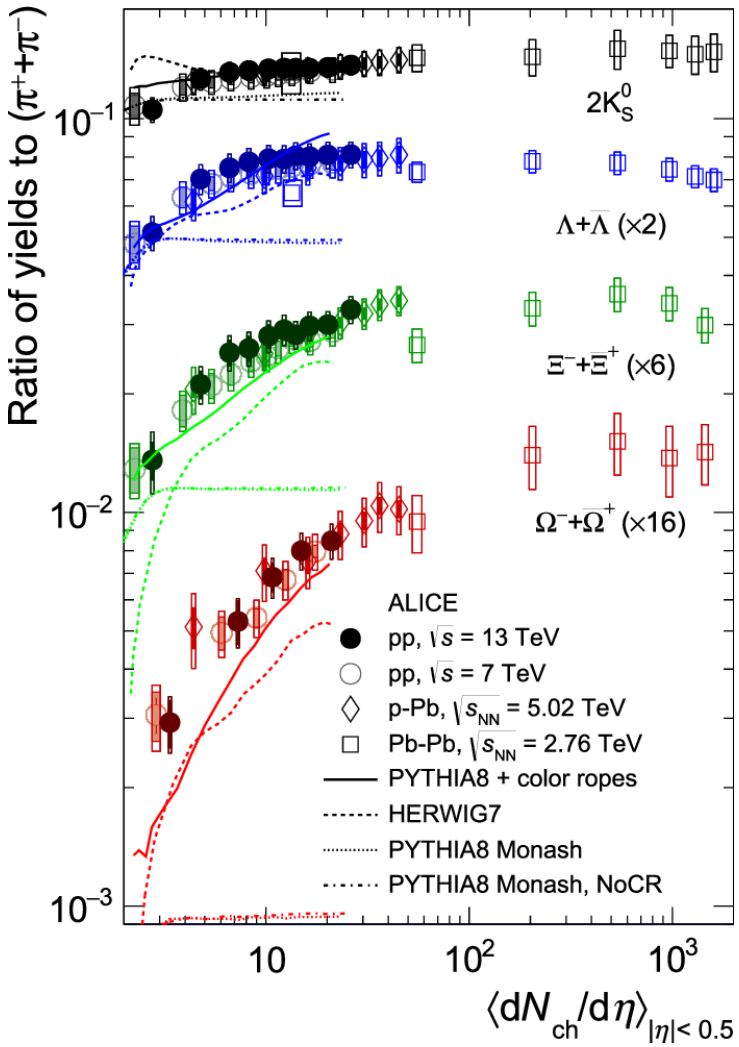

Figure 1.7: Hadron to pion ratios as a function of $\langle dN_{ch}/d\eta \rangle$ measured in different collision systems and energies, with predictions from different MC generators for pp collisions[26].

1.5.2 Collective Flow

In high-energy heavy-ion collisions, the QGP, a deconfined state of quarks and gluons, behaves similarly to a nearly perfect fluid with exceptionally low viscosity [28]. Initially, spatial irregularities in the collision induce pressure gradients within the QGP, leading to collective motion among its constituent particles. This collective motion results in correlated velocities among particles, resembling fluid dynamics behaviour. In contrast, non-collective flow exhibits random and uncorrelated particle velocities. The coherent movement of particles within the strongly interacting QGP reflects the presence of collective flow phenomena in heavy-ion collisions, offering valuable insights into the characteristics and evolution of the produced matter [29].

Collective flow in heavy-ion collisions can be categorized into two main types: radial flow (perpendicular to the reaction plane) and anisotropic flow (along the beam axis) [30].

Radial Flow

Radial flow describes the outward movement of particles originating from the collision zone, driven by pressure gradients induced by the expanding Quark-Gluon Plasma (QGP). This collective expansion, primarily occurring along the radial direction, is a consequence of the pressure imbalances within the system. Understanding radial flow dynamics is crucial for gaining insights into the expansion processes and discerning the equation of state characterizing the produced matter [29].

Anisotropic Flow

Anisotropic flow arises from the preferential alignment of emitted particles along specific azimuthal angles, a consequence of the initial geometric asymmetries between colliding nuclei and subsequent hydrodynamic evolution as shown in Figure 1.8. It is characterized by various harmonic components, like elliptic flow (v_2) and triangular flow (v_3), each reflecting distinct azimuthal symmetries. These flow coefficients measure the extent to which momentum of particles deviate from the reaction plane. Analyzing the magnitude and azimuthal distribution of these coefficients provides researchers with crucial insights

into the transport properties and equation of state of the Quark-Gluon Plasma[30, 31].

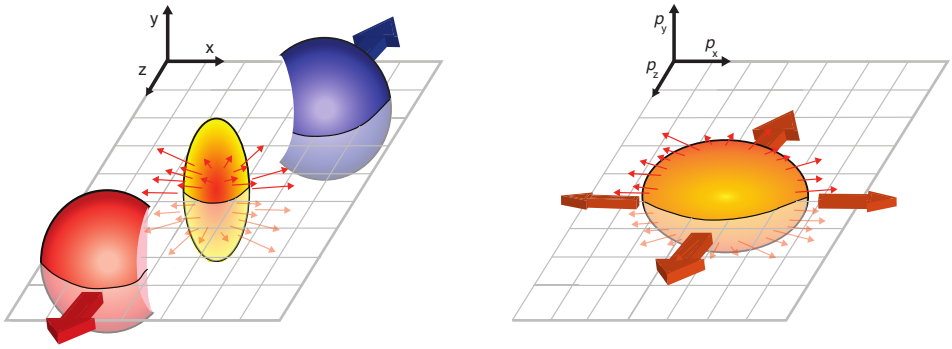

Figure 1.8: A schematic diagram illustrating the conversion of spatial anisotropy (left panel) into momentum anisotropy (right panel) [32].

The anisotropy in azimuthal particle distributions can be effectively described using a Fourier expansion [31, 33]. This expansion method allows us to decompose the azimuthal distribution of particles into a sum of cosine functions of different harmonics. Mathematically, the Fourier expansion can be represented as:

$$E\frac{d^3N}{dp^3} = \frac{1}{2\pi}\frac{d^2N}{p_T dp_T dy}\left(1 + 2\sum_{n=1}^{\infty} v_n \cos[n(\phi - \Psi_{RP})]\right) \tag{1.6}$$

Here, E and p_{T} denote the energy and transverse momentum of a particle within the rapidity y, respectively. The symbol ϕ represents the azimuthal angle, while Ψ_{RP} signifies the reaction plane angle. The v_n coefficients are Fourier coefficients of order n, describing the anisotropy observed in particle production. A large value of v_n indicates a significant anisotropic component in the emitted particles. Specifically, the coefficients v_1, v_2, and v_3 are commonly referred to as directed flow, elliptic flow, and triangular flow coefficients, respectively. These coefficients provide valuable insights into the collective behaviour and flow dynamics of particles produced in heavy-ion collisions.

Directed Flow

Directed flow, observed in heavy-ion collisions, results from the preferential emission of particles along the beam axis due to initial geometry and pressure gradients. It offers insights into the asymmetry of the initial overlap region, early-time collision dynamics,

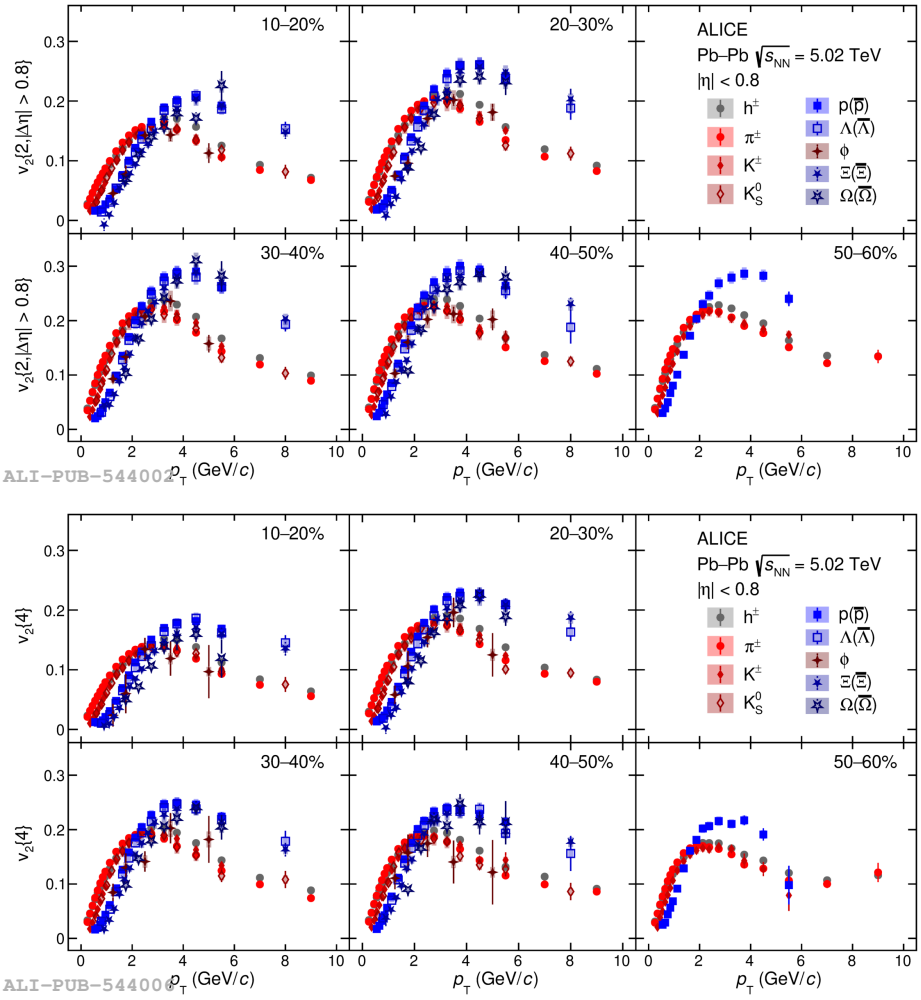

Figure 1.9: p_{T}-differential v_2 measured using (upper panel) two-particle correlations and (lower panel) four-particle cumulants for $|\Delta\eta| < 0.8$ for various particle species and centralities in Pb–Pb collisions at $\sqrt{s_{\mathrm{NN}}} = 5.02$ TeV [34].

and properties of the produced matter, including the equation of state and early-stage QGP characteristics. Additionally, it provides information about the net momentum transfer and asymmetries in the initial state of the collision system [31, 35, 36].

Elliptic Flow (v_2)

Elliptic flow[30], observed in heavy-ion collisions, describes the anisotropic collective motion of particles emitted from the collision zone. It is characterized by the preferential alignment of particles along the long axis of the almond-shaped overlap region formed by colliding nuclei. This phenomenon arises due to the anisotropic pressure gradient induced by the collision geometry.

In heavy-ion collisions, particles emitted in the plane perpendicular to the collision axis exhibit collective motion, leading to an azimuthal anisotropy. This azimuthal anisotropy is characterized by the second harmonic (v_2) in the Fourier expansion of the particle azimuthal distribution.

As a fundamental signature of the initial geometry and subsequent hydrodynamic evolution of the QGP, elliptic flow provides valuable insights into crucial parameters such as viscosity, thermalization time, and the shear viscosity to entropy density ratio (η/s).

Elliptic flow is predominantly observed in non-central heavy-ion collisions, where the almond-shaped overlap region leads to collective motion perpendicular to the collision axis.

The recent results from the ALICE experiment [34], depicted in Figure 1.9, showcase the p_{T}-differential elliptic flow using both two-particle and four particle cumulant method for the same particle species. These measurements are conducted with a pseudorapidity gap of $|\Delta\eta| < 0.8$ and encompass various particle species, including charged hadrons ($h^{\pm}$), pions ($\pi^{\pm}$), kaons ($\mathrm{K}^{\pm}$), protons and antiprotons ($p + \bar{p}$), strange mesons (($\mathrm{K}^0_{\mathrm{S}}$, ϕ), and hyperons ($\Lambda + \bar{\Lambda}$, $\Xi^- + \Xi^+$, $\Omega^- + \Omega^+$), extracted from Pb–Pb collisions at a center-of-mass energy of $\sqrt{s_{\mathrm{NN}}} = 5.02$ TeV. These measurements provide invaluable insights into the collective behaviour of strongly interacting matter generated in high-energy heavy-ion collisions.

The observed trend of increasing v_2 with collision centrality for a given p_{T} interval

elucidates the final-state anisotropy, stemming from the spatial eccentricity ε_2 inherent in non-central collisions' initial-state ellipsoidal geometry. Moreover, these measurements manifest intriguing phenomena known as mass ordering and meson–baryon particle type grouping.

The mass ordering phenomenon, commonly observed in heavy-ion collisions, is attributed to the radial flow of the system. This effect entails heavier particles exhibiting larger v_2 values compared to lighter ones at a given p_{T}, indicative of a collective expansion of the system.

Furthermore, the meson–baryon particle type grouping in the intermediate p_{T} phenomenon suggests a dynamic interplay between partonic flow development and subsequent quark coalescence into hadrons. This phenomenon is observed for distinct groups of particles exhibiting similar v_2 behaviour and provides interesting information about the underlying dynamics of hadronization in heavy-ion collisions.

Triangular Flow (v_3)

Triangular flow, observed in heavy-ion collisions, is distinguished by the anisotropic emission of particles perpendicular to the reaction plane, forming a triangular shape in momentum space. This flow phenomenon stems from fluctuations in the initial geometry and density profile of the colliding nuclei. Its measurement offers valuable insights into event-by-event fluctuations and the higher-order coefficients of the QGP. By studying triangular flow, researchers gain a deeper understanding of the dynamics and properties of the QGP, shedding light on the intricate interplay between geometric fluctuations and collective motion in heavy-ion collisions [37, 38].

1.5.3 Jet Quenching and Partonic Energy Loss

Jets are collimated sprays of particles that arise from the fragmentation of final-state partons produced in the initial stages of heavy-ion or hadronic collisions. As high-momentum jets pass through the hot and dense medium of QCD matter, they lose energy primarily through gluon emissions. These emitted gluons, in turn, produce hadrons with significantly lower momenta. This process, termed as jet quenching, illustrates the energy loss

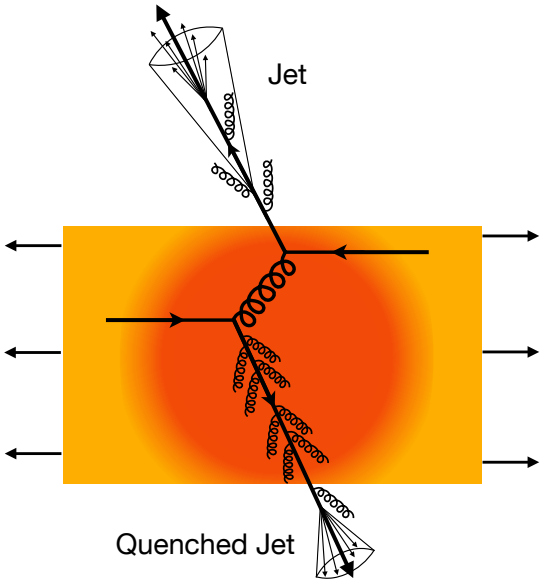

Figure 1.10: A schematic diagram of jet quenching in nucleus-nucleus collision [39].

experienced by jets as they traverse the dense QCD medium, altering their structure and reducing their overall observed energy and particle yield [40]. Initially, J.D. Bjorken theorized in 1982 that elastic parton scattering would be the dominant mechanism for energy loss in the medium [41]. However, subsequent studies by Gyulassy and collaborators proposed that induced gluon bremsstrahlung is the more significant mechanism for parton energy loss, which was later extensively studied by Baier, Dokshitzer, Mueller, Peigné, and Schiff [42, 43].

In contrast, e^+e^- collisions, such as those observed at the OPAL experiment at LEP, exhibit back to back di-jet events due to energy and momentum conservation. Unlike in heavy-ion collisions, no underlying event is present in these interactions, leading to a clean and distinct correlation between the jets [44].

In small collision systems like pp collisions, hard-scattered partons fragment in the QCD vacuum, creating jets alongside low p_{T} activities called underlying events, which include initial and final-state radiation, multiple parton interactions, and beam remnants. In heavy-ion collisions, however, the dynamics become more complex. After the initial hard scattering between quarks, one quark travels mostly unaffected through the vacuum, while the other interacts heavily with the hot and dense medium, losing energy through collisions and radiation. This energy loss leads to a modified fragmentation process,

resulting in fewer high-p_{T} hadrons − a phenomenon known as jet quenching [32].

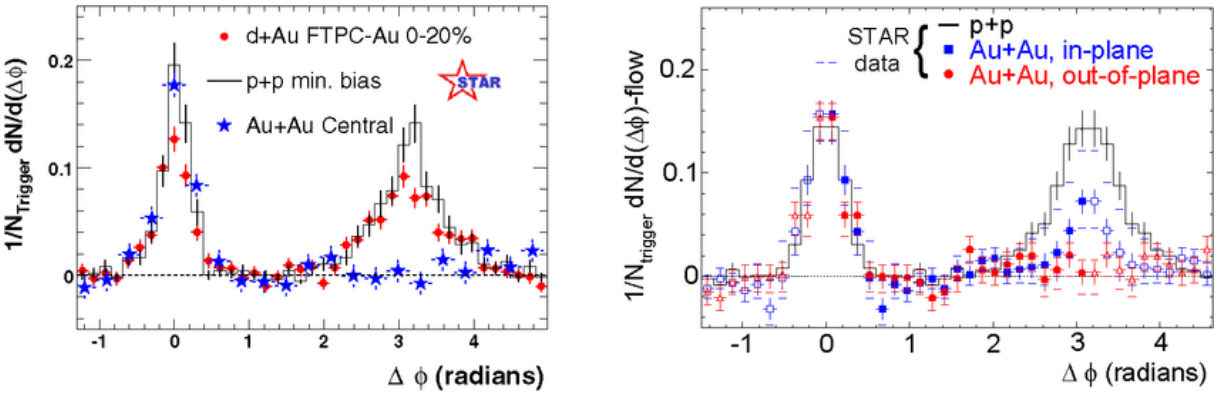

Figure 1.11: Dihadron azimuthal correlations at high p_{T}. Left: Correlations for p+p, central d+Au, and central Au+Au collisions at $\sqrt{s_{NN}}$ = 200 GeV (background subtracted). Right: Background-subtracted high p_{T} dihadron correlations for different trigger hadron orientations relative to the Au+Au reaction plane [28].

Experimentally, jet quenching can be studied using the two-particle correlation method and the nuclear modification factor.

Two Particle Correlation Method:

The STAR experiment studied jet quenching using two-particle correlations in heavy-ion collisions, comparing results from pp, Au–Au, and d–Au collisions at $\sqrt{s}$ = 200 GeV as shown in Figure 1.11. The azimuthal angular correlations for all three systems show similar trends for both near-side and away-side peaks. However, while the near-side peaks are consistent across systems, the away-side peak is suppressed only in Au–Au collisions, not in pp or d–Au collisions. This indicates that the suppression is due to final-state interactions with the dense medium in Au–Au collisions, rather than initial-state effects [28].

The ALICE experiment at the LHC studied jet quenching in Pb–Pb collisions at $\sqrt{s_{\mathrm{NN}}}$ = 2.76 TeV by measuring particle-yield modification through azimuthal dihadron correlations as shown in Figure 1.12. The key observable, I_{AA}, is defined as the ratio of correlation yield in heavy-ion collisions to that in pp collisions. An I_{AA} value of 1 indicates no medium effects, while deviations suggest energy loss in the medium. In

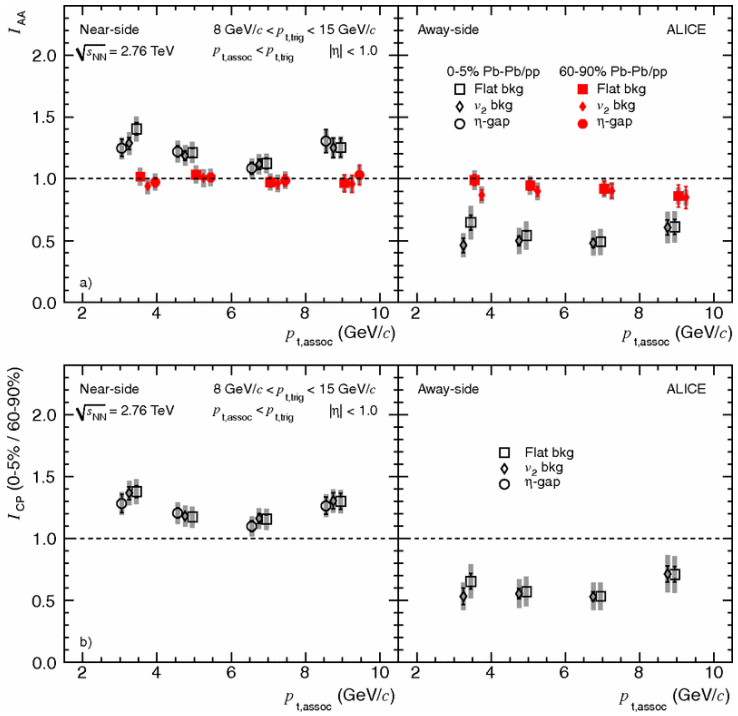

Figure 1.12: I_{AA} for central (0-5% Pb–Pb/pp, open black symbols) and peripheral (60-90% Pb–Pb/pp, filled red symbols) collisions. Various background subtraction methods are employed: flat pedestal (squares), v_2 subtraction (diamonds), and large $|\Delta\eta|$ region subtraction (circles, near-side only) [45].

central collisions, I_{AA} for the away-side (AS) is reduced to 0.6, indicating significant energy loss. In peripheral collisions, I_{AA} approaches unity, showing no medium effects. Interestingly, a 20-30% increase in the near-side (NS) I_{AA} in central collisions suggests possible changes in fragmentation or the quark/gluon jet ratio[45].

Nuclear Modification Factor:

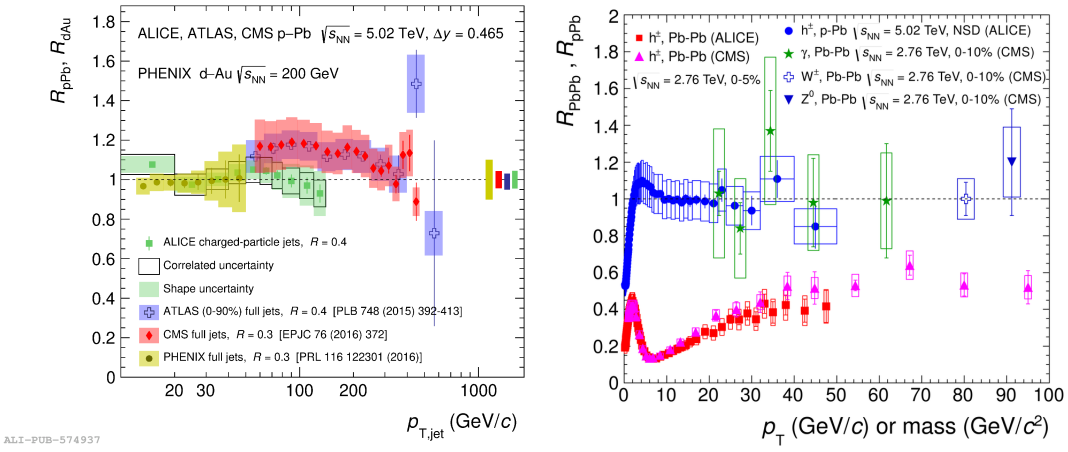

Figure 1.13: Left: Nuclear modification factors of charged-particle jets in p–Pb at $\sqrt{s_{\rm NN}}$ = 5.02 TeV (LHC) and d–Au at $\sqrt{s_{\rm NN}}$ = 200 GeV (RHIC) [46]. Right: $R_{\rm AA}$ of charged hadrons in central Pb–Pb collisions at $\sqrt{s_{\rm NN}}$ = 2.76 TeV and minimum bias p–Pb collisions at $\sqrt{s_{\rm NN}}$ = 5.02 TeV as a function of $p_{\rm T}$ [47].

The nuclear modification factor $R_{\rm AA}$ compares particle yields in heavy-ion collisions to those in proton-proton (pp) collisions:

$$R_{\rm AA} = \frac{1}{\langle T_{\rm AA} \rangle} \frac{d^2 N_{\rm AA}/(dy\, dp_{\rm T})}{d^2 \sigma_{\rm pp}/(dy\, dp_{\rm T})} \tag{1.7}$$

where $\langle T_{\rm AA} \rangle$ is the average nuclear overlap function, $\frac{d^2 N_{\rm AA}}{dy\, dp_{\rm T}}$ is the particle yield in heavy-ion collisions, and $\sigma_{\rm pp}$ is the production cross section in pp collisions. A value of $R_{\rm AA} = 1$ indicates a simple superposition of proton-proton interactions, while deviations from 1 suggest medium effects.

In Figure 1.13 the nuclear modification factor ($R_{\rm pPb}$) for jets in p–Pb collisions at

$\sqrt{s_{\mathrm{NN}}}$ = 5.02 TeV, measured by ALICE, is compared with results from ATLAS, CMS, and PHENIX. ATLAS and CMS measured full jets (including both charged and neutral particles), whereas ALICE focused only on charged-particle jets, complicating direct comparisons. Nevertheless, the ALICE results qualitatively align with ATLAS and CMS, with the latter experiments showing a slight enhancement above unity, though this requires more precise measurements to confirm. ALICE extends the measurements down to 10 GeV/c, providing additional insight into jet production [46].

In Figure 1.13 the right panel shows the nuclear modification factor for charged hadrons in minimum-bias p–Pb collisions at $\sqrt{s_{\mathrm{NN}}}$ = 5.02 TeV. In this case, no significant jet quenching is observed, as the R_{pPb} remains near unity above 10 GeV/c, indicating that high-p_{T} hadron production is largely unaffected by the medium in p–Pb collisions. The lack of suppression in R_{pPb} contrasts with the strong suppression seen in Pb–Pb collisions, suggesting that jet quenching is primarily a phenomenon of the dense medium created in heavy-ion collisions [47].

1.5.4 Quarkonium Suppression

Quarkonium suppression refers to the reduction in the production of quarkonium states, which are mesonic-bound states formed by heavy quark-antiquark pairs. Examples of quarkonium states include charmonium, such as J/ψ (bound state of $c\bar{c}$) and ψ', as well as bottomonium, such as Υ (bound state of $b\bar{b}$). These states are observed in heavy-ion collisions and compared to their production in pp collisions. Quarkonia experiences changes in their production rates when interacting with the QGP. These changes arise from a competition between suppression induced by the medium and recombination mechanisms occurring within the medium or during hadronization, particularly for charmonium. Therefore, the suppression in the yield of quarkonium states serves as a signature of QGP formation [48].

In the hot and dense QGP medium, quarkonium states experience various suppression mechanisms. Firstly, at high temperatures, thermal gluons screen the binding potential between quarks and antiquarks, causing the dissolution of quarkonium states and making them susceptible to dissociation. Additionally, as the temperature rises, the Debye

screening length decreases, defining the effective range of the strong interaction within the QGP. This leads to intensified gluon interactions with quarkonium states, resulting in their suppression. Despite this suppression, quarkonium states can be regenerated through recombination mechanisms within the QGP. Heavy quarks and antiquarks can combine to form quarkonium states, contributing to their production. However, the balance between suppression and regeneration depends on factors such as temperature, energy density, and the evolution of the QGP medium over time.

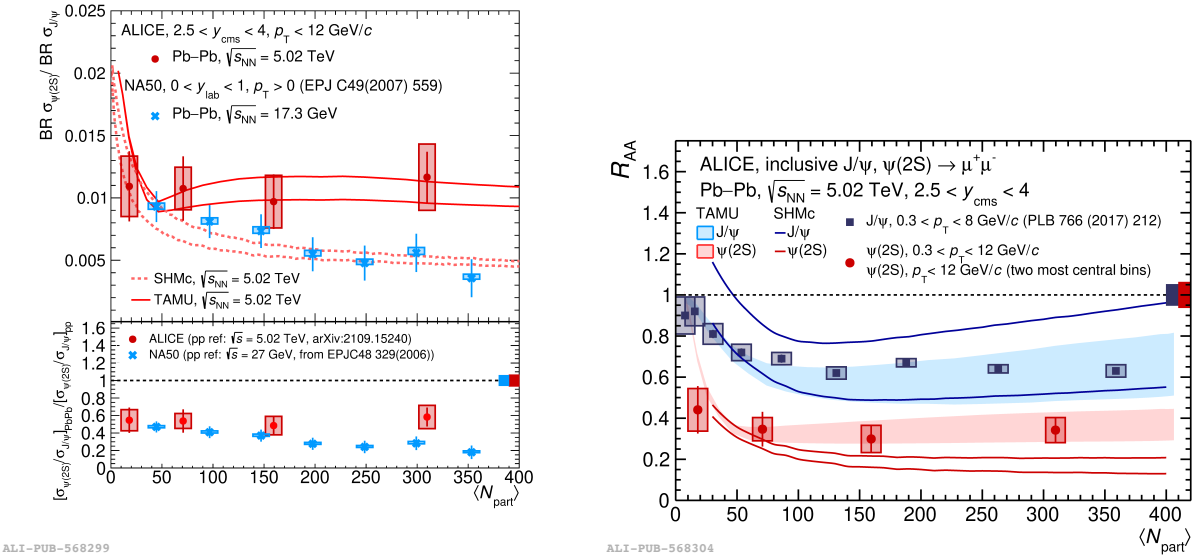

Figure 1.14: (Left side) Ratio of the $\psi(2S)$ and J/ψ [48] inclusive cross sections as a function of $\langle N_{\text{part}} \rangle$. (Right side) The R_{AA} for the $\psi(2S)$ and J/ψ as a function of $\langle N_{\text{part}} \rangle$. Data are compared to predictions of the TAMU[49] and SHMc[50] model.

The left side of Figure 1.14 shows the ratio of the inclusive cross sections of the $\psi(2S)$ and J/ψ particles in Pb–Pb collisions as a function of the average number of participating nucleons ($\langle N_{\text{part}} \rangle$). This ratio quantifies the suppression of $\psi(2S)$ relative to J/ψ in Pb–Pb collisions compared to pp collisions. The data indicate that in Pb–Pb collisions, $\psi(2S)$ is suppressed by a factor of 2 compared to J/ψ. The TAMU model demonstrates good agreement with experimental data across centrality bins, while the SHMc model tends to underestimate the ratios, particularly in central Pb–Pb collisions.

The right panel illustrates the nuclear modification factor (R_{AA}) for both $\psi(2S)$ and J/ψ particles as a function of centrality or transverse momentum (p_{T}). R_{AA} is calculated

as the ratio of the yield of particles in Pb–Pb collisions to the yield in pp collisions, normalized by the nuclear overlap function. In this case, it specifically shows the suppression of $\psi(2S)$ resonance yield in Pb–Pb collisions compared to pp collisions. The factor of up to ~ 3 suppression indicates a strong suppression of $\psi(2S)$ production in the heavy-ion collisions [48].

1.5.5 Direct Photon Production

One effective approach for estimating the properties of QGP involves the measurement of direct photons produced during heavy-ion collisions [51]. Direct photons are emitted directly in the early stages of collisions without subsequent interactions. Their emission carries crucial information regarding the temperature and density of the medium created in the collision. These photons can be classified into two main categories: prompt and thermal.

Prompt Photons: It is produced during the initial stages of heavy-ion collisions through various processes such as hard scattering of partons, quark-antiquark pair annihilation, Compton scattering, and jet fragmentation. In hard scattering, high-energy partons collide and emit photons directly. Quark-antiquark annihilation occurs when an incoming quark and antiquark annihilate to produce two or more photons. Compton scattering involves quarks and gluons scattering off each other, emitting photons. Lastly, partons produced in the collision can fragment into jets, emitting photons during the fragmentation process.

Thermal Photons: These are generated from interactions of partons within the hot and dense medium of the QGP. The primary processes include the scattering of partons with thermalized partons from the QGP, as well as scattering among thermalized partons within the medium. These interactions lead to the emission of thermal photons. Due to the thermal motion of the partons within the QGP, thermal photons typically have lower transverse momenta compared to prompt photons.

In the ALICE experiment, the direct-photon p_T-differential spectrum has been measured for the 10% most central Pb–Pb collisions at $\sqrt{s_{\mathrm{NN}}} = 5.02$ TeV, as shown in Figure 1.15. The invariant yield of direct photons is consistent with the prompt photon contri-

bution; however, the central values of the data are systematically higher. These results also include contributions from thermal photons, which dominate at $p_T < 3\,\mathrm{GeV}/c$ [51].

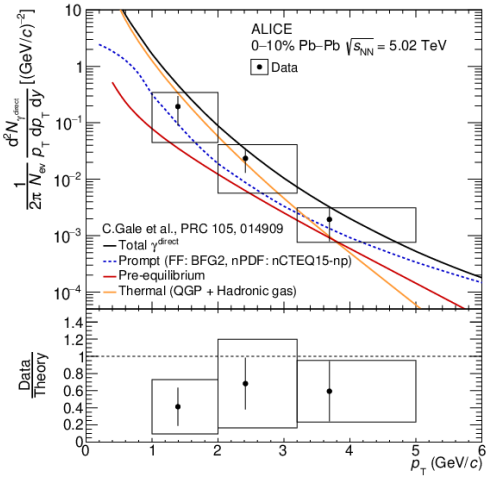

Figure 1.15: Direct photon spectra in different centrality classes in Pb–Pb collisions at $\sqrt{s_{NN}} = 5.02$ TeV and compared with different theoretical calculations [51].

1.5.6 Resonance Production

The study of hadronic resonances is crucial for understanding the QGP phase in heavy-ion collisions. As the collision system evolves, resonances may decay inside the medium before thermal freeze-out, leading to a reduction in their yield due to the rescattering of their daughter particles. This effect alters the momenta of the daughter particles, affecting the reconstructed resonance signal.

The interplay between medium effects such as rescattering and regeneration is investigated by comparing the ratios of resonance to stable hadron yields with similar quark content. Figure 1.16 displays particle ratios of K^{*0}/K and ϕ/K as functions of the average charged-particle multiplicity density, a proxy for system size, in various collision systems (Pb–Pb, p–Pb, and pp) at different center-of-mass energies[52–54]. The K^{*0}/K ratio decreases from peripheral to central collisions, indicating modification by rescattering effects. Conversely, the ϕ/K ratio remains constant across collision systems. Model predictions from EPOS3 with and without the hadronic phase modelled by UrQMD[55] are compared with the measurements, showing good agreement with the observed trends[56].

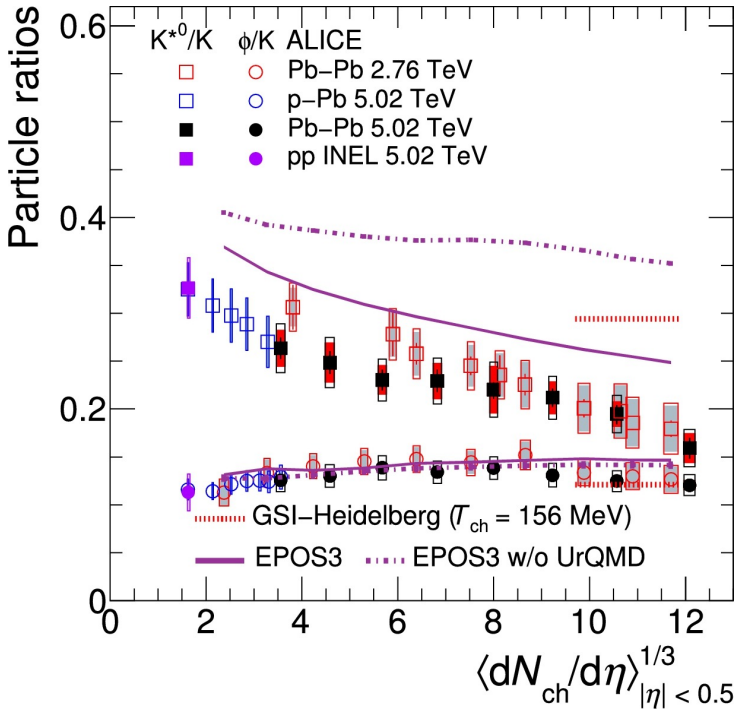

Figure 1.16: The p_{T}-integrated particle yield ratios of $\mathrm{K}^{*0}/\mathrm{K}^{-}$ and ϕ/K^{-} as functions of N_{ch} in pp, p–Pb, and Pb–Pb collisions at LHC energies [56].

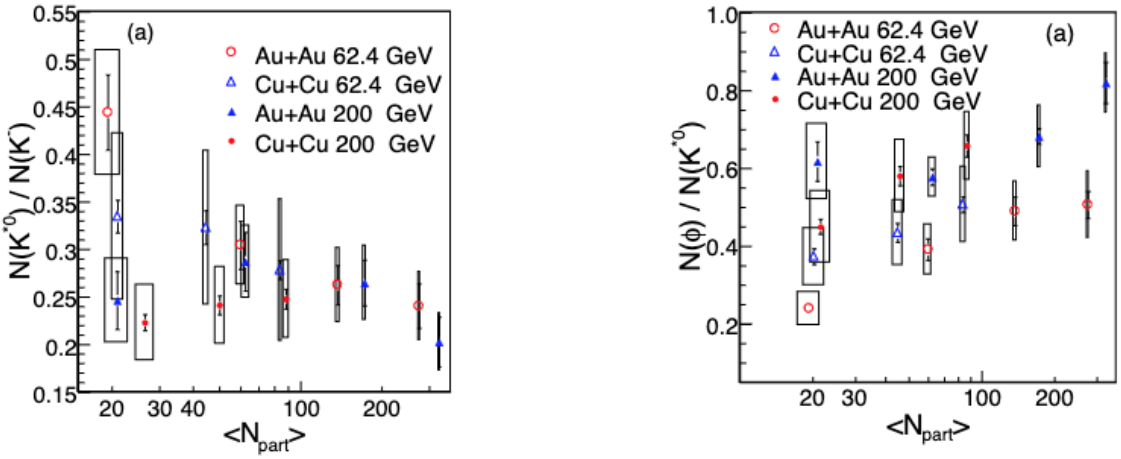

Figure 1.17: Particle yield ratios of $\mathrm{N}(\mathrm{K}^{*0})/\mathrm{N}(\mathrm{K}^{-})$ and $\mathrm{N}(\phi)/\mathrm{N}(\mathrm{K}^{*0})$ as a functions of $\langle N_{\mathrm{part}} \rangle$ in Au+Au and Cu+Cu collision systems at $\sqrt{s_{\mathrm{NN}}} = 62.4$ GeV and 200 GeV [57].

Similar trends have been discussed at lower energies by the STAR collaboration as shown in Figure 1.17. STAR has measured the $K^{*0}(892)$ resonance production at mid-rapidity in Au+Au and Cu+Cu collision systems at $\sqrt{s_{NN}}$ = 62.4 GeV and 200 GeV. The $N(K^{*0})/N(K^{-})$ ratio in central Au+Au collisions at both energies is much smaller compared to the respective values in pp collisions, suggesting a stronger rescattering of $K^{*0}(892)$ daughter particles relative to regeneration. Similarly, the $N(\phi)/N(K^{*0})$ ratio in central Au+Au collisions exceeds that of pp collisions, supporting the dominance of rescattering effects and indicating potential strangeness enhancement. These measurements enable a quantitative estimation of the $K^{*0}(892)$ elliptic flow and support the quark coalescence model. Additionally, the observed nuclear modification factor R_{CP} for $K^{*0}(892)$ in Au+Au collisions suggests a prevalence of rescattering over regeneration effects[57, 58].

The upcoming chapter provides further insights into the significance of resonance production, shedding light on its role in indicating the formation of the QGP in heavy ion collisions. Additionally, it explores resonance production in small systems, aiming to understand its importance. Furthermore, the chapter delves into the motivation behind investigating the $\Lambda(1520)$ resonance in small systems.

1.6 Organisation of Thesis

This thesis presents a comprehensive analysis of the production of the $\Lambda(1520)$ and $K^{*0}(892)$ resonances in pp collisions at $\sqrt{s}$ = 5.02 and 13 TeV by using data collected from the ALICE experiment at the LHC. The thesis is organized into several chapters as follows:

Chapter 1 provides an introduction to heavy-ion collisions and the characteristics of the QGP. **Chapter 2** offers a brief review focused on resonance particles, outlining the rationale behind studying specific resonances such as the $\Lambda(1520)$ in pp collisions. **Chapter 3** presents a detailed discussion of the ALICE detector, its role in data collection, and its capabilities in particle identification. The data analysis methods employed for resonances are described in **Chapter 4**, including event and track selection criteria as well

as systematic uncertainty estimation, ensuring the accuracy and reliability of the results. It also discusses the systematic uncertainties and how they affect the interpretation of the results.

Chapter 5 provides a comprehensive discussion of the high-multiplicity analysis performed for $\Lambda(1520)$ and $K^{*0}(892)$ resonance in this thesis. **Chapter 6** presents the results of the analyses, highlighting the main findings and observations across different multiplicity classes. This includes key results such as the p_{T}-differential yield in various p_{T} bins, particle ratios, p_{T}-integrated yield, and the $\langle p_{\mathrm{T}} \rangle$ of the $\Lambda(1520)$ resonance in pp collisions at $\sqrt{s} = 5.02$ and 13 TeV.

Finally, **Chapter 7** summarizes the key findings of the thesis, discusses their broader implications, and offers suggestions for future research directions in the field of resonance production in pp collisions.

Chapter 2

Resonance Production in Small Collision Systems

2.1 QGP-like Effects in Small Collision System

The proton-proton (pp) and proton-nucleus (p–A) collisions are considered "small systems" due to their smaller size and lower particle multiplicities compared to nucleus-nucleus (A–A) collisions. These collisions serve as baseline measurements for heavy-ion collisions, where the formation of a QGP is expected.

Recent experimental results might suggest that certain observations in small systems mimic the signatures associated with the formation of QGP. These observations include phenomena like collective behaviour, long-range correlations, and enhancements in strange particle production in high multiplicity pp collisions. Additionally, effects such as mass-dependent hardening of transverse momentum distributions, typically linked to the presence of a strongly interacting, collectively expanding QGP medium in nuclear collisions, have been detected in high-multiplicity pp and p–Pb collisions at the LHC.

- **Collective Behavior:** High-multiplicity pp collisions exhibit signs of collective behaviour, such as the emergence of ridge-like structures in the two-particle correlation function. These structures suggest that particles are correlated not only in momentum space but also in position space, indicative of collective motion akin to hydrodynamic flow.

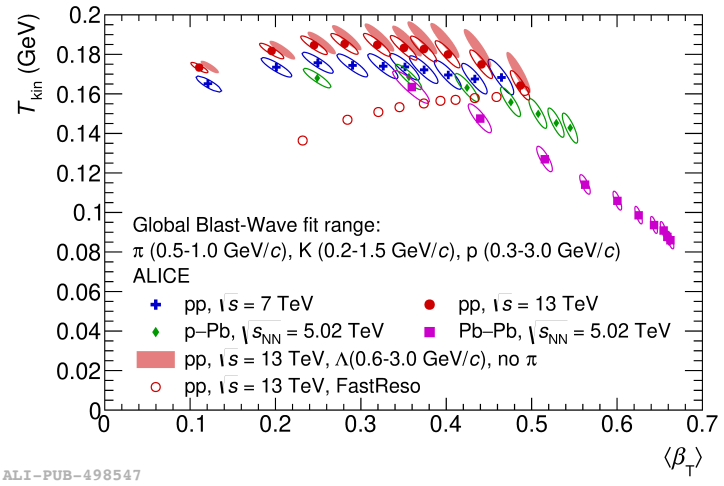

Figure 2.1: Correlation between kinetic freeze-out temperature and average expansion velocity from Blast-Wave fits across different collision systems[26].

The Blast-Wave fit outcomes for the kinetic freeze-out temperature (T_{kin}) and radial flow velocity ($\langle\beta_T\rangle$) extracted from low transverse momentum (p_T) spectra of identified particles are depicted in Figure 2.1. It reveals consistent parameters like kinetic freeze-out temperature and average expansion velocity across different collision systems. However, strong dependence on collision centrality indicates variations in radial flow behaviour, reflecting the complex dynamics of high-energy collisions.

- **Enhanced Strangeness Production:** The production of strange hadrons as described in Chapter 1, such as strange baryons (e.g., Λ, Ξ) and mesons containing strange quarks (e.g., K), is found to be significantly enhanced in high-multiplicity pp collisions compared to what is expected based on simpler hadronic models. This enhancement is reminiscent of the increased strangeness production observed in heavy-ion collisions, which is attributed to the elevated temperatures and densities reached in the QGP phase [26, 27].

- **Long-Range Correlations:** High-multiplicity pp collisions exhibit long-range correlations between particles over a wide range of pseudorapidity. These correlations extend beyond what would be expected from independent particle production, suggesting the presence of collective effects and extended spatial correlations in the collision system.

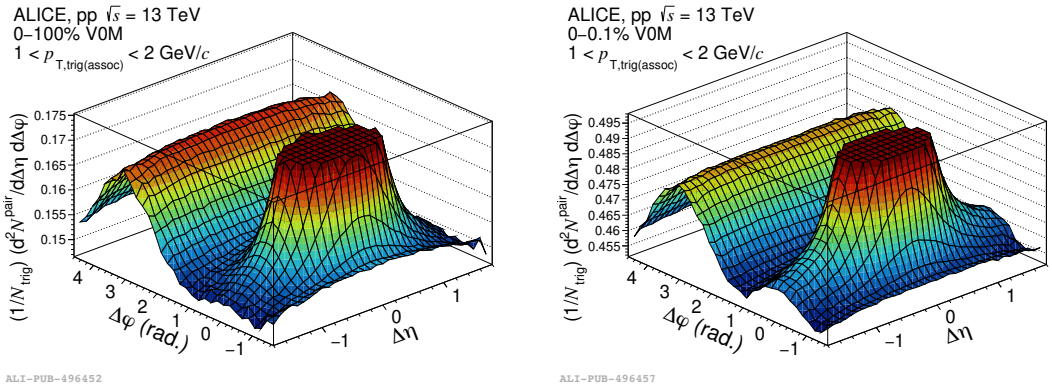

Figure 2.2: Two-particle correlation functions as functions of $\Delta\eta$ and $\Delta\phi$ in minimum-bias events (0–100%, left) and high-multiplicity (0–0.1%, right) [59].

Additionally, the above study has been extended to the measurements of the ridge yield to the low multiplicity region. Figure 2.2 illustrates the per-trigger yield obtained for $1 < p_{T,\mathrm{trig}}, p_{T,\mathrm{assoc}} < 2$ GeV/c in pp collisions at $\sqrt{s} = 13$ TeV for minimum bias events (left) and high-multiplicity events (right). The ridge structure is prominently observed in the high-multiplicity class, while it is less pronounced in the minimum bias events. The away-side yield is predominantly populated by back to back jet correlations[59].

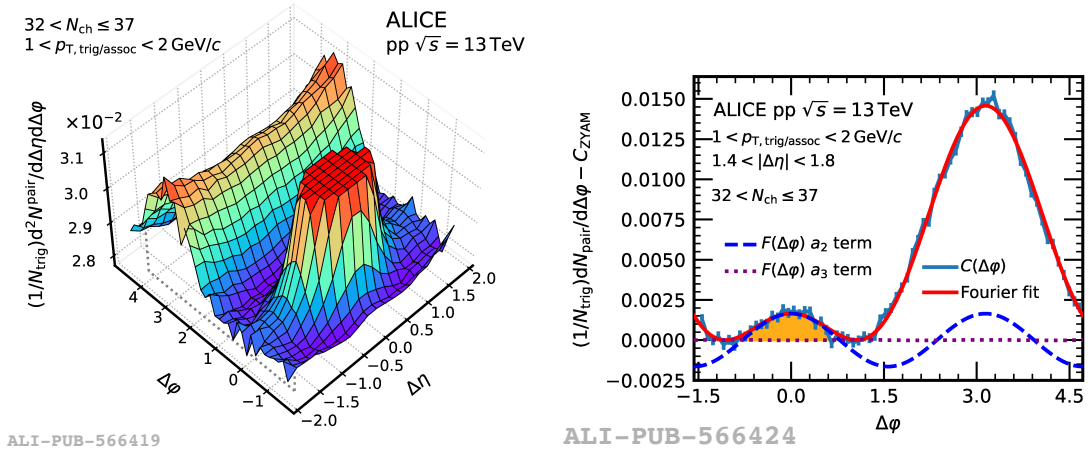

Figure 2.3: The two-particle per-trigger yield for trigger and associated particle momentum in the range $1 < p_T < 2$ GeV/c is investigated within the multiplicity interval $32 < N_{\mathrm{ch}} \leq 37$ [60].

Figure 2.3 shows the two-particle per-trigger yield for charged track pairs within

$1 < p_{\mathrm{T,trig}} < 2$ GeV/c and $1 < p_{\mathrm{T,assoc}} < 2$ GeV/c, for the multiplicity range $32 < N_{\mathrm{ch}} \leq 37$. The jet-fragmentation peak at $(\Delta\eta, \Delta\phi) = (0, 0)$ and a broad away-side structure at $\Delta\phi = \pi$ are visible. For $|\Delta\eta| \geq 1.4$ and $\Delta\phi \approx 0$, the ridge structure is present in high-multiplicity pp collisions. The right panel shows the zero-suppressed $\Delta\varphi$ projection overlaid with $F(\Delta\varphi)$ (red line), indicating the area where the ridge yield is extracted. The ridge yield, reflecting collective effects, aligns with flow coefficient measurements in small systems and is interpreted as a sign of collective expansion of the QGP medium in heavy-ion collisions[60].

- **Mass-dependent hardening of transverse momentum distributions**

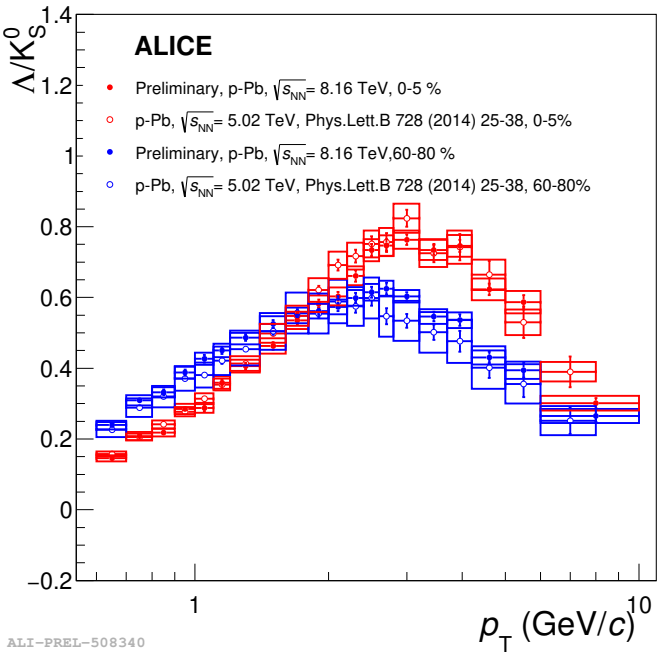

Figure 2.4: $\Lambda/\mathrm{K}^0_\mathrm{S}$ as a function of p_T [61].

The transverse momentum (p_T) distributions of identified hadrons offer insight into collective behaviour in particle production. If radial flow develops, it affects the p_T distribution shape, particularly for different particle masses. In pp and p–Pb collisions, p_T distributions become harder with increasing multiplicity[26, 62].

The ratio of $\Lambda/\mathrm{K}^0_\mathrm{S}$ p_T-differential yield of lower to different multiplicity classes is shown in Figure 2.4. The baryon to meson ratio observed at intermediate p_T in p–

Pb collisions displays a notable peak, primarily attributed to radial flow effects and recombination processes occurring during the hadronization of the QGP. Notably, the peak is more pronounced in high-multiplicity collisions (0–5%) compared to low-multiplicity collisions (60–80%) and shows no dependence on collision energy within uncertainties [61].

2.2 Significance of Resonance Production in A–A, p–A and pp Collisions

Resonance particles, characterized by their short lifetimes and decay through strong interactions, play a crucial role as probes for understanding the properties of the Quark-Gluon Plasma formed in heavy-ion collisions. Despite sharing the same quark content as their longer-lived ground state particles, resonances may differ in mass, spin, isospin, and parity. Their significantly shorter lifetimes result in broad states, with widths determined by the uncertainty principle ($\Delta E \Delta t \sim \hbar$), leading to extremely short decay lengths of the order of a few femtometers. Resonance particles serve as essential probes for investigating the characteristics of the QGP and the dynamics of the medium formed in heavy-ion collisions.

Although resonances decay before being directly detected in the detector, they can be reconstructed by studying the invariant mass of their decay daughters. This attribute makes resonances valuable for exploring in-medium phenomena such as rescattering and regeneration processes, providing insights into the interaction dynamics within the dense and hot medium. The Table 2.1 presents a list of resonance particles along with their masses, lifetimes, branching ratios, and decay modes, offering crucial information for such studies and enhancing our understanding of the underlying physics in heavy-ion collisions[63].

During the evolution of heavy-ion collisions, hadronic resonance states are formed during the hadronization stage, where three quarks or quark-anti-quarks form colour-neutral hadrons. The inelastic collisions between these hadrons cease at chemical freeze-out, so the abundance of most longer-lived particles becomes fixed. However, the hadrons con-

Resonance	Lifetime (fm/c)	Width (MeV)	Quark Contents	Decay Mode (BR (%))
$\Delta^{++}(1232)$	1.2	117 ± 3	uuu	$p + \pi^+$ (100)
$\rho(770)$	1.3	149.1 ± 0.8	$(uu + dd)/\sqrt{2}$	$\pi^+ + \pi^-$ (100)
$\mathrm{K}^{*0}(892)$	4.2	50.8 ± 0.9	$d\bar{s}, \bar{d}s$	$\mathrm{K}^+ + \pi^-$ (66.6)
$\Sigma(1385)^{\pm}$	5.5	36.0 ± 0.7	uus, dds	$p + \pi^+ + \pi^+$ (87.0)
$\Lambda(1520)$	12.6	15.6 ± 1.0	uds	$\mathrm{K}^+ + \mathrm{p}$ (22.5)
$\Xi^0(1530)$	21.7	15.6 ± 1.0	uss	$p + 2\pi^+ + \pi^-$ (66.7)
$\phi(1020)$	46	4.26 ± 0.04	$s\bar{s}$	$\mathrm{K}^+ + \mathrm{K}^-$ (48.9)

Table 2.1: Properties of resonance particles including their lifetimes, masses, valence quark contents, and dominant decay modes with branching ratios (BR)[63].

tinue to interact elastically till they reach the kinetic freeze-out stage where the momenta of the particles get modified.

Due to their short lifetimes, some resonance particles decay within the dense hadronic medium before reaching kinetic freeze-out. This means that their decay daughters, such as pions, kaons and protons, can still interact with the surrounding hadrons in the medium. These interactions can involve elastic scattering, where the decay daughters exchange momentum with the surrounding particles, or other types of interactions, depending on the specific resonance and the properties of the surrounding medium. These interactions between resonance decay daughters and surrounding hadrons contribute to the modification of the final-state hadron spectra observed in heavy-ion collisions.

Medium Effect on Resonance Production

In heavy-ion collisions, resonances can experience rescattering interactions with other particles in the medium, resulting in elastic scattering of their decay daughters. This alteration in momentum leads to a loss of reconstructable resonance yield and hence it interferes with the detection of resonance signals. Despite this loss, some resonances may be regenerated through pseudo-elastic interactions after chemical freeze-out, a phenomenon referred to as the regeneration effect. This effect leads to an enhancement in the resonance yield compared to what would be expected based solely on rescattering. The interplay

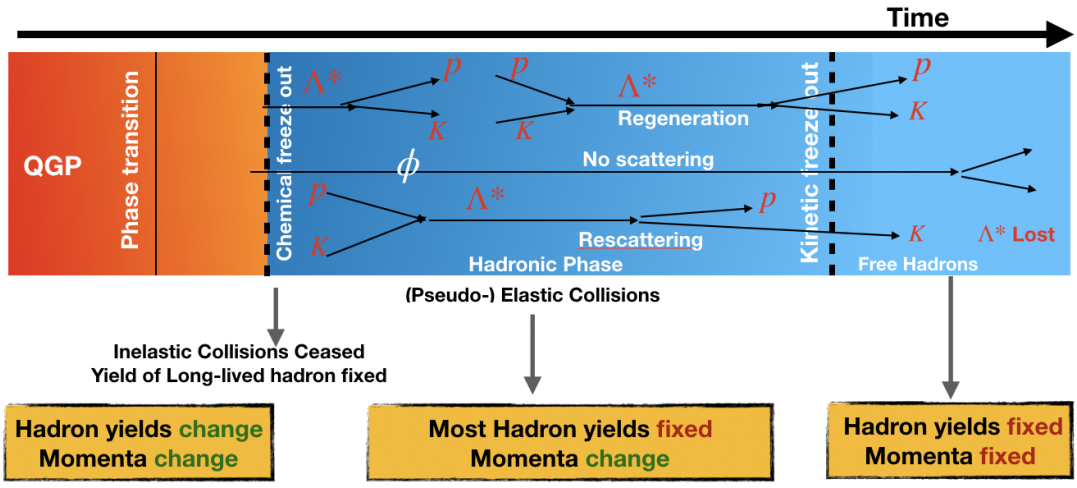

Figure 2.5: Illustration of the rescattering and regeneration effects on Λ(1520) resonance.

between rescattering and regeneration processes introduces complexity to the study of resonances in heavy-ion collisions as these effects affect resonance particles differently depending on their lifetime and decay daughters. Therefore, the study of resonance particles provides valuable insights into the dynamics of the QGP and the properties of the medium created in these collisions. Figure 2.5 illustrates the rescattering and regeneration effects of Λ(1520) resonance.

Resonance to stable hadrons yield ratio

The ratio of resonance yields to stable hadrons is crucial for studying the evolution of the QGP and understanding the interplay between various in-medium processes such as rescattering, regeneration, and thermalization. The ALICE Collaboration has measured resonance to stable particle ratios with varying lifetimes in several systems and energies. Figure 2.6 illustrates these ratios plotted as a function of the cubic root of the average charged-particle density for various resonances in different collision systems and energies, as measured by the ALICE and STAR Collaborations.

In Pb–Pb collisions, the ratios of resonance yields, such as ρ^0/π, K^{*0}/K, $K^{*\pm}/K$, and

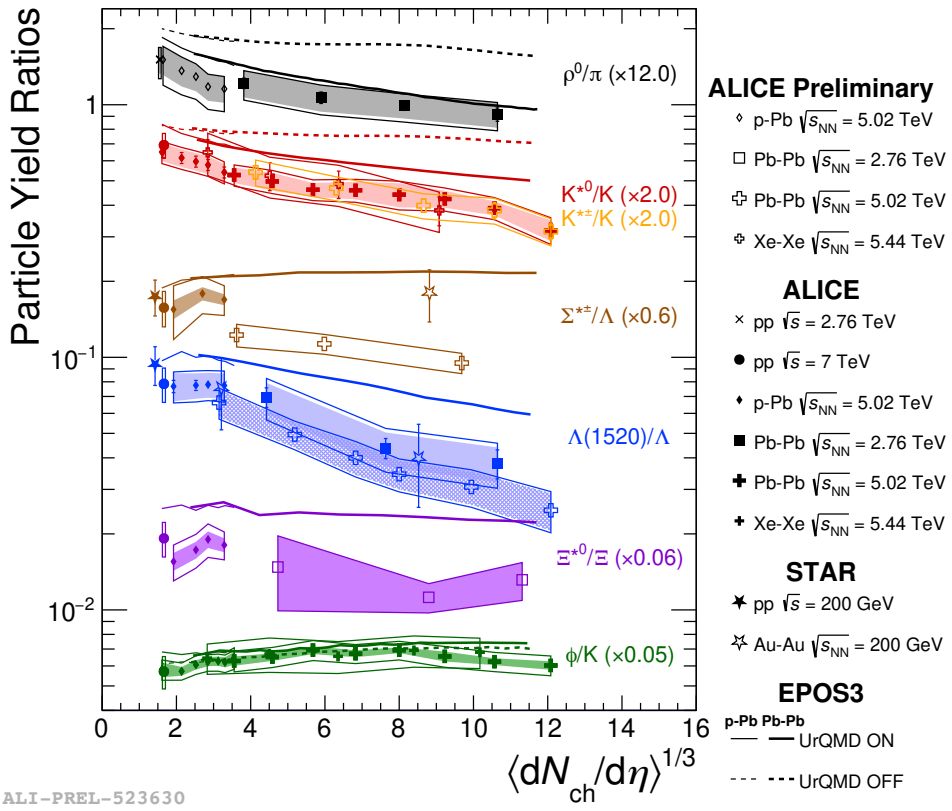

Figure 2.6: Particle yield ratios ρ^0/π, K^{*0}/K, $K^{*\pm}/K$, $\Sigma^{*\pm}/\Lambda$, $\Lambda(1520)/\Lambda$, Ξ^0/Ξ, ϕ/K as a function of multiplicity for pp, p–Pb, Xe–Xe, and Pb–Pb collisions, with comparisons to EPOS3 predictions and STAR [57] data.

$\Lambda(1520)/\Lambda$, exhibit a decreasing trend from peripheral to central collisions. Meanwhile, ratios like $\Sigma^{*\pm}/\Lambda$, Ξ^{*0}/Ξ, and ϕ/K remain relatively constant across all systems and centrality classes. Recent measurements of $K^{*\pm}$ align with previous findings for K^{*0} in Pb–Pb collisions at $\sqrt{s_{NN}} = 5.02$ TeV, indicating the dominance of rescattering effects over regeneration in the hadronic phase. Despite its longer lifetime, $\Lambda(1520)/\Lambda$ experiences more suppression than K^{*0}/K and $K^{*\pm}$/K, highlighting the complex interplay between resonance characteristics and multiplicity [52, 56, 64].

The suppression observed in the yield of $K^{*0}(892)$ and $\Lambda(1520)$ resonances in central Pb–Pb collisions can be attributed to the interaction of these particles within the dense and hot medium created in the collision. These interactions, including scattering and regeneration processes, can modify the resonance yields, leading to their suppression. The absence of such suppression for the $\phi(1020)$ resonance can be attributed to its longer lifetime (42 fm/c) which decays outside the hadronic phase [52, 56, 64].

In pp collisions, the suppression in the yield for $K^{*0}(892)$ resonance might indicate that initial-state effects or partonic interactions may also contribute to the observed suppression, highlighting the complex interplay of various factors in determining resonance production in different collision systems [65].

The description of resonance suppression based solely on lifetime is insufficient. Factors such as the mean free path within the hadron gas phase and achieving (partial) chemical equilibrium are essential for a comprehensive understanding of resonance behaviour in such environments. Therefore, the interplay of various factors plays a crucial role in determining resonance production in different collision systems, highlighting the complexity of the underlying physics.

2.2.1 Significance of $\Lambda(1520)$ Resonance Production in pp Collisions

The $\Lambda(1520)$ resonance holds significance due to its intermediate lifetime, approximately 12.6 fm/c, positioned between the shorter lifetime of the $K^{*0}(892)$ ($\sim$ 4 fm/c) and the longer lifetime of the $\phi(1024)$ ($\sim$ 42 fm/c) resonances. The $K^{*0}(892)$ resonance yield is gradually suppressed as centrality in A–A collisions as well as a slight suppression is

observed for high multiplicity pp collisions as shown in Figure 2.6. However, the behaviour of the $\Lambda(1520)$ resonance differs. As shown in Figure 6.6 the $\Lambda(1520)/\Lambda$ ratio remains constant as a function of charged particle multiplicity in p–Pb collisions. However, in central Pb–Pb collisions, a clear suppression is observed [64, 66]. The observed suppression in A–A collision is attributed to possible rescattering effects in the hadronic phase [67].

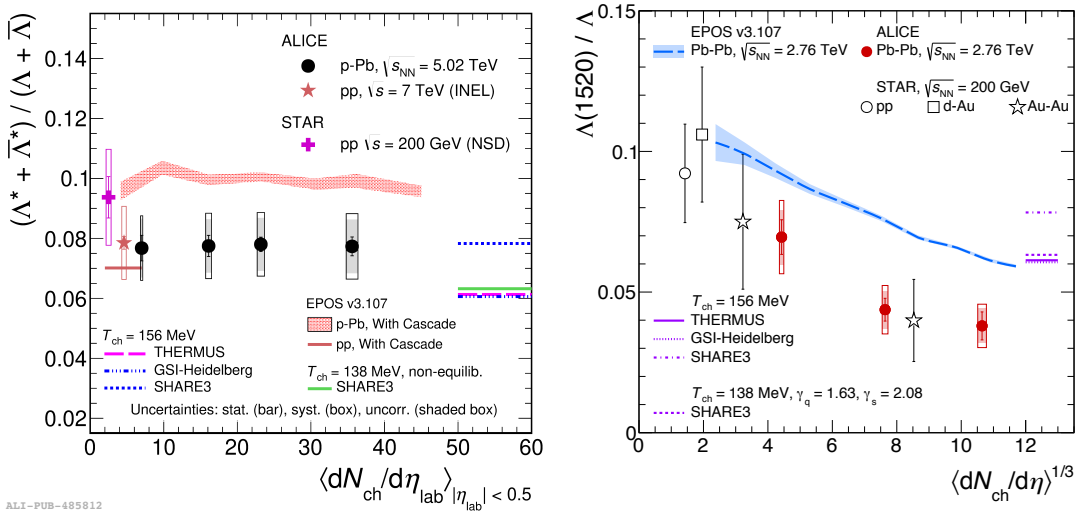

Figure 2.7: Particle yield ratios of $\Lambda(1520)/\Lambda$ as a function of centrality for p–Pb [66], Pb–Pb [64] collisions.

The observed suppression prompts further investigation into the multiplicity dependence of $\Lambda(1520)$ resonance production in pp collisions, as it serves as a baseline for estimating the lifetime between hadronic freeze-out stages by leveraging the lifetimes of other resonances. Understanding the behaviour of the $\Lambda(1520)$ resonance in different collision systems provides valuable insights into the dynamics of the collision medium and sheds light on the underlying physics mechanisms governing resonance production.

This thesis focuses on a detailed analysis of $\Lambda(1520)$ resonance production in pp collisions at center-of-mass energies of $\sqrt{s} = 5.02$ and 13 TeV, performed at mid-rapidity ($|y| < 0.5$). The analysis is conducted across five different multiplicity classes, as well as a minimum bias to provide an inclusive overview of $\Lambda(1520)$ production in a small collision system. Furthermore, this study extends to the investigation of both $\Lambda(1520)$ and $K^{*0}(892)$ resonances in high-multiplicity (HM) pp collisions at 13 TeV. These measurements are performed within three distinct high-multiplicity classes.

Chapter 3

The ALICE Experiment at the LHC

This chapter briefly describes the LHC (Large Hadron Collider) accelerator and the ALICE (A Large Ion Collider Experiment) detector setup.

3.1 The Large Hadron Collider

The European Organisation for Nuclear Research (CERN) was established close to Geneva on the French-Swiss border in 1954 to investigate the fundamental structures of the universe. The Large Hadron Collider (LHC), the world's largest and most powerful circular particle accelerator with a circumference of 27 kilometres, commenced operations on September 10, 2008. Situated between the Jura mountains and the Alps, it spans across both France and Switzerland. It is constructed underground at a depth of 100 meters to provide effective shielding against radiation.

Inside the tunnel, there are two beam pipes maintained at ultra-high vacuum, encircled by superconducting electromagnets. These magnets are maintained at a temperature of -271.3°C (1.9K) to leverage the superconducting state. The accelerator is connected to an extensive liquid helium distribution system responsible for cooling the magnets and other essential services. Two high-energy particle beams circulate in opposite directions at nearly the speed of light through the beam pipes. A total of 1232 dipole magnets are used to bend the beams, while 392 quadrupole magnets are employed to focus them. These beams collide at four main interaction points within the collider.

The four major experiments of LHC are ATLAS (A Toroidal LHC Apparatus), ALICE (A Large Ion Collider Experiment), CMS (Compact Muon Solenoid), and LHCb (LHC-beauty) situated at points 1, 2, 5, and 8 along the LHC ring, respectively. These experiments contribute significantly to our understanding of particle physics. ATLAS is one of the largest experiments designed to explore a wide range of physics, including the search for the Higgs boson, extra dimensions, and particles that could make up dark matter. Like ATLAS, CMS is also a general-purpose detector, built to search for various phenomena including the Higgs boson, supersymmetry, and extra dimensions. ALICE specializes in studying heavy-ion collisions, particularly focusing on the formation of QGP, reflecting the condition of the early universe. Finally, LHCb investigates the subtle distinctions between matter and antimatter, with a keen interest in particles containing beauty quarks. Each experiment plays a crucial role in pushing the boundaries of particle physics and unravelling the mysteries of the universe. The schematic diagram of LHC at CERN Geneva is shown in Figure 3.1.

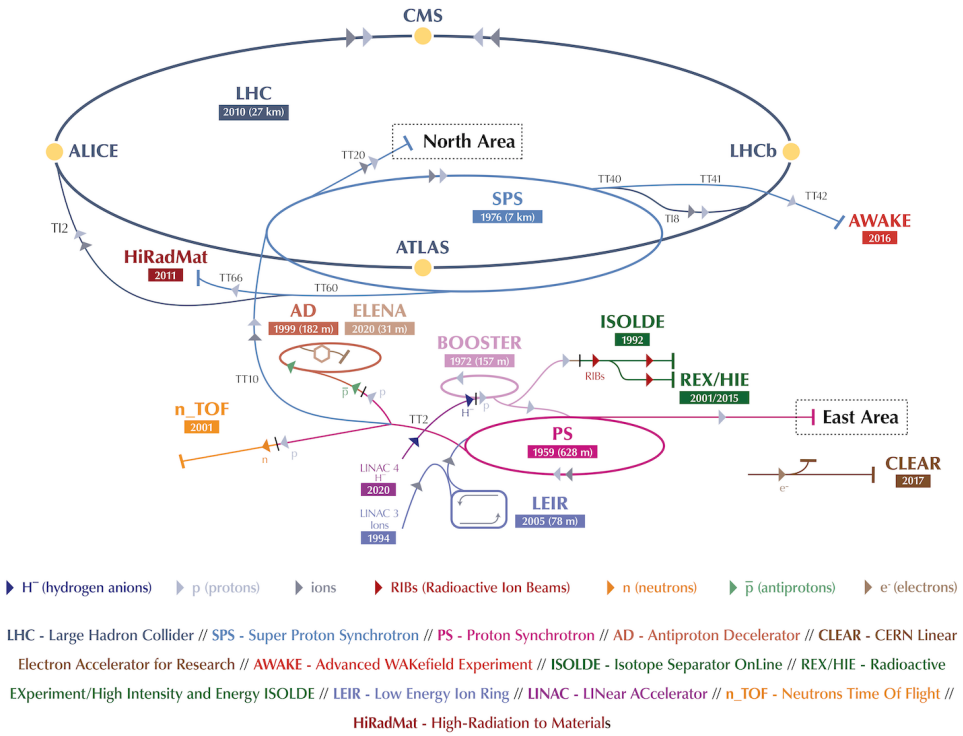

Figure 3.1: A schematic diagram of CERN LHC accelerator complex [68].

3.1.1 Accelerating Proton

To achieve ultra-relativistic energies, particles undergo a multi-stage acceleration process before entering the LHC. For proton-proton (pp) collisions, isolated protons are obtained by stripping electrons from hydrogen atoms. These protons are then accelerated to 50 MeV using the Linear Accelerator 2 (LINAC 2). Following this, the protons are propelled by an electric field into the Booster, where they reach speeds of nearly one-third of the speed of light. Subsequently, the protons enter the Proton Synchrotron Booster (PSB). In the PSB, they circulate multiple times which further increases their energy. Through this repeated circulation, the protons achieve speeds up to 91.6% of the speed of light and are accelerated to an energy of 1.4 GeV. Within the Proton Synchrotron (PS), proton beams reach 99.9% of the speed of light and an energy of 25 GeV. After the PS, the proton beam is injected into the Super Proton Synchrotron (SPS), where it accelerates to 450 GeV. Subsequently, the high-energy proton beam is split into two and injected into the Large Hadron Collider (LHC). Here, they undergo acceleration in opposite directions within beam pipes spanning 26.7 kilometres in circumference. Each proton beam undergoes 11,000 cycles of acceleration, gradually increasing the energy of the protons. Eventually, each proton in the bunch achieves its maximum energy of 6.5 TeV. Once the proton beams achieve their maximum energy, they are allowed to collide at different interaction points within the LHC.

3.1.2 Accelerating Lead

The lead isotope used in the LHC, Pb-208, has 82 protons and typically around 126 neutrons, totalling a mass number of 208. The injection process for Pb-ions into the LHC ring involves several steps. Initially, a pure lead piece is heated to form lead atom vapour, from which lead ions are created by stripping off electrons with an electric current. These ions undergo further acceleration up to 4.5 MeV per nucleon in LINAC 3. After that, the ions pass through a carbon foil to become Pb^{54+}. Subsequently, in the Low Energy Ion Ring (LEIR), they are accelerated to 72 MeV per nucleon. After injection of the beam into the PS for further acceleration of up to 5.9 GeV per nucleon, where aluminium foil further strips electrons to create Pb^{82+}, which are accelerated to 5.9 GeV per nucleon

before being injected into the SPS. The SPS accelerates them to 177 GeV per nucleon and finally injects them into the LHC ring in two directions. Each Pb-ion collision involves 600 bunches, each containing 7×10^7 lead ions, providing a designed luminosity of $10^{27}\text{cm}^2\text{s}^{-1}$ [69].

3.2 A Large Ion Collider Experiment

A Large Ion Collider Experiment (ALICE), is located at Point 2 of the LHC. It is specifically designed to study Quark-Gluon Plasma (QGP) formed in heavy-ion collisions. With a focus on collisions involving heavy ions, ALICE explores extreme energy densities and temperatures that can lead to the creation of a QGP-like state of matter. Its primary goal is to investigate various properties of QGP and gain insights into the physics of strongly interacting matter. Additionally, ALICE examines the proton-proton (p-p) and proton-nucleus (p–Pb) collisions, which act as a baseline and contribute valuable knowledge to the dynamics of heavy-ion collisions. The ALICE detector is designed to operate effectively in

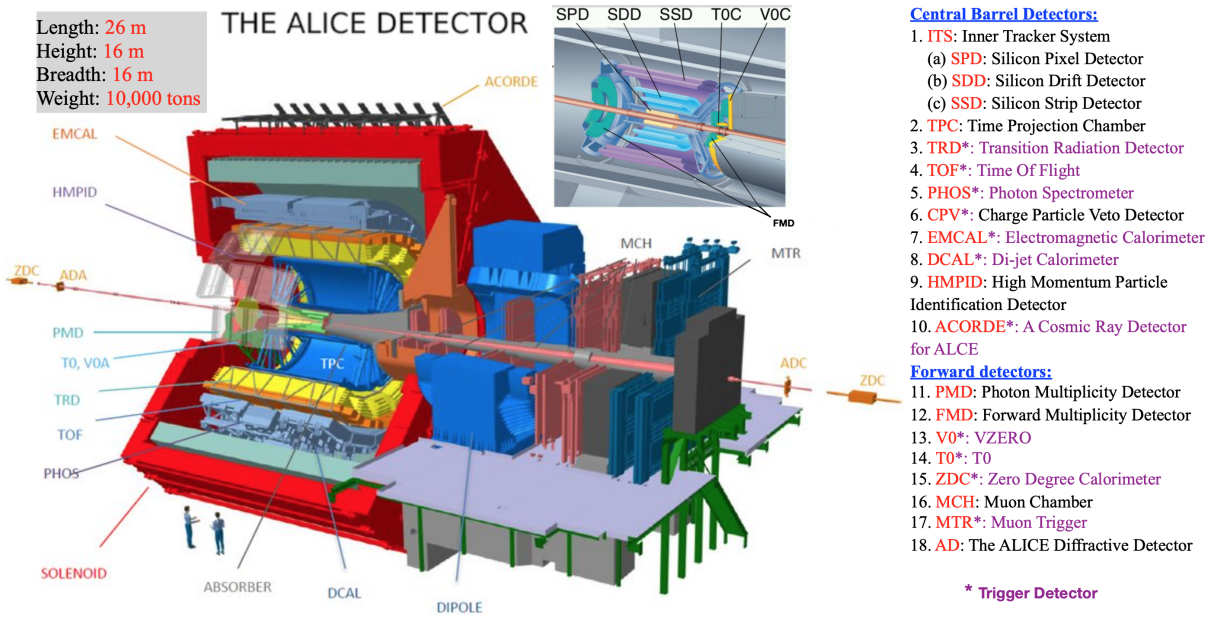

Figure 3.2: A schematic diagram of ALICE and its sub-detectors [39].

environments with high-charged particle multiplicities, enabling the tracking and identification of particles spanning a wide momentum range from 0.1 GeV/c to 100 GeV/c. The

detector weighs approximately 10,000 tons and measures 26 meters in length, 16 meters in height and 16 meters in breadth. The key components include a magnet generating a 0.5 T magnetic field, a vertex detector for precise primary vertex positioning, a tracking chamber for trajectory imaging, a calorimeter for measuring electromagnetic energy, a muon spectrometer for isolating muons, and a trigger for event quality assessment and rare event isolation. The schematic diagram of ALICE is shown in Figure 3.2. ALICE has 17 sub-detectors which are categorized into central barrel detectors and forward detectors [70, 71].

Central Barrel Detectors

The central barrel of ALICE is surrounded by a large solenoidal magnet (L3 magnet taken from the LEP experiment) generating a magnetic field of 0.5 T. It covers the pseudorapidity interval of $-0.9 < \eta < 0.9$, corresponding to polar angles between 45° and 135°.

Positioned around the interaction point (IP), the central barrel region encompasses sub-detectors such as Inner Tracking System (ITS), Time Projection Chamber (TPC), Transition Radiation Detector (TRD), Time Of Flight (TOF), High Momentum Particle Identification Detector (HMPID), Electromagnetic Calorimeter (EMCAL), Photon Spectrometer (PHOS) and A Cosmic Ray Detector (ACORDE). The tracking in the central barrel primarily relies on the ITS and TPC. Additionally, the Transition Radiation Detector (TRD) improves p_T resolution at high momentum. The ITS supports high-multiplicity triggering and secondary vertex reconstruction. Particle identification (PID) within the ALICE detector is accomplished using various sub-detectors. The TPC plays a crucial role in both tracking and PID capabilities, allowing for the determination of charged particle momentum. Additionally, the TOF, TRD, HMPID, and EMCal detectors contribute to PID by providing complementary information about particle properties. An array of scintillators known as ACORDE serves as the cosmic rays trigger detector.

3.2.1 Inner Tracking System (ITS)

The Inner Tracking System (ITS) [71, 72] consists of six cylindrical layers of silicon detectors, comprising two layers each of Silicon Pixel Detector (SPD), Silicon Drift Detector (SDD), and Silicon Strip Detector (SSD). This is the innermost sub-detector of ALICE, positioned at radial distances of 3.9 to 43 cm from the beam pipe and covers the entire azimuth with a pseudorapidity range of $|\eta| < 0.9$. Primarily, the ITS plays a crucial role in primary vertex determination and secondary vertex reconstruction. With its superior resolution, it helps in tracking and particle identification, particularly for particles with very low momentum ($p_{\mathrm{T}} < 200$ MeV/c). Furthermore, it contributes to reconstructing particles traversing through the dead channels of the TPC, enhancing the momentum and angle resolution of particles reconstructed via the TPC. A schematic diagram of the ITS is illustrated in Figure 3.3.

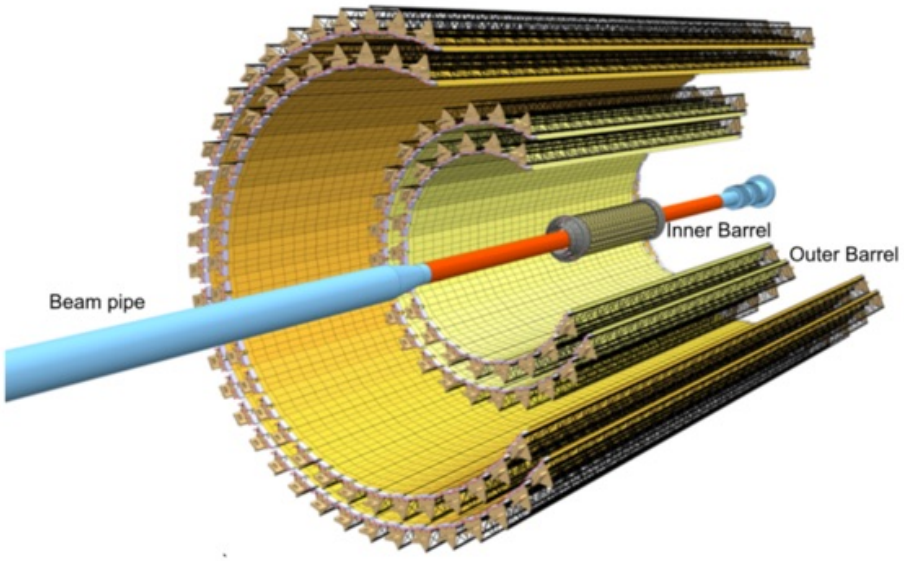

Figure 3.3: A schematic diagram of ITS [71].

The first and second layers of ITS, referred to as Silicon Pixel Detectors (SPD), are positioned at radii of 3.9 cm and 7.6 cm from the interaction point and cover the pseudorapidity ranges $|\eta| < 2.0$ and $|\eta| < 1.4$ respectively. They consist of modules housing a total of 9.8×10^6 hybrid silicon pixel detectors. These detectors generate binary signals upon interaction with charged particles, facilitating particle counting. The SPD primarily

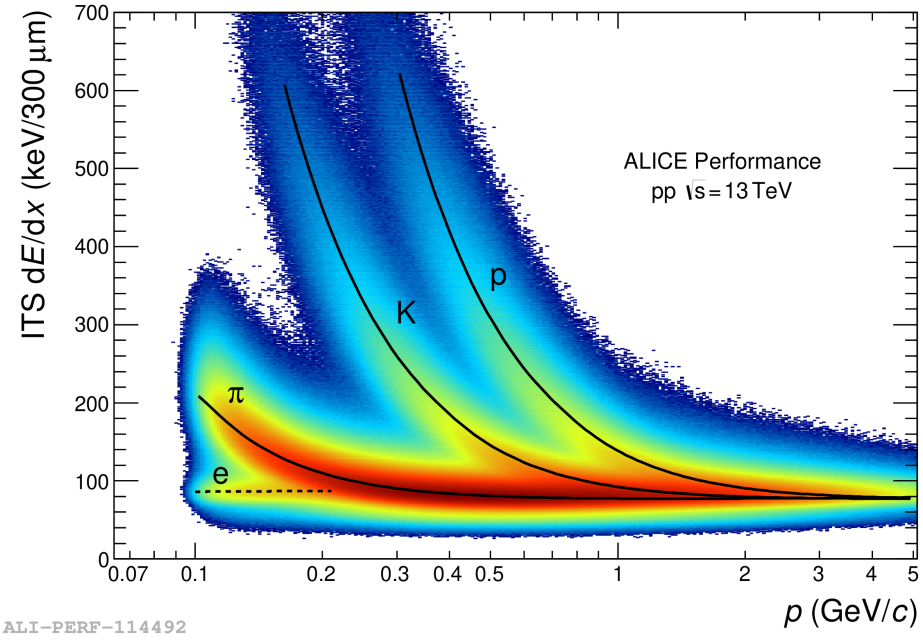

Figure 3.4: Average dE/dx of charged particles as a function of momentum for ITS pure standalone tracks measured in pp collisions at $\sqrt{s} = 13$ TeV.

operates to reconstruct collision primary vertices and trigger data acquisition. Moreover, it contributes to achieving an impact-parameter resolution surpassing 50 μm for tracks with transverse momentum $p_{\mathrm{T}} > 1.3$ GeV/c.

The third and fourth layers of ITS, known as the Silicon Drift Detector (SDD), are situated at radii of 15.0 cm and 23.9 cm, covering $|\eta| < 0.9$. They provide two-dimensional spatial information ($r\phi$ and z) with a spatial resolution of 35 μm ($r\phi$) and 25 μm (z). The SDD assists in track separation and particle identification through $\mathrm{d}E/dx$ measurements. It determines particle positions using drift time estimation and charge centroid measurement. Additionally, the SDD is structured into two drift regions by a central cathode, facilitating precise particle tracking.

The two outermost layers of ITS consist of Silicon Strip Detectors (SSD), located at radial distances of 38.0 cm and 43.0 cm, covering $|\eta| < 1.0$. These double-sided silicon detectors provide a spatial resolution of 27 μm ($r\phi$) and 830 μm (z), with a fast readout time of 1 μs. They play a crucial role in track reconstruction by connecting tracks from the TPC to the ITS and contributing to particle identification. Each SSD module consists of a 1536-strip double-sided sensor that is connected to twelve front-end chips. When

charged particles traverse through the strips, they generate hits that furnish position and energy deposition details.

When particles pass through the ITS detector, their energy loss distribution (dE/dx) is measured by the four outer layers of the detector, where cluster charge determines the value per layer. Figure 3.4 shows the truncated mean energy loss distribution as a function of momentum in the ITS detector.

3.2.2 Time Projection Chamber (TPC)

The Time Projection Chamber (TPC) [71, 73] serves as the primary tracking detector within the central barrel of the ALICE experiment, serving as a cornerstone for particle tracking and identification. It is positioned at radial distances ranging from 85 to 247 cm from the beam pipe, extending along the beam direction with a total length of 510 cm. It offers comprehensive coverage across the full azimuthal range and within the pseudorapidity range of $|\eta| < 0.9$. A schematic diagram of the TPC is illustrated in Figure 3.5.

TPC combines the principles of Multi-Wire Proportional Chambers (MWPCs) and drift chambers to function. A schematic diagram illustrating particle tracking is depicted in Figure 3.6. As charged particles traverse the TPC's gas volume, typically filled with a mixture of Argon (Ar) and CO_2 in an 88:12 ratio, they ionize the gas atoms, creating electron-ion pairs. These ionization electrons then drift towards sensing electrodes under a uniform electric field, typically achieved by applying a high voltage of around 100 kV between the central electrode and the readout plates. This high voltage generates a uniform electrostatic field of about 400 V/cm within the TPC volume, facilitating the electron drift process. The ionization electrons drift with a speed of approximately 2.7 cm/s, corresponding to a maximum drift time of around 92 microseconds. This drift process allows for the spatial localization of the ionization event along the particle's trajectory. By measuring the drift times of these electrons, typically through the use of segmented readout planes equipped with sensitive detectors such as wire chambers or pad detectors, the TPC reconstructs particle trajectories in three dimensions.

Additionally, the presence of a uniform magnetic field of 0.5 Tesla along the z-direction

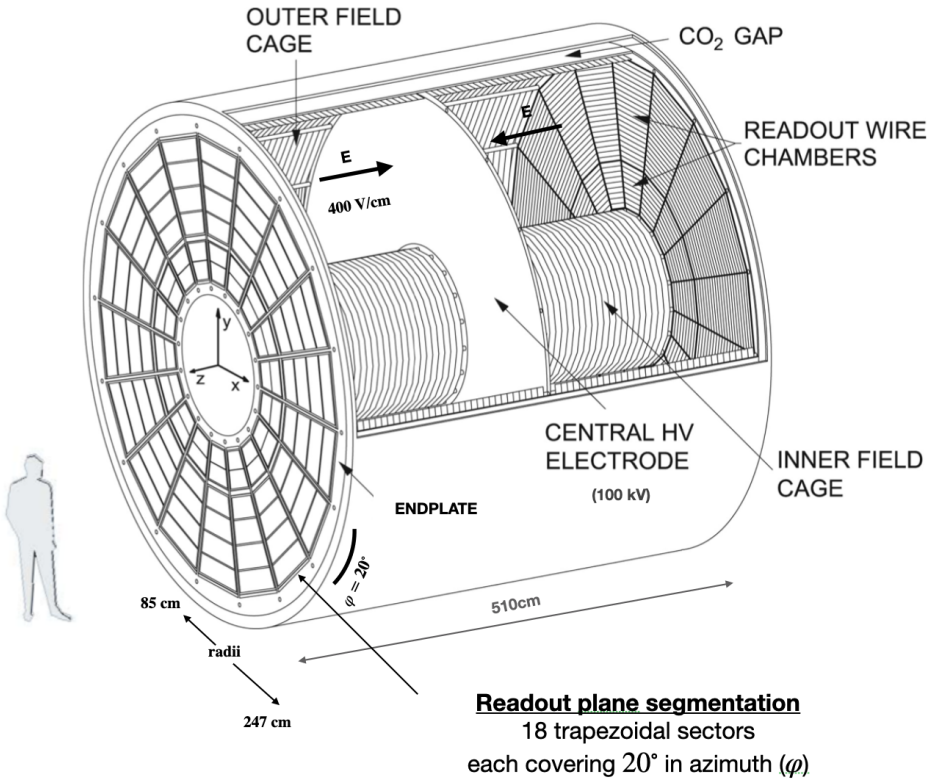

Figure 3.5: A schematic diagram of TPC [71, 73].

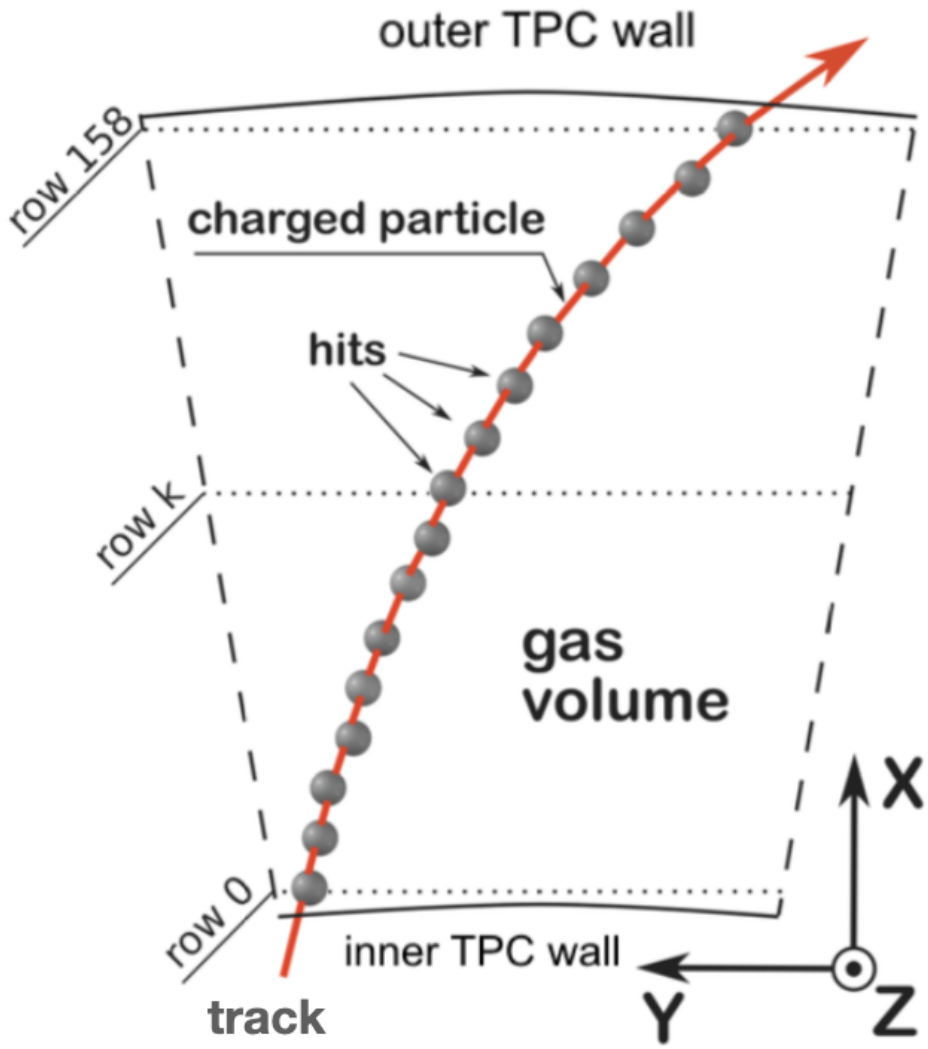

Figure 3.6: A diagram for TPC tracking [74].

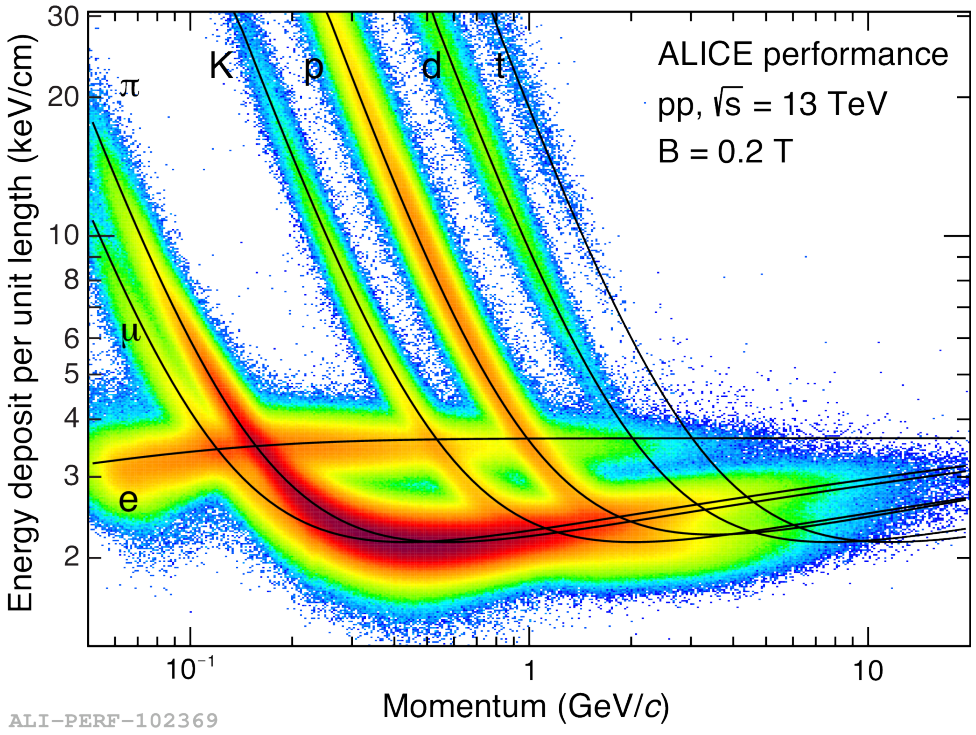

Figure 3.7: Energy deposit per unit length as a function of momentum measured with the ALICE TPC.

which is generated by the L3 magnet, causes charged particles to bend in curved paths. It enables precise momentum measurements based on the curvature of the trajectories. This magnetic field configuration is essential for extracting momentum information crucial for particle identification and physics analyses.

The TPC identifies particles by measuring their energy loss (dE/dx) as they traverse the gas volume. The measurement of dE/dx serves as a method for particle identification as shown in Figure 3.7.

3.2.3 Time Of Flight (TOF) Detector

The Time-Of-Flight (TOF) detector in the ALICE experiment at CERN is a critical component utilized for identifying and measuring the momentum of charged particles generated in high-energy collisions [71, 75]. Positioned as the outermost layer of the central barrel detectors, the TOF detector spans radial distances from 370 cm to 399 cm from the beam line. It ensures comprehensive coverage across the pseudorapidity

region of $|\eta| < 0.9$ with full azimuthal coverage. The primary objectives of the TOF detector include the identification of charged particles within the intermediate momentum range, particularly up to 2.5 GeV/c for pions and kaons, and up to 4 GeV/c for protons. Additionally, the TOF detector plays a crucial role in providing triggering capabilities for cosmic ray events and ultra-peripheral collisions. A schematic layout of the TOF detector is shown in Figure 3.8.

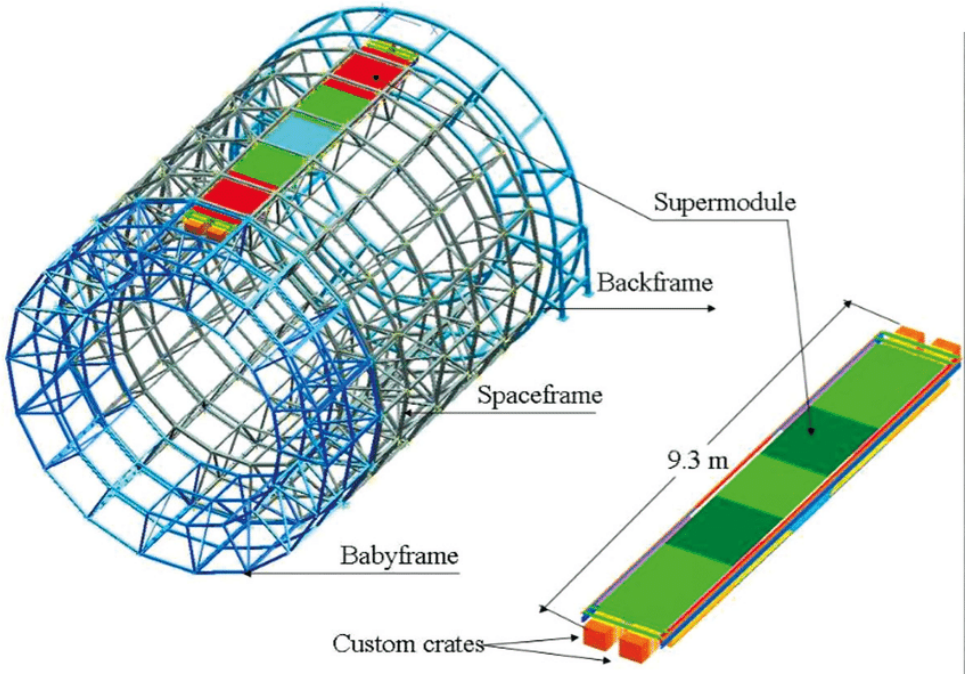

Figure 3.8: A schematic layout of TOF detector [71].

The TOF detector comprises 1593 Multi-Gap Resistive Plate Chamber (MRPC) strip detectors organized into 18 azimuthal sectors. Each MRPC strip is divided into two rows of 48 pickup pads, a total of 96 pads per strip and 152,928 readout channels. This layout ensures low detector occupancy for precise measurements. The TOF detector achieves an impressive time resolution of better than 50 ps and an efficiency close to 100% [71].

The TOF detector measures the time taken by charged particles to travel from the collision point to the detector, providing crucial information about the particle's velocity as shown in Figure 3.9. By using the known distance between the collision point and the TOF detector, along with the measured time-of-flight, the velocity (v) and momentum (p) of the particle can be calculated. Different particle species exhibit distinct velocities for

a given momentum due to variations in their masses. Therefore, by accurately measuring the velocity of particles using TOF information, it becomes possible to identify different particle species based on their characteristic velocities.

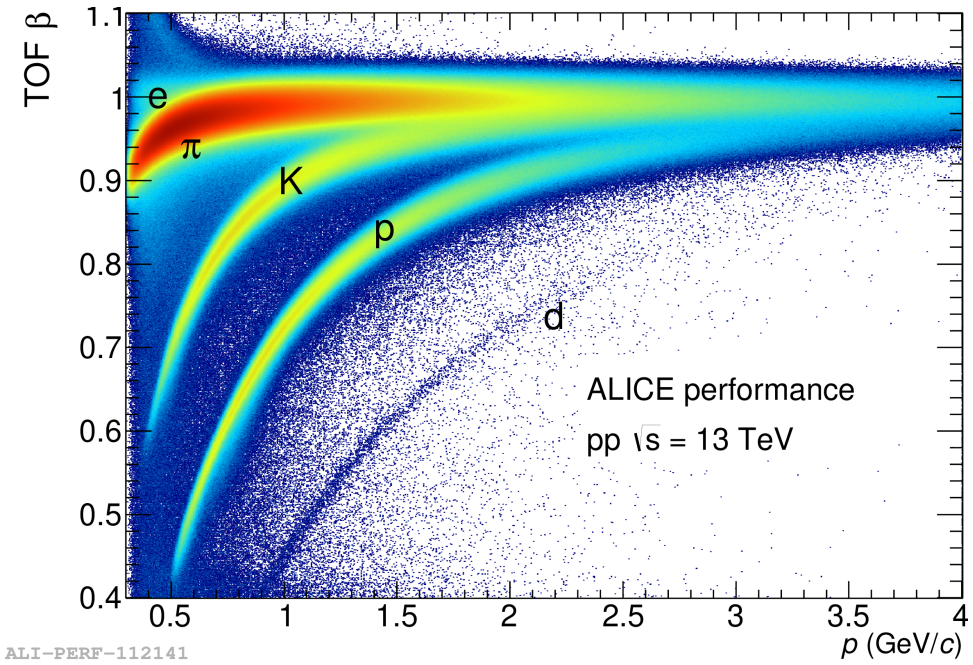

Figure 3.9: TOF β as a function of momentum in pp collisions at $\sqrt{s} = 13$ TeV.

Particle identification can be done by measuring the time difference between the collision and the arrival of particles. Specifically, it distinguishes between pions and kaons with p_{T} less than 2.5 GeV/c, while protons with transverse momenta around 4 GeV/c are identified.

Moreover, when integrated with the ITS and TPC, the TOF detector enhances particle identification capabilities within the low transverse momentum range of 1 GeV/c. This combination allows for improved identification of pions, kaons, and protons based on their distinct time-of-flight signatures.

3.2.4 Transition Radiation Detector (TRD)

The Transition Radiation Detector (TRD) [71, 76] plays a crucial role in electron identification and triggering processes within particle collision experiments. Positioned between the TPC and TOF detector, it covers a pseudorapidity range of $|\eta| < 0.84$ and ensures

full acceptance in the azimuthal direction. With a total of 522 detectors divided into 18 super modules in the azimuthal direction, each super module contains 30 modules arranged in 5 stacks along the beam axis, with each stack further arranged in 6 layers. This configuration results in approximately 1.15 million readout channels.

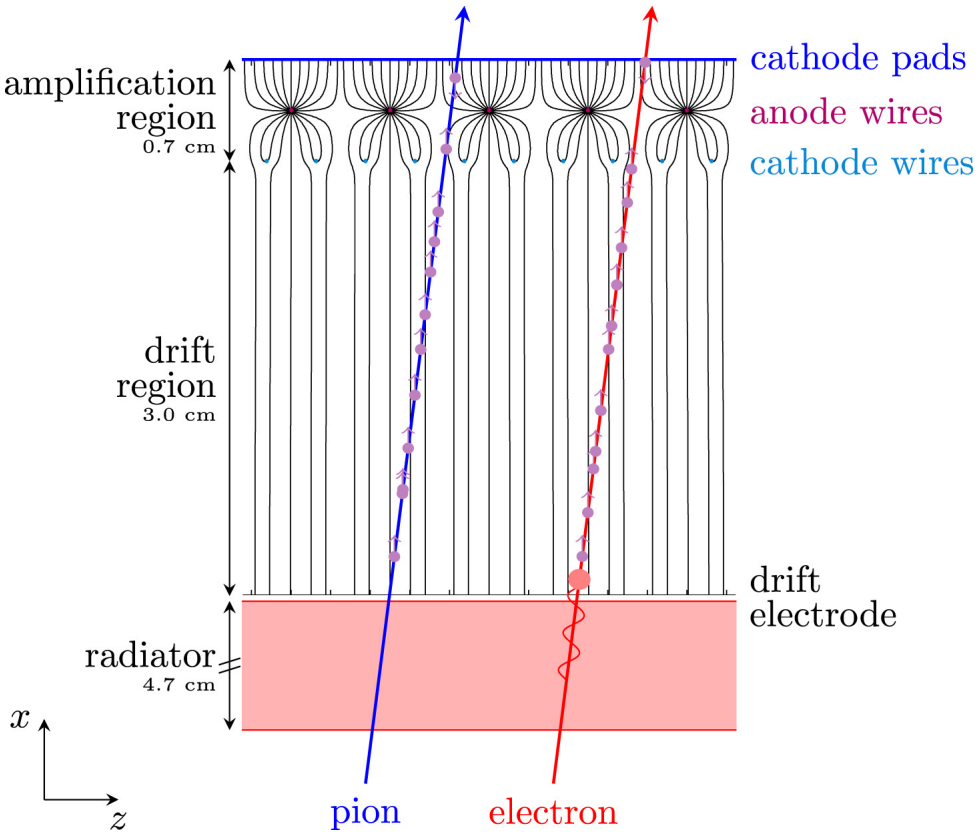

Figure 3.10: Schematic cross-section of TRD chamber in the xy-plane (perpendicular to the wires) with tracks of a pion and an electron to illustrate the ionisation energy deposition and the Transition Radiation (TR) contribution [76].

Figure 3.10 illustrates a cross-section of a Transition Radiation Detector (TRD) chamber in the xy plane, perpendicular to the wires. Tracks of a pion and an electron are shown to demonstrate ionisation energy deposition and the Transition Radiation (TR) contribution. The TRD operates using Multi-Wire Proportional Chambers (MWPCs) and radiators, with an active gas mixture of Xenon (Xe) and Carbon Dioxide (CO_2) in an 85:15 proportion. Its primary function is to identify electrons in the high momentum region ($p > 1$ GeV/ c), where discriminating between electrons and pions using traditional dE/dx techniques becomes challenging.

In this high momentum regime, the TRD uses the transition radiation process to distinguish electrons from other particles such as pions. When a charged particle traverses between two media with different dielectric constants, it emits transition radiation, with the emitted radiation proportional to the Lorentz factor ($\gamma = v/c$) of the particle. Since different particles have different masses and velocities, they emit varying amounts of transition radiation. By analyzing the amount of transition radiation emitted, the TRD effectively identifies electrons, thus enhancing the overall electron detection efficiency.

Moreover, it accurately identifies electrons that contribute to the enhancement of the yield of J/Ψ particles, which are important for understanding various aspects of particle physics. Overall TRD improves the accuracy of particle identification and triggering processes.

3.2.5 Photon Spectrometer (PHOS)

The Photon Spectrometer (PHOS)[71]is an electromagnetic calorimeter known for its high spatial and energy resolution. It comprises approximately 12,544 channels based on a scintillating material called Lead Tungstate ($PbWO_4$). Positioned on the outer region of the Time-Of-Flight (TOF) detector and at the bottom of the ALICE detector, it is situated at a radial distance of 4.6m from the interaction point. PHOS covers a pseudo-rapidity range of $-0.12 < \eta < 0.12$ and provides coverage of 70 in the azimuthal direction. With a dynamic energy range of 0.1 GeV to 100 GeV, PHOS identifies photons and reconstructs neutral mesons. Its main goal is to measure QGP temperature, and space-time dimensions, and study deconfinement through jet quenching. Furthermore, PHOS significantly contributes to studying deconfinement phenomena by investigating jet quenching. By examining the high transverse momentum π^0 spectra and identifying jets through jet-jet correlations, PHOS enhances our understanding of particle interactions in high-energy collisions.

3.2.6 High-Momentum Particle Identification Detector (HMPID)

The High Momentum Particle Identification Detector (HMPID) [71, 77] is a low-acceptance detector that contributes about 5% to the central barrel region of the ALICE detectors.

Its primary purpose is to identify high-momentum ($p_T > 1$ GeV/c) charged hadrons that cannot be detected by the energy loss method in the TPC or the time of flight method in the TOF detector. It covers a pseudo-rapidity range of $-0.6 < \eta < 0.6$ and azimuth from 10° to 59°, consisting mainly of two parts: the radiator and the photon detector. Comprising seven Ring Imaging Cherenkov (RICH) detectors, each with a size of 1.82 m^2 (1.4m × 1.3m), the HMPID is capable of identifying charged hadrons up to 5 GeV/c. Its main role is to enhance Particle Identification capability beyond the momentum range achieved by the ionisation energy loss measurement (in ITS and TPC) and by the TOF. The HMPID extends the range for identifying protons and kaons on a track-by-track basis, up to 3 GeV/c and 5 GeV/c, respectively.

3.2.7 Electromagnetic Calorimeter (EMCaL)

The Electromagnetic Calorimeter[71], situated 4.36m from the interaction point, detects high-energy particles like photons, electrons, neutral pions, and jets within $-0.7 < \eta < 0.7$ and 80° to 187° azimuthal angles. Comprising 17,664 towers grouped into 4,416 modules, it employs Avalanche Photo Diodes (APDs) for readout. This detector not only identifies high-energy particles but also enhances energy resolution across various momenta, enabling precise measurements of jet quenching, high-energy jets, and high-momentum electrons and photons.

3.2.8 A Cosmic Ray Detector (ACORDE)

ACORDE [71] serves as ALICE's cosmic ray detector, featuring an array of 60 plastic scintillator counters positioned on the upper surface of the L3 magnet, 850 cm from the interaction point. Positioned at the extreme top of the ALICE detector, ACORDE covers $|\eta| < 1.3$ and an azimuthal angle of 30° to 150°. It provides a fast (L0) trigger signal for the calibration and assessment of ITS and TPC detectors. It also detects atmospheric muons in conjunction with TPC, TRD, and TOF. ACORDE, with its Cosmic-Ray Trigger system of 60 plastic scintillator counters, provides precise cosmic ray information from 10^{15} to 10^{17} eV.

Forward Detectors

The forward detectors include the Photon Multiplicity Detector (PMD), Forward Multiplicity Detector (FMD), Cherenkov detector T0, plastic scintillator detector V0, and Zero Degree Calorimeter (ZDC) and cover rapidity range $-3.4 < \eta < 5.1$. These detectors are strategically positioned to capture events and facilitate triggering processes in the forward region. Complementing these detectors is the muon spectrometer, located outside the solenoid along one side of the beam direction. Together, these components form a comprehensive detector array essential for capturing and analyzing particle interactions in the forward direction.

3.2.9 VZERO detector (V0)

The V0 detector [71, 78] in the ALICE experiment at CERN serves as a vital forward detector, comprising two plastic scintillator counters known as V0A and V0C. Positioned asymmetrically on both sides of the nominal interaction point (IP), V0A is located at $z = 340$ cm, while V0C is situated at $z = -90$ cm. V0A covers the pseudorapidity region of $2.8 < \eta < 5.1$, while V0C spans $-3.7 < \eta < -1.7$. The two VZERO arrays, along with other detectors are shown in Figure 3.11.

Functionally, the V0 detector fulfils several critical roles in both proton-proton and nucleus-nucleus (A-A) collisions within the ALICE experiment:

- **Minimum Bias Triggering:** The V0 detector provides a minimum bias trigger signal, enabling the detection of a broad range of inelastic collision events without introducing significant selection bias. This trigger signal is crucial for capturing a comprehensive sample of collision events for further analysis in the central barrel detectors.

- **Improved Vertex Determination:** The VZERO detectors effectively reject the background events generated due to the interaction of beams with residual gas within the beam pipe and with mechanical structures along the beamline by utilizing the time gap between signals from V0A and V0C (11.3 ns and 3 ns, respectively).

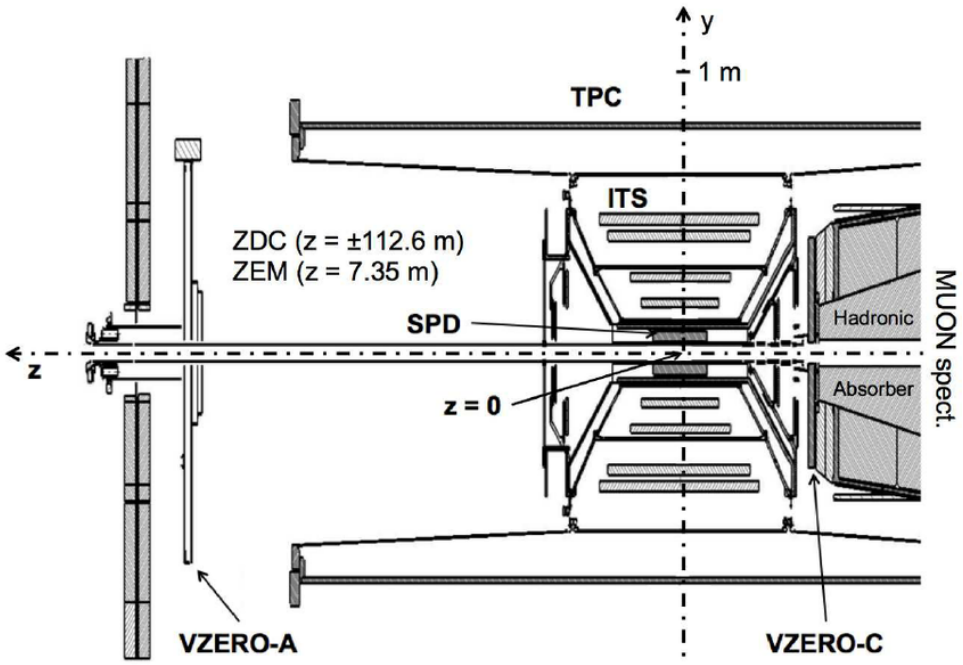

Figure 3.11: The two VZERO arrays, along with other detectors.

Additionally, the V0 detector aids in improving vertex determination by providing spatial information about collision vertices.

- **Centrality Estimation:** The V0 detector assists in estimating collision centrality by measuring the charged particle multiplicity or V0 multiplicity (V0M) using the signal amplitude. This information is valuable for characterizing the centrality of collision events, which is essential for understanding the collision geometry and interpreting experimental results accurately.

Overall, the V0 detector plays a crucial role in enhancing the efficiency and accuracy of event selection and vertex determination in the ALICE experiment, contributing significantly to the study of high-energy particle collisions and the exploration of the properties of the QGP.

3.2.10 T0 Detectors

The T0 detector[71, 79] consists of two arrays, T0C and T0A, each containing 12 quartz Cherenkov radiator detectors. Positioned 70 cm and 3.6 m from the interaction point,

respectively, T0C covers the pseudorapidity range $2.9 \leq \eta \leq 3.3$, while T0A covers $4.5 \leq \eta \leq 5$. Its primary function is to provide a fast timing signal for the TOF detector, serving as a collision time reference. Additionally, it triggers early signals for TRD and L0.

3.2.11 Photon Multiplicity Detector (PMD)

The Photon Multiplicity Detector (PMD) [71, 80] positioned 364 cm from the interaction point and perpendicular to the beam direction, covers a pseudorapidity range of $2.3 \leq \eta \leq 3.7$. It measures photon multiplicity and spatial distribution, aiding in estimating the reaction plane for studying charged particle flow. Its honeycomb structured gas proportional counters are installed in Charge Plane Veto (CPV) and preshower planes. Each plane contains 24 modules with 4608 honeycomb cells per module. A 1.5-unit-thick lead converter between the planes generates electromagnetic showers when photons pass through it, affecting multiple cells. The combined information from CPV and pre-shower planes facilitates photon identification and reaction plane estimation.

3.2.12 Forward Multiplicity Detector (FMD)

The Forward Multiplicity Detector (FMD), referenced in[71, 79], is strategically positioned 320 cm from the interaction point (IP) and spans an η range from 3.68 to 5.03. Consisting of FMD1, FMD2, and FMD3 detectors, FMD1 is equipped with an inner-type silicon sensor ring, whereas FMD2 and FMD3 feature both inner and outer-type silicon sensor rings. FMD2 covers an η range of 1.7 to 3.68, while FMD3 spans from -1.7 to 3.68 in η. This detector measures charged particle multiplicity distribution in both backward ($3.4 < \eta < 1.7$) and forward regions ($1.7 < \eta < 5$). It also helps to study the flow and jets by analyzing collision orientations.

3.2.13 Zero Degree Calorimeter (ZDC)

The Zero Degree Calorimeter (ZDC) [71, 81] is positioned on both sides of the interaction point at a distance of 116 m. It consists of four calorimeters, two for protons (ZP) and two

for neutrons (ZN), on each side. ZDC measures the energy of spectator nucleons, assisting in centrality estimation and luminosity detection in heavy-ion collisions. By determining collision geometry and overlap regions of colliding nuclei, it estimates the number of participant nucleons. ZDC enhances centrality triggers and facilitates the estimation of the reaction plane angle in A-A collisions.

3.2.14 Muon Spectrometer

The muon spectrometer is a crucial detector of ALICE, located 14 m in the negative beam direction, with a pseudorapidity range of $-4 < \eta < -2.5$ and full azimuth coverage. Composed of an absorber made of concrete and steel, complemented by tracking chambers and a dedicated dipole magnet, it reconstructs muons with $p_{\mathrm{T}} > 4\,\mathrm{GeV}/c$. Its large dipole magnet and trigger chambers aid in muon trajectory reconstruction and event triggering, respectively. Shielded by a dense absorber tube, it prevents unwanted particles from entering. The spectrometer plays a vital role in reconstructing quarkonia resonances, such as J/ψ and Υ, in their dimuon decay channels, enabling the study of heavy-ion collisions and the behaviour of quarkonia in high-temperature QCD plasma. Measuring their production rates as a function of collision centrality and transverse momentum offers insights into quarkonia suppression mechanisms.

3.2.15 ALICE Trigger System

The ALICE experiment at CERN relies on a sophisticated trigger system to efficiently select and record collision events for detailed analysis. This system is essential for managing the immense data volume produced by the LHC. At the core of this system is the Central Trigger Processor (CTP), which processes signals from various detectors and utilizes the LHC bunch-filling scheme to make rapid and precise trigger decisions. The CTP, in conjunction with a three-tiered trigger hierarchy, ensures that only the most relevant events are captured for further studies.

Central Trigger Processor (CTP)

The Central Trigger Processor (CTP) is the core of the ALICE trigger system. It generates trigger decisions based on signals from various detectors and the LHC bunch-filling scheme, typically within approximately 0.9 microseconds.

Three-Level Trigger

- **Level 0 (L0) Trigger**:

  The L0 trigger decision is the fastest, made approximately $\sim 0.9\,\mu s$ after a collision. It relies on fast-response detectors such as V0, T0, EMCal, PHOS, and the Muon Trigger (MTR). The L0 trigger identifies initial events of interest, providing a first layer of filtering.

- **Level 1 (L1) Trigger**: The L1 trigger decision is made after about 260 LHC clock cycles, which is $\sim 6.5\,\mu s$ post-collision. This delay accommodates the processing time for detectors with longer latencies, like the TRD and EMCal, and the propagation time for signals from distant detectors such as the ZDC, positioned 113 meters from the Interaction Point 2. Events passing the L0 criteria are further refined at the L1 stage.

- **Level 2 (L2) Trigger**: The L2 decision occurs after about 100 μs, aligning with the drift time of the TPC. At this level, the system evaluates events in greater detail and selects those that are sent to the Data Acquisition (DAQ) system and the High-Level Trigger (HLT). The HLT operates as a software-based trigger system, allowing for sophisticated real-time event analysis and filtering.

Trigger Types

- **Minimum Bias Triggers (MBAND and MBOR)**: These triggers were used extensively during all pp and Pb–Pb collision data-taking, especially in the 2010 run. The MBOR trigger, characterized by its high efficiency, was favoured at low luminosities. As luminosity and background levels rose, the high-purity MBAND trigger became more advantageous. During high luminosity Pb–Pb runs in 2011, the V0-based MBAND trigger was supplemented by signals from both ZDCs (referred to as MBZ) to suppress electromagnetic interactions between the lead ions. MBAND is used for the pp collisions in RUN2. It requires a logical AND of hits in both the V0A and V0C detectors. Additionally, the trigger condition requires at least one charged particle track in the SPD detector.

- **High-Multiplicity (HM) Trigger**: This trigger is based on the hit SPD in coincidence with MB. Typically, the multiplicity threshold is set between 80–100 hits, corresponding to 60–80 SPD tracklets (pairs of matching clusters in the SPD's two layers). The threshold is chosen to maximize the inspected luminosity while minimizing contamination from multiple-interaction events. The HM trigger is particularly useful for selecting events with exceptionally high particle multiplicities, crucial for studying rare processes and extreme conditions.

- **Central and Semi-Central Triggers (CENT and SEMI)**: These triggers are used in Pb–Pb collisions to focus on events with significant overlap between the nuclei (central collisions) or moderate overlap (semi-central collisions). For the central 0–10% (CENT) and semi-central 0–50% (SEMI) Pb–Pb triggers, V0 thresholds are applied to the summed signals of V0A and V0C. A coincidence requirement between these two sides ensures accurate centrality determination.

- **Pile-Up Rejection**: The system includes mechanisms to reject pile-up events, where multiple collisions occur in a single bunch crossing, ensuring cleaner event samples for analysis.

By utilizing this multi-tiered trigger system, ALICE effectively handles data from diverse collision scenarios, filtering out the most significant events for detailed study. This capability is essential for exploring the fundamental properties of matter under extreme conditions and for investigating rare particle interactions.

3.3 ALICE Offline Framework

In the ALICE experiment at the LHC, collisions between protons or heavy ions are recorded at various interaction points. Each collision is termed an event, and within each event, numerous particles are generated through diverse physics processes. These particles leave digital signatures in different sub-detectors placed along their paths, manifesting as raw data. Before the final physics analysis, these raw data undergo processing. The schematic diagram of the event reconstruction flow is shown in Figure 3.13.

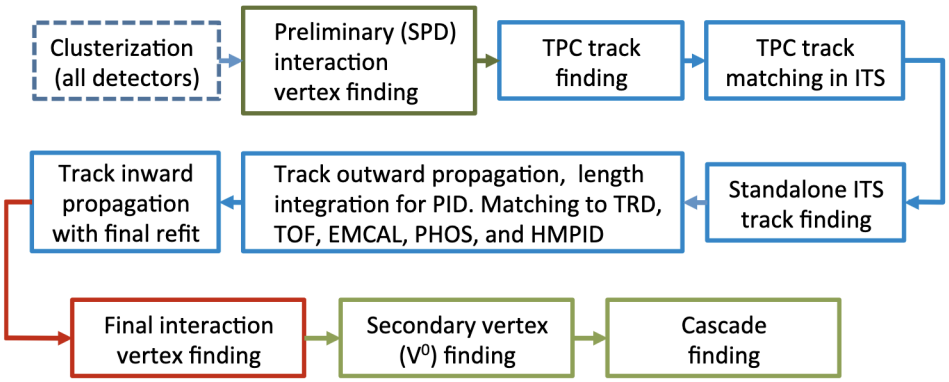

Figure 3.12: Event reconstruction flow [71].

AliRoot serves as an offline computing framework designed to process and reconstruct tracks from raw data, encompassing five main steps:

- **Cluster Finding Algorithm**: This step involves applying algorithms to identify clusters of signals in the various detectors used in the experiment. These clusters represent the presence of particles or interactions within the detector.
- **Primary Vertex Reconstruction**: The primary vertex is the point where the colliding particles initially interact. The Silicon Pixel Detector (SPD) is used to reconstruct this vertex, providing crucial information about the collision geometry.
- **Track Reconstruction with Kalman Filter**: The Kalman filter is a mathematical technique used to estimate the state of a system based on noisy measurements. This step applies to reconstructing the trajectories of particles emerging from the collision using information from the detector signals.

- **Track Reconstruction with Better Resolution**: This step involves refining the track reconstruction process for tracks exhibiting higher resolution than those reconstructed using the primary vertex information from the SPD.

- **Secondary Vertex Reconstruction**: Secondary vertices are points where particles produced in the collision decay into other particles. This step involves reconstructing these secondary vertices, particularly those associated with particle decays known as V0s.

These steps collectively form the reconstruction process, where raw detector signals are processed and converted into reconstructed particle tracks, providing valuable information for physics analysis. AliPhysics, another integral component, hosts codes for specific physics analyses and is built upon the ROOT software framework. While AliPhysics codes are predominantly written in C++, some AliRoot codes are composed in Fortran. Together, AliRoot and AliPhysics form essential tools for data processing and physics analysis within the ALICE experiment, leveraging advanced computational techniques for unravelling the mysteries of particle collisions at the LHC.

Additionally, AliRoot facilitates the generation of simulated data using GEANT4, which is derived from Monte Carlo event generators. These simulations are crucial for fixing errors in real data, understanding how well the detectors work, and figuring out what kinds of particles they can detect. It comprises two main components: event generators and transport codes. The event generators (like PYTHIA, EPOS, or HIJING) are used to simulate collisions, similar to what happens in real experiments. Then, the output from these event generators is fed into GEANT4, which simulates how the particles from these collisions interact with the detectors. This helps to understand how well the detectors work and correct any mistakes in the real data. Overall, simulations are essential to interpret and analyze the data collected from actual collisions.

After the reconstruction, the data is stored in Event Summary Data (ESD) files containing detailed information from all sub-detectors. These files are too large for local analysis, so smaller Analysis Object Data (AOD) files are created from them. AOD files only include the necessary information for specific analyses, making them more manageable. Both collision and simulated data go through reconstruction to make ESD files,

which are then simplified into AOD files for easier analysis. These AOD files are used for local analysis, providing essential data for physics research while keeping file sizes small.

3.3.1 Vertex Reconstruction

The Primary Vertex (PV) refers to the point where the two particle beams are expected to collide. Initially, the PV is estimated using the first two layers of the ITS known as the Silicon Pixel Detector (SPD), referred as the SPD Vertex. SPD is ideal for fast vertex measurements and online monitoring as it provides a quick response, is closest to the interaction point, and has excellent transverse plane resolution due to its high granularity. The SPD Vertex is found by minimizing the distance among tracklets, which connect clusters within the same azimuthal window in the SPD layers. At least two tracklets are needed for a 3D primary vertex reconstruction, but in proton-proton collisions, often only one tracklet is available. In such cases, the algorithm looks for the maximum in the z-distribution of the distance of the closest approach of the tracklets to the beam axis. The final PV is reconstructed after full track reconstruction by minimizing distances among tracks. The resolution differs between the SPD Vertex and the Primary Vertex, with a resolution of 10 μm in Pb–Pb collisions and 150 μm in pp collisions at $\sqrt{s} = 7$ TeV [71].

In ALICE, three primary algorithms are used for vertex reconstruction [82]:

- **VertexerSPDz**: Provides the measurement of the z-coordinate of the interaction point using the SPD. It is faster than VertexerSPD3D and is used for Pb–Pb collision events. It calculates the z-coordinate from tracklet correlations in the SPD layers and iteratively refines the estimate by focusing on the peak of the z-distribution.

- **VertexerSPD3D**: Offers a three-dimensional measurement of the primary vertex using the SPD. This algorithm provides a 3D measurement of the primary vertex using SPD tracklets. It involves three steps repeated twice: finding tracklets, selecting pairs based on the distance of closest approach (< 1 mm), and determining the vertex by minimizing the distance among tracklets. The initial vertex estimate is refined by discarding tracklets with larger approach distances.

- **VertexerTracks**: Provides a three-dimensional measurement of the primary vertex

using reconstructed tracks. It involves track selection, estimating the vertex position based on minimal track distances, and refining this estimate by extrapolating tracks. The final vertex position and its covariance matrix are obtained through a fitting process.

3.3.2 Track Reconstruction

The track reconstruction in ALICE is a multi-stage process that uses the Kalman filter algorithm to accurately determine the trajectory of particles as they pass through the detector layers. The process follows an inward–outward–inward approach, ensuring comprehensive tracking across the TPC and the ITS, and extending to other detectors like the TRD and the TOF detector [84–86]. Figure 3.13 demonstrates the distinct stages involved in this tracking process.

TPC Track Reconstruction

The track reconstruction in ALICE begins at the outer radius of the TPC detector, utilizing the Kalman filter algorithm to refine the tracks [84]. Initially, track seeds are formed using either two TPC clusters and the SPD vertex or three clusters without applying the vertex constraint. These seeds are then propagated inward, with a proximity cut applied at each step to refine the tracks. Tracks are only accepted if they have at least 20 associated clusters (out of a possible 159) and have missed fewer than 50% of the expected clusters.

The efficiency of the track reconstruction process is influenced by the transverse momentum (p_{T}) of the tracks. Efficiency drops below $p_{\mathrm{T}} < 0.5$ GeV/c due to energy loss in the detector material, while higher p_{T} tracks, which are typically straighter, may encounter reduced efficiency in areas where clusters are lost due to dead zones between readout sectors. Figure 3.14 shows the TPC track reconstruction efficiency for primary particles in pp and Pb–Pb collisions, demonstrating that the efficiency is not affected by detector occupancy [71].

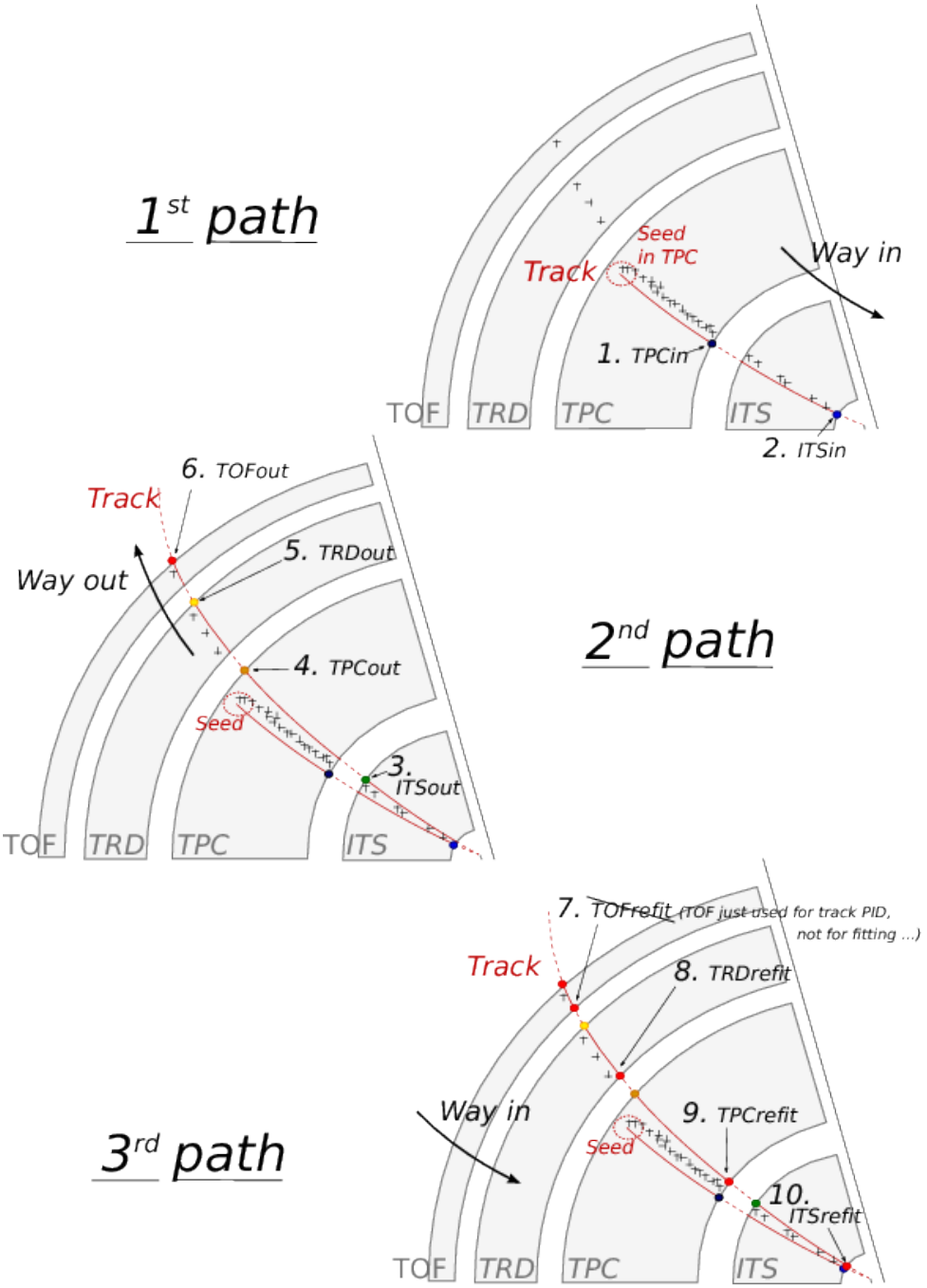

Figure 3.13: Principles of tracking for an ALICE event, showing the three successive paths allowing to build a track and refine its parameters. Numbers ranging from 1 to 10 mention the bits that are activated in case of success during the propagation of the Kalman filter at the considered stage [83].

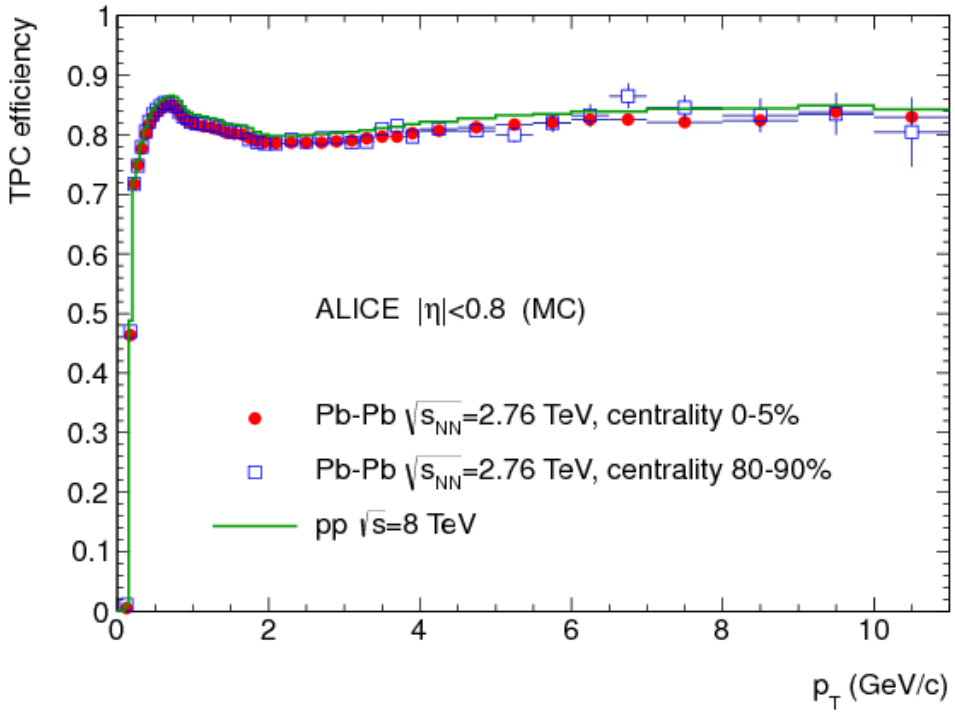

Figure 3.14: TPC track finding efficiency for primary particles in pp and Pb–Pb collisions (simulation). The efficiency does not depend on the detector occupancy [71].

ITS-TPC Track Matching

Once the TPC tracks are reconstructed, they are matched to hits in the outermost layer of the ITS, specifically the Silicon Strip Detector (SSD). These matches then serve as seeds for further track reconstruction within the ITS. As these seeds are propagated inward through the ITS layers, they are continuously updated by incorporating clusters within a defined proximity cut. Each update generates new seeds, creating a tree of track hypotheses. The final candidates for ITS+TPC tracks are selected based on their χ^2 values, with penalties applied if clusters are not found during extrapolation, except in the case of dead zones in the detector.

Figure 3.15 shows the ITS–TPC matching efficiency as a function of p_{T}, illustrating how well the tracks reconstructed in the TPC align with hits in the ITS across various transverse momentum values.

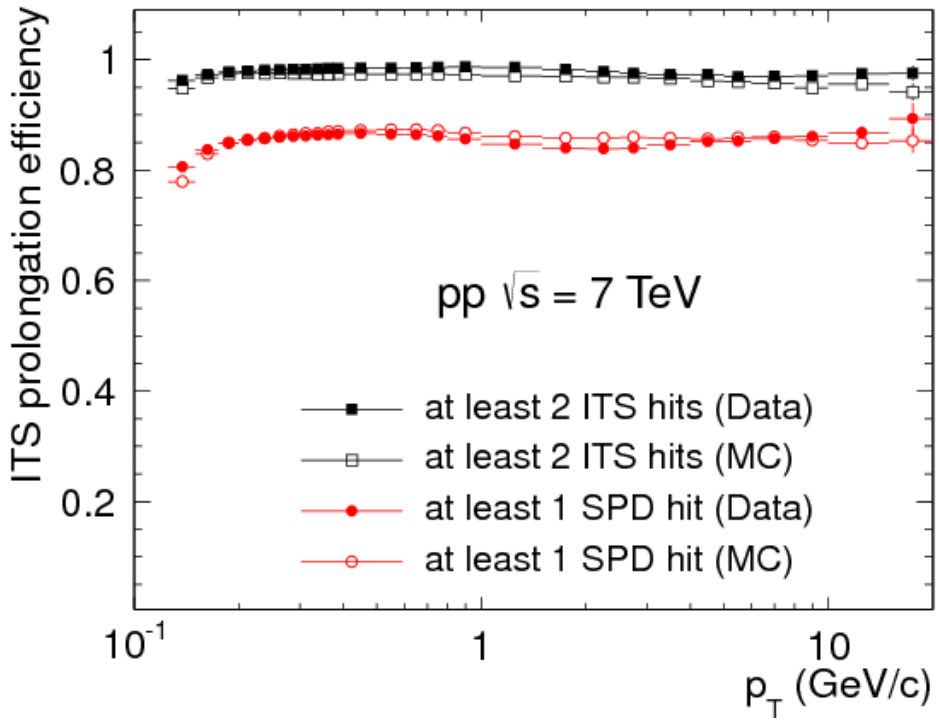

Figure 3.15: ITS–TPC matching efficiency as a function of p_{T} for data and Monte Carlo simulations in pp collisions [71].

Re-fitting and Finalization

Following the reconstruction of ITS-TPC tracks, the tracks are propagated outward to match with clusters in the TRD and TOF detectors, as well as signals from other outer detectors. The final stage involves back-propagating all tracks to the innermost ITS layer for a Kalman filter refit. This inward pass uses all previously found clusters to refine the track's parameters. The Kalman filter provides the final track parameters, including position, direction, and inverse curvature, along with the associated covariance matrix. The entire process ensures accurate track reconstruction by incorporating information from all stages of the detector system.

Track Resolution

The precision of the track's transverse momentum (p_{T}) is reflected in the resolution of the inverse transverse momentum ($1/p_{\mathrm{T}}$), which is derived from the Kalman filter's covariance matrix. The track resolution ranges from 1% to 10% across the p_{T} range of 0.1 to 100

GeV/c. Factors influencing this resolution include energy loss at low p_{T} and the presence of dead zones between detector readout sectors.

The relationship between the resolution of p_{T} and the resolution of $1/p_{\mathrm{T}}$ is expressed by the formula:

$$\frac{\sigma_{p_{\mathrm{T}}}}{p_{\mathrm{T}}} = \frac{\sigma_{1/p_{\mathrm{T}}}}{1/p_{\mathrm{T}}} \tag{3.1}$$

3.3.3 Distance of Closest Approach and Secondary Vertex Determination

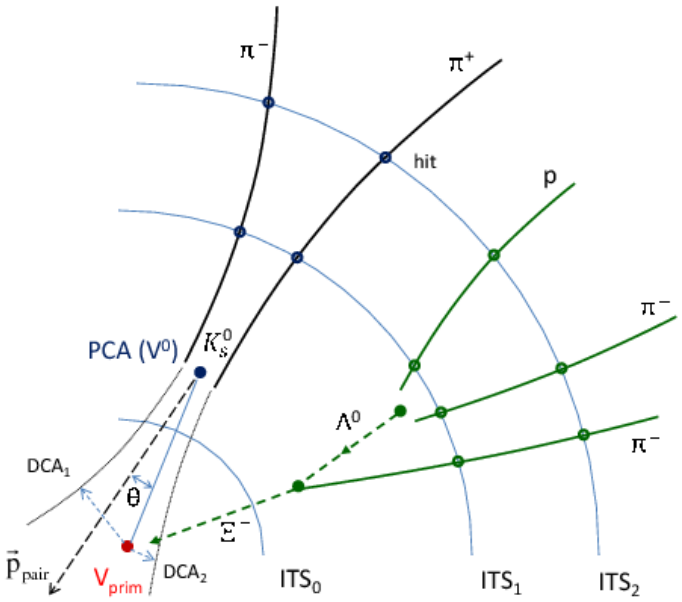

Figure 3.16: The principle of secondary vertex reconstruction is demonstrated with examples of K_S^0 and Ξ^- decays. Solid lines indicate the reconstructed tracks of charged particles, which are extrapolated to the secondary vertex candidates. Dashed lines represent the extrapolations to the primary vertex and auxiliary vectors [71].

Distance of closest approach (DCA) is the minimum distance between the trajectory of a reconstructed track and the primary vertex. This distance, also known as the impact parameter is crucial for identifying and analyzing secondary vertices. In ALICE, the DCA is used in conjunction with tracking data from the TPC and ITS to identify secondary vertices, which can arise from long-lived particles or interactions with detector material.

In ALICE, secondary vertex reconstruction begins by selecting tracks with DCA greater than 0.5 mm in pp collisions or 1 mm in Pb–Pb collisions. For each pair of selected tracks with opposite charges, known as V0 candidates, the point of closest approach (PCA) between the tracks is calculated. These V0 candidates are then subjected to further selection criteria which include the distance between the tracks at their PCA being less than 1.5 cm, the PCA being closer to the interaction vertex than the innermost hit of either track, and the cosine of the angle between the total momentum vector of the pair and the line connecting the primary and secondary vertices must be greater than 0.9 [71].

Figure 3.16 illustrates the measurement of the DCA and secondary vertex reconstruction with examples of K^0_S and Ξ^- decays.

3.3.4 Centrality Estimation and Multiplicity

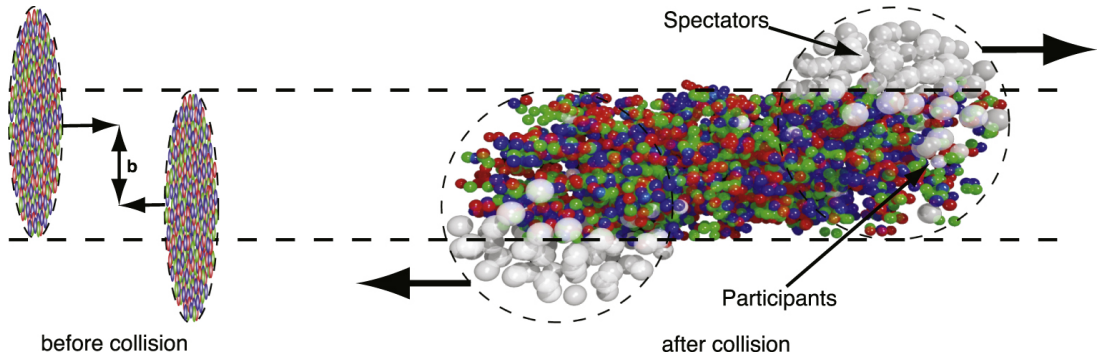

Figure 3.17: (Left) Two heavy-ions before collision with impact parameter b. (Right) the spectators continue unaffected, while in the participant zone particle production takes place [87].

In heavy-ion collisions, the centrality is a measure of how head-on or peripheral the collision is, which has a significant impact on the system created. Centrality is estimated

using the amplitude of signals from detectors like the V0, which are proportional to the charge deposited in scintillators by the particles produced in the collision. Theoretically, centrality is linked to the impact parameter (the distance between the centers of the two colliding nuclei), although this parameter cannot be directly measured. The two heavy-ions before the collision with impact parameter b are shown in Figure 3.17 [87].

The impact parameter is crucial for determining the number of participating nucleons (those involved in the collision) and the spectator nucleons (those that do not interact). While the impact parameter cannot be measured directly, the number of charged particles produced and the behaviour of spectator nucleons provide insights into the collision's geometry and centrality class. By analyzing these observables, researchers can reconstruct the overall dynamics of the collision and categorize events into different centrality classes, which are vital for studying the QGP and other phenomena in heavy-ion physics.

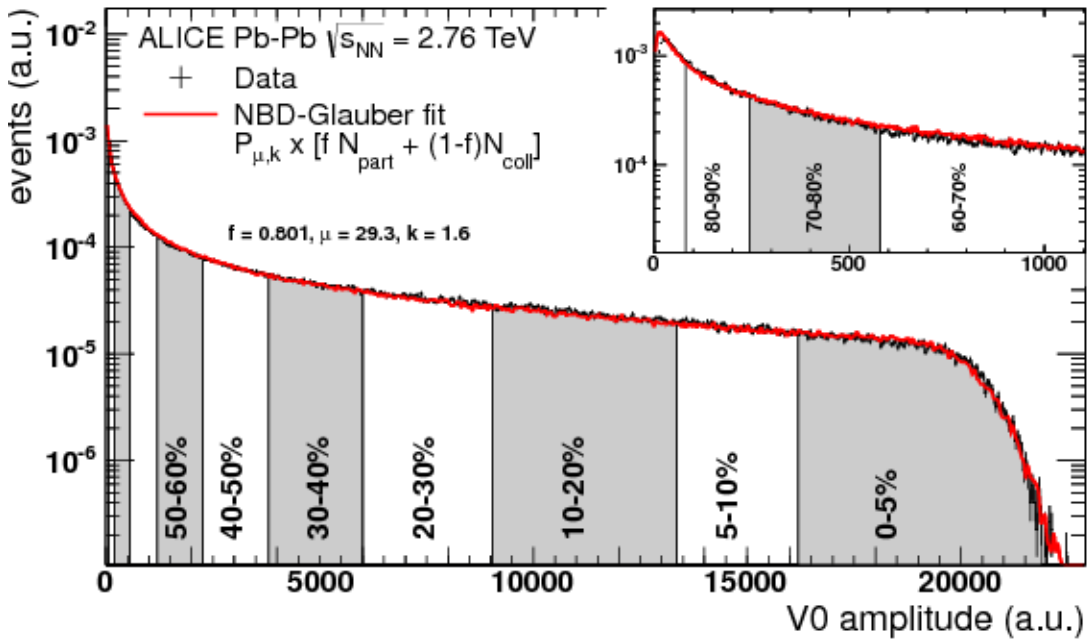

Figure 3.18: Distribution of the V0 amplitude (sum of V0A and V0C)[71].

In Figure 3.18 the centrality in Pb–Pb collisions at $\sqrt{s_{NN}} = 2.76$ TeV is determined using the sum of the V0A and V0C amplitudes, which reflect the charged-particle multiplicity in the collision. The centrality bins are defined by integrating the charged-particle multiplicity distribution, which is fitted to a Glauber Monte Carlo model to connect the experimental data with the collision geometry [71].

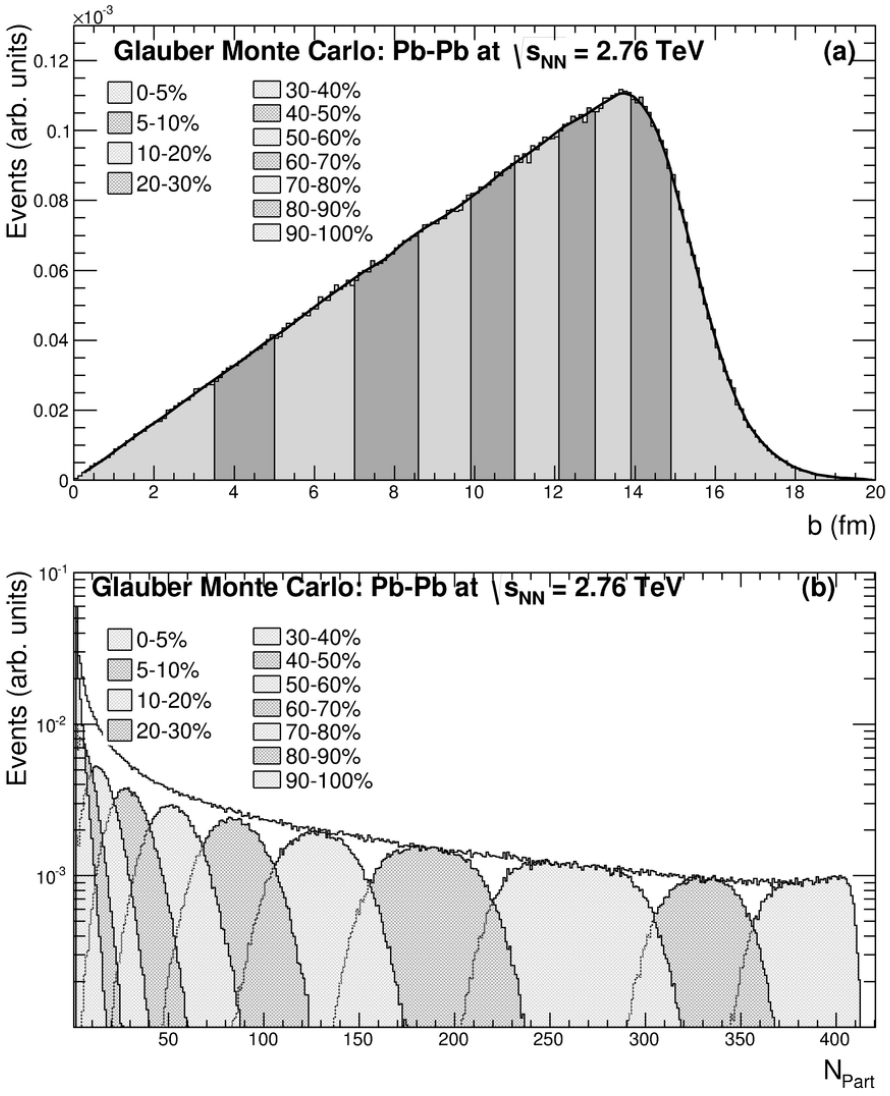

Figure 3.19: Geometric properties of Pb–Pb collisions at $\sqrt{s_{\mathrm{NN}}} = 2.76$ TeV from a Glauber Monte Carlo calculation. The upper panel shows the impact parameter distribution, segmented into percentiles of the hadronic cross-section, while the below panel displays the corresponding distributions of the number of participants for different centrality classes [88].

The Glauber model is essential for understanding the geometric and dynamical aspects of heavy-ion collisions. It provides a framework for translating the observed particle multiplicities into information about the collision geometry [89]. This model provides insight into the dependence of the number of participating nucleons (N_{part}) and binary nucleon-nucleon collisions (N_{coll}) on the impact parameter (b) in heavy-ion collisions, as illustrated in Figure 3.19.

The Glauber model operates under the assumption that nucleons follow straight-line trajectories and interact through binary collisions, governed by an inelastic nucleon-nucleon cross-section. It uses the nuclear density profile to estimate the number of binary collisions (N_{coll}) and participating nucleons (N_{part}) for a given impact parameter. The model correlates multiplicity distributions with collision geometry by fitting parameters such as f, which denotes the fraction of soft processes in particle production. This framework is pivotal for translating particle multiplicities into centrality, which classifies collisions by their geometric properties, aiding in the understanding of collision spatial extent and refining measurements [88].

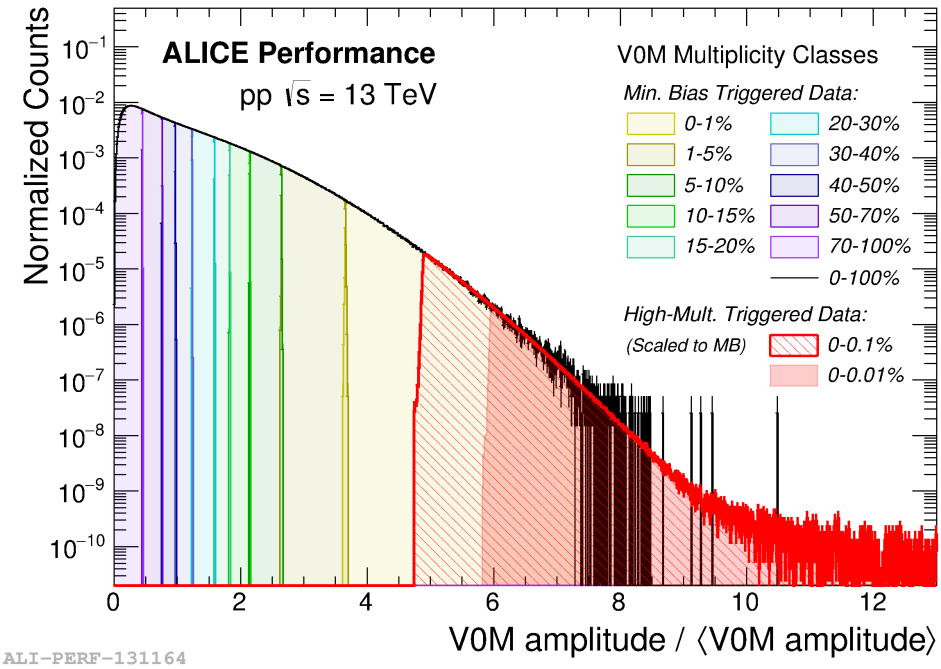

Figure 3.20: VOM normalized distributions for V0M multiplicity classes for MB and HM triggers.

In pp collisions, the particle multiplicity is determined using the V0M amplitude, where V0M denotes the combined signals from the V0A and V0C detectors. This approach is analogous to the centrality determination in heavy-ion collisions. The V0M amplitude measures the charge deposited in the scintillators of these detectors, which is directly related to the number of charged particles produced in the collision.

The multiplicity in pp collisions is categorized based on the percentile distribution of the V0M signal amplitude. The events are divided into ten multiplicity classes. Class I represents the highest multiplicity events (0-1% of the distribution), while Class X corresponds to the lowest multiplicity events (70-100% of the distribution). This classification provides a framework for analyzing particle production and event characteristics across different scales of pp collisions, as illustrated in Figure 3.20.

3.3.5 Data Acquisition and Trigger System

The ALICE computing system consists of several subsystems, each playing a crucial role in handling the data and facilitating analysis. These subsystems include: Data Acquisition (DAQ), Central Trigger Processor (CTP), High-Level Trigger (HLT), and Control Systems.

Data Acquisition (DAQ):

This subsystem is responsible for the collection of raw data from the detectors during collisions. It coordinates the readout process and ensures that data is transferred efficiently to the central data storage system for further processing.

Central Trigger Processor (CTP):

The CTP manages the trigger signals received from various detectors to initiate data readout when interesting collision events occur. It plays a crucial role in determining the events that are to be recorded for further analysis based on predefined trigger criteria.

High-Level Trigger (HLT):

The HLT performs fast online data processing to select collision events of interest for further analysis. It applies more sophisticated algorithms to identify specific particle interactions or phenomena in real time, allowing for quick decision-making on whether to retain or discard data.

Control Systems:

This subsystem oversees the operation and coordination of various components within the ALICE experiment. It ensures that all systems are functioning correctly, monitors environmental conditions, and manages safety protocols to maintain the integrity and reliability of the experiment.

Chapter 4

$\Lambda(1520)$ production in pp collisions at $\sqrt{s}$ = 5.02 and 13 TeV

This chapter outlines the methodology for measuring $\Lambda(1520)$ production in pp collisions at $\sqrt{s}$ = 5.02 and 13 TeV. Section 4.1 introduces the analysis goals and the software utilized. The criteria for event and track selection and particle identification procedures are described in section 4.2. Section 4.3 focuses on the $\Lambda(1520)$ reconstruction, including the invariant mass reconstruction technique and yield estimation. Additionally, various correction factors—such as reconstruction efficiency, trigger efficiency correction, vertex efficiency correction, and signal loss correction factors are discussed to ensure accurate measurements. The systematic uncertainty estimation is carried out using the grouping method, and the Barlow criteria outlined in section 4.5.

4.1 Introduction

Resonances, being short-lived particles, serve as sensitive probes of the properties and dynamics of the medium formed in relativistic heavy-ion collisions. Their yields can be affected by the rescattering and regeneration effects within the hadronic phase. Studying resonance production provides insights into the evolution of the medium formed in relativistic heavy-ion collisions from thermal to kinetic freeze-out. In Pb–Pb collisions,

suppression in resonance yields like $K^{*0}(892)$ and $\Lambda(1520)$ has been observed in central collisions, largely attributed to rescattering effects in the dense medium. However, resonances with longer lifetimes, such as the $\phi(1020)$, exhibit no suppression due to its decay outside the hadronic phase, indicating the crucial role of a particle's lifetime in determining resonance yields.

The study of the $\Lambda(1520)$ resonance is particularly important due to its intermediate lifetime (12.6 fm/c), which lies between the short-lived $K^{*0}(892)$ ($\sim$ 4 fm/c) and the long-lived $\phi(1020)$ ($\sim$ 42 fm/c). In proton-proton collisions, investigating the multiplicity and energy dependence of $\Lambda(1520)$ production would help to establish a baseline for understanding the hadronic freeze-out dynamics. While a slight suppression in $K^{*0}(892)$ is seen for high-multiplicity pp collisions, the behaviour of $\Lambda(1520)$ differs, as its yield shows no suppression in p–Pb collisions but a clear suppression in central Pb–Pb collisions. Therefore studying resonance production in pp collisions provides a reference for examining the effects of system size and collision dynamics, while also establishing a baseline for interpreting results from more complex systems like p–Pb and Pb–Pb.

Experimental Datasets

Analysis Software

The analysis utilized the AliRSN package, which is integrated into the AliRoot and AliPhysics framework. The code for this package is available in the official repository of the ALICE Collaboration, where it is used to conduct various specific analyses. The analysis was run on the GRID using the LF_pp_AOD LEGO train, employing the latest versions of AliRoot and AliPhysics. LHC Run2 data are used for all of the analyses. The specification of datasets used for pp collisions at $\sqrt{s} = 5.02$ and 13 TeV analysis are given in Table 4.1. The total number of events analysed in pp collisions at $\sqrt{s} = 5.02$ and 13 TeV is approximately 980 M and 2915 M, respectively.

Energy	LHC Datasets	Triggers	AOD Version
5.02 TeV	LHC15n	-	AOD208
	LHC17p	Fast, CentwoSDD	AOD234
	LHC17q	Fast, CentwoSDD	AOD234
13 TeV	LHC15f, h, i	-	AOD208
	LHC16d, e, g, h, i, o, p	-	AOD208
	LHC16k, l	-	-
	LHC17c, e, f, g, h, i, j, k, l, m, o, r	-	-
	LHC18b, d, e, f, g, h, i, k, l, m, n, p	-	-

Table 4.1: Datasets used for the analysis in pp collisions at $\sqrt{s} = 5.02$ and 13 TeV.

4.2 Event Selection

The analysis utilizes the kINT7 minimum bias trigger for the multiplicity-dependent analysis, ensuring a hit in the SPD detector and a hit either in the V0A or V0C detectors [90, 91].

The determination of the primary collision vertex relies on the reconstruction of charged tracks in both the ITS and TPC. Events are selected based on the position of the primary vertex along the beam axis. Typically, primary vertices are expected to spread over a few centimeters. The reconstructed vertex was required to be within $\pm$ 10 cm along the beam axis from the nominal interaction point to ensure a uniform acceptance in the pseudorapidity region $|\eta| < 0.8$ across the TPC, maintaining consistency in tracking efficiency. Pileup events, resulting from same-bunch-crossing pileups involving multiple collisions within the same bunch-crossing, and out-of-time pileups, which occur when collisions from previous or subsequent bunch crossings interfere with the current event, are rejected. The criteria used for selecting good event are summarized in Table 4.2.

The number of events selected after applying good event cuts is shown in Figure 5.1

The analyses considered the inelastic (INEL > 0) event class which is defined as a set of inelastic collisions that involve at least one charged particle with $|\eta| < 1$ [92]. The INEL > 0 event is divided into five multiplicity classes based on the total charged particle

Event selection criteria
Trigger: kINT7
Standard Physics Selection
INEL>0 selection: At least one SPD tracklet within $\|\eta\| < 1$
IsIncompleteDAQ check
Pileup rejection using AliESDEvent::IsPileUpFromSPDInMultBins()
SPD clusters vs. tracklets check with standard parameters
SPD vertex z resolution < 0.02 cm
z-position difference between track and SPD vertex < 0.5 cm
Vertex z position: $\|V_z\| < 10$ cm

Table 4.2: Event selection criteria for good events

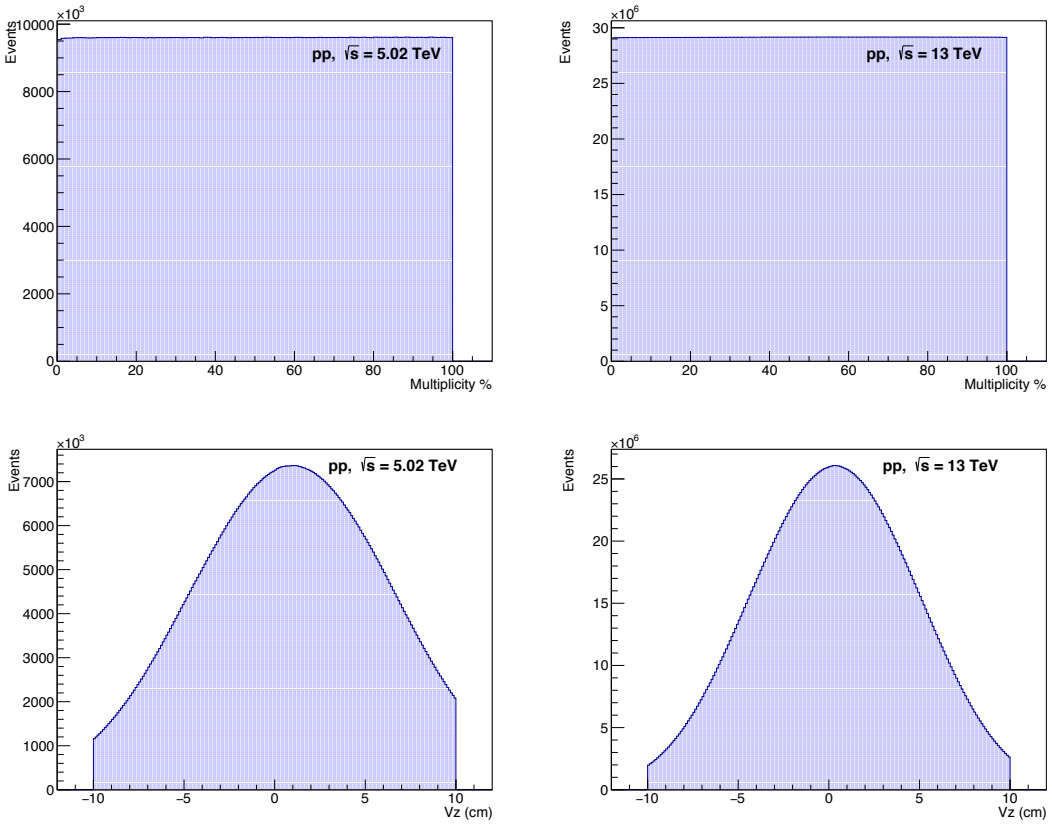

Figure 4.1: The upper panels show the distribution of the selected number of events for different multiplicity classes and the lower panels show the vertex z distribution in pp collisions at $\sqrt{s} = 5.02$ and 13 TeV.

multiplicity measured by both V0 detectors(called V0M amplitude). To avoid autocorrelation between the yield and multiplicity estimator, the $\Lambda(1520)$ yield is measured in the

mid-rapidity($|y| < 0.5$) region utilizing TPC. The total number of events selected for the different multiplicity classes is reported in Table4.3.

Multiplicity (%)	**13 TeV**		**5.02 TeV**	
	$\langle dN_{\rm ch}/d\eta \rangle \,|_{\eta<0.5}$	Events (10^8)	$\langle dN_{\rm ch}/d\eta \rangle \,|_{\eta<0.5}$	Events (10^8)
0–10%	18.567 ± 0.28	2.911	13.68 ± 0.185	0.958
10–30%	11.51 ± 0.17	6.118	8.75 ± 0.125	2.016
30–50%	7.275 ± 0.11	6.122	5.75 ± 0.085	2.016
50–70%	4.64 ± 0.07	6.124	3.92 ± 0.06	2.017
70–100%	2.55 ± 0.04	9.039	2.40 ± 0.04	2.978

Table 4.3: Number of events used for the analysis in pp collisions

4.3 Track Selection

Proton-proton collisions produce numerous particles, which are detected as tracks in various detectors. To ensure accurate measurements, several track selection criteria are applied to select high-quality tracks.

Tracks with $p_{\rm T} > 0.15\,{\rm GeV/c}$ are considered for the analysis. The tracks are required to have pseudorapidity of $|\eta| < 0.8$ for optimal detector coverage and uniform track acceptance. To filter out tracks originating from pileup vertices, a $|{\rm DCA}_Z| < 2.0\,{\rm cm}$ criterion is applied.

Additionally, the transverse impact parameter $|{\rm DCA}_{XY}|$ must satisfy the condition $|{\rm DCA}_{XY}| < (0.0105 + 0.0350/p_T^{1.1})$, ensuring that tracks are close to the primary vertex while eliminating secondary particle tracks. Tracks are required to undergo refitting in the TPC and ITS to achieve high precision. The selection also includes the rejection of kink daughters, which are daughter tracks from reconstructed secondary weak decay topologies.

A minimum of one cluster in the SPD along with more than 70 crossed rows in the TPC is required to ensure good track quality. Furthermore, the minimum ratio of the

number of crossed rows to the number of findable clusters (R_{TPC}) in the TPC must be at least ≥ 0.82. The $\chi^2/\mathrm{N_{cluster}}$ for the TPC tracks is required to be less than 4 to suppress contamination from poor-quality tracks, while for the ITS, it is required to be less than 36 to reduce contamination from secondary particle tracks. A pair rapidity cut of $|y_{\mathrm{pair}}| < 0.5$ ensures rapidity consistency for pairs of tracks. These comprehensive track selection criteria collectively enhance the reliability of the analysis outcomes and are tabulated in Table 4.4.

Track Selection Criteria	**Value**
p_{T}	$> 0.15\,\mathrm{GeV/c}$
$\|\eta\|$	< 0.8
$\|DCA_Z\|$	$< 2.0\,\mathrm{cm}$
$\|DCA_{XY}\|$	$< 0.0105 + 0.0350/p_{\mathrm{T}}^{1.1}$
TPC and ITS refits	Required
Rejection of kink daughters	Required
Minimum number of clusters in SPD	1
Number of crossed rows in TPC	> 70
R_{TPC}	≥ 0.82
χ^2/Ncluster for TPC	< 4
χ^2/Ncluster for ITS	< 36
$\|y_{\mathrm{pair}}\|$	< 0.5

Table 4.4: Track selection criteria for the multiplicity-dependent analysis.

4.4 Particle Identification (PID)

Accurate identification of the decay daughters is crucial for reconstructing the $\Lambda(1520)$ resonance signal. This identification process relies on the combined information from the TPC and TOF detectors. Achieving high purity in the identification of these particles is essential to reduce the combinatorial background, which can arise from the misidentification of tracks forming candidate pairs.

The particle identification (PID) of the decay daughters of the $\Lambda(1520)$, specifically kaons and protons, is performed using information from both the TPC and TOF detectors. The TPC measures the specific ionization energy loss (dE/dx), as shown in Figure 5.2,

as a function of track momentum, making it an excellent tool for PID and significantly reducing the combinatorial background. The TOF detector provides precise time-of-flight information, which, when integrated with the TPC data, enhances the accuracy and reliability of particle identification.

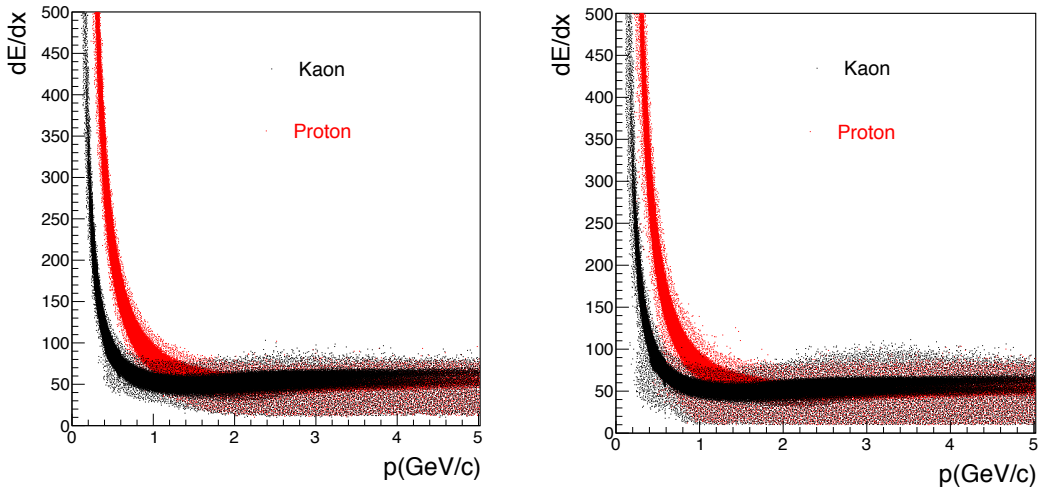

Figure 4.2: The left and right panel shows the TPC-specific energy loss (dE/dx) selected for protons and kaons as a function of momentum in pp collisions at $\sqrt{s}$ = 5.02 and 13 TeV, respectively.

The measured energy loss dE/dx as a function of the particle momentum is obtained by using the TPC through the Bethe-Bloch formula given by:

$$f(\beta,\gamma) = \frac{P_1}{\beta^{P_4}} \cdot \left(P_2 - \beta^{P_4} - \ln\left(P_3 + \frac{1}{(\beta\gamma)^{P_5}} \right) \right) \tag{4.1}$$

$$\tag{4.2}$$

Here β is the particle velocity, γ is the Lorentz factor, and P_1, P_2, P_3, P_4 and P_5 are tuned parameters. This formula is employed for particle identification using the $n\sigma$-cut method.

The PID strategy employed in this analysis is the "$n\sigma$-cut" method, which is detailed below. Here, the subscript i denotes the detector used for PID (i = TPC, TOF), and the subscript j represents the particle species hypothesis. The "$n\sigma$-cut" method is based on

defining a discriminating variable as follows:

$$n_{i,j} = \frac{Y_i - \langle Y_{i,j} \rangle}{\sigma_{i,j}} \tag{4.3}$$

where $n_{i,j}$ represents the normalized deviation for detector i and particle hypothesis j. Here, Y_i denotes the measured quantity in detector i such as the specific ionization energy loss (dE/dx) for the TPC or the time-of-flight for the TOF. The term $\langle Y_{i,j} \rangle$ is the expected value of this measured quantity for a given particle species j in detector i, based on theoretical predictions or empirical models. $\sigma_{i,j}$ is the standard deviation (or resolution) of the measured quantity for the particle hypothesis j in detector i, which quantifies the detector's accuracy in measuring this specific quantity.

The variable $n_{i,j}$ quantifies the number of standard deviations by which the measured quantity Y_i deviates from the expected value $\langle Y_{i,j} \rangle$ for a given particle species j in detector i. Particles are identified if the value of $n_{i,j}$ falls within a specified range.

For the TPC detector, the specific energy loss (dE/dx) of a track is compared with the expected energy loss, calculated using the Bethe-Bloch formula, for various particle species. The variable n_{TPC}, which represents the deviation from the expected energy loss for a particular particle species hypothesis in terms of the detector's resolution, is defined as:

$$n\sigma_{\mathrm{TPC}} = \frac{\langle dE/dx \rangle_{\mathrm{measured}} - \langle dE/dx \rangle_{\mathrm{expected}}}{\sigma_{\mathrm{TPC}}} \tag{4.4}$$

where $\langle dE/dx \rangle_{\mathrm{measured}}$ is the measured average energy loss of tracks in the TPC, and $\langle dE/dx \rangle_{\mathrm{expected}}$ is the theoretical prediction for the average energy loss of a proton or kaon track. The $\langle dE/dx \rangle$ is calculated from the truncated mean of 60% of the measured clusters to minimize fluctuations due to ionization and TPC edge effects. The σ_{TPC} is the

PID resolution of the TPC, typically around 5.2% for proton-proton collisions and 6.5% for central 0–5% of A–A collisions.

The TOF detector identifies particles by combining the flight time measured in the TOF detector with the momentum information from the ITS and TPC detectors. The start time of the flight is assumed to be the collision time, determined for each event from the T0 detector. The n_{TOF} is defined as:

$$n\sigma_{\mathrm{TOF}} = \frac{\tau_{\mathrm{measured}} - \tau_{\mathrm{expected}}}{\sigma_{\mathrm{TOF}}} \tag{4.5}$$

where τ_{measured} is the flight time of a particle measured in the TOF detector, and τ_{expected} is the expected time calculated from the track length and its momentum. The σ_{TOF} is the PID resolution of the TOF, typically around 56 ps.

This approach allows precise identification of the Λ(1520) decay products, facilitating detailed studies of its properties in high-energy collisions.

The criteria used to identify protons and kaons are summarized in Table 4.5.

Condition	**Selection Criteria**
$n\sigma$ TPC cut (TPC without TOF hit) for protons	3σ (protons: $0.15 < p < 1.1$ GeV/c)
$n\sigma$ TPC cut (TPC without TOF hit) for kaons	3σ (kaons: $0.15 < p < 0.6$ GeV/c)
$n\sigma$ TOF cut (Track present in TOF)	$n\sigma_{\mathrm{TPC}} = 5\sigma$, $n\sigma_{\mathrm{TOF}} = 3$
Track rejection	$p_{\mathrm{T}} < 0.15$ GeV/c or $\lvert\eta\rvert > 0.8$
Pair rapidity	$\lvert y_{\mathrm{pair}}\rvert < 0.5$

Table 4.5: PID selection criteria for protons and kaons.

Figure 4.3 shows the nσ distribution of protons and kaons when the track is present only in the TPC while Figure 4.4 shows the nσ distribution of protons and kaons when the track is present in both TPC and TOF in pp collisions at $\sqrt{s}$ = 5.02 and 13 TeV.

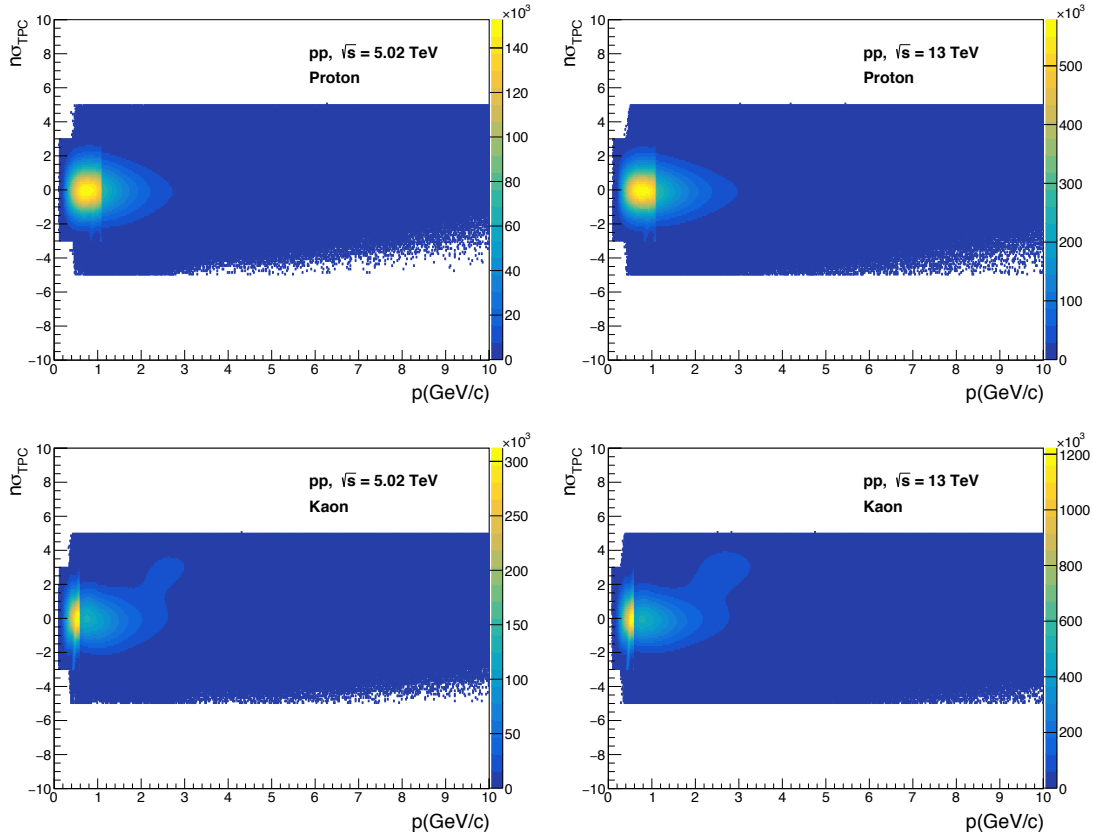

Figure 4.3: nσ distribution of protons and kaons of TPC tracks in pp collisions at $\sqrt{s}$ = 5.02 and 13 TeV.

4.5 Reconstruction of $\Lambda(1520)$

4.5.1 Invariant Mass Reconstruction

Due to the very short lifetime of resonances, it is not possible to directly measure them using the detector. The decay vertices of the resonance cannot be distinguished from the primary vertex. The measurement of the baryonic resonance particle $\Lambda(1520)$ at mid-rapidity ($|y| < 0.5$) in pp collisions at $\sqrt{s}$ = 5.02 and 13 TeV as a function of charged-particle multiplicity is carried out using the invariant mass reconstruction technique. The $\Lambda(1520)$ resonance is reconstructed via its hadronic decay channel $\Lambda(1520)(\bar{\Lambda}(1520)) \rightarrow pK^-(\bar{p}K^+)$, with a branching ratio of $22.5 \pm 0.5\%$. The $\Lambda(1520)$ particle has a mass of $m_{\mathrm{PDG}} = (1519.5 \pm 1.0)$ MeV/c^2 and a width of $\Gamma_{\mathrm{PDG}} = (15.6 \pm 1.0)$ MeV. The properties

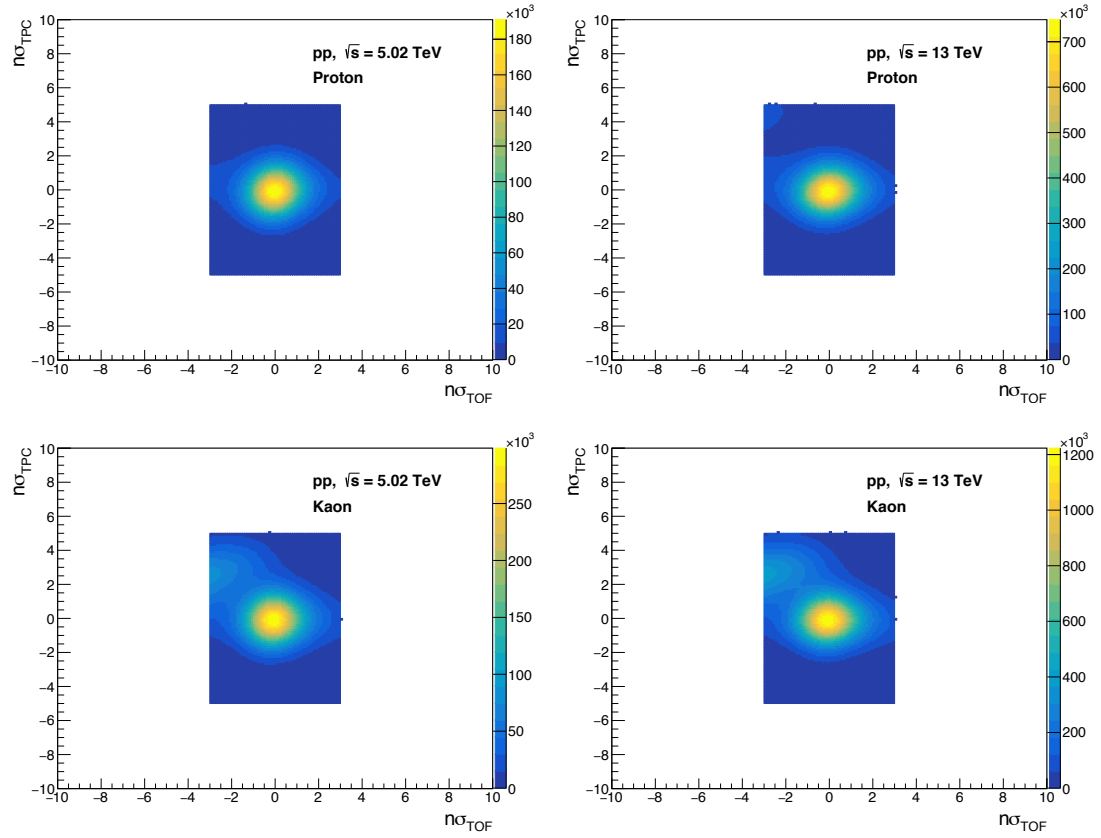

Figure 4.4: nσ distribution of protons and kaons when tracks are present in both TPC and TOF in pp collisions at $\sqrt{s}$ = 5.02 and 13 TeV.

of Λ(1520) is given in Table 4.6

The invariant mass of the Λ(1520) decay into a proton and a kaon can be obtained by:

$$m^2_{\Lambda(1520)} = (E_p + E_{K^-})^2 - |\vec{p}_p + \vec{p}_{K^-}|^2 \tag{4.6}$$

$$E_p = \sqrt{m_p^2 c^4 + |\vec{p}_p|^2 c^2} \tag{4.7}$$

$$E_{K^-} = \sqrt{m_{K^-}^2 c^4 + |\vec{p}_{K^-}|^2 c^2} \tag{4.8}$$

$$m^2_{\Lambda(1520)} = \left(\sqrt{m_p^2 c^4 + |\vec{p}_p|^2 c^2} + \sqrt{m_{K^-}^2 c^4 + |\vec{p}_{K^-}|^2 c^2}\right)^2 - |\vec{p}_p + \vec{p}_{K^-}|^2 \tag{4.9}$$

The same-event invariant mass distributions are obtained for unlike-sign ($m_{\text{same},Kp,\text{unlike}}$) and like-sign ($m_{\text{same},Kp,\text{like}}$) pairs across various p_{T} bins and multiplicity classes. Unlike-

Property	**Value**
Decay Channel	$\Lambda(1520)\bar{\Lambda}(1520) \rightarrow pK^{-}(\bar{p}K^{+})$
Branching Ratio	$22.5 \pm 0.5\,\%$
Mass (m_{PDG})	$(1519.5 \pm 1.0)\,\mathrm{MeV}/c^2$
Width (Γ_{PDG})	$(15.6 \pm 1.0)\,\mathrm{MeV}$
Quark Content	uds

Table 4.6: $\Lambda(1520)$ Resonance Characteristics

sign pairs are formed randomly, leading to a small correlated signal amidst a substantial combinatorial background from uncorrelated pairs, which dominates the distribution.

To separate the signal from the background, both the correlated and uncorrelated pairs of background are estimated using the same events. This background is subtracted from the unlike-charge distribution to isolate the resonance signal. The uncorrelated background is estimated using the mixed-event technique, where ten events are mixed. The events chosen to be mixed are required to have a difference in $\mathrm{V_Z}$ to be less than 1 cm, and a difference in the multiplicity to be less than five to ensure the uncorrelated pairs have similar event characteristics. The uncorrelated background thus obtained is appropriately normalized to have the same integral as the same event, unlike charge distribution in the invariant mass range of (1.6 - 1.7) GeV/c^2. This normalization ensures that the mixed event background and the same-event pairs have a similar structure in this region. The estimated background is subtracted from the same event unlike charge distribution to obtain the signal.

After subtracting the combinatorial background, a residual background near the peak region is observed due to correlated pairs. This residual background arises from various sources, such as jets, resonance decays where one of the daughter particles is misidentified, and decays involving more than two daughter particles. These processes contribute to the residual background, which can affect the shape and properties of the observed resonance peak. A combined fit function is employed to analyze the unlike-charge distribution after the background subtraction. This combined fit function consists of a polynomial function describing the residual background and a peak function describing the signal. The

resonance peak in the unlike-charge distribution is described using a Voigtian function. The Voigtian function is obtained through the convolution of a Breit-Wigner function, which represents the ideal resonance shape, with a Gaussian function that accounts for the mass resolution of the detector.

The functional form of the Voigtian function is given by:

$$\frac{dN}{dM_{pK}} = A\frac{\Gamma}{(2\pi)^{3/2}\sigma}\int_{-\infty}^{\infty} e^{-\frac{(M_{pK}-m_0)^2}{2\sigma^2}}\frac{1}{(m_0-M)^2+\frac{\Gamma^2}{4}}\,dM_{pK} \tag{4.10}$$

where, A is the normalization constant, M is a fit parameter that represents the mass of the resonance, Γ indicates the width of the resonance, and σ is the Gaussian width.

Figure 4.5 shows the invariant mass distribution of pK pairs before and after background subtraction in pp collisions at $\sqrt{s}$ = 5.02 and 13 TeV.

The mass resolution varies with p_{T}, but it has a limited effect on the reconstructed peak shape due to the large intrinsic width of the Λ(1520) resonance (15.73 MeV/c^2) [93].

The invariant mass distribution of pK pairs in pp collisions at $\sqrt{s}$ = 5.02 TeV in different multiplicity classes are shown in Figure 4.6, 4.7, 4.8, 4.9, 4.10 and 4.11.

The invariant mass distribution of pK pairs in pp collisions at $\sqrt{s}$ = 13 TeV in different multiplicity classes are shown in Figure 4.12, 4.13, 4.14, 4.15, 4.16 and 4.17.

4.5.2 Raw Yield Estimation

Two different methods are used to calculate the raw yield: the bin counting method and the function integral method. The bin counting method is used as the default method, whereas function integral is employed for systematic study.

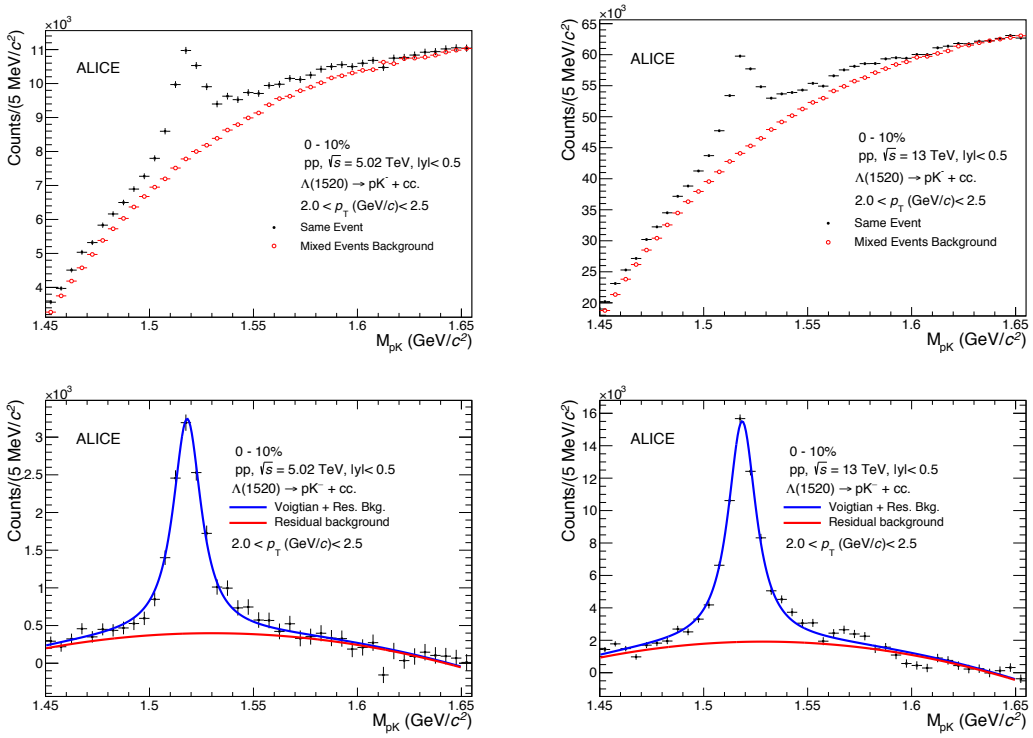

Figure 4.5: Invariant mass distribution of pK pairs for pp collisions at $\sqrt{s}$ = 5.02 TeV (left panel) and 13 TeV (right panel) for $2 < p_T < 2.5$ GeV/ c. The upper panels display the unlike-sign pK pair before background subtraction, while the bottom panels illustrate the same after background subtraction. The solid blue curve represents the combined fit fits, while the solid red lines correspond to the residual background.

Bin Counting Method

The bin counting method involves summing the bin content of the invariant mass histogram within a specific range, typically corresponding to the mass window of the resonance particle. This accumulated bin content reflects the total number of counts associated with the signal peak.

The raw yield Y_{BC}, is calculated using the following equation

$$Y_{\mathrm{BC}} = B - I_2 + I_3 + I_4 \tag{4.11}$$

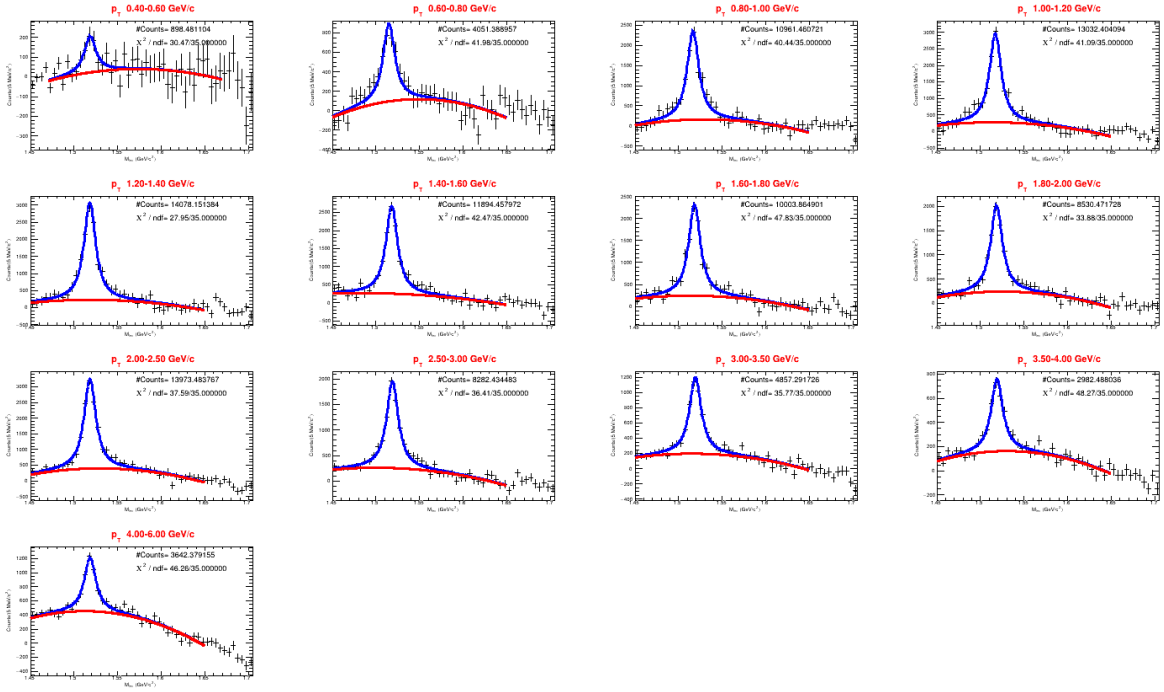

Figure 4.6: The invariant mass distribution of pK pairs for $0-10\%$ multiplicity class in pp collisions at $\sqrt{s} = 5.02$ TeV for different p_{T} bins after subtracting the normalized mixed-event background distribution.

where,

- B: Total counts in the mass range, including both signal and background.
- I_2: Integral of the peak part of the fit function within the mass range $I_{\mathrm{min}} - I_{\mathrm{max}}$ subtracted to correct for the resonance peak contribution included in B.
- I_3 and I_4: Integral of tail part, added to account for background contributions from the tails of the resonance peak.

To obtain the actual resonance yield, the integral I_2, representing the peak contribution within the range, is subtracted from B to avoid double counting. Additionally, the integrals I_3 and I_4 are added to account for background contributions from the tails of the resonance peak. This approach ensures that both sides of the peak are considered, leading to a more accurate estimation of the true yield by effectively managing the influence of

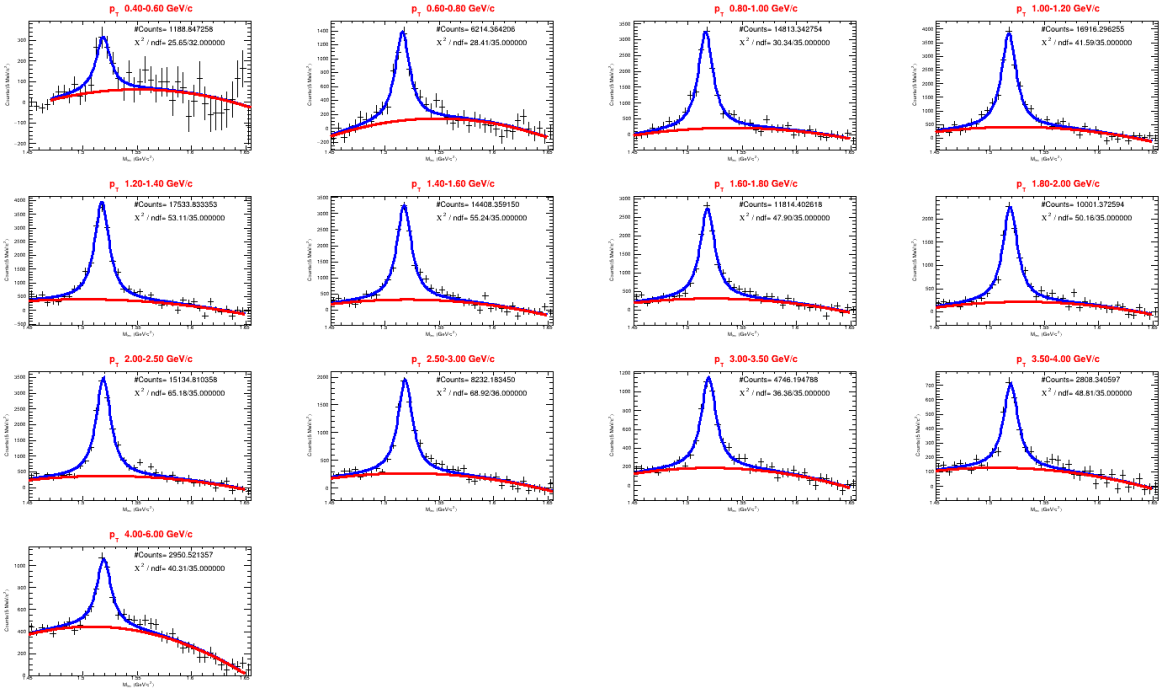

Figure 4.7: The invariant mass distribution of pK pairs for $10-30\%$ multiplicity class in pp collisions at $\sqrt{s} = 5.02$ TeV for different p_{T} bins after subtracting the normalized mixed-event background distribution.

background noise.

Function Integral Method

In the Function Integral method, the raw yield for Λ(1520) can be obtained by integrating the invariant mass peak using the fitting function. The parameter A represents the integral of the peak function from 0 to ∞. However, the mass region, $0 < m_{pK} < m_p + m_K$ (where $m_p + m_K = 1.431$ GeV/c^2 is the combined mass of the proton and kaon) is kinematically forbidden. Therefore, the yield is calculated as:

$$\mathrm{Yield} = \mathrm{A} \int_{\mathrm{m_p+m_K}}^{\infty} \mathrm{f_{fit}(m)\,dm} \tag{4.12}$$

Figure 4.18 shows the raw yield of the Λ(1520) in pp collisions at $\sqrt{s} = 5.02$ and 13 TeV using both methods.

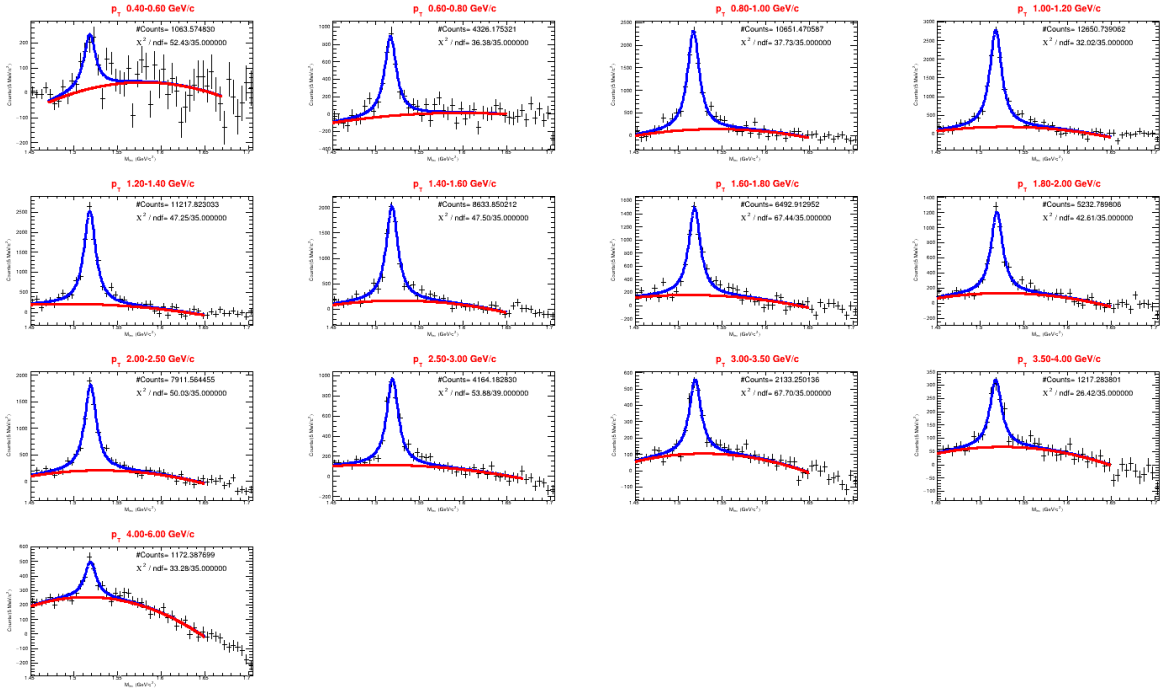

Figure 4.8: The invariant mass distribution of pK pairs for $30-50\%$ multiplicity class in pp collisions at $\sqrt{s}$ = 5.02 TeV for different p_{T} bins after subtracting the normalized mixed-event background distribution.

4.6 Correction Factors

To determine the raw yield of Λ(1520), various techniques are employed, including the implementation of different event cuts, good-quality track cuts, and signal extraction methods. However, several corrections need to be applied to the raw yield to obtain the corrected yield for the INEL > 0 event class across different multiplicity classes.

The raw yield is initially corrected by considering the branching ratio, vertex efficiency, trigger efficiency and a correction factor to compensate for signal loss and track efficiency cuts.

4.6.1 Efficiency × Acceptance

The p_{T}-dependent acceptance and efficiency corrections are determined by analyzing the fraction of generated Λ(1520) resonances that are successfully reconstructed within the

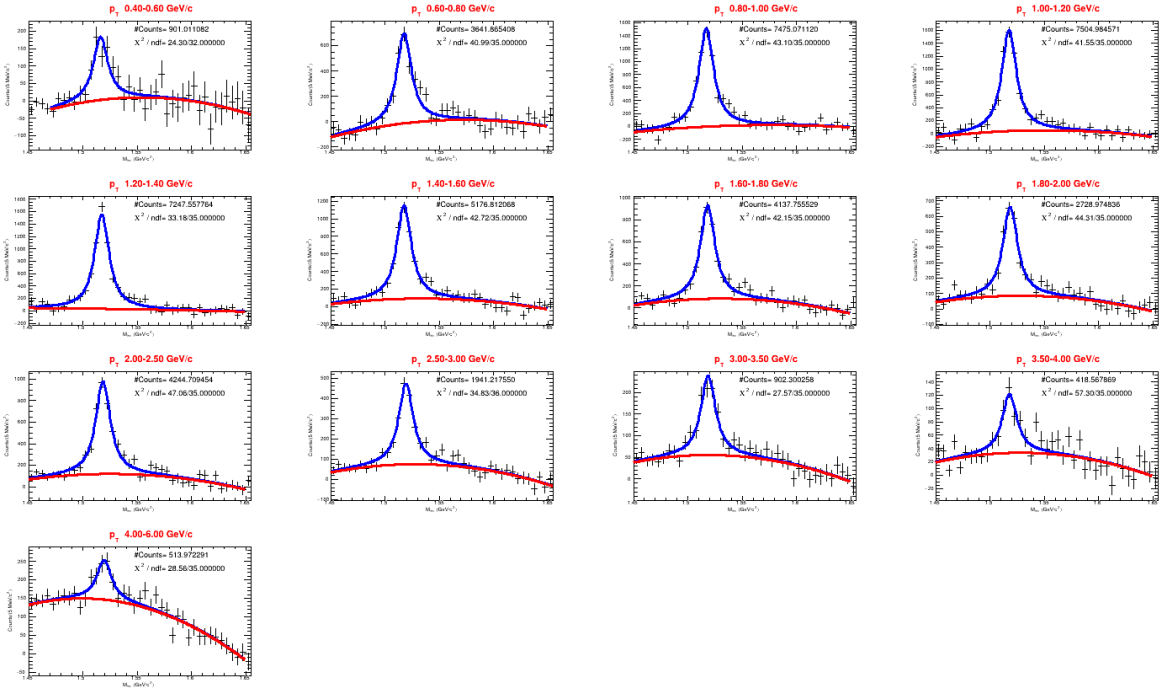

Figure 4.9: The invariant mass distribution of pK pairs for $50-70\%$ multiplicity class in pp collisions at $\sqrt{s} = 5.02$ TeV for different p_{T} bins after subtracting the normalized mixed-event background distribution.

rapidity interval $|y| < 0.5$. Simulated datasets are used to extract the $\Lambda(1520)$ reconstruction efficiency and acceptance. $\Lambda(1520)$ production and decay are simulated using event generator Pythia8 (tuned with Monash 2013 [94]), while interactions with the detector material are simulated using GEANT3.

Both real and simulated data were subjected to the same event selection and track quality cuts. Generated particles were those produced by the event generator without detector effects, while reconstructed tracks were those identified after passing the required selection criteria. The $\Lambda(1520)$ was reconstructed from these daughter tracks. These corrections reflect the detector's acceptance and tracking efficiency.

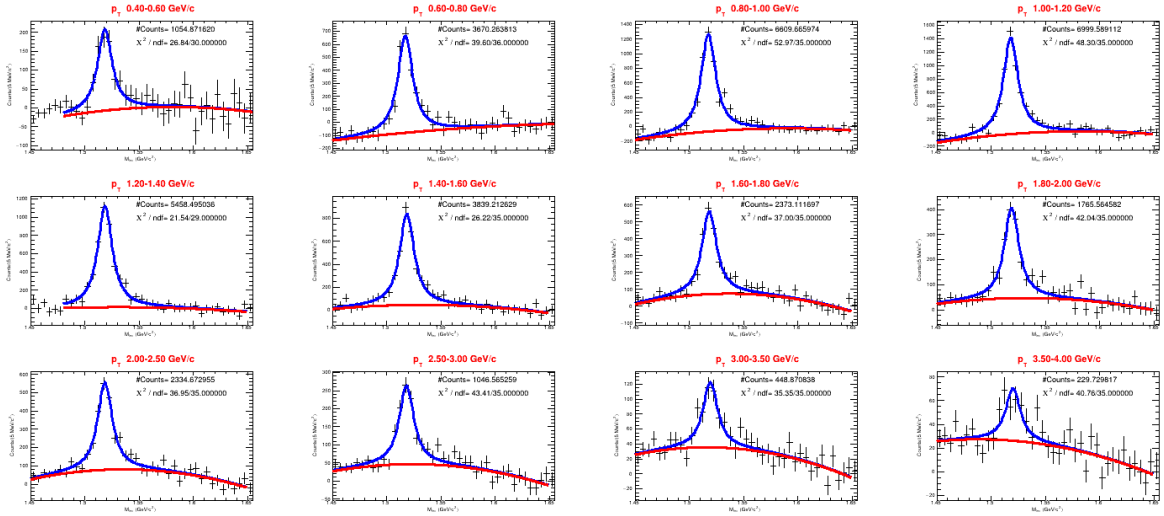

Figure 4.10: The invariant mass distribution of pK pairs for $70-100\%$ multiplicity class in pp collisions at $\sqrt{s}$ = 5.02 TeV for different p_{T} bins after subtracting the normalized mixed-event background distribution.

The reconstruction efficiency × acceptance ($\varepsilon_{\mathrm{rec}}$) is calculated using the simulation datasets in the considered p_{T} bin. $\varepsilon_{\mathrm{rec}}$ is defined as:

$$\varepsilon_{\mathrm{rec}} = \frac{N_{\mathrm{reconstructed}}}{N_{\mathrm{generated}}} \tag{4.13}$$

where,

- $N_{\mathrm{generated}}$: the number of generated Λ(1520) with $|y_{\mathrm{gen}}| < 0.5$.
- $N_{\mathrm{reconstructed}}$: the number of Λ(1520) with $|y_{\mathrm{rec}}| < 0.5$ which is reconstructed after passing all the selection criteria.

The same event selection criteria are used for both the numerator and denominator. Figure 4.19 shows the Λ(1520) reconstruction acceptance × efficiency ($\varepsilon_{\mathrm{rec}}$) as a function

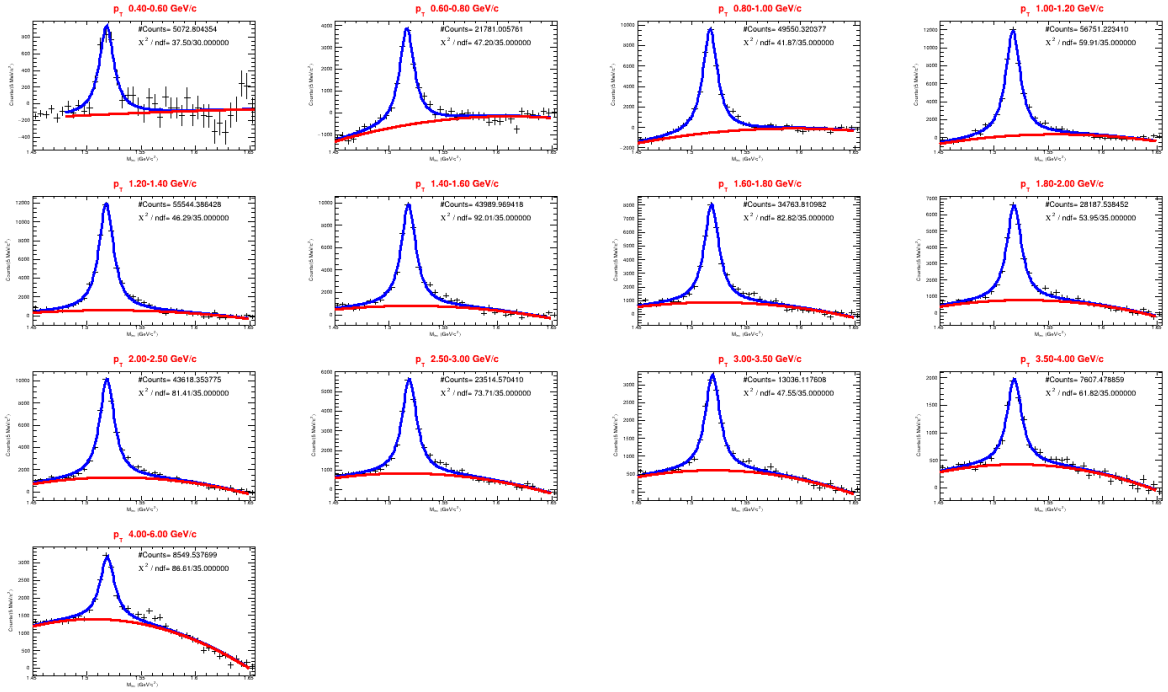

Figure 4.11: The invariant mass distribution of pK pairs for $0-100\%$ multiplicity class in pp collisions at $\sqrt{s} = 5.02$ TeV for different p_{T} bins after subtracting the normalized mixed-event background distribution.

of p_{T} for different multiplicity classes.

Since the events of the numerator and denominator are correlated, the uncertainty in $\varepsilon_{\mathrm{rec}}$ was calculated using the Bayesian approach [95]. The standard deviation of a ratio $\varepsilon = \frac{k}{n}$, where the numerator k is a subset of the denominator n, is given by:

$$\sigma_{\varepsilon} = \sqrt{\frac{k+1}{n+2}\left(\frac{k+2}{n+3} - \frac{k+1}{n+2}\right)} \tag{4.14}$$

4.6.2 Reweighted Efficiency

Due to differences between the shapes of the generated and reconstructed p_{T} spectra as shown in Figure 4.20, a reweighted efficiency was used to correct the raw yield.

The generated and reconstructed spectra are used to estimate the reconstruction effi-

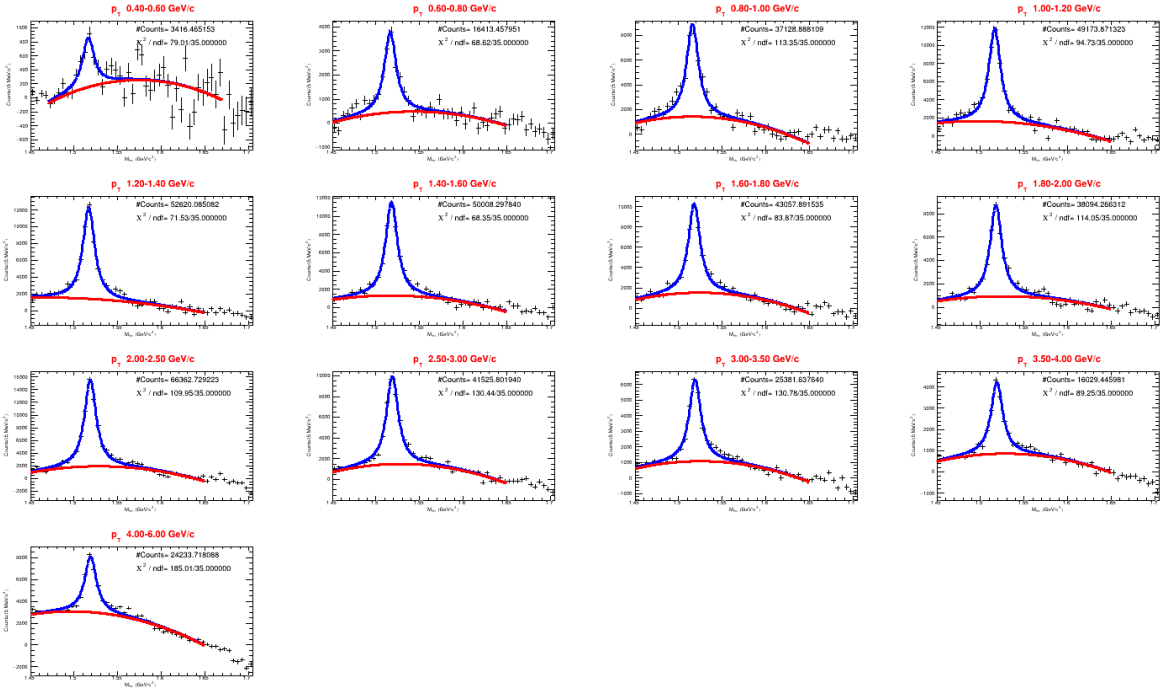

Figure 4.12: The invariant mass distribution of pK pairs for $0-10\%$ multiplicity class of in pp collisions at $\sqrt{s} = 13$ TeV for different p_{T} bins after subtracting the normalized mixed-event background distribution.

ciency ϵ_{rec} and to determine the weighting factor to correct ϵ_{rec} with the following iterative procedure:

1. The unweighted ϵ_{rec} is calculated using the generated and reconstructed $\Lambda(1520)$ spectra.

2. This ϵ_{rec} is used to correct the measured $\Lambda(1520)$ spectrum.

3. The corrected $\Lambda(1520)$ spectrum is fitted using a Lévy-Tsallis function.

4. This Lévy-Tsallis fit is used to weight the simulated $\Lambda(1520)$ spectra. A p_{T}-dependent weight is applied to the generated spectrum so that it follows the fit. The same weight is applied to the reconstructed spectrum.

5. The weighted ϵ_{rec} is calculated.

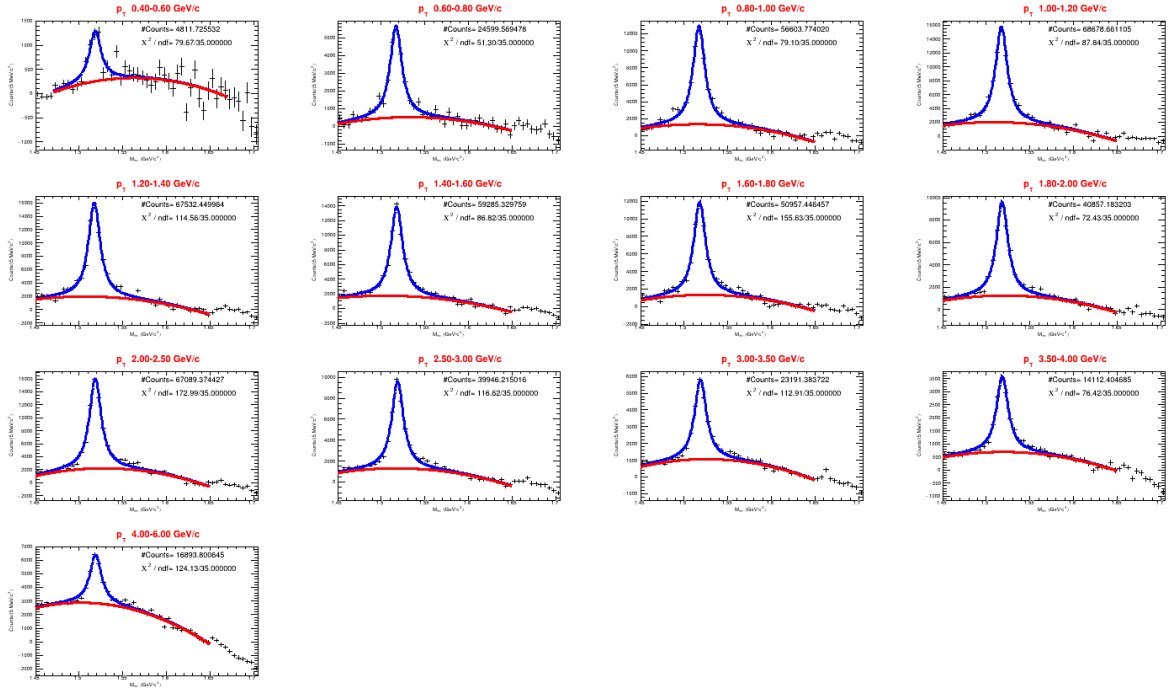

Figure 4.13: The invariant mass distribution of pK pairs for $10-30\%$ multiplicity class of in pp collisions at $\sqrt{s} = 13$ TeV for different p_{T} bins after subtracting the normalized mixed-event background distribution.

6. Steps 2-5 are repeated (with the weighted ϵ_{rec} from step 5 used as the input for step 2 until the ϵ_{rec} values change by less than 0.1% between iterations. It was observed that two iterations are usually sufficient for this procedure to converge.

Figure 4.21 compares the weighted and unweighted efficiencies for both energies, with their ratio shown in the lower panel. The difference between the reweighted efficiency and the unweighted efficiency is noticeable only for $p_{\mathrm{T}} < 1$ GeV/c, highlighting the shape difference between the simulated and measured spectra.

4.6.3 Trigger and Vertex Efficiency Correction

The selected events used for this analysis (kINT7 trigger) are only a subset of the total number of inelastic events. The trigger efficiency is defined as:

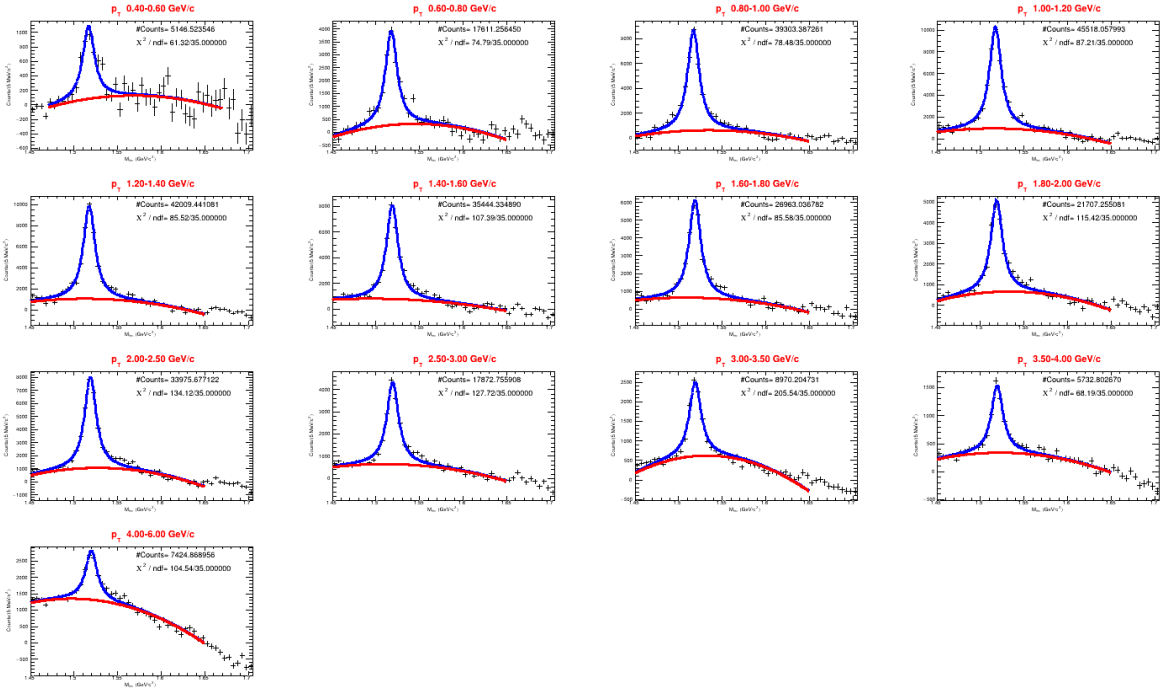

Figure 4.14: The invariant mass distribution of pK pairs for $30-50\%$ multiplicity class in pp collisions at $\sqrt{s} = 13$ TeV for different p_{T} bins after subtracting the normalized mixed-event background distribution.

$$f_{\mathrm{trig/kINT7}} = \frac{N^{\mathrm{evt}}_{\mathrm{kINT7\ |\ TrueINEL>0}}}{N^{\mathrm{evt}}_{\mathrm{TrueINEL>0}}} \tag{4.15}$$

where, the denominator is the number of MC events that pass the kINT7 trigger criterion and pass the physics selection criteria. and the numerator is the number of MC events that have at least one physical primary charged track that has p_{T} larger than 0 in the range of $|\eta| < 1$.

Similarly, vertex efficiency is defined as:

$$f_{\mathrm{vtx}} = \frac{N^{\mathrm{vtx}}_{\mathrm{TrueINEL>0}}}{N^{\mathrm{trig}}_{\mathrm{TrueINEL>0}}} \tag{4.16}$$

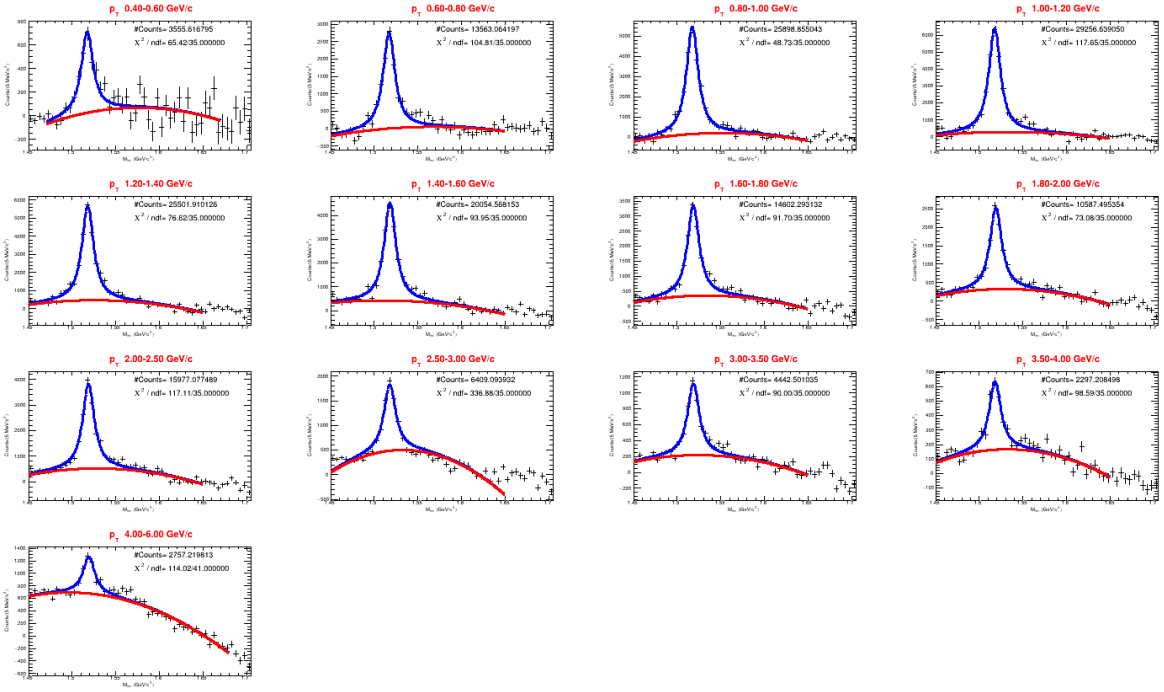

Figure 4.15: The invariant mass distribution of pK pairs for $50-70\%$ multiplicity class in pp collisions at $\sqrt{s} = 13$ TeV for different p_{T} bins after subtracting the normalized mixed-event background distribution.

where, the numerator is the number of MC events that have been generated after applying $|\mathrm{V_{z,generated}}| < 10$ cm and the denominator is the number of events generated without the vertex cut.

The trigger and vertex efficiency correction factors are tabulated in Table 4.7.

4.6.4 Signal Loss Correction

The signal-loss correction factor, f_{SL}, accounts for the loss of $\Lambda(1520)$ particles incurred by selecting events that satisfy the kINT7 trigger, rather than all inelastic events. Applying this factor allows the recovery of the inelastic p_{T}-spectrum. This correction factor is p_{T}-dependent and peaks at low p_{T}, indicating that events failing the kINT7 selection have softer $\Lambda(1520)$ p_{T}-spectra compared to the average inelastic events. The expression for f_{SL} is given by:

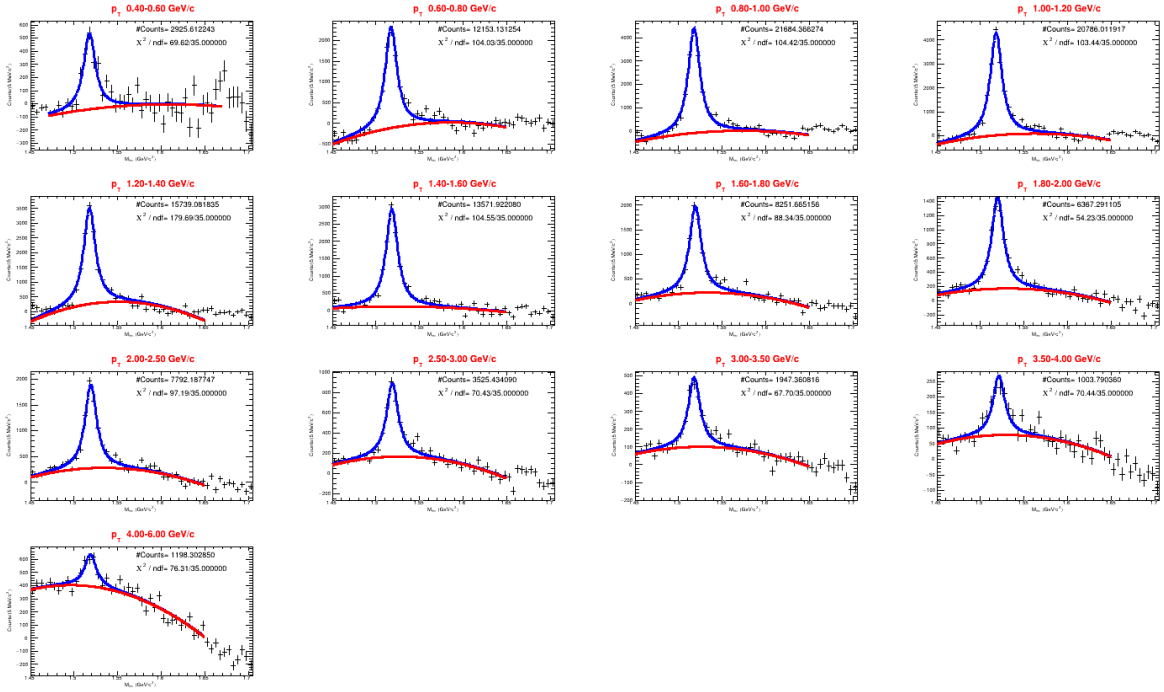

Figure 4.16: The invariant mass distribution of pK pairs for $70-100\%$ multiplicity class in pp collisions at $\sqrt{s}$ = 13 TeV for different p_{T} bins after subtracting the normalized mixed-event background distribution.

$$f_{\mathrm{SL}} = \frac{\mathrm{Num}}{\mathrm{Den}} \tag{4.17}$$

where,

- **Num**: The p_{T} spectrum generated from inelastic events with a cut on the z-position of the generated primary vertex: $|V_{z,\mathrm{generated}}| < 10$ cm.
- **Den**: The p_{T} spectrum generated after triggering and applying all event-selection cuts, including the cut on the z-position of the reconstructed primary vertex.

Due to the low production cross-section of Λ(1520), calculating f_{SL} directly from Monte Carlo (MC)is statistically challenging. Instead, transverse mass m_T scaling ($\mathrm{m}_{\mathrm{T}}^2 = \mathrm{m}^2 + \mathrm{p}_{\mathrm{T}}^2$) is used to estimated f_{SL} for Λ(1520). This method uses other abundant particles

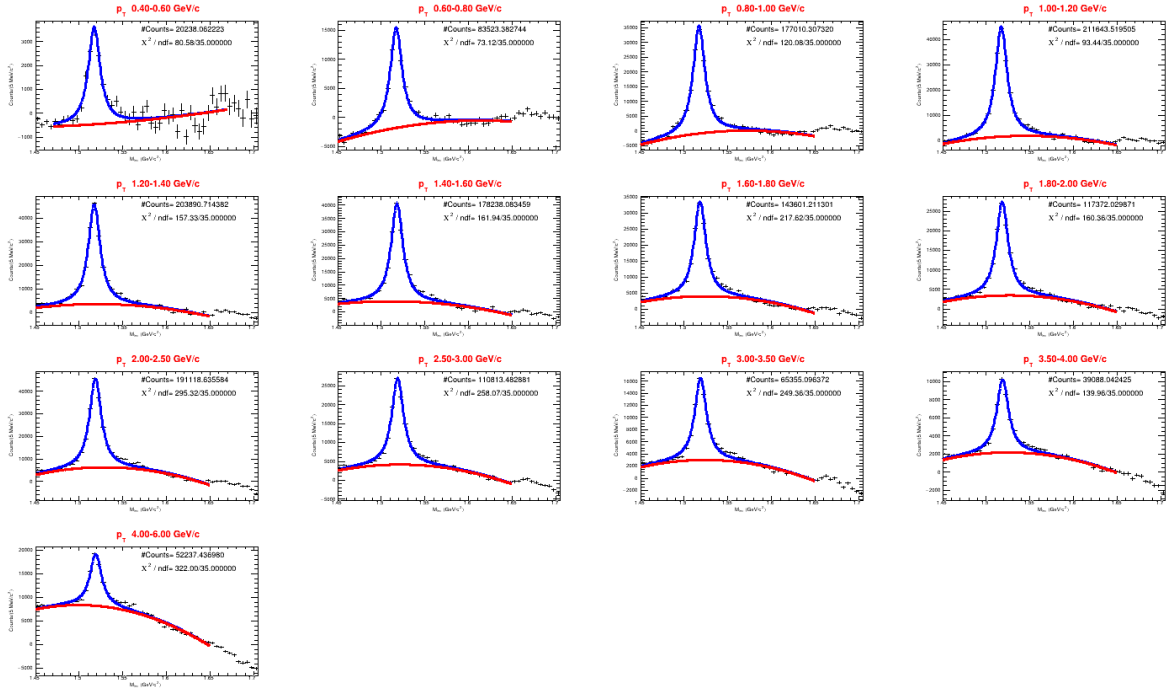

Figure 4.17: The invariant mass distribution of pK pairs for $0-100\%$ multiplicity class in pp collisions at $\sqrt{s} = 13$ TeV for different p_{T} bins after subtracting the normalized mixed-event background distribution.

(Proton, Lambda, Xi, Omega), under the assumption that the slope of their m_T spectra is identical across all the considered baryons. m_T-scaling is employed because it provides a more accurate representation of the transverse momentum distribution of particles, especially in high-energy collisions. This method accounts for the relativistic effects and the mass of the particles involved, allowing for a direct comparison of spectra from different particles, even when their production mechanisms may vary.

The relationship between the transverse momentum (p_{T}) and the transverse mass (m_T) spectra is expressed as:

$$\frac{1}{2\pi m_T}\frac{d^2N}{dm_T dy} = \frac{1}{2\pi p_T}\frac{d^2N}{dp_T dy}$$

The following transformation is used to obtain the p_{T} of $\Lambda(1520)$.

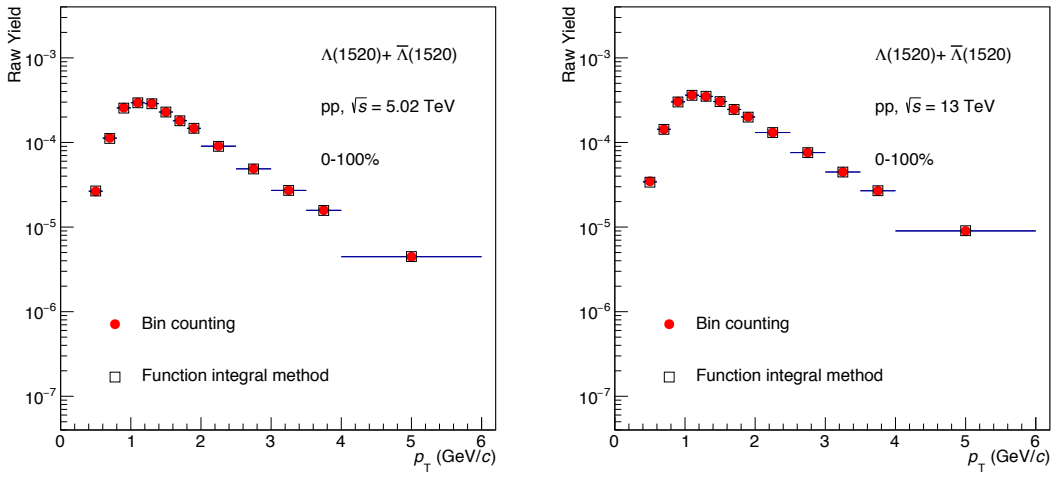

Figure 4.18: Raw yield of $\Lambda(1520)$ using the bin counting and function integral method in pp collisions at $\sqrt{s} = 5.02$ (left side) and 13 TeV (right side).

Multiplicity (%)	13 TeV		5.02 TeV	
	f_{trig}	f_{vtx}	f_{trig}	f_{vtx}
0-10	0.996 ± 0.185	0.998	1.000 ± 0.000	1.000
10-30	0.979 ± 0.125	0.990	0.999 ± 0.000	0.999
30-50	0.941 ± 0.085	0.972	0.995 ± 0.001	0.995
50-70	0.890 ± 0.060	0.950	0.978 ± 0.001	0.985
70-100	0.706 ± 0.040	0.895	0.860 ± 0.002	0.971
0-100	0.958 ± 0.000	0.965	0.945 ± 0.001	0.987

Table 4.7: Trigger and vertex efficiency correction factors for different multiplicity classes at $\sqrt{s} = 13$ TeV and 5.02 TeV

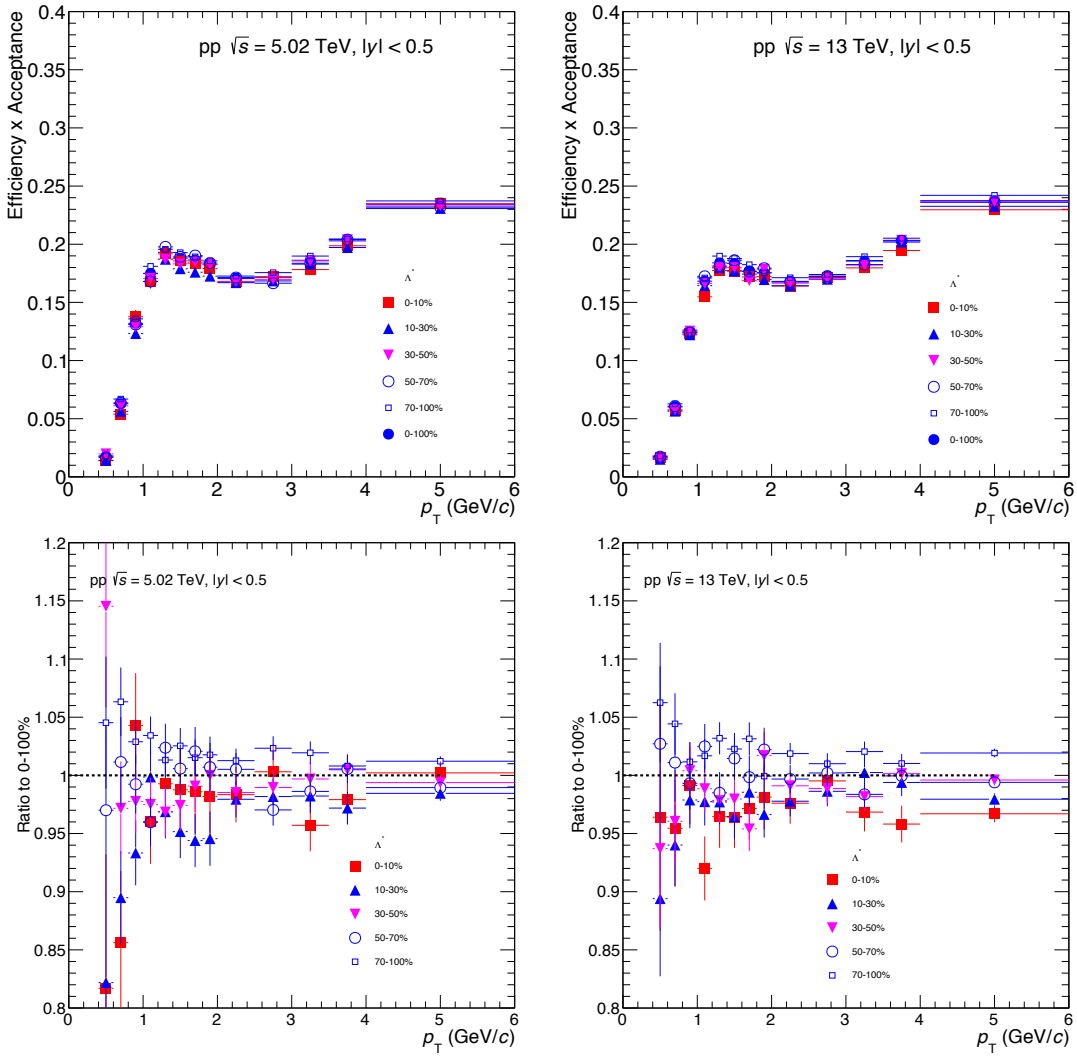

Figure 4.19: The $\varepsilon_{\mathrm{rec}}$ for the $\Lambda(1520)$ as a function of p_{T} for different multiplicity classes. The bottom panels present the ratio of $\varepsilon_{\mathrm{rec}}$ values for different multiplicity classes to the (0-100)% multiplicity class for pp collisions at $\sqrt{s} = 5.02$ TeV (left) and 13 TeV (right).

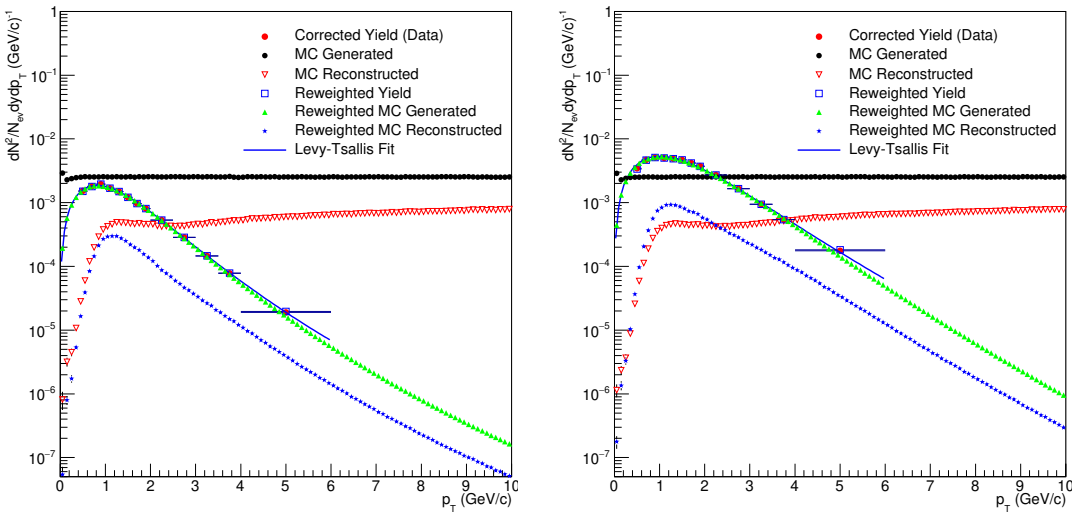

Figure 4.20: The $\Lambda(1520)$ yield (red dots) is shown along with the Lévy-Tsallis fit (blue curve). The unweighted generated spectrum (black circles) and reconstructed spectrum (red inverted triangles) are displayed. Additionally, the re-weighted reconstructed spectra (blue stars) and re-weighted generated spectra (green triangles) in pp collisions at $\sqrt{s} =$ 5.02 TeV (left) and 13 TeV (right) are included.

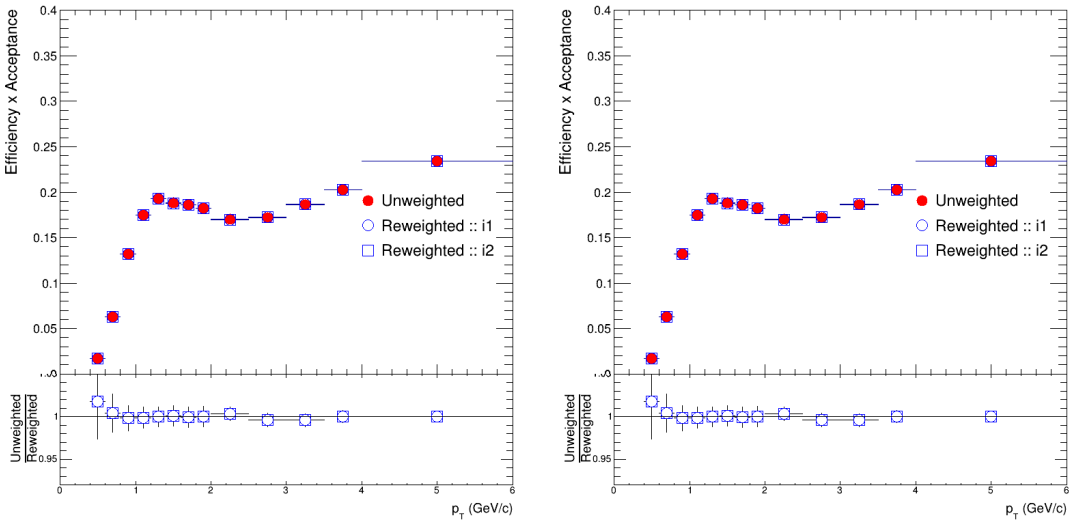

Figure 4.21: The unweighted efficiency and re-weighted efficiency from different iterations for the 0-100% multiplicity class are shown in pp collisions at $\sqrt{s} = 5.02$ TeV (left) and 13 TeV (right), including the ratio of weighted to unweighted efficiency.

$$p_T(\Lambda(1520)) = \sqrt{p_T^2(\text{proton}) + \text{m}^2(\text{proton}) - \text{m}^2(\Lambda(1520))} \tag{4.18}$$

where, m(proton) and m(Λ(1520)) are the masses of the proton and Λ(1520), respectively.

The true and accepted p_{T} spectra are obtained for protons. These proton p_{T} spectra are then converted to the Λ(1520) p_{T} spectra using the equation provided above. Thereafter, the ratio of the converted p_{T} spectra is calculated to estimate f_{SL}. Finally, different reference particles, such as Lambda or Xi instead of protons, are used to estimate the uncertainty of f_{SL}.

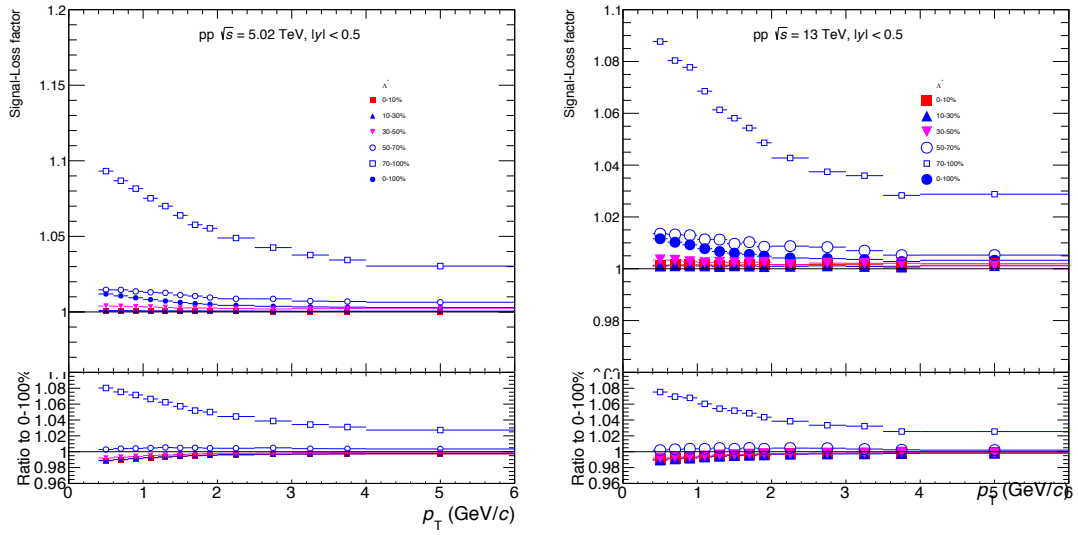

Figure 4.22: f_{SL} estimated for Λ(1520) in pp collisions at $\sqrt{s}$ = 5.02 (left) and 13 TeV (right) respectively in different multiplicity classes.

f_{SL} estimated for Λ(1520) from the proton, Lambda, and Xi in different multiplicity classes in pp collisions at $\sqrt{s}$ = 5.02 and 13 TeV are shown in Figures 4.23 and 4.24 respectively. The signal loss correction factor for Λ(1520) in different multiplicity classes is shown in Figure 4.22.

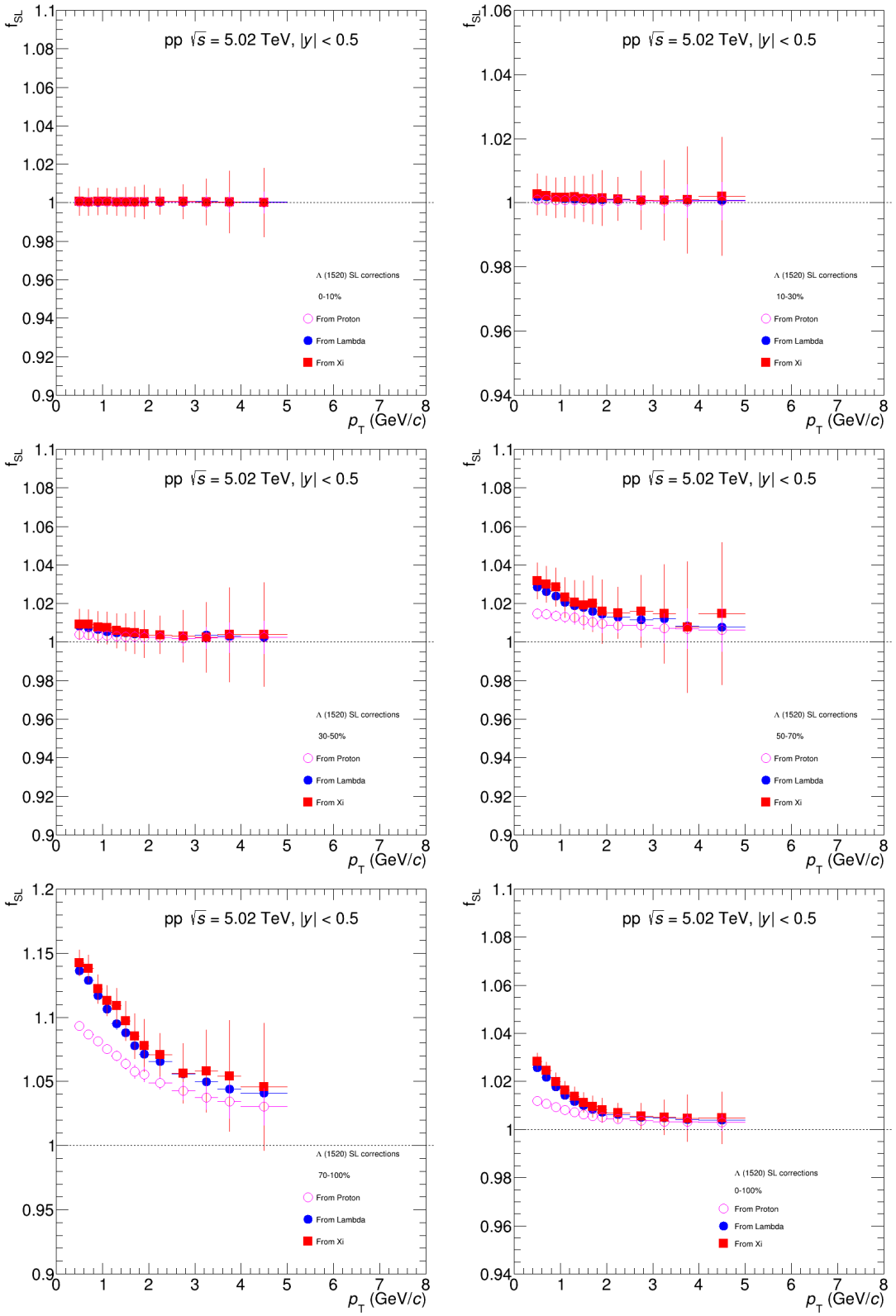

Figure 4.23: f_{SL} estimated for $\Lambda(1520)$ from the proton, Lambda, and Xi in pp collisions at $\sqrt{s} = 5.02$ TeV in different multiplicity classes.

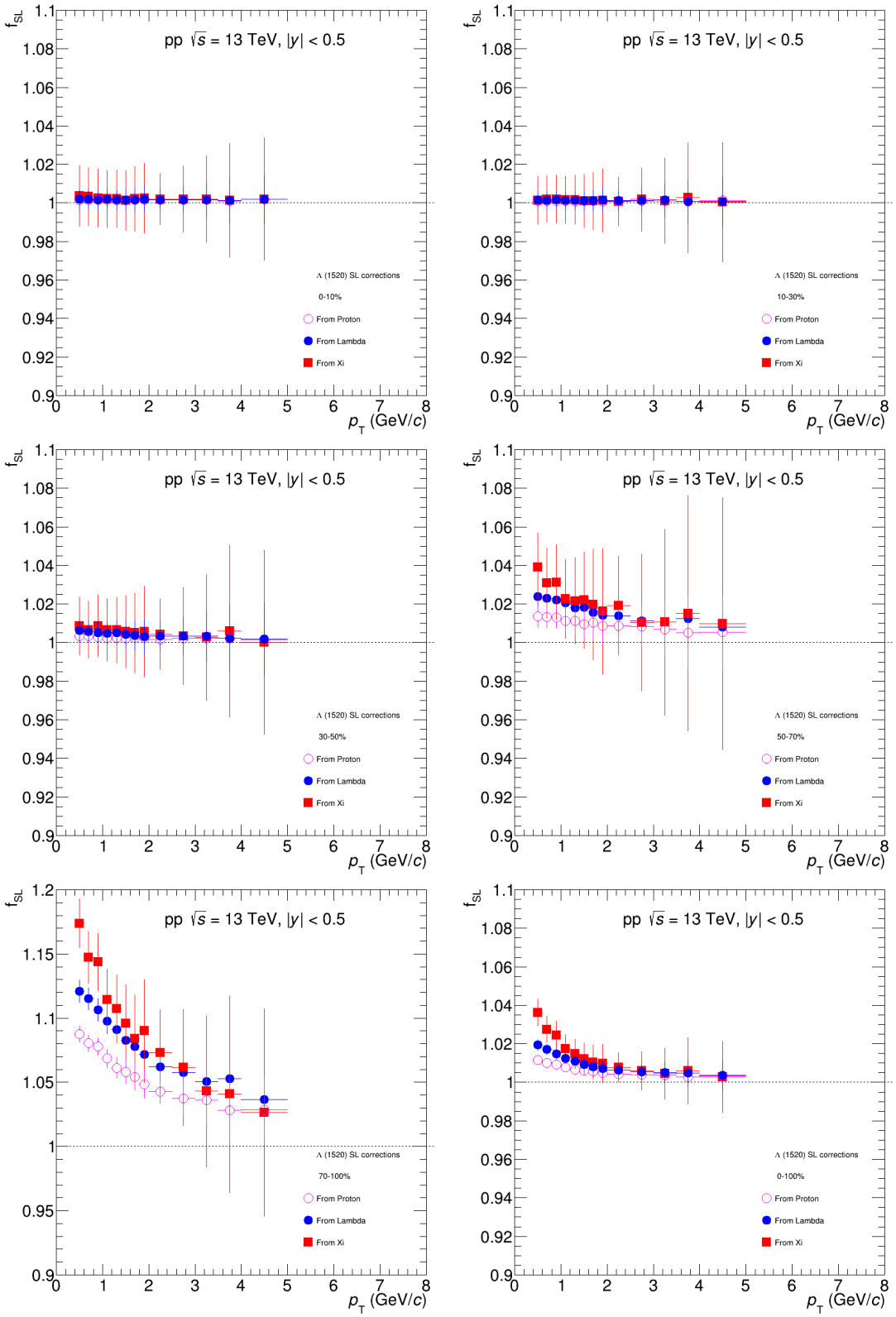

Figure 4.24: f_{SL} estimated for $\Lambda(1520)$ from the proton, Lambda, and Xi in pp collisions at $\sqrt{s} = 13$ TeV respectively in different multiplicity classes.

4.7 Estimation of Systematic Uncertainties

Systematic uncertainty pertains to biases or errors that may emerge from systematic effects inherent in the experimental setup, data acquisition, or analytical methods. These uncertainties arise from consistent and repeatable factors that can affect measurements, distinguishing them from statistical uncertainties

The systematic uncertainties are estimated by utilizing a comprehensive approach which involves examining all possible permutations of various analysis parameters. The sources of systematic uncertainty are categorized into grouped and ungrouped uncertainty as listed in Table 4.8, based on their correlation with analysis settings.

Sources of Systematic Uncertainties

Grouped Uncertainties	**Ungrouped Uncertainties**
Signal extraction	Material budget
Track selection cuts (including PID)	Global tracking efficiency
	Signal loss correction
	Hadronic interaction
	PileUp

Table 4.8: Grouped and Ungrouped Uncertainties.

The basic principles followed for evaluating systematic uncertainties are outlined below:

The corrected yield for each p_{T} bin is first determined using the default configuration. Thereafter, a cut parameter is altered at a time, and the corrected yield for the altered parameter is determined. This is followed by estimating the relative error for these variations.

To ensure that systematic uncertainties are not influenced by statistical fluctuations (since results are derived from subsets of other data), the Barlow criteria is applied. If the variations observed for all p_{T} bins are found to be inconsistent with Barlow checks, they are taken as sources of systematic uncertainties.

Barlow Criteria

Systematic uncertainties in particle yield measurements are assessed by comparing a default measurement to several alternate measurements obtained by varying analysis parameters. This approach, known as Barlow check, helps to determine whether the observed differences are statistically significant or merely a result of overlapping uncertainties [96].

A brief description of the Barlow check is provided below.

Let Y_{def} be the default yield measurement, representing the value obtained with the standard set of analysis parameters, with its associated statistical uncertainty denoted as σ_{def}. Let Y_{var} be the alternate yield measurement, indicating the value obtained after varying one set of analysis parameters among the considered sources of uncertainty, with its statistical uncertainty represented as σ_{var}.

The difference between the default and alternate measurements can be expressed as Δ. The combined uncertainty, represented by σ_{cc}, is calculated as the square root of the squared differences in the standard deviations of the default and alternate measurements, which is given by:

$$\Delta = Y_{\text{var}} - Y_{\text{def}} \tag{4.19}$$

$$\sigma_{cc} = \sqrt{|\sigma^2_{\text{var}} - \sigma^2_{\text{def}}|} \tag{4.20}$$

Δ/σ_{cc} distributions are obtained for each multiplicity classes. If the variations between Y_{var} and Y_{def} are purely statistical, the resulting distribution of Δ/σ_{cc} should ideally follow a Gaussian shape, characterized by a mean of 0 and a standard deviation of 1. Significant deviations from expected behaviour suggest that the variations are not purely statistical and should be incorporated into the systematic uncertainties. A distribution with a standard deviation significantly less than 1 is still considered, provided it remains approximately Gaussian and the mean is close to 0.

If observed variations for all p_{T} bins are not consistent according to the Barlow check, it is considered a source of systematic uncertainty. The criteria for this analysis are:

$$\text{Mean of } |\Delta/\sigma_{cc}| > 0.1 \tag{4.21}$$

$$\text{Standard deviation} > 1.1 \tag{4.22}$$

If either of these criteria is satisfied, then the given cut variation is included in the systematic uncertainty.

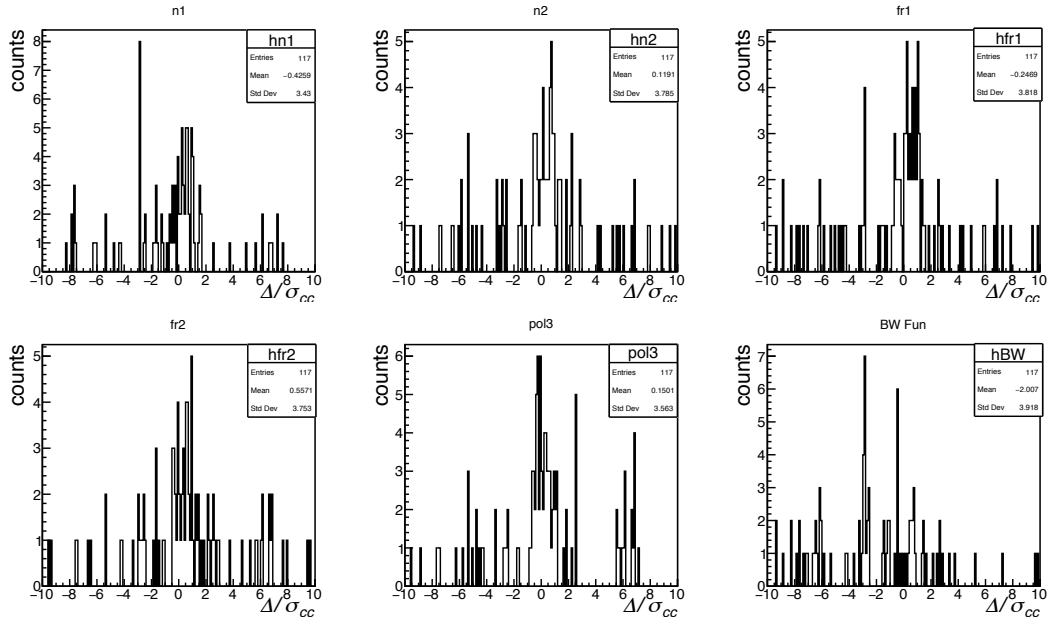

Figure 4.25: Barlow checks for various signal extraction sources in 0-100% multiplicity classes for $\Lambda(1520)$ in pp collisions at $\sqrt{s} = 5.02$ TeV.

Figures 4.25 and 4.26 show the Barlow checks for various signal extraction sources and Figure 4.27 show the Barlow checks for various track and PID selection criteria in 0-100% multiplicity classes in pp collisions $\sqrt{s} = 5.02$ and 13 TeV respectively.

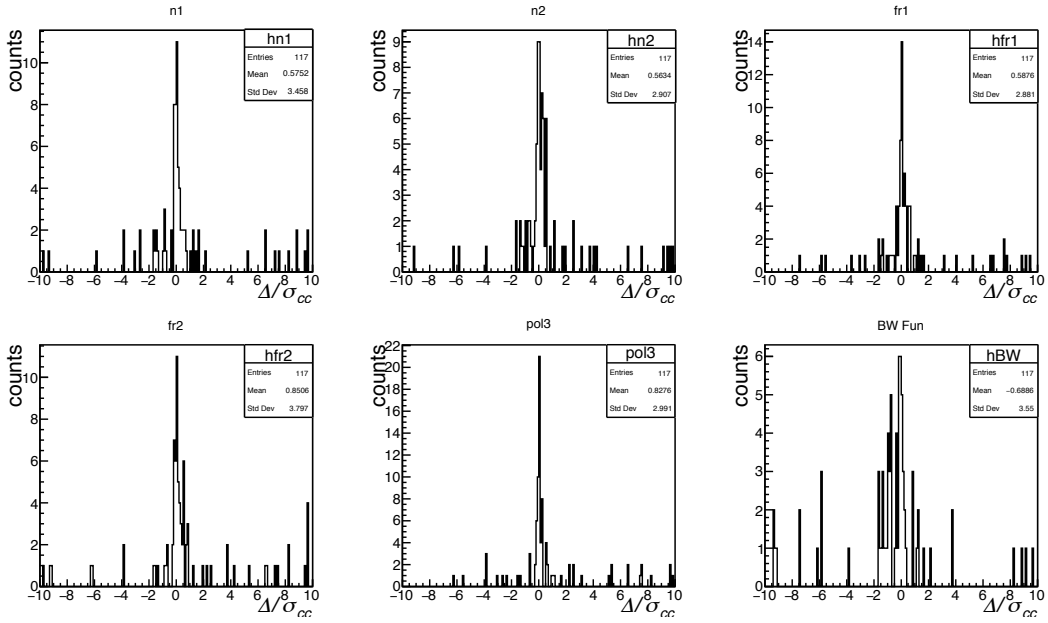

Figure 4.26: Barlow checks for various signal extraction sources in 0-100% multiplicity classes for $\Lambda(1520)$ in pp collisions at $\sqrt{s} = 13$ TeV.

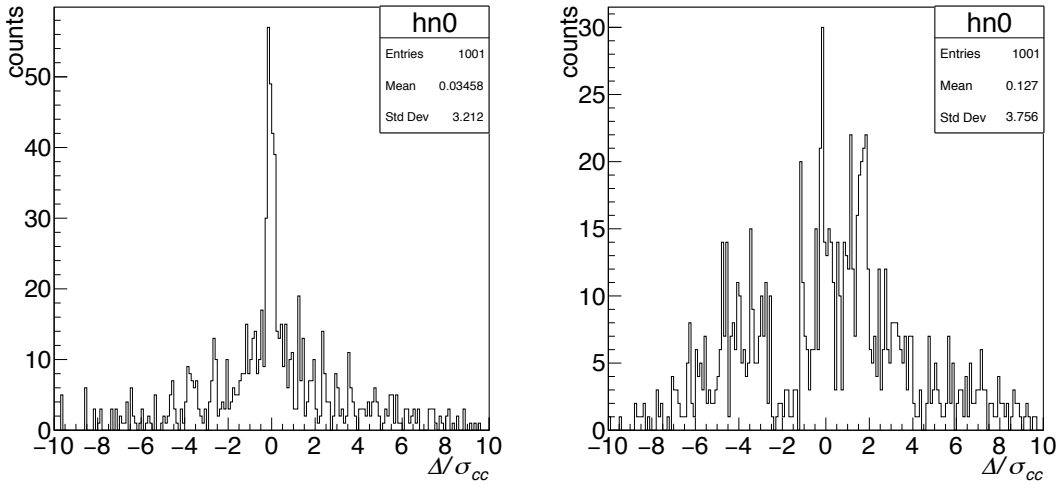

Figure 4.27: Barlow checks for various track and PID selection in 0-100% multiplicity classes for $\Lambda(1520)$ in pp collisions at $\sqrt{s} = 5.02$ (left) and 13 TeV (right) respectively.

4.7.1 Signal Extraction Systematic Uncertainty

To estimate the systematic uncertainty due to signal extraction, several parameters were individually adjusted by varying the default cuts. This included altering the normalization range, tweaking the residual background function, and modifying the fit region and fit function. These variations led to systematic uncertainties in signal extraction, which ranged from 2 - 15%, depending on the transverse momentum. The systematics due to signal extraction in various multiplicity classes are within 5%. The default and alternative selection criteria are listed in Table 4.9.

Parameters	**Variations**
Fit Range	1.45–1.65 (Default) 1.48–1.62 1.42–1.68
Normalization Range	1.6 < Minv < 1.7 (Default) 1.55 < Minv < 1.65 1.7 < Minv < 1.8
Fit Function	Voigtian Function (Default) Breit-Wigner Function (BW)
Background Function	Pol2 (Default) Pol3
Background Description	Event Mixing (Default) Like-Sign
Yield Extraction	Bin Counting (Default) Function Integral

Table 4.9: Summary of fitting parameters and variations used to estimate signal extraction systematic uncertainty.

4.7.2 Track Selection and PID Systematic Uncertainty

The systematic uncertainty due to track selection and PID is estimated by varying each parameter individually. These parameters include the minimum number of rows crossed in the TPC, the ratio of the number of crossed rows to the number of findable clusters in the TPC, the chi-squared per cluster in both the TPC and the ITS, and the Distance of Closest Approach in the z-direction (DCAz) and the transverse direction (DCAxy).

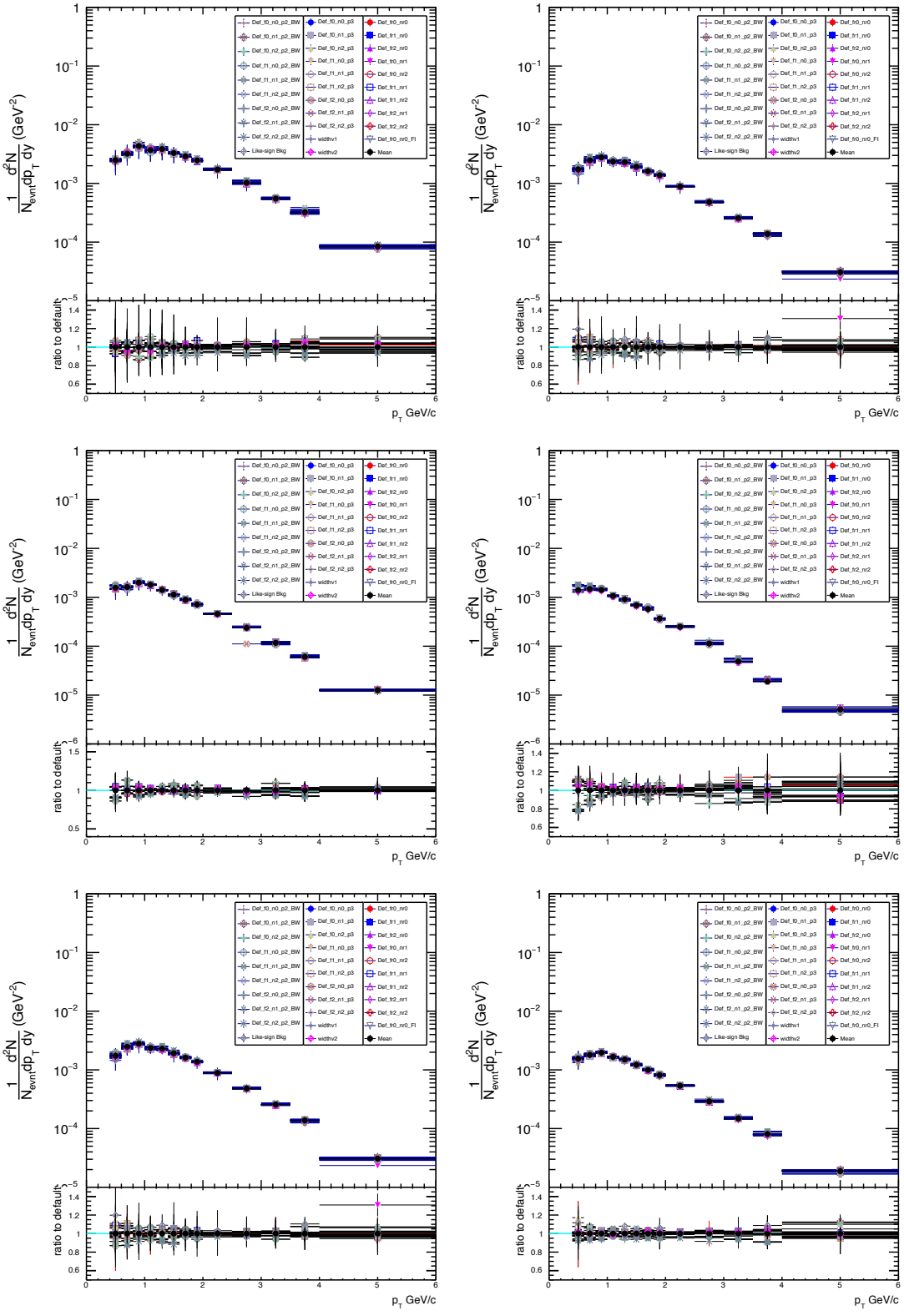

Figure 4.28: Corrected $\Lambda(1520)$ spectrum and ratio to default due to variation in signal extraction parameters in pp collisions at $\sqrt{s} = 5.02$ TeV.

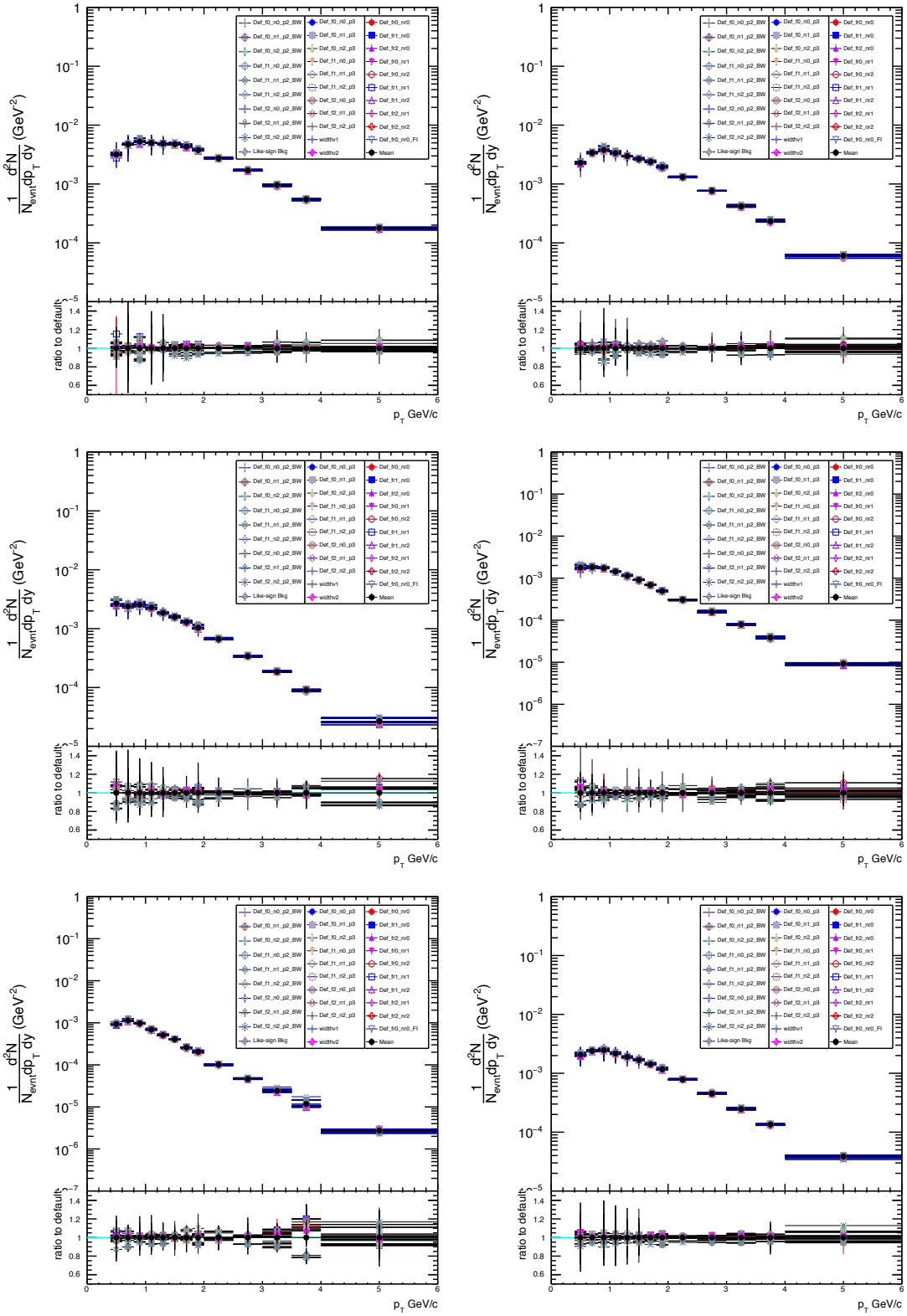

Figure 4.29: Corrected $\Lambda(1520)$ spectrum and ratio to default due to variation in signal extraction parameters in pp collisions at $\sqrt{s} = 13$ TeV.

For each of these selection criteria, two or three variations were tested to evaluate their impact on the systematic uncertainty. The default and alternative selection criteria are listed in Table 4.10.

Selection criteria	**Variations**
Number of crossed rows in TPC	$N_{TPC-cluster} > 70$ (Default) $N_{TPC-cluster} > 60$ $N_{TPC-cluster} > 100$
Crossed rows to findable clusters in TPC	$R_{TPC} > 0.8$ (Default) $R_{TPC} > 0.9$ $R_{TPC} > 0.7$
DCAz	DCAz < 2 cm (Default) DCAz < 1 cm DCAz < 0.2 cm
Track Quality ($\chi^2/N_{\mathbf{TPC,\ cluster}}$)	$\chi^2/rmN_{TPC,\ cls} < 4$ (Default) $\chi^2/rmN_{TPC,\ cls} < 3$
PID	$\lvert n\sigma_{TPC}\rvert = 3$, $\lvert n\sigma_{TOF}\rvert = 3$ (Default) $\lvert n\sigma_{TPC}\rvert = 2.5$, $\lvert n\sigma_{TOF}\rvert = 2.5$ $\lvert n\sigma_{TPC}\rvert = 3.5$, $\lvert n\sigma_{TOF}\rvert = 3.5$

Table 4.10: Summary of fitting parameters and variations used to estimate track selection systematic uncertainty.

4.7.3 Systematic due to Signal Loss

The systematic uncertainties arising from the signal loss correction factor are evaluated as outlined in Section 4.6.4. In this method, the default approach for estimating the signal loss for the $\Lambda(1520)$ particle is based on m_T-scaling measurements from protons and other particles, such as Ξ and Λ, which are considered to contribute to the systematic uncertainty.

4.7.4 Systematic due to Global Tracking Efficiency

Estimating the global tracking efficiency is essential for accurately determining the $\Lambda(1520)$ yield, as this particle decays into protons and kaons, both of which need to be detected individually and have different tracking efficiency. Any inefficiency in tracking these decay

products directly impacts the precision of the $\Lambda(1520)$ measurement. To mitigate this, a detailed assessment of the tracking efficiency is performed. This includes simulating the generation of 100 million $\Lambda(1520)$ particles and their decay into protons and kaons to analyze the tracking performance across various p_{T} bins. These estimates are crucial for correcting potential detection inefficiencies and incorporating them into the global tracking uncertainty, ensuring more reliable results. A systematic uncertainty due to global tracking efficiency of 1.51% and 2.03% is estimated for pp collisions at $\sqrt{s} = 5.02$ and 13 TeV respectively.

4.7.5 Material Budget

The systematic uncertainty arising from the ALICE material budget was estimated using the uncertainty data for the $\Lambda(1520)$ in Pb–Pb collisions at $\sqrt{s_{NN}} = 5.02$ TeV. This uncertainty is less than 4% for low p_{T} values (below 2 GeV/c) and becomes negligible at higher p_{T}.

4.7.6 Pile Up Events

The systematic uncertainty due to potential residual contamination from pileup events was estimated by varying the pileup rejection criteria. This variation showed an uncertainty of 1%. Additionally, the uncertainty arising from the reconstruction efficiency across different multiplicity bins in Monte Carlo (MC) simulations is considered to be 2% and is treated as a p_{T}-independent error.

A smoothing procedure was implemented due to the presence of substantial fluctuations in systematic uncertainties across adjacent bins. This procedure involves assigning the average fractional uncertainty between the $(i-1)^{th}$ and $(i+1)^{th}$ bins to the i^{th} p_{T}-bin.

4.7.7 Total Systematic Uncertainty

The total systematic uncertainties (U_{Total}) are estimated by taking the quadrature sum of each grouped systematic uncertainty. These groups include the uncertainties from signal extraction (U_{Signal}), track and PID selection cuts (U_{Trackcut}), material budget (U_{MB}), tracking efficiency (U_{TE}), pileup (U_{PL}), and multiplicity-dependent reconstruction efficiency (U_{Multi}). The total systematic uncertainty is calculated using the following formula:

$$U_{\text{Total}} = \sqrt{U^2_{\text{Signal}} + U^2_{\text{Trackcut}} + U^2_{\text{MB}} + U^2_{\text{TE}} + U^2_{\text{PL}} + U^2_{\text{Multi}}} \tag{4.23}$$

In Table 4.11, the fractional uncertainty is quoted as a percentage for each source of uncertainty across the full transverse momentum (p_{T}) range.

Source	**Multiplicity (%)**				
	0 - 10%	10 - 30%	30 - 50%	50 - 70%	70 - 100%
Signal Extraction	4.27	3.91	4.01	5.62	4.79
	3.60	3.58	4.56	4.03	4.71
Track cut selection	2.18	2.39	2.07	2.28	1.77
	2.31	2.74	3.33	2.99	3.42
Signal loss	0.02	0.08	0.27	0.92	3.14
	0.07	0.07	0.32	1.10	4.01
Global tracking efficiency	1.51	1.52	1.52	1.52	1.52
	2.03	2.03	2.03	2.03	2.03
Material budget	1.81	1.81	1.81	1.81	1.81
	1.81	1.81	1.81	1.81	1.81
Hadronic interaction	2	2	2	2	2
	2	2	2	2	2
Total	5.41	5.39	5.31	7.07	7.37
	5.39	5.49	6.67	6.29	8.19

Table 4.11: Summary of the systematic uncertainties (%) on the $\Lambda(1520)$ p_{T} spectra for different multiplicity classes in pp collisions at $\sqrt{s} = 5.02$ TeV (upper values)and $\sqrt{s} =$ 13 TeV (lower values).

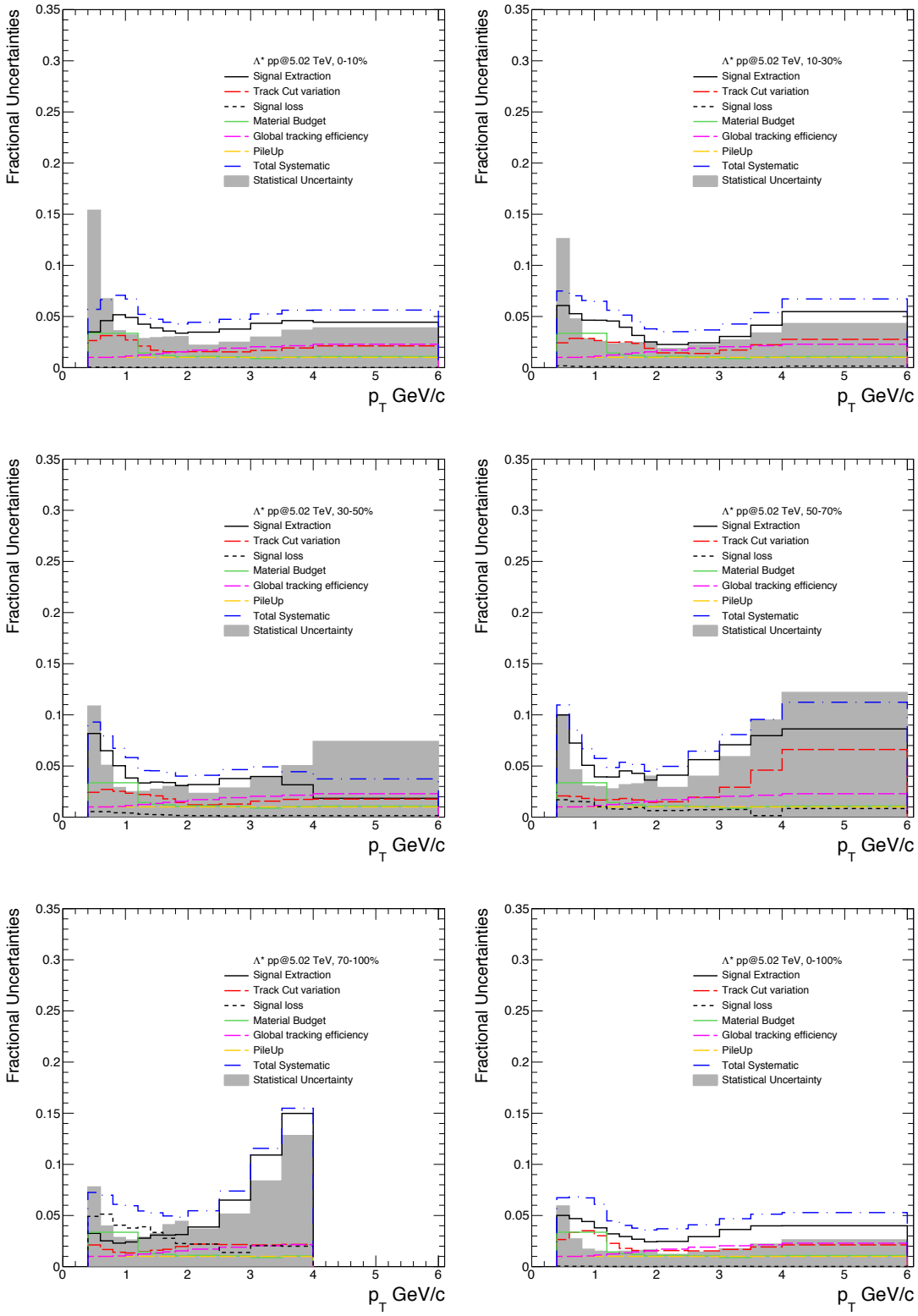

Figure 4.30: Total fractional correlated uncertainty due to various sources after smoothening for different multiplicity classes. The grey-shaded area shows the total statistical uncertainty in pp collisions at $\sqrt{s} = 5.02$ TeV.

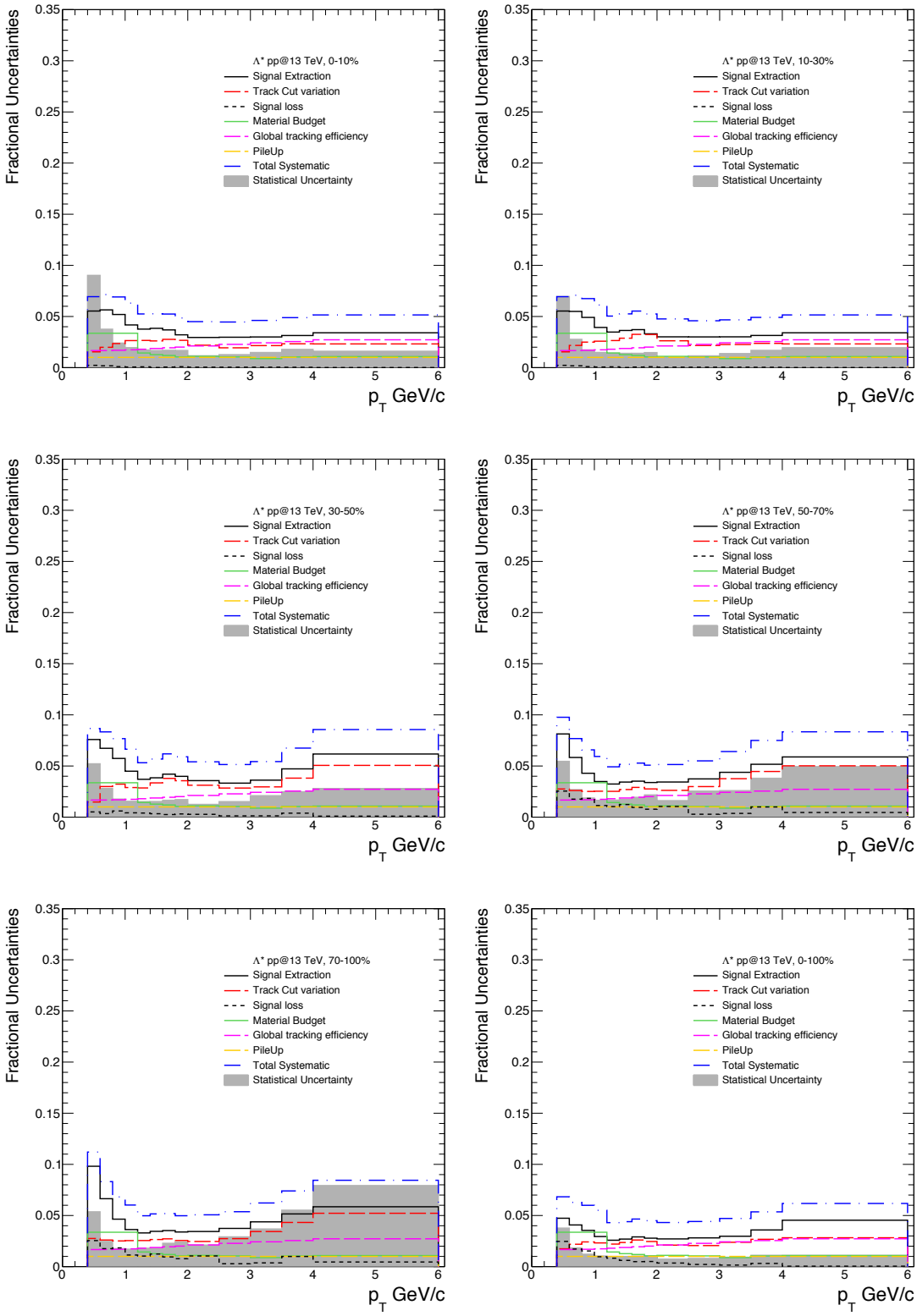

Figure 4.31: Total fractional correlated uncertainty due to various sources after smoothening for different multiplicity classes. The grey-shaded area shows the total statistical uncertainty in pp collisions at $\sqrt{s} = 13$ TeV.

Uncorrelated Systematic Uncertainty

The uncorrelated systematic uncertainty in the measurement of the baryonic resonance $\Lambda(1520)$ is estimated by summing contributions from various independent sources such as signal extraction, track selection, and signal loss. This approach is consistent with the method described for calculating uncorrelated systematic uncertainty. Specifically, each uncertainty is squared and summed in quadrature, which reflects only the independent variations without assuming any correlation between the sources. This method ensures that the final value represents the uncorrelated uncertainty across different multiplicity classes, excluding contributions that are common to all classes.

Extrapolated Systematic Uncertainty

To estimate the integrated yield of the $\Lambda(1520)$ resonance, it is essential to account for the yield in the unmeasured p_{T} region. This process involves fitting the measured p_{T}-differential yields using several fit functions, including $\mathrm{m_T}$-exponential, p_{T}-exponential, Boltzmann, Blast-Wave, Power law, and Lévy-Tsallis functions. For the default approach to low p_{T} extrapolation, the Lévy-Tsallis function is used, while the Power law function is employed for high p_{T} extrapolation. The measured $\Lambda(1520)$ yields in the low and high p_{T} extrapolated regions for pp collisions at $\sqrt{s}$ = 5.02 TeV and 13 TeV are shown in Figure 4.32 and Figure 4.33, respectively. The lines in these figures represent fits using the $\mathrm{m_T}$-exponential, p_{T}-exponential, Boltzmann, Blast-Wave, Power law, and Lévy-Tsallis functions.

To quantify the systematic uncertainty, multiple fits are performed by varying the p_{T} distribution functions to explore the range of possible yields based on the systematic uncertainties associated with the data. The low-p_{T} and high-p_{T} extrapolated yields are calculated by varying the fitting functions for the p_{T} distributions. All other fit functions are utilized to estimate systematic uncertainties, with parameters allowed to vary freely.

The total p_{T}-integrated yield is computed as $\frac{dN_{\mathrm{low}}}{dy} + \frac{dN_{\mathrm{data}}}{dy} + \frac{dN_{\mathrm{high}}}{dy}$ for each fitting

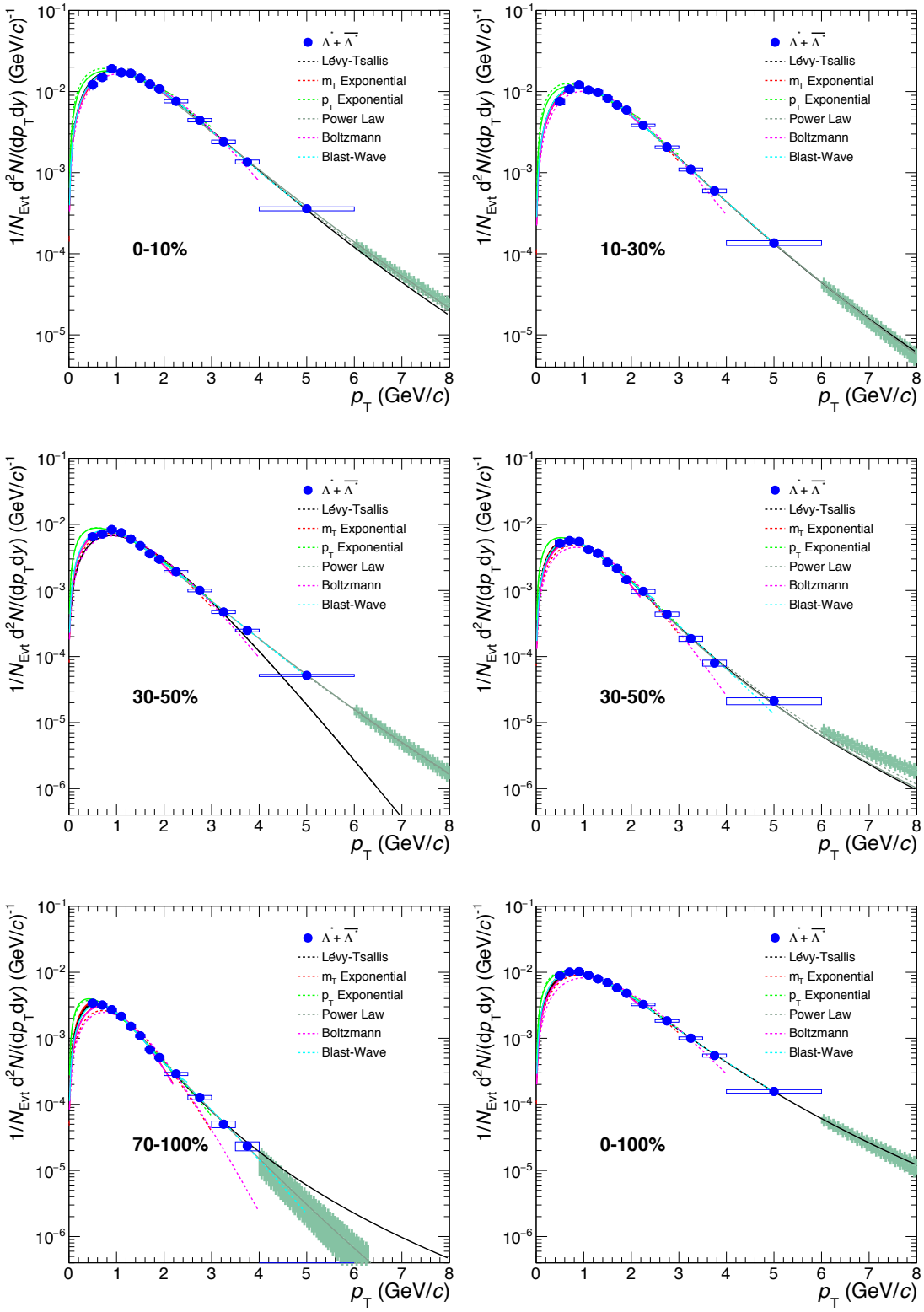

Figure 4.32: Measured Λ1520 in Low and high p_{T} extrapolated region in pp collisions at $\sqrt{s} = 5.02$ TeV. The lines represent the $\mathrm{m_T}$-exponential, p_{T}-exponential, Boltzmann, Blast-Wave, Power law, and Lévy-Tsallis functions fit.

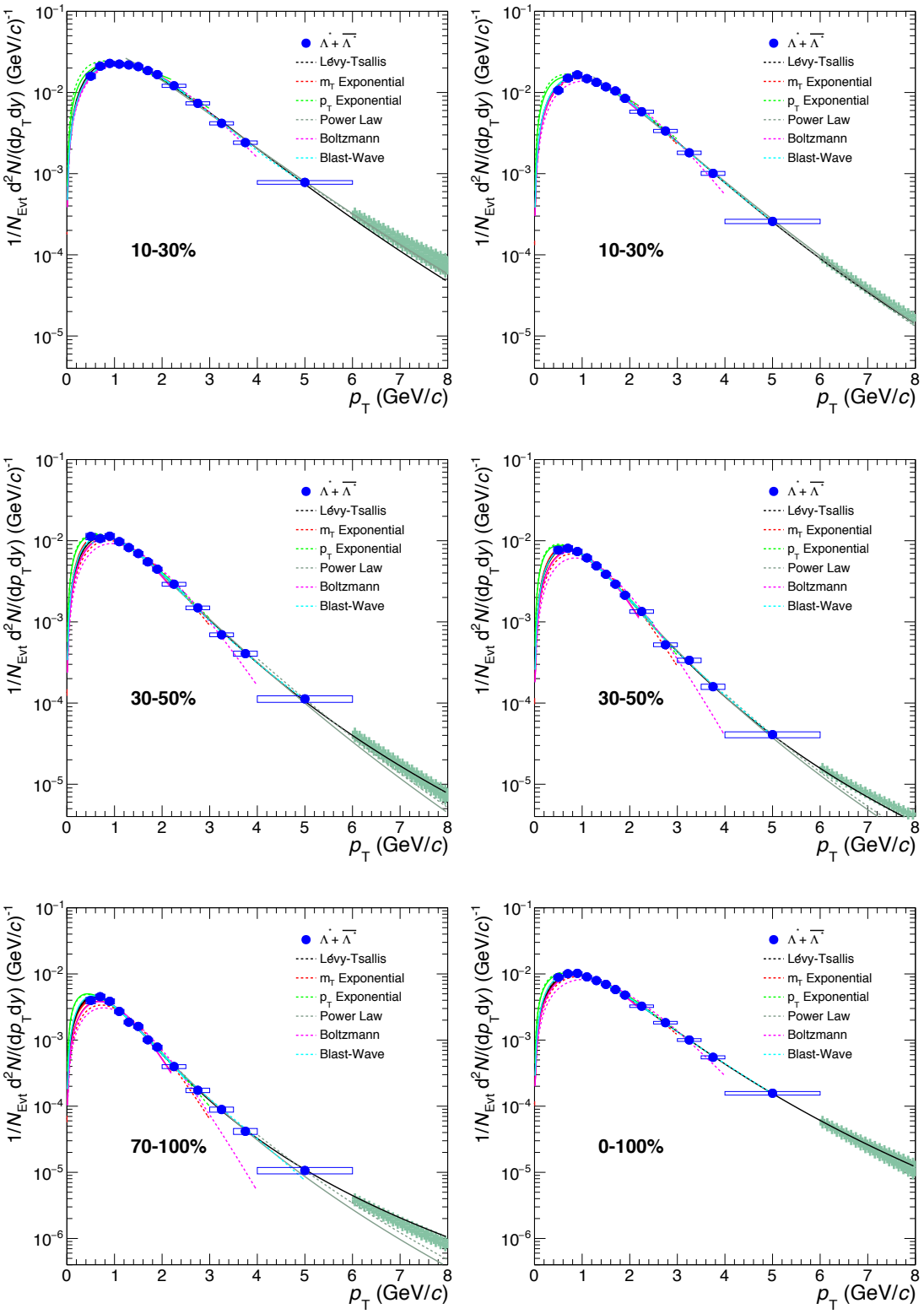

Figure 4.33: Measured Λ1520 in Low and high p_{T} extrapolated region in pp collisions at $\sqrt{s}$ = 13 TeV. The lines represent the $\mathrm{m_T}$-exponential, p_{T}-exponential, Boltzmann, Blast-Wave, Power law, and Lévy-Tsallis functions fit.

function. Additionally, the systematic uncertainty for the average transverse momentum $\langle p_{\mathrm{T}} \rangle$ is estimated using a similar approach as described above.

Chapter 5

$\Lambda(1520)$ and $\mathrm{K}^{*0}(892)$ Production in High Multiplicity pp Collisions at $\sqrt{s} = 13\,\mathrm{TeV}$

In high multiplicity pp and p–Pb collisions at LHC energies, phenomena such as strangeness enhancement and collective expansion were observed which closely resemble to those observed in A–A collisions. These findings imply the potential formation of a mini QGP-like system in high multiplicity pp collisions. Notably, this reveals intriguing features, including the enhancement of strange particles and the observation of ridge-like structures. High multiplicity pp collisions are crucial for understanding the dynamic processes and mechanisms, including particle production, that govern these high-energy environments [27, 59, 60].

5.1 Analysis Details

The $\Lambda(1520)$ baryon, with a mass, $m_{\mathrm{PDG}} = (1519.5 \pm 1.0)\,\mathrm{MeV}$ and a width, $\Gamma_{\mathrm{PDG}} = (15.6 \pm 1.0)\,\mathrm{MeV}$, decays into pK^- or $\bar{\mathrm{p}}\mathrm{K}^+$ with a branching ratio of $(22.5 \pm 0.5)\%$. The $\mathrm{K}^{*0}(892)$ particle, with a mass, $m_{\mathrm{PDG}} = (892 \pm 2)\,\mathrm{MeV}$ and a width, $\Gamma_{\mathrm{PDG}} = (47.3 \pm$

2.0) MeV, decays into $K^+\pi^-$ or $K^-\pi^+$ with a branching ratio of $(0.66 \pm 0.5)\%$. The production of these particles in pp collisions at a center-of-mass energy of $\sqrt{s} = 13$ TeV is studied in three high multiplicity classes (0 - 0.01%, 0.01 - 0.05%, 0.05 - 0.1%) using the ALICE detector. The total number of events for high multiplicity classes is approximately 10^9 events.

In this analysis, both the particle and antiparticle states of $\Lambda(1520)$ and $K^{*0}(892)$ are considered. The signal extraction procedure follows the methodology described in Chapter 4. A high multiplicity trigger is used for the high multiplicity analysis. The signal extraction involves subtracting the normalized mixed-event combinatorial background to isolate the true signal from background noise. For the $K^{*0}(892)$ signal, a Breit-Wigner function is used for fitting, while the residual background is modelled with a third-order polynomial. In the case of the $\Lambda(1520)$ signal, a Voigtian function is employed, and the residual background is fitted with a second-order polynomial.

For both $K^{*0}(892)$ and $\Lambda(1520)$, events are selected based on the vertex z-position ($|v_z| < 10, \text{cm}$) and the use of the kHighMultV0 trigger, which is a high multiplicity trigger for pp collisions. The same event selection criteria as described in Chapter 4 are used to obtain good events. Figure 5.1 shows the event distribution across high multiplicity classes for different datasets used in pp collisions at $\sqrt{s} = 13$ TeV.

5.1.1 Track Selection

The track selection criteria for the high multiplicity-dependent analysis, as shown in Table 5.1, are designed to ensure high-quality tracks for accurate measurements. A transverse momentum cut of $p_{\mathrm{T}} > 0.15\,\mathrm{GeV/c}$ is implemented to maintain uniform TPC reconstruction efficiency, alongside a pseudorapidity requirement of $|\eta| < 0.8$ for optimal detector coverage. To filter out tracks from pileup vertices, a cut of $|\mathrm{DCA}_Z| < 2.0\,\mathrm{cm}$ is applied, along with a transverse impact parameter condition of $|\mathrm{DCA}_{XY}| < (0.0105 + 0.0350/p_T^{1.1})$ to ensure tracks are close to the primary vertex. Refit of tracks in the TPC and ITS

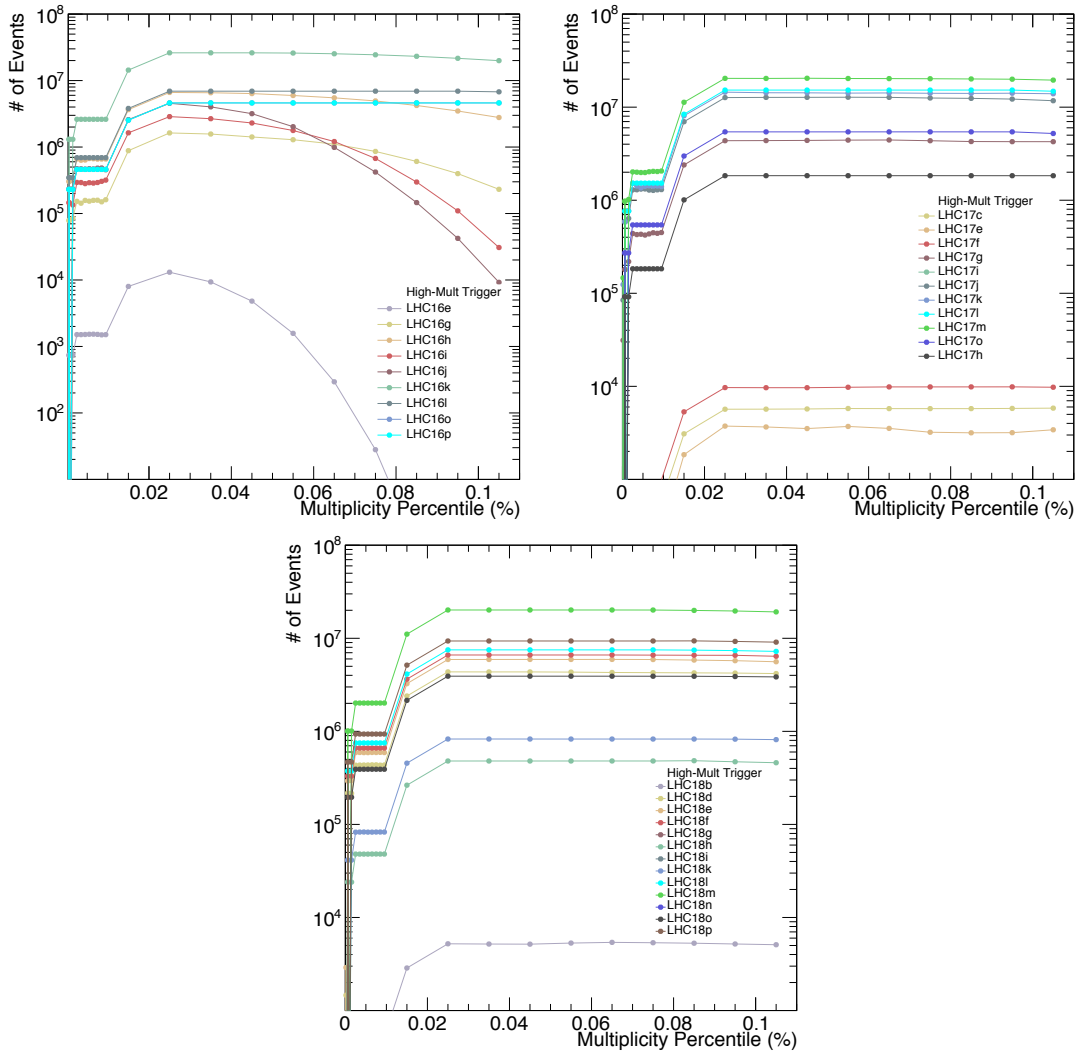

Figure 5.1: The event distribution across high multiplicity classes for different datasets used in pp collisions at $\sqrt{s} = 13$ TeV.

is required for selecting good quality tracks. The track originating from secondary weak decays, known as kink daughters, is rejected. Additionally, at least one cluster in the SPD and more than 70 crossed rows in the TPC are required, with a minimum ratio of crossed rows to findable clusters in the TPC to be ≥ 0.82. The $\chi^2/\mathrm{N_{cluster}}$ criterion is required to be less than 4 for the TPC and less than 36 for the ITS to suppress contamination from poor quality and secondary particle tracks. A pair rapidity cut of $|y_{\mathrm{pair}}| < 0.5$ is imposed to ensure rapidity consistency for the considered pairs of tracks. The reliability of the outcomes of the analysis is collectively enhanced by these aforementioned criteria.

Track Selection	Value
p_{T}	$> 0.15\,\mathrm{GeV}/c$
$\lvert\eta\rvert$	< 0.8
$\lvert\mathrm{DCA}_Z\rvert$	$< 2.0\,\mathrm{cm}$
$\lvert\mathrm{DCA}_{XY}\rvert$	$< (0.0105 + 0.0350/p_T^{1.1})$
TPC and ITS refits	Required
Rejection of kink daughters	Required
Minimum number of clusters in SPD	1
Number of crossed rows in TPC	> 70
R_{TPC}	≥ 0.82
$\chi^2/\mathrm{N}_{\mathrm{cluster}}$ for TPC	< 4
$\chi^2/\mathrm{N}_{\mathrm{cluster}}$ for ITS	< 36
$\lvert y_{\mathrm{pair}}\rvert$	< 0.5

Table 5.1: Track selection criteria for the multiplicity-dependent analysis.

5.1.2 Particle Identification

The particle identification (PID) of the decay daughters of the $\mathrm{K}^{*0}(892)$, specifically kaons and pions, is performed using information from both the TPC and TOF detectors. The TPC measures the specific energy loss (dE/dx), as shown in Figure 5.2. The TOF detector provides precise time-of-flight information, which, when integrated with the TPC data, enhances the accuracy and reliability of particle identification. The selection criteria for Λ daughters is similar to the multiplicity-dependent analysis described in Chapter 4 and the criteria for the $\mathrm{K}^{*0}(892)$ daughters are mentioned in the following table.

nσ cuts	**Value**
$\lvert n\sigma_{\mathrm{TPC}}\rvert$ (Tracks hit only in TPC detector)	< 2.0
$\lvert n\sigma_{\mathrm{TOF}}\rvert$ (Tracks hit both TPC and TOF detector)	< 3.0

Table 5.2: nσ cuts applied for particle identification using TPC and TOF.

5.2 Signal Extraction and Correction

Resonance analysis involves the reconstruction of both particle and antiparticle states of $\Lambda(1520)$ and $\mathrm{K}^{*0}(892)$. The signal extraction method for high multiplicity analysis is

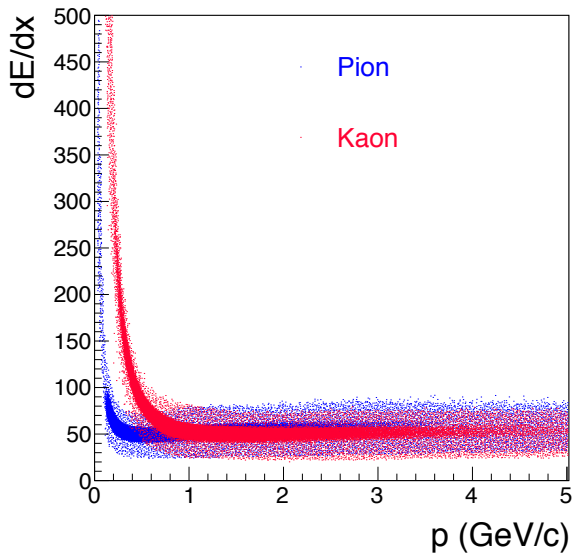

Figure 5.2: TPC specific energy loss (dE/dx) of selected kaons and pions as a function of momentum in pp collisions at $\sqrt{s} = 13$ TeV.

similar to that outlined in Chapter 4.

For $\Lambda(1520)$, the yield is estimated across 13 p_{T} bins, ranging from 0.4 to 6.0 GeV/c except for 0-0.01% multiplicity class. The invariant mass distribution of pK pairs ($p^{\pm}K^{\mp}$)in different high multiplicity classes are shown in Figure 5.4, 5.5, and 5.6.

For the $K^{*0}(892)$ resonance, the signal extraction process is similar to that of $\Lambda(1520)$. The raw yield of $K^{*0}(892)$ is determined across 14 p_T bins, from 0.0 to 10.0 GeV/c. The $K^{*0}(892)$ meson, decaying into πK pairs is reconstructed. The combinatorial background is estimated using the event-mixing technique. This background is normalized in the mass range of 1.1 to 1.2 GeV/c^2 and is subsequently subtracted from the same-event distribution. The residual background is modelled with a third-order polynomial, while the $K^{*0}(892)$ signal peak is described using the sum of the Breit-Wigner function and third-order polynomial. The Breit-Wigner function is defined as follows:

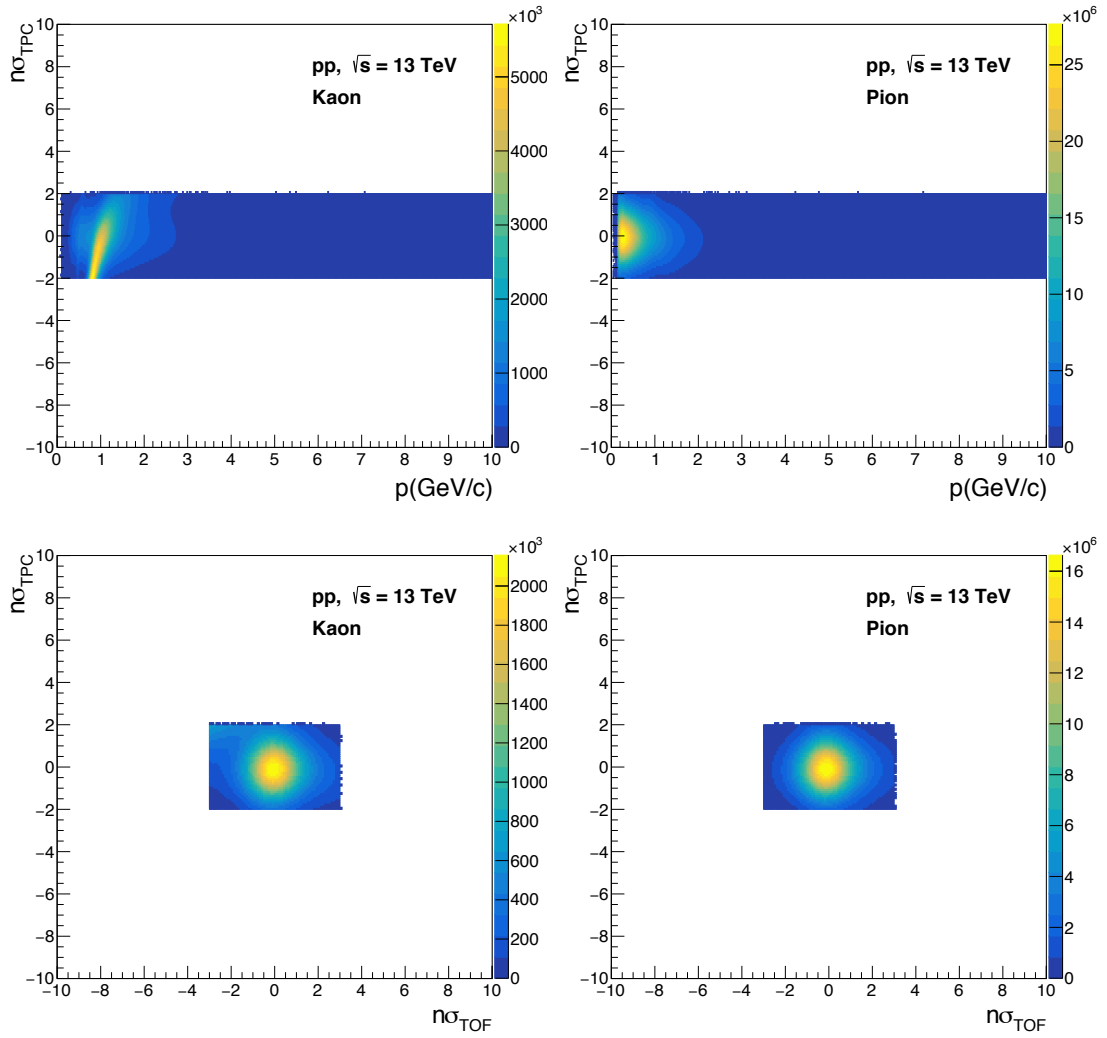

Figure 5.3: The upper panels show the nσ distribution of kaons and pions when tracks are present only in the TPC, while the lower panels show the distribution when tracks are present in both the TPC and TOF.

$$BW(M_{\pi\mathrm{K}}) = \frac{A \cdot \Gamma}{(M_{\pi\mathrm{K}}^2 - m_0^2)^2 + m_0^2\Gamma^2} \tag{5.1}$$

The parameters involved in the Breit-Wigner function for the $\mathrm{K}^{*0}(892)$ resonance include A, which is the normalization factor; $M_{\pi\mathrm{K}}$, representing the invariant mass of the $\pi\mathrm{K}$ pairs; m_0, denoting the mass of the $\mathrm{K}^{*0}(892)$ resonance; and Γ, which indicates the

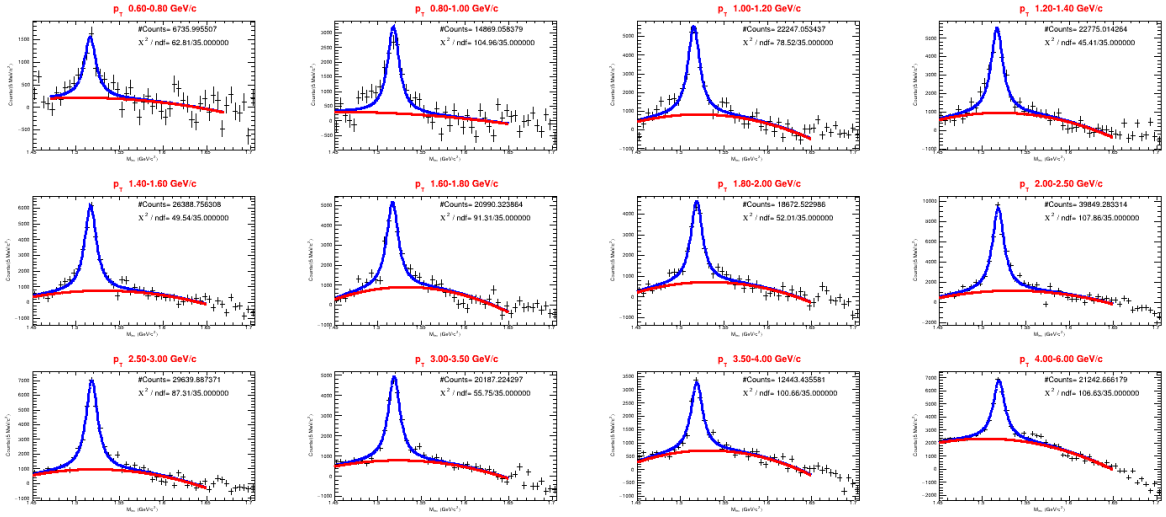

Figure 5.4: The invariant mass distribution of pK pairs for $0 - 0.01\%$ high multiplicity class in pp collisions at $\sqrt{s} = 13$ TeV for different p_{T} bins after subtracting the normalized mixed-event background distribution.

width of the resonance.

The invariant mass distribution of πK pairs in different high multiplicity classes are shown in Figure 5.7, 5.8, and 5.9.

The raw yield is estimated by using the bin counting method as described in Chapter 4. Figure 5.10 and 5.11 show the raw yield as a function of p_T for $\Lambda(1520)$ and $K^{*0}(892)$ respectively in high multiplicity pp collisions at $\sqrt{s} = 13$ TeV. The estimation from the function integral method is also shown in the figure.

For $\Lambda(1520)$, various correction factors are applied to account for experimental effects, to obtain the corrected yield. The minimum bias efficiency factor is used to correct the raw yield in high multiplicity classes. As the efficiency was observed to be independent of multiplicity %. The trigger and vertex efficiency correction factors are set to one while the f_{SL} factor was kept similar to that obtained from the minimum bias $\Lambda(1520)$ analysis.

For $K^{*0}(1520)$ the trigger and vertex efficiency correction factors are set to one while

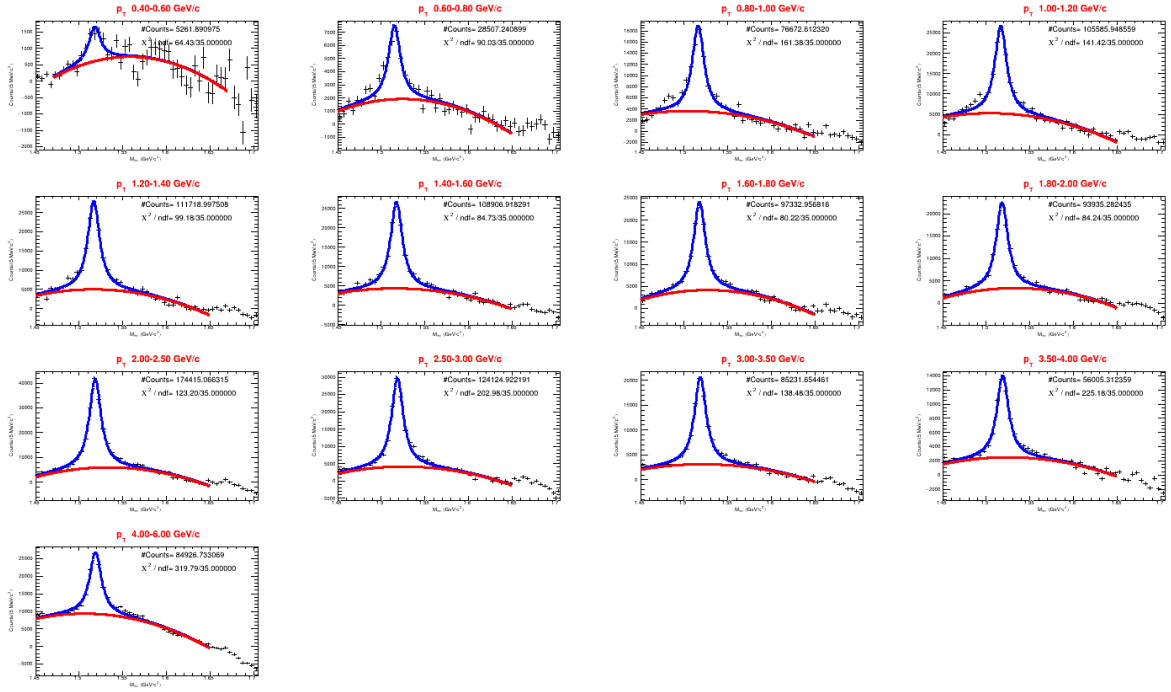

Figure 5.5: The invariant mass distribution of pK pairs for $0.01-0.05\%$ high multiplicity class in pp collisions at $\sqrt{s} = 13$ TeV for different p_{T} bins after subtracting the normalized mixed-event background distribution.

the f_{SL} factor is not considered. The variation of reconstruction efficiency estimated for different multiplicity classes are shown in Figure 5.12. The efficiency correction factor specific to each multiplicity class is applied to correct the raw yield.

5.3 Systematic Uncertainty

The systematic uncertainty estimation procedure is described in Chapter 4. The total systematic uncertainties, after the smoothing procedure, for different multiplicity classes are shown in Figure 5.13 for $\Lambda(1520)$. This figure illustrates the total fractional uncertainty arising from various sources, with the grey shaded area indicating the total statistical uncertainty for $\Lambda(1520)$ in high multiplicity pp collisions at $\sqrt{s} = 13$ TeV.

The total p_{T}-integrated yield is computed as $\frac{dN_{\mathrm{low}}}{dy} + \frac{dN_{\mathrm{data}}}{dy} + \frac{dN_{\mathrm{high}}}{dy}$ for each fitting function. Additionally, the systematic uncertainty for the average transverse momentum

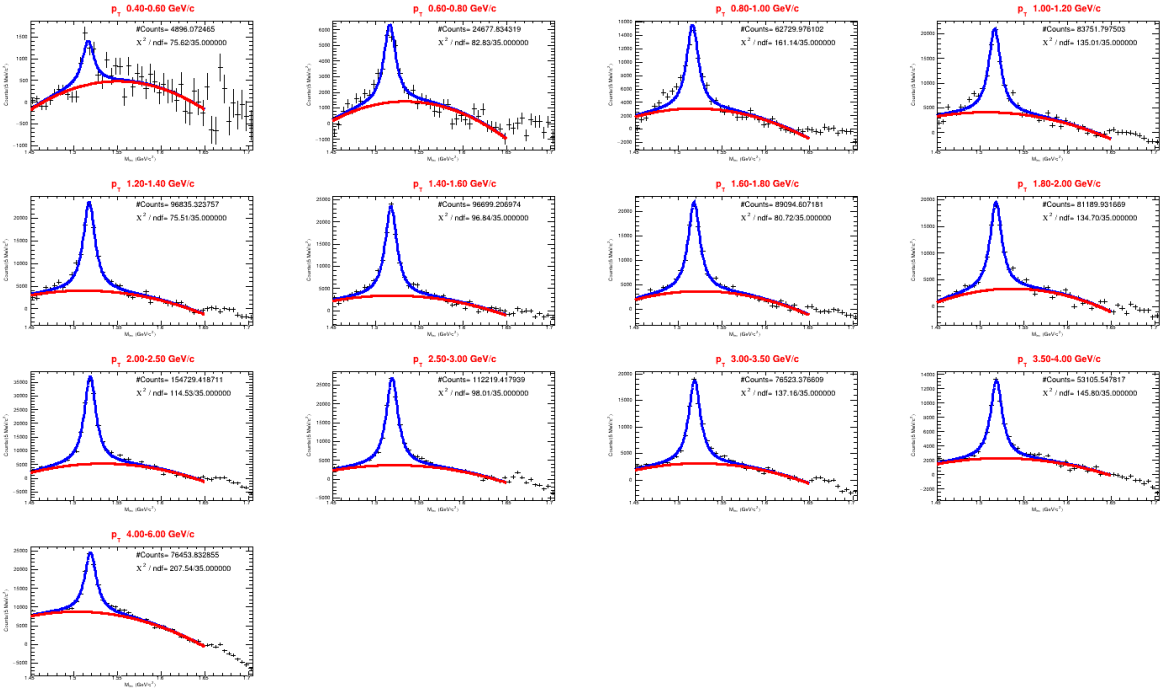

Figure 5.6: The invariant mass distribution of pK pairs for $0.05 - 0.1\%$ high multiplicity class in pp collisions at $\sqrt{s} = 13$ TeV for different p_{T} bins after subtracting the normalized mixed-event background distribution.

$\langle p_{\mathrm{T}} \rangle$ is estimated using a similar approach as described in Chapter 4. The systematic uncertainty of $K^{*0}(892)$ for 0-1% multiplicity class is used for other high multiplicity classes [65].

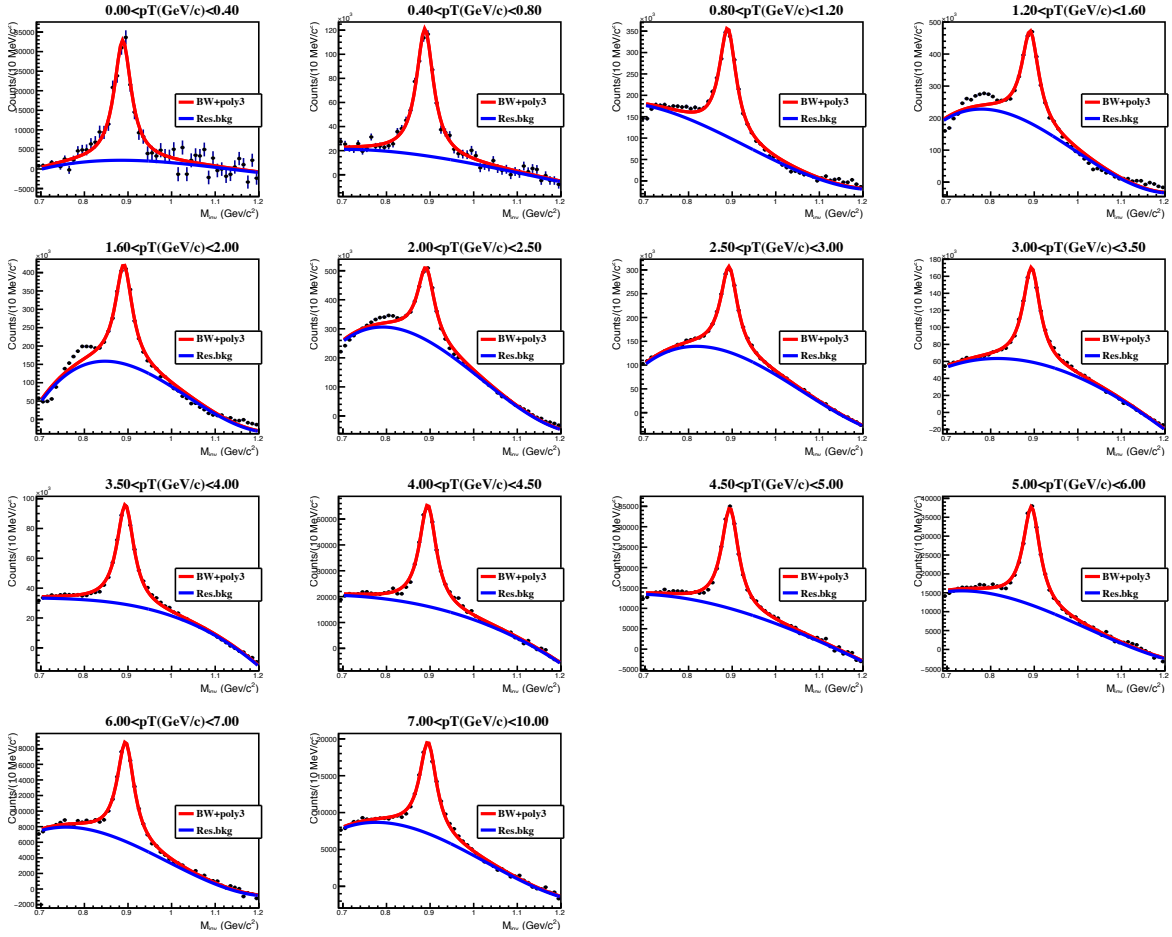

Figure 5.7: The invariant mass distribution of πK pairs for $0-0.01\%$ multiplicity class in pp collisions at $\sqrt{s}$ = 13 TeV for different p_{T} bins after subtracting the normalized mixed-event background distribution.

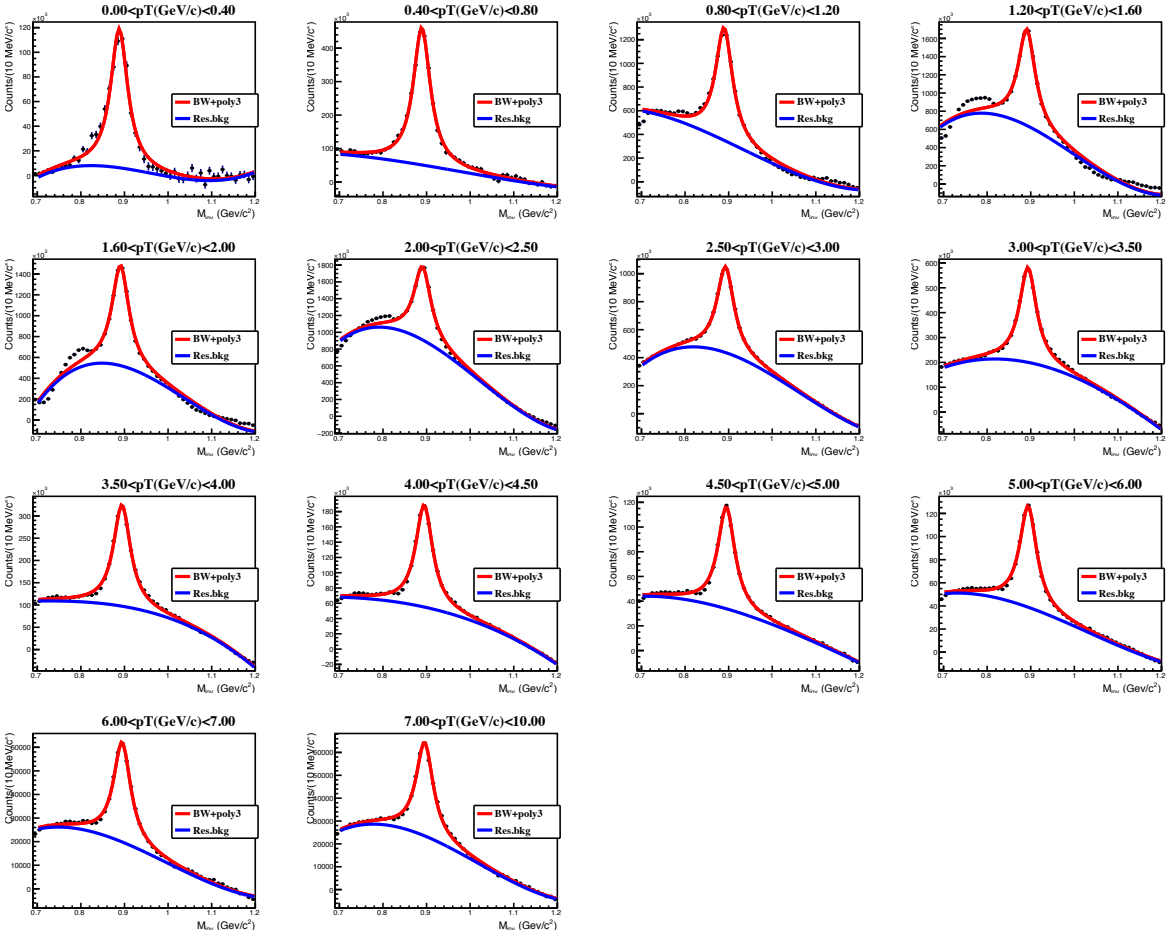

Figure 5.8: The invariant mass distribution of πK pairs for $0.01-0.05\%$ multiplicity class in pp collisions at $\sqrt{s} = 13$ TeV for different p_{T} bins after subtracting the normalized mixed-event background distribution.

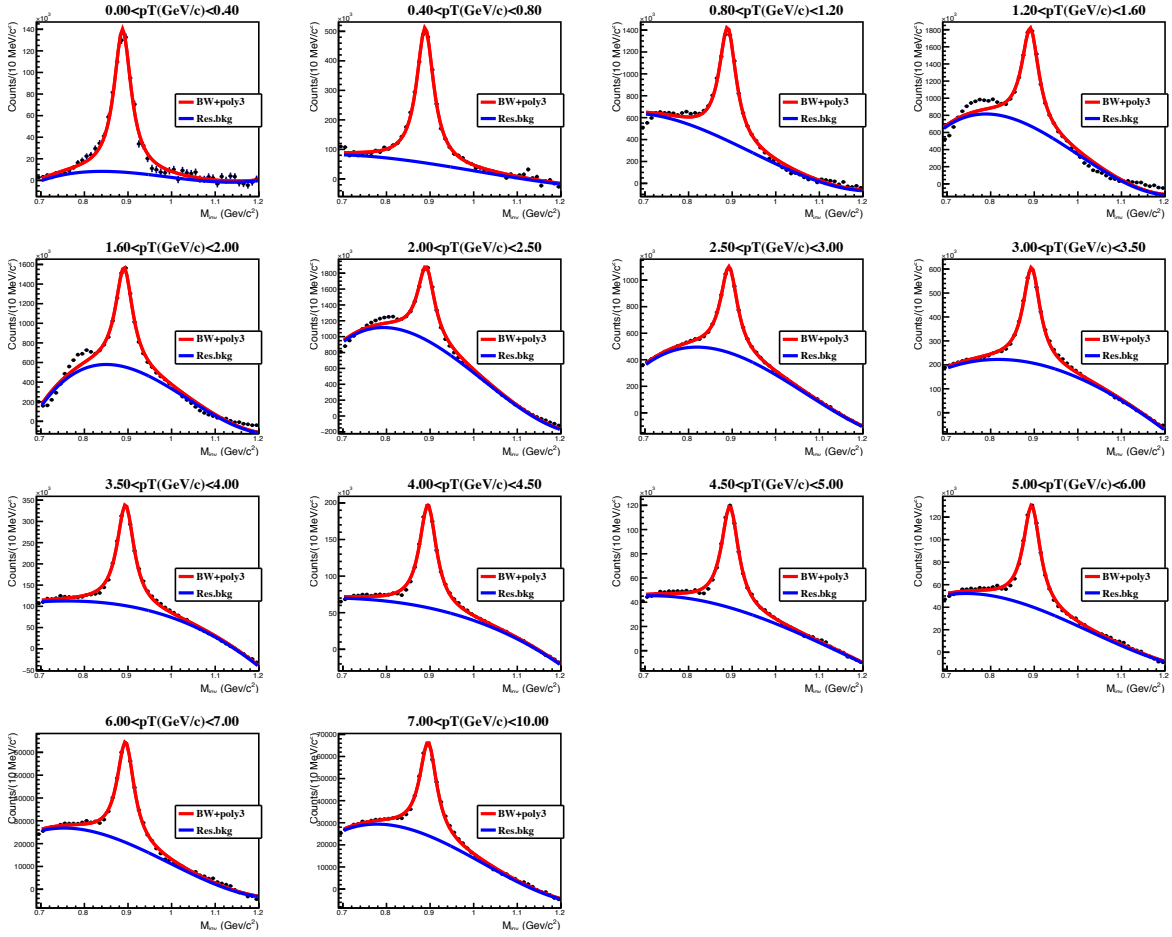

Figure 5.9: The invariant mass distribution of πK pairs for $0.05-0.1\%$ multiplicity class in pp collisions at $\sqrt{s}$ = 13 TeV for different p_{T} bins after subtracting the normalized mixed-event background distribution.

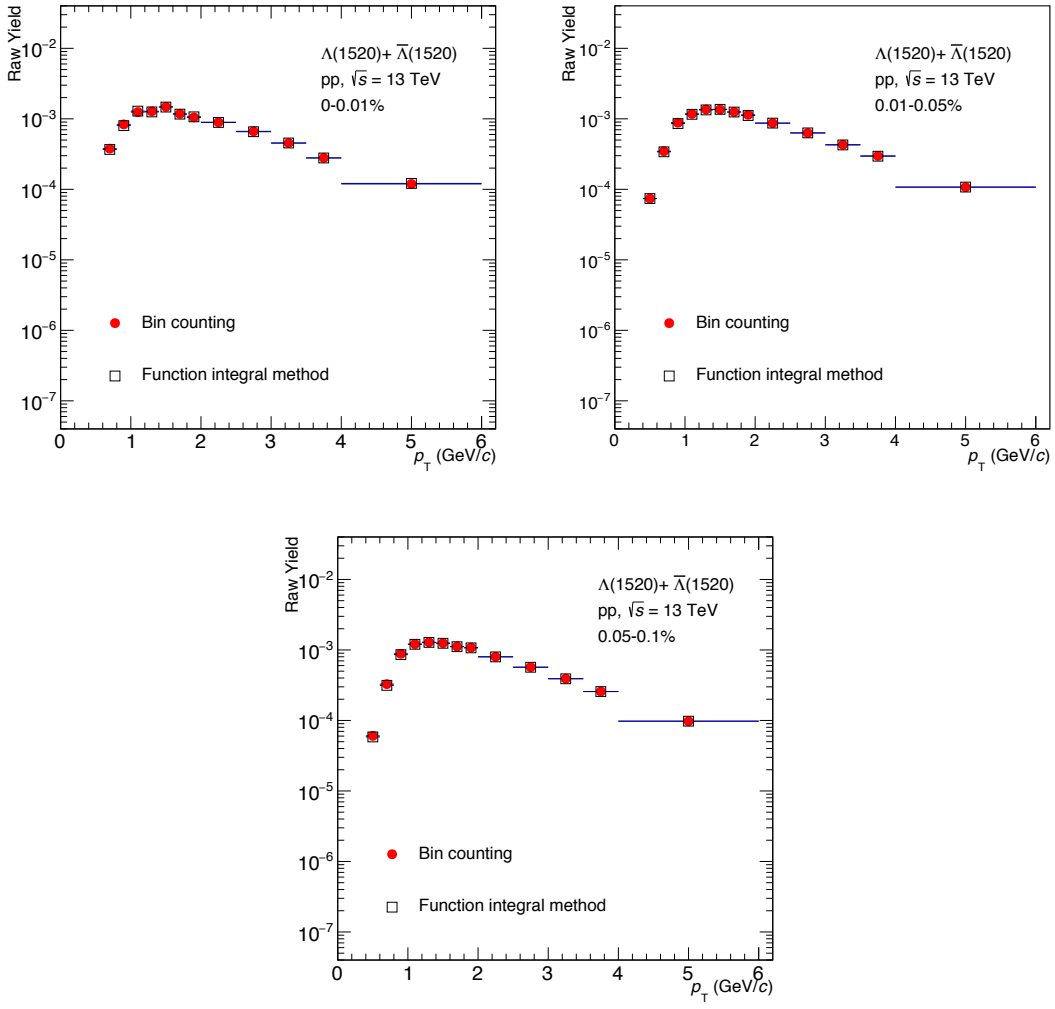

Figure 5.10: The raw yield estimated by Function Integral and Bin Counting methods for different high multiplicity classes (0 - 0.01% (upper left), 0.01 - 0.05% (upper right), and 0.05 - 0.1% (bottom)) of $\Lambda(1520)$ in pp collisions at $\sqrt{s} = 13$ TeV.

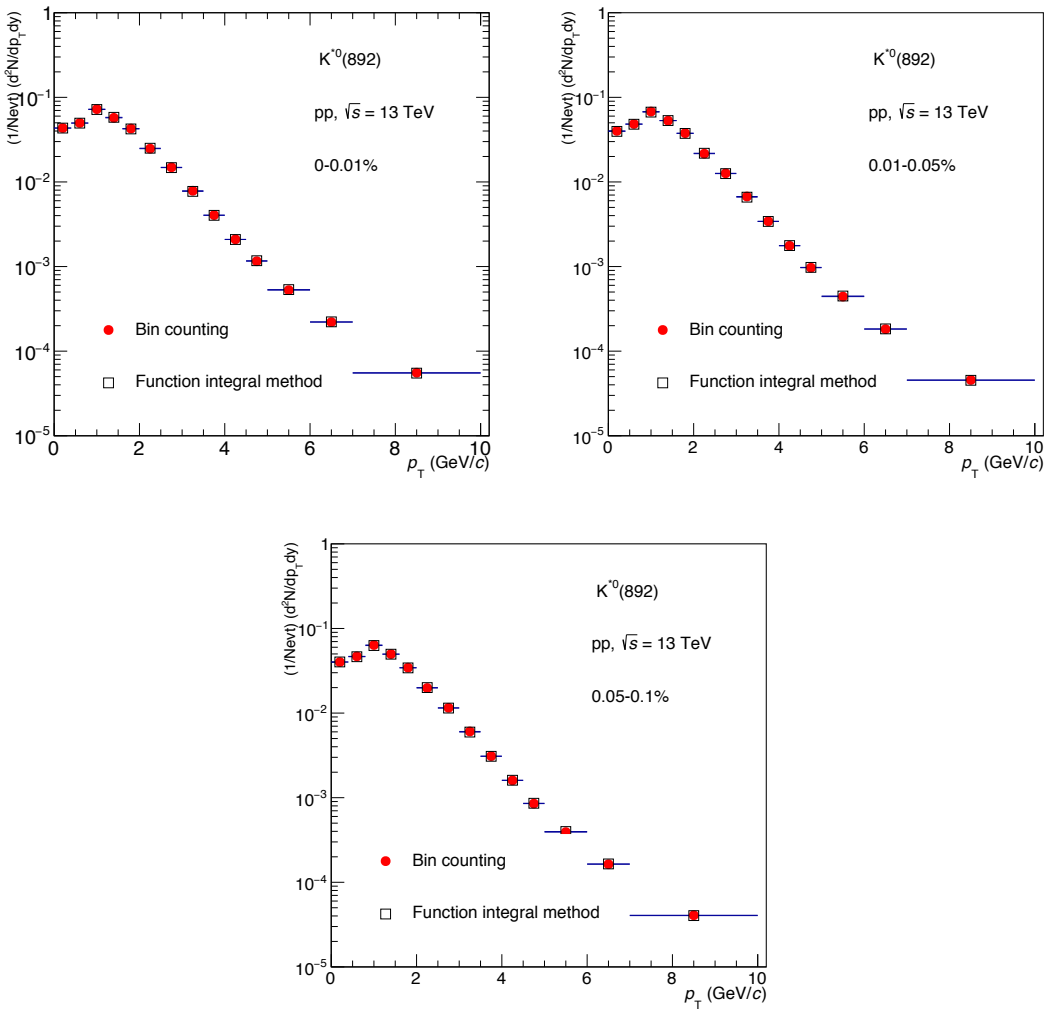

Figure 5.11: The raw yield estimated by Function Integral and Bin Counting methods for different high multiplicity classes of $K^{*0}(892)$ in pp collisions at $\sqrt{s} = 13$ TeV.

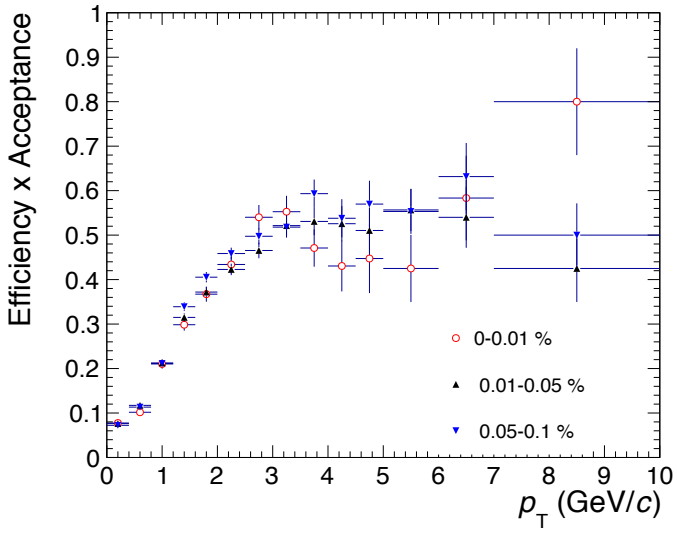

Figure 5.12: Efficiency and acceptance for $K^{*0}(1520)$ in high multiplicity pp collisions at $\sqrt{s} = 13$ TeV.

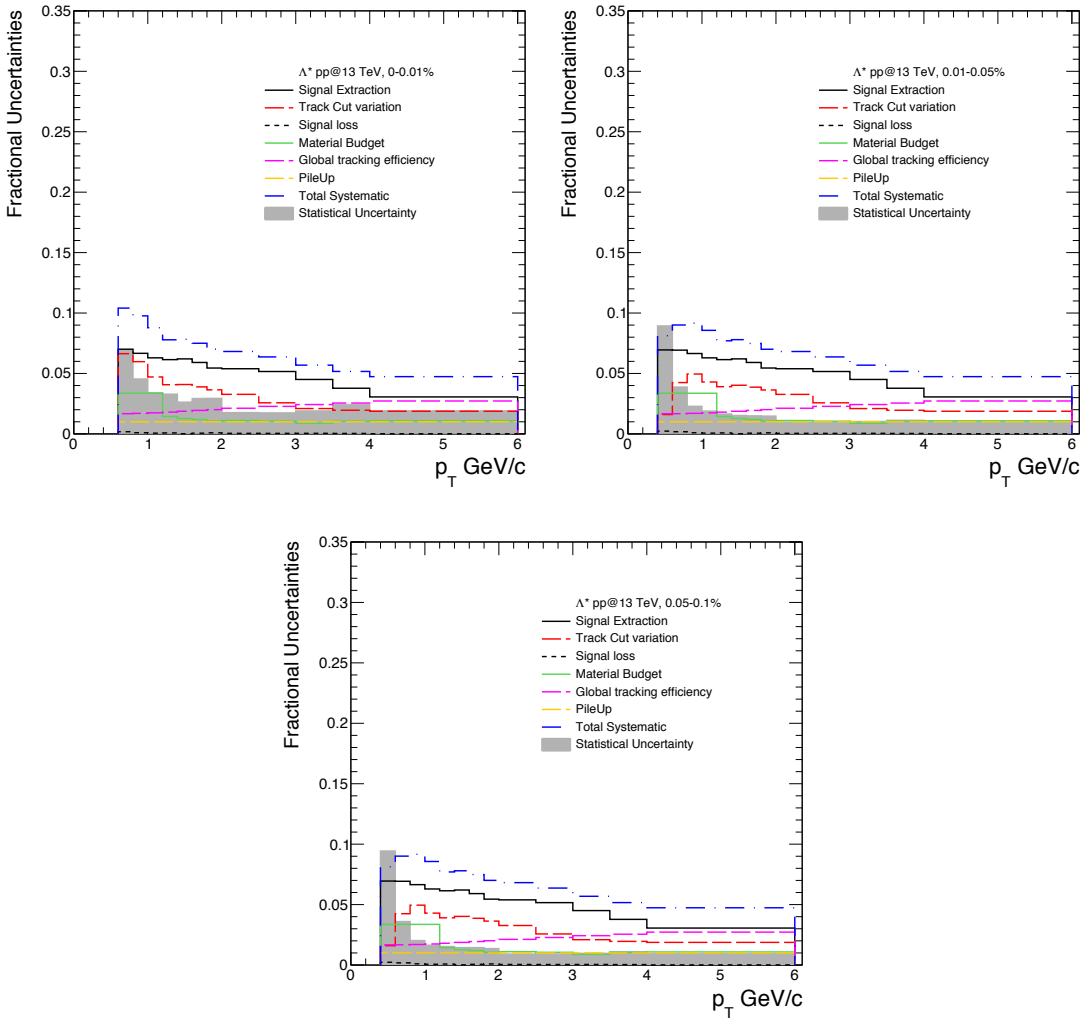

Figure 5.13: Total fractional uncertainty due to various sources. The grey shaded area shows the total statistical uncertainty for $\Lambda(1520)$ in high multiplicity pp collisions at $\sqrt{s} = 13$ TeV.

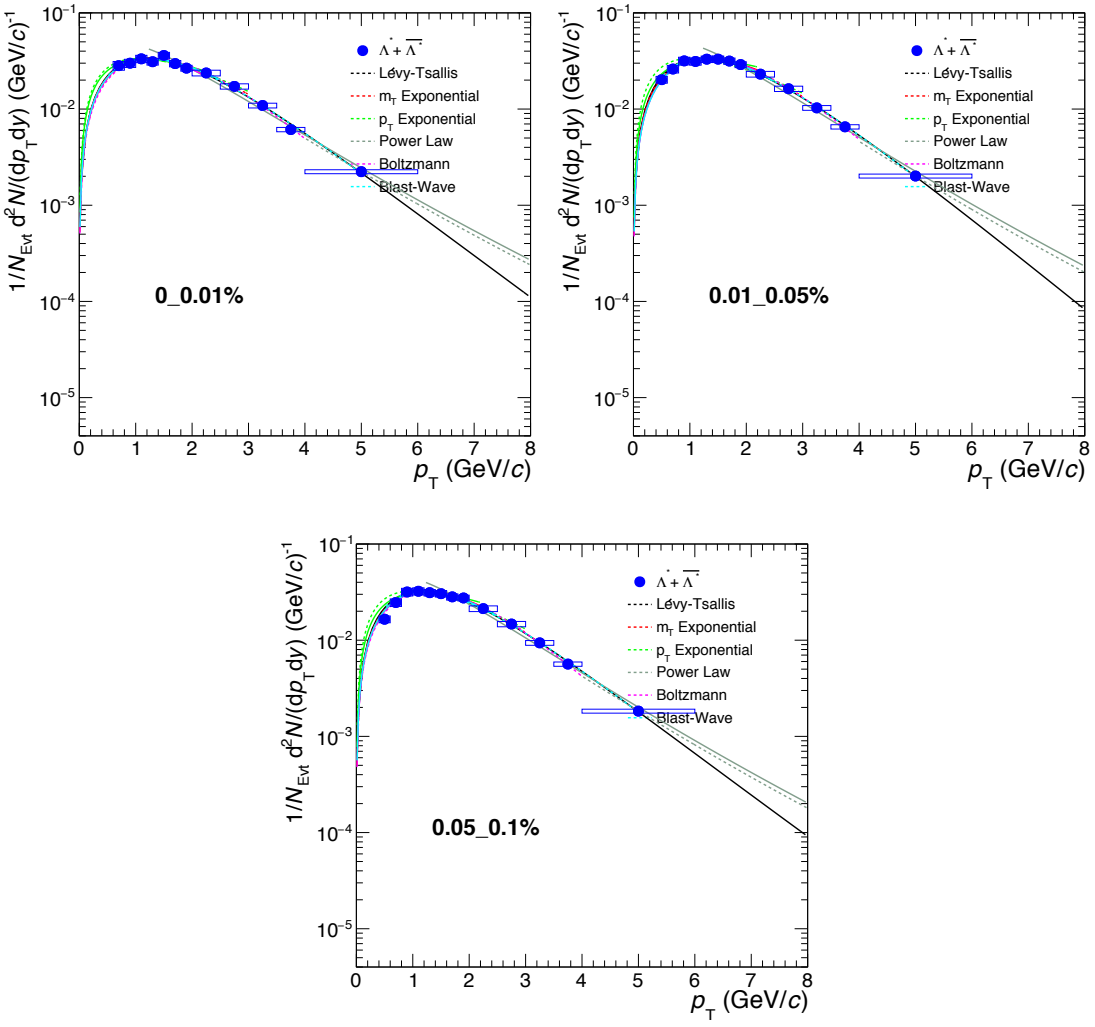

Figure 5.14: Measured $\Lambda(1520)$ in low and high p_{T} extrapolated region in high multiplicity pp collisions at $\sqrt{s}$ =13 TeV. The lines represent the m_{T}-exponential, p_{T}-exponential, Boltzmann, Blast-Wave, Power law, and Levy-Tsallis functions fit.

Chapter 6

Results

In this chapter, the results of the analysis related to the measurement of $\Lambda(1520)$ resonance production across various multiplicity classes, as well as $K^{*0}(892)$ and $\Lambda(1520)$ in high multiplicity (HM) events, are described. This includes the transverse momentum spectra, p_{T}-integrated yields ($\langle \mathrm{dN/dy} \rangle$), mean transverse momentum ($\langle p_{\mathrm{T}} \rangle$), and particle yield ratios. Detailed discussions of the results are provided in the following sections.

6.1 Transverse Momentum Spectra

The corrected spectra, or p_{T}-differential yield, are calculated using the following equation:

$$\frac{d^2N}{dp_{\mathrm{T}}dy} = \frac{1}{BR \times N_{\mathrm{ev}}} \cdot \frac{Y_{\mathrm{raw}}}{dp_{\mathrm{T}}dy} \cdot \frac{f_{\mathrm{SL}} \cdot f_{\mathrm{vtx}} \cdot f_{\mathrm{trig}}}{\epsilon_{\mathrm{res}}} \tag{6.1}$$

where the yield is normalized by the number of events (N_{ev}) and corrected for the branching ratio (BR). The factors f_{SL}, f_{vtx}, and f_{trig} account for the signal loss correction, vertex efficiency correction, and trigger efficiency correction factor, respectively. Additionally, ϵ_{res} is the reweighted efficiency correction factor used to account for detector effects.

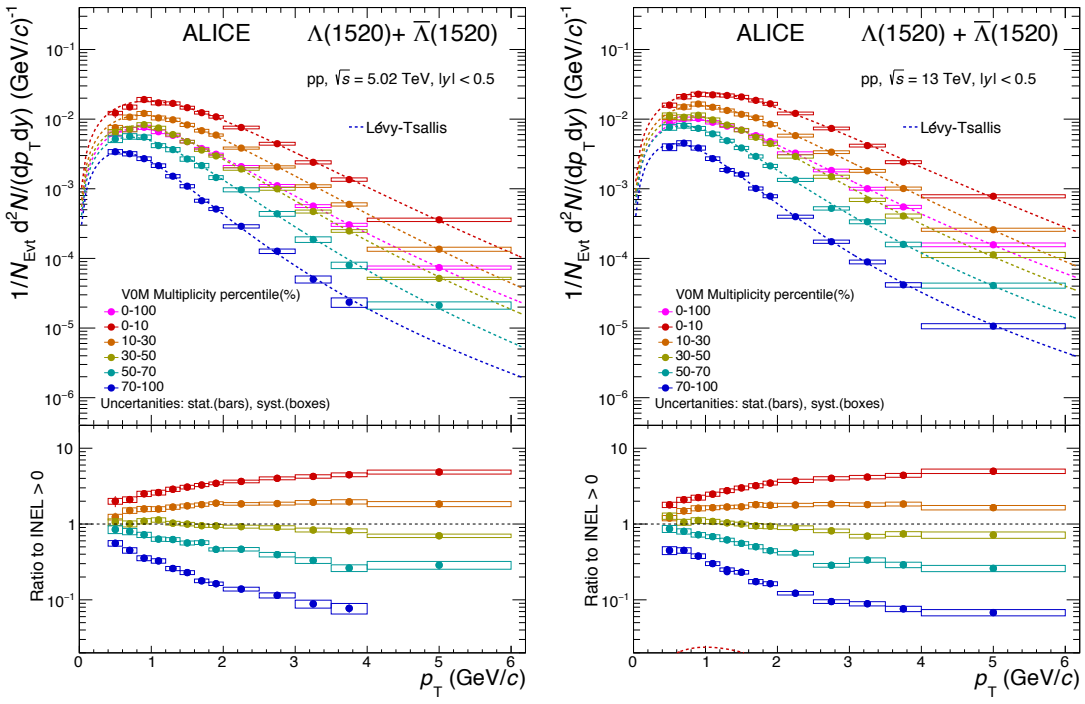

Figure 6.1: Transverse momentum spectra of $\Lambda(1520)$ measured in pp collisions at $\sqrt{s} =$ 5.02 TeV (left panel) and 13 TeV (right panel) in different multiplicity classes. The bottom panel illustrates the ratio of the spectra in different multiplicity classes to that in the 0-100% event class. The boxes represent systematic uncertainties, while the error bars indicate statistical uncertainties.

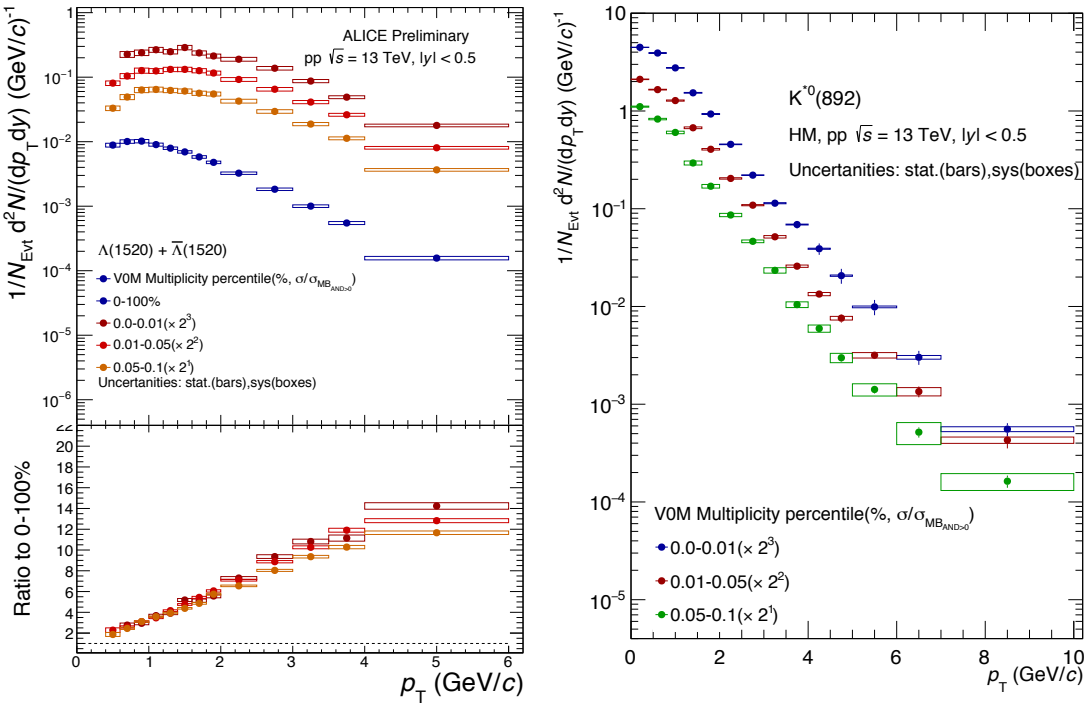

Figure 6.2: Transverse momentum spectra of Λ(1520) and K^{*0}(892) measured in high multiplicity pp collisions at $\sqrt{s}$ = 13 TeV in different high multiplicity classes. The bottom panel illustrates the ratio of the spectra in different multiplicity classes to that in the 0-100% event class. The boxes represent systematic uncertainties, while the error bars indicate statistical uncertainties.

Correcting the p_{T}-differential yield of resonances like $\Lambda(1520)$ is essential to ensure that the measured yields accurately reflect the true particle production, enabling precise comparisons across multiplicity classes and collision systems.

The transverse momentum spectra of the $\Lambda(1520)$ resonance in the various multiplicity classes in pp collisions at $\sqrt{s} = 5.02$ TeV (left panel) and 13 TeV (right panel) are shown in Figure 6.1. The bottom panel shows the ratio of the spectra in different multiplicity classes to the spectrum of $0 - 100\%$ multiplicity. Figure 6.2 shows the p_{T} spectra of $\Lambda(1520)$ and $\mathrm{K}^{*0}(892)$ for different multiplicity classes in high multiplicity pp collisions at $\sqrt{s} = 13$ TeV. The boxes represent the systematic uncertainty while error bars indicate statistical uncertainties in both of the figures. A clear hardening of the spectra is observed when going from low to high multiplicity classes. This trend signifies an augmentation of high-p_{T} particle production in higher multiplicity classes in comparison to minimum bias events.

6.2 The p_{T}-Integrated Yield ($\langle \mathrm{d}N/\mathrm{d}y \rangle$)

After fitting and extrapolating the spectrum, the particle yield ($\langle dN/dy \rangle$) and $\langle p_{\mathrm{T}} \rangle$ are calculated. To estimate $\langle dN/dy \rangle$, the spectrum is integrated over the entire p_{T} range, including both the measured and extrapolated regions.

In each of these multiplicity classes, the yield of $\Lambda(1520)$ is extrapolated to the unmeasured low p_{T} region ($p_{\mathrm{T}} < 0.4$ GeV/c) by fitting a Lévy-Tsallis function to the measured p_{T} spectra. Uncertainties in $\langle \mathrm{d}N/\mathrm{d}y \rangle$ are estimated considering different fit ranges and choices of fit functions, including an m_T-exponential function, p_{T}- exponential, a Boltzmann distribution, and a power-law function. The systematic uncertainty has two contributions: one coming from systematic uncertainties of spectra and the second from the extrapolation of spectra in the unmeasured regions. The systematic uncertainty due to extrapolation of spectra is obtained for the considered fit functions and estimated by calculating the quadrature sum of the standard deviation for all the fit functions.

The p_{T}-integrated yields ($\langle \mathrm{d}N/\mathrm{d}y \rangle$) are determined for various multiplicity classes, as shown in Figure 6.3. In this, figure the p_{T} integrated yield of $\Lambda(1520)$ is shown as a function of average charged-particle multiplicity density ($\langle dN_{\mathrm{ch}}/d\eta \rangle|_{|\eta|<0.5}$) in pp collisions at $\sqrt{s} = 5.02$ TeV and 13 TeV. The boxes represent systematic uncertainties, while the error bars indicate statistical uncertainties.

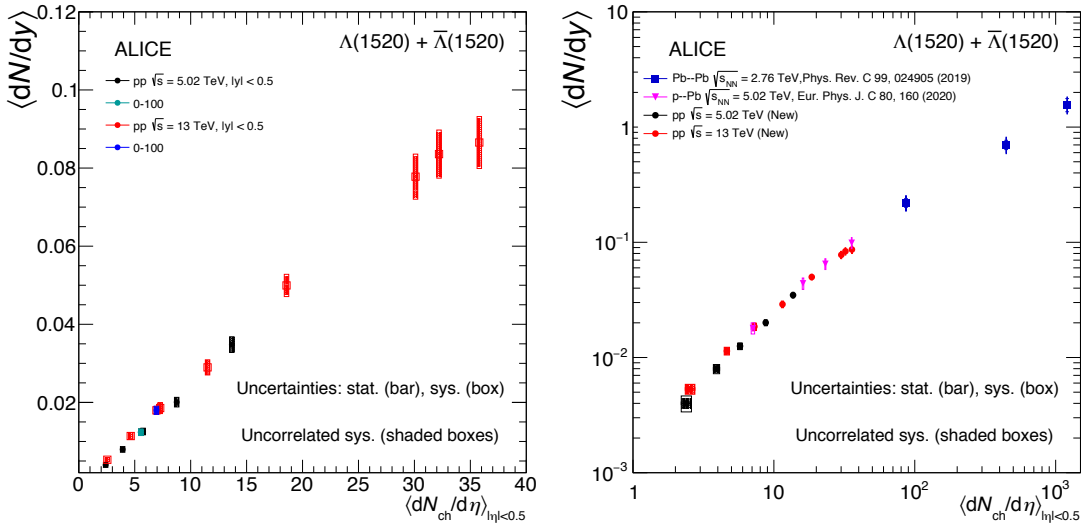

Figure 6.3: The p_{T} integrated yield of $\Lambda(1520)$ as a function of average charged-particle multiplicity density ($\langle dN_{\mathrm{ch}}/d\eta \rangle|_{|\eta|<0.5}$) in pp collisions at $\sqrt{s} = 5.02$ TeV and 13 TeV. The right panel shows the same for different collisions system. The boxes represent systematic uncertainties, while the error bars indicate statistical uncertainties.

The right panel of Figure 6.3 shows the comparison of the same for different collision systems at various energies [64, 66]. It can be observed that the $\langle dN/dy \rangle$ increases with increasing multiplicity. This trend is consistent across different collision systems and energies, suggesting that the production rate of $\Lambda(1520)$ is largely driven by multiplicity (or event activity) rather than the specific collision system or energy.

6.3 Mean Transverse Momentum ($\langle p_{\mathrm{T}} \rangle$)

The $\langle p_{\mathrm{T}} \rangle$ is estimated by using the following expression:

$$\langle p_{\mathrm{T}} \rangle = \frac{\int p_{\mathrm{T}} \frac{dN}{dp_{\mathrm{T}}} dp_{\mathrm{T}}}{\int \frac{dN}{dp_{\mathrm{T}}} dp_{\mathrm{T}}} \tag{6.2}$$

The variation of ($\langle p_{\mathrm{T}} \rangle$) as a function of $\langle dN_{\mathrm{ch}}/d\eta \rangle|_{|\eta|<0.5}$ is shown in Figure 6.4. The uncertainties in $\langle p_{\mathrm{T}} \rangle$ are assessed by considering variations in the fitting procedure and extrapolation methods.

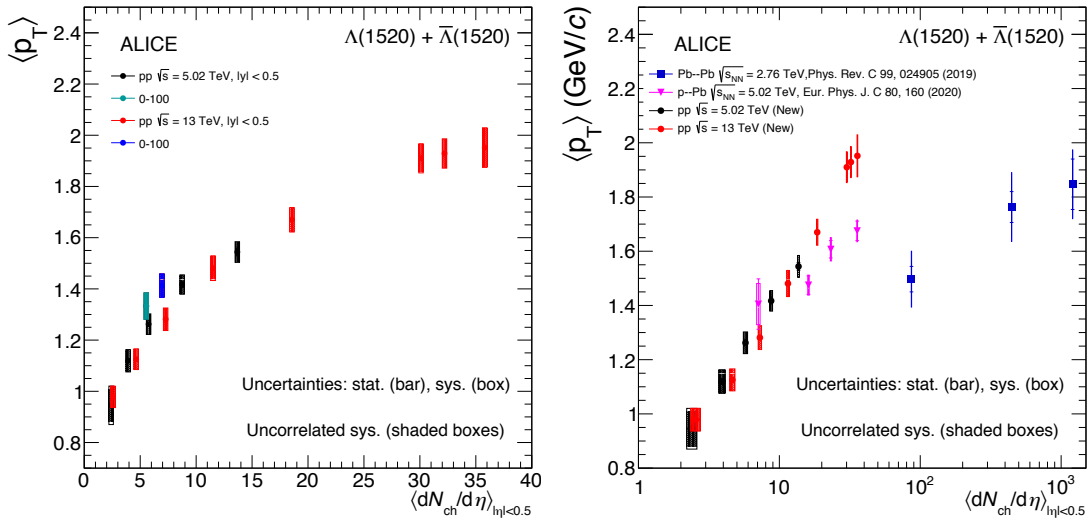

Figure 6.4: The ($\langle p_{\mathrm{T}} \rangle$) of $\Lambda(1520)$ as a function of $\langle dN_{\mathrm{ch}}/d\eta \rangle|_{|\eta|<0.5}$ in pp collisions at $\sqrt{s} = 5.02$ TeV and 13 TeV. The right panel shows the same for different collisions system. The boxes represent systematic uncertainties, while the error bars indicate statistical uncertainties.

It is observed that the $\langle p_{\mathrm{T}} \rangle$ increases with increase in $\langle dN_{\mathrm{ch}}/d\eta \rangle|_{|\eta|<0.5}$ and there is no significant energy dependence. The right panel of the figure shows the comparison of $\langle p_{\mathrm{T}} \rangle$ for different collisions systems at different energies. Notably, the slope of the $\langle p_{\mathrm{T}} \rangle$ trend in pp collisions is steeper than that observed in p–Pb collisions and considerably greater than that of Pb–Pb collisions. The observed differences in Pb–Pb collisions could be attributed to rescattering effect of the decay daughters in the dense medium created in heavy-ion collisions. Additionally, the suppression of high-p_{T} $\Lambda(1520)$ resonances can be associated to jet-quenching effects.

In Figure 6.5, the $\langle p_{\mathrm{T}} \rangle$ values for $\Lambda(1520)$ are compared with those of other particles such as K^{*0}, ϕ, $\Lambda + \bar{\Lambda}$, $\Xi^- + \Xi^+$, $\Omega^- + \Omega^+$, and protons, measured in pp collisions at $\sqrt{s} = 13$ TeV. A consistent increase in $\langle p_{\mathrm{T}} \rangle$ is observed with rising $\langle dN_{\mathrm{ch}}/d\eta \rangle|_{|\eta|<0.5}$ for all particles.

In central A–A collisions, a phenomenon known as mass ordering is evident, where particles of similar mass exhibit comparable $\langle p_{\mathrm{T}} \rangle$ values [25, 53]. This mass ordering is believed to arise from radial flow effects, which significantly influence the hadron p_{T} spectra in these collisions. However, this effect is less pronounced in peripheral Pb–Pb collisions, as well as in p–Pb and pp collisions, where such ordering is not observed.

In proton-proton collisions at $\sqrt{s} = 13$ TeV, notable differences emerge in the $\langle p_T \rangle$ values between baryons and mesons. For instance, the ϕ resonance, despite having a mass comparable to that of protons, exhibits a higher $\langle p_T \rangle$. Similarly, the K^{*0} resonance shows higher $\langle p_T \rangle$ values than both protons and Λ particles. Furthermore, the $\langle p_T \rangle$ for the ϕ resonance surpasses that of the Λ and approaches the values observed for $\Xi^{\pm}$, even though the mass of the ϕ is about 30% lower than that of the $\Xi^{\pm}$. Although $\Omega^{\pm}$ is heavier than $\Lambda(1520)$, the $\langle p_T \rangle$ values of $\Lambda(1520)$ are comparable within the uncertainty. These differences imply that there may be fundamental distinctions in the p_{T} spectra of mesons and baryons as well as for resonance particles, potentially arising from fragmentation effects at high p_T or m_T [25–27].

6.4 Resonance to Stable Particle Yield Ratios

The resonance to stable particle ratios serve as sensitive probes of the thermal and dynamic properties of the hadronic phase. These ratios in the presence of a medium are significantly influenced by rescattering effects, where hadronic resonances interact within the medium. Such interactions can diminish the observed abundance of resonances. Analyzing these ratios provides crucial insights into the properties and dynamics of the hadronic phase in heavy-ion collisions.

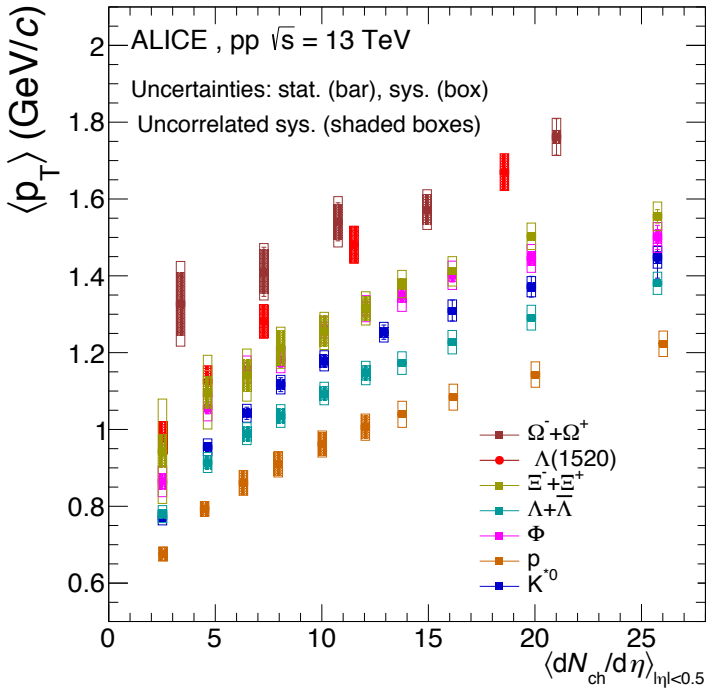

Figure 6.5: The $\langle p_T \rangle$ for $\Lambda(1520)$ is compared with those for K^{*0}, ϕ, $\Lambda + \bar{\Lambda}$, $\Xi^- + \Xi^+$, and $\Omega^- + \Omega^+$ and protons in pp collisions at $\sqrt{s} = 13$ TeV as a function of $\langle dN_{\mathrm{ch}}/d\eta \rangle|_{|\eta|<0.5}$, The boxes represent systematic uncertainties, while the error bars indicate statistical uncertainties [25–27].

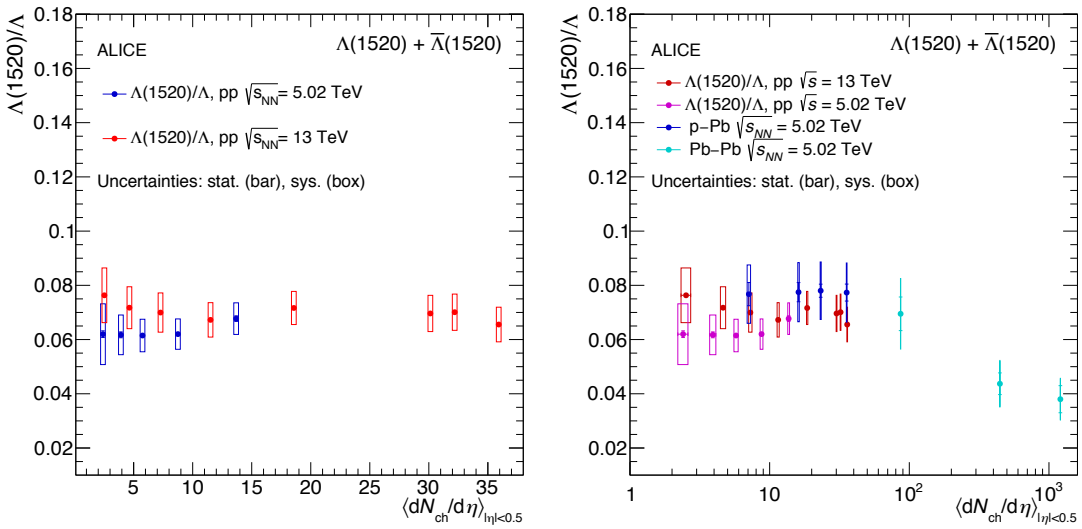

Figure 6.6: Left panel shows $\Lambda(1520)/\Lambda$ yield ratio as a function of $\langle dN_{\rm ch}/d\eta\rangle|_{|\eta|<0.5}$ in pp collisions at $\sqrt{s} = 5.02$ and 13 TeV. The error bars indicate statistical uncertainties, while the boxes represent systematic uncertainties. Shaded boxes denote uncorrelated systematic errors. Additionally, the right panel shows the comparison with various collision systems and energy [64, 66].

A slight decrease in the $\rm K^{*0}/K^{\pm}$ ratio is observed with increasing $\langle dN{\rm ch}/d\eta\rangle_{|\eta|<0.5}$ in all three pp, p–Pb and Pb–Pb collision systems. In contrast, the $\phi/\rm K^{\pm}$ ratio remains relatively constant as a function of $\langle dN{\rm ch}/d\eta\rangle_{|\eta|<0.5}$ in the three collisions system [52, 65]. Since $\Lambda(1520)$ has a lifetime which lies in between the values for $\rm K^{*0}(892)$ and ϕ resonances, it is particularly interesting to investigate the behaviour of the $\Lambda(1520)/\Lambda$ ratio in pp collisions.

In Figure 6.6 shows the variation of $\Lambda(1520)/\Lambda$ as a function of $\langle dN_{\rm ch}/d\eta\rangle|_{|\eta|<0.5}$ in pp collisions at $\sqrt{s} = 5.02$ and 13 TeV. The right panel of the figure include the measurements from p–Pb and Pb–Pb collisions.

It can be observed that the ratio remains relatively constant with $\langle dN_{\rm ch}/d\eta\rangle|_{|\eta|<0.5}$ when transitioning from small to large collision systems, up to an approximate value of $\langle dN_{\rm ch}/d\eta\rangle|_{|\eta|<0.5} = 100$. However, for larger multiplicity values, a notable suppression is observed in Pb–Pb system. This suppression is attributed to the prevalence of rescattering effects involving the decay products of $\Lambda(1520)$, overshadowing the regeneration effect

within the hadronic phase.

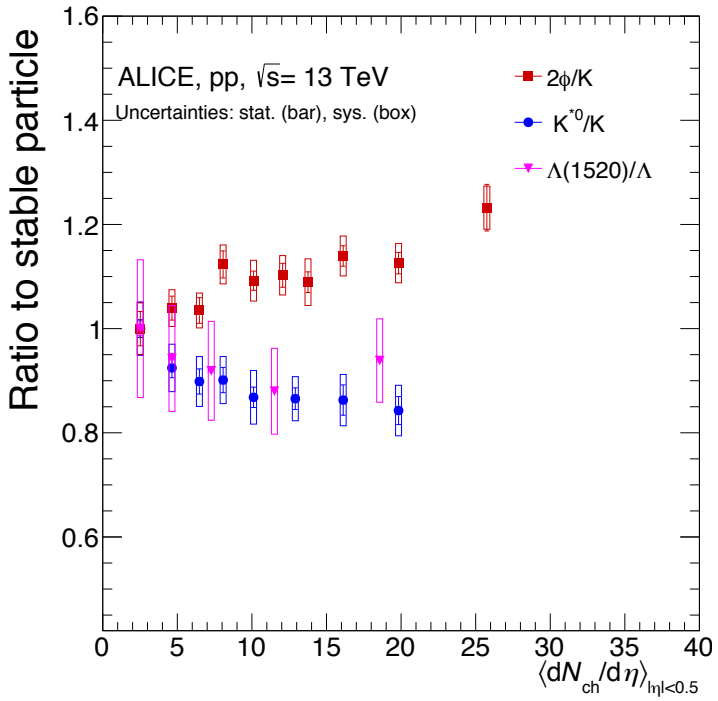

Figure 6.7: The $\Lambda(1520)/\Lambda$ is compared with $K^{*0}(892)/K^{\pm}$ and $2\phi/K^{\pm}$ in pp collisions at $\sqrt{s} = 13$ TeV . $K^{*0}(892)/K^{\pm}$ and $2\phi/K^{\pm}$ ratio is taken from [65].

In Figure 6.7, the $\Lambda(1520)/\Lambda$, $K^{*0}/K^{\pm}$, and $2\phi/K^{\pm}$ are shown as a function of $\langle dN_{\rm ch}/d\eta\rangle|_{|\eta|<0.5}$ in pp collisions at $\sqrt{s} = 13$ TeV. The first data point, corresponding to the lowest multiplicity, is normalized to unity. The results suggest a slight indication of suppression in the production yield of K^{*0}. The $2\phi/K^{\pm}$ ratio shows a slight enhancement with weak multiplicity dependence, which could be attributed to strangeness enhancement. For the $\Lambda(1520)/\Lambda$ ratio, the first four central values reveal a decreasing trend similar to that of $K^{*0}/K^{\pm}$. However, the value corresponding to the highest multiplicity is slightly higher. One cannot demonstrate a decreasing trend with multiplicity due to the larger uncertainties in the measurements [65].

$\Lambda(1520)/\pi^{\pm}$ and $\Lambda(1520)/\mathrm{K}^{\pm}$ ratios

The investigation of the ratios $\Lambda(1520)/\pi^{\pm}$ and $\Lambda(1520)/\mathrm{K}^{\pm}$ is motivated by the potential observation of strangeness enhancement in high-energy pp collisions. The ratio to kaons, which contain strange quarks, can mitigate the effects of strangeness in the measurement. In contrast, the ratio to pions, which do not contain strange quarks, emphasizes the contribution of strange quarks in the production process. An increasing ratio of resonance particle to $\pi^{\pm}$ would suggest enhanced strangeness production.

The $\Lambda(1520)/\pi^{\pm}$ and $\Lambda(1520)/\mathrm{K}^{\pm}$ ratios are presented for different multiplicity classes in pp collisions at $\sqrt{s} = 13$ TeV, as illustrated in Figure 6.8. Both ratios exhibit no significant change with increasing $\langle dN_{\mathrm{ch}}/d\eta\rangle|_{|\eta|<0.5}$ within experimental uncertainties. Furthermore, the $\Lambda(1520)/\pi^{\pm}$ and $\Lambda(1520)/\mathrm{K}^{\pm}$ ratios are compared with the $\mathrm{K}^{*0}(892)/\mathrm{K}^{\pm}$, $2\phi/\mathrm{K}^{\pm}$, $\mathrm{K}^{*0}(892)/\pi^{\pm}$, and $2\phi/\pi^{\pm}$ ratios in pp collisions at $\sqrt{s} = 13$ TeV. These ratios do not indicate any enhancement across different multiplicity classes in proton-proton collisions [65, 92].

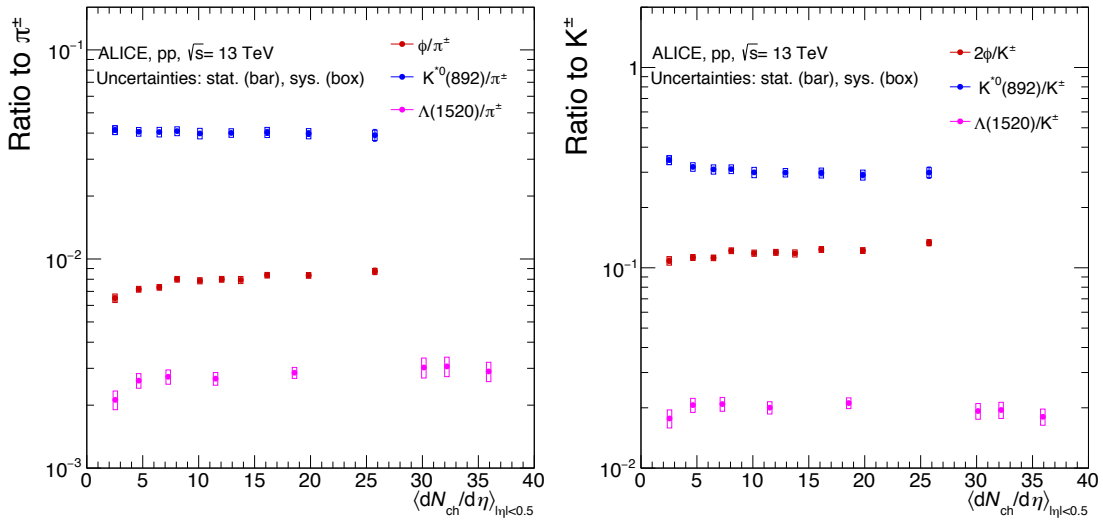

Figure 6.8: $\Lambda(1520)/\pi^{\pm}$ and $\Lambda(1520)/\mathrm{K}^{\pm}$ ratio as a function of $\langle dN_{\mathrm{ch}}/d\eta\rangle|_{|\eta|<0.5}$ for different classes compared with the $\mathrm{K}^{*0}(892)/\mathrm{K}^{\pm}$, $2\phi/\mathrm{K}^{\pm}$ and $\mathrm{K}^{*0}(892)/\pi^{\pm}$, $2\phi/\pi^{\pm}$ in pp collisions at $\sqrt{s}$= 13 TeV.

6.5 p_{T}-Differential Particle Ratio

In Figure 6.9, the investigation into the production mechanism and the potential presence of collective effects in small collision systems is extended through the examination of the yield ratio of $\Lambda(1520)/\mathrm{K}^{\pm}$ as a function of p_{T} for various multiplicity classes. Conventionally, radial flow effects often manifest as a pronounced peak in the baryon to meson ratio in the intermediate p_{T} range. However, in proton-proton collisions, no discernible structure is observed in the $\Lambda(1520)/\mathrm{K}^{\pm}$ ratio. Instead, a rising trend with p_{T} is consistently observed across all multiplicity classes at low p_T, followed by a plateauing effect at higher p_{T} values. Notably, the saturation of the ratio measured in low-multiplicity collisions occurs at lower p_{T} values compared to those observed in the highest multiplicity collisions.

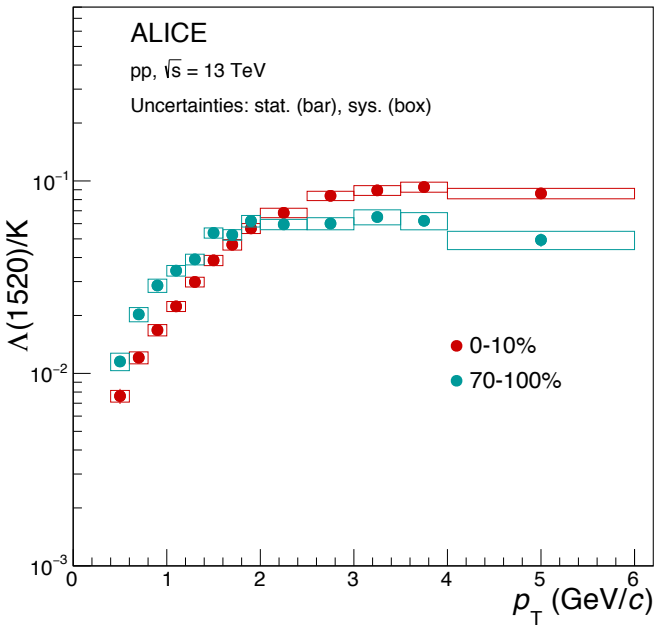

Figure 6.9: Yield ratio $\Lambda(1520)/\mathrm{K}^{\pm}$ as a function of p_{T} for the multiplicity classes 0–10% and 70–100%. The boxes represent systematic uncertainties, while the error bars indicate statistical uncertainties.

Chapter 7

Summary and Outlook

Hadronic resonances are effective tools for studying the hadronic phase in ultrarelativistic heavy-ion collisions. Due to their short lifetime, these particles can be identified by the method of invariant mass reconstruction of the decay daughters. The invariant mass reconstruction is affected by rescattering and regeneration of these resonances, which depends on the in-medium hadronic interaction cross-section, chemical freeze-out time and kinetic freeze-out time in heavy-ion collisions. This process can be unravelled by calculating the resonance to stable particle yield ratio. This ratio can be used to study the properties of the hadronic phase and also the rescattering of resonance decay products in the hadronic phase. Additionally, comparing results from smaller collision systems, such as pp and p–Pb, with larger systems like Xe–Xe and Pb–Pb collisions highlights potential collective phenomena and variations in the lifetime of the hadronic phase.

This thesis focuses on the multiplicity dependence of the $\Lambda(1520)$ resonance in proton-proton collisions at $\sqrt{s} = 5.02$ TeV and 13 TeV, examining its production mechanism in small collision systems. The $\Lambda(1520)$ signal is reconstructed using the invariant mass technique, which involves isolating the signal from the background in the invariant mass distribution of pK pairs. The raw yield of $\Lambda(1520)$ is extracted using the bin counting method followed by applying various correction factors to obtain the corrected p_{T}-spectra. The corrected transverse momentum (p_{T}) spectra reveal a clear trend of hardening with

increasing multiplicity, indicating a shift towards higher p_{T} particles in high-multiplicity events.

The p_{T}-integrated yield ($\langle \mathrm{d}N/\mathrm{d}y \rangle$) across different multiplicity classes shows an increase in $\langle \mathrm{d}N/\mathrm{d}y \rangle$ with $\langle dN_{\mathrm{ch}}/d\eta \rangle|_{|\eta|<0.5}$. This trend is consistent across different collision systems and energies, suggesting that the production rate of $\Lambda(1520)$ is largely driven by multiplicity (or event activity) rather than the specific collision system or energy.

The mean transverse momentum ($\langle p_{\mathrm{T}} \rangle$) across different multiplicity classes shows an increase with multiplicity with no significant energy dependence. The slope of the $\langle p_{\mathrm{T}} \rangle$ trend in pp collisions was observed to be steeper than p–Pb collisions and considerably greater than the Pb–Pb collisions. The observed differences in Pb–Pb collisions could be attributed to rescattering effect of the decay daughters in the dense medium created in heavy-ion collisions.

Further, the $\langle p_{\mathrm{T}} \rangle$ values for $\Lambda(1520)$ was compared with other particle species and no mass ordering was observed for pp collisions at $\sqrt{s} = 13$ TeV. However, notable differences in the $\langle p_{\mathrm{T}} \rangle$ of baryons and mesons were observed. These differences implied distinct production mechanisms for baryons, mesons as well as for resonance particles, potentially arising from fragmentation effects.

The ratios of $\Lambda(1520)$ to stable particles (Λ, $\pi^{\pm}$, and $\mathrm{K}^{\pm}$) as a function of $\langle dN_{\mathrm{ch}}/d\eta \rangle|_{|\eta|<0.5}$ exhibited interesting features. It was observed that the ratio remained relatively constant with $\langle dN_{\mathrm{ch}}/d\eta \rangle|_{|\eta|<0.5}$ when transitioning from small to large collision systems, up to an approximate value of $\langle dN_{\mathrm{ch}}/d\eta \rangle|_{|\eta|<0.5} = 100$. For larger multiplicity values, a notable suppression was observed in the Pb–Pb system, attributed to the rescattering effects in heavy-ion collisions. However, no such suppression was observed in the case of pp collisions. The $\Lambda(1520)/\pi^{\pm}$ and $\Lambda(1520)/\mathrm{K}^{\pm}$ ratios also remained relatively unchanged with multiplicity in pp collisions.

Examining the $\Lambda(1520)/\mathrm{K}^{\pm}$ ratio as a function of p_{T} across various multiplicity classes revealed a consistent increase with p_{T}, followed by a plateau, without the distinct peaks associated with radial flow like effects in larger systems. This suggested a uniform pro-

duction mechanism across different multiplicities, despite the rising trend at lower p_{T}.

The study of the $\Lambda(1520)$ and $\mathrm{K}^{*0}(892)$ resonance in high-multiplicity pp collisions was also performed to gain more insights in high multiplicity regime.

7.1 Oulook

Looking forward, future studies using Run 3 data of the LHC will offer significantly increased statistics, allowing for more precise measurement in narrower multiplicity bins. This improved precision would help to clarify the behaviour of resonance production and its dependence on event characteristics, further contributing to the understanding of particle production dynamics in high-energy collisions.

A precise measurement of resonance flow can be carried out which would shed light on the nature of particle production in high-multiplicity pp collisions and the possible existence of medium-like effects.

In addition, the investigations of resonance production within jets provides crucial insights into the dynamics of high-energy collisions. The presence of resonances, such as the $\Lambda(1520)$, inside jets can reveal information about the partonic energy loss and the fragmentation processes that occur in the presence of the medium. For instance, the modifications in the yield and spectral shapes of resonances within jets compared to those produced in the underlying event can indicate the effects of collective flow and interactions within the medium.

References

[1] Ernest Rutherford. The scattering of α and β particles by matter and the structure of the atom. *Philosophical Magazine*, 34(197):663–665, 1917.

[2] J.J. Thomson. Discovery of the electron. *Nature*, 59(1534):424, 1899.

[3] Max Planck. On the law of distribution of energy in the normal spectrum. *Annalen der Physik*, 309(3):553–563, 1900.

[4] Albert Einstein. On the electrodynamics of moving bodies. *Annalen der Physik*, 17(10):891–921, 1905.

[5] Niels Bohr. On the constitution of atoms and molecules. *Philosophical Magazine*, 26(151):1–25, 1913.

[6] B. Rossi. The distribution of showers produced by cosmic rays. *Physical Review*, 51(2):110, 1937.

[7] J.C. Street. Positive muons. *Physical Review*, 54(2):111, 1938.

[8] C.F. Powell, G. Occhialini, and E. Persico. New particles from the cosmos. *Nature*, 159(4040):694–697, 1947.

[9] C.D. Anderson. The positive electron. *Physical Review*, 43(6):491, 1933.

[10] Martin Breidenbach, Jerome I. Friedman, Henry W. Kendall, Elliott D. Bloom, D. H. Coward, H. C. DeStaebler, J. Drees, Luke W. Mo, and Richard E. Taylor. Observed

behavior of highly inelastic electron-proton scattering. *Phys. Rev. Lett.*, 23:935–939, 1969.

[11] John Smith. The standard model: A comprehensive framework for particle physics. *Journal of Particle Physics*, 25(4):123–135, 2020.

[12] David J. Griffiths. *Introduction to Elementary Particles*. Wiley, 2017.

[13] ATLAS Collaboration. Observation of a new particle in the search for the standard model higgs boson with the atlas detector at the lhc. *Physics Letters B*, 716:1 – 29, 2012.

[14] CMS Collaboration. Observation of a new boson at a mass of 125 gev with the cms experiment at the lhc. *Physics Letters B*, 716:30 – 61, 2012.

[15] The Nobel Prize in Physics 2013. The nobel prize in physics 2013. NobelPrize.org, 2013.

[16] P.A. Zyla, R.M. Barnett, J. Beringer, O. Dahl, D.A. Dwyer, D.E. Groom, C.-J. Lin, K.S. Lugovsky, E. Pianori, et al. Review of particle physics. *Progress of Theoretical and Experimental Physics*, 2020(8):083C01, 2020.

[17] H David Politzer. Asymptotic freedom: An approach to strong interactions. *Physical Review Letters*, 30(26):1346, 1973.

[18] David J Gross and Frank Wilczek. Ultraviolet behavior of non-abelian gauge theories. *Physical Review Letters*, 30(26):1343, 1973.

[19] C. Montag and A. Fedotov. Beam-beam effects in space charge dominated ion beams. In *ICFA Mini-Workshop on Beam-Beam Effects in Hadron Colliders*, pages 63–68, 2014.

[20] M. Arslandok et al. Hot QCD White Paper. 3 2023.

[21] S. Acharya et al. The ALICE experiment: a journey through QCD. *Eur. Phys. J. C*, 84(8):813, 2024.

[22] J. D. Bjorken. Highly relativistic nucleus-nucleus collisions: The central rapidity region. *Physical Review D*, 27(1):140–151, 1983.

[23] Mattia. Evolution of collisions and qgp, 2016.

[24] Johann Rafelski and Berndt Müller. Strangeness production in the quark-gluon plasma. *Physical Review Letters*, 48(16):1066, 1982.

[25] Betty Bezverkhny Abelev et al. Multi-strange baryon production at mid-rapidity in Pb-Pb collisions at $\sqrt{s_{NN}} = 2.76$ TeV. *Phys. Lett. B*, 728:216–227, 2014. [Erratum: Phys.Lett.B 734, 409–410 (2014)].

[26] Shreyasi Acharya et al. Multiplicity dependence of π, K, and p production in pp collisions at $\sqrt{s} = 13$ TeV. *Eur. Phys. J. C*, 80(8):693, 2020.

[27] Jaroslav Adam et al. Enhanced production of multi-strange hadrons in high-multiplicity proton-proton collisions. *Nature Phys.*, 13:535–539, 2017.

[28] John Adams et al. Experimental and theoretical challenges in the search for the quark gluon plasma: The STAR Collaboration's critical assessment of the evidence from RHIC collisions. *Nucl. Phys. A*, 757:102–183, 2005.

[29] Ulrich Heinz and Raimond Snellings. Collective flow and viscosity in relativistic heavy-ion collisions. *Ann. Rev. Nucl. Part. Sci.*, 63:123–151, 2013.

[30] Raimond Snellings. Elliptic Flow: A Brief Review. *New J. Phys.*, 13:055008, 2011.

[31] S. Voloshin and Y. Zhang. Flow study in relativistic nuclear collisions by Fourier expansion of Azimuthal particle distributions. *Z. Phys. C*, 70:665–672, 1996.

[32] Megan Connors, Christine Nattrass, Rosi Reed, and Sevil Salur. Jet measurements in heavy ion physics. *Rev. Mod. Phys.*, 90:025005, 2018.

[33] Arthur M. Poskanzer and S. A. Voloshin. Methods for analyzing anisotropic flow in relativistic nuclear collisions. *Phys. Rev. C*, 58:1671–1678, 1998.

[34] Shreyasi Acharya et al. Anisotropic flow and flow fluctuations of identified hadrons in Pb–Pb collisions at $\sqrt{s_{\rm NN}} = 5.02$ TeV. *JHEP*, 05:243, 2023.

[35] Shreyasi Acharya et al. Probing the effects of strong electromagnetic fields with charge-dependent directed flow in Pb-Pb collisions at the LHC. *Phys. Rev. Lett.*, 125(2):022301, 2020.

[36] Santosh K. Das et al. Dynamics of Hot QCD Matter – Current Status and Developments. *Int. J. Mod. Phys. E*, 31:12, 2022.

[37] B. Alver and G. Roland. Collision geometry fluctuations and triangular flow in heavy-ion collisions. *Phys. Rev. C*, 81:054905, 2010. [Erratum: Phys.Rev.C 82, 039903 (2010)].

[38] Jaroslav Adam et al. Higher harmonic flow coefficients of identified hadrons in Pb-Pb collisions at $\sqrt{s_{\rm NN}} = 2.76$ TeV. *JHEP*, 09:164, 2016.

[39] Baidyanath Sahoo. *Ph.D. Thesis*. PhD thesis, IIT Bombay, 2022. CERN-THESIS-2022-121, 212 p.

[40] Ahmed Ali and Gustav Kramer. Jets and QCD: A Historical Review of the Discovery of the Quark and Gluon Jets and its Impact on QCD. *Eur. Phys. J. H*, 36:245–326, 2011.

[41] J. D. Bjorken. Highly Relativistic Nucleus-Nucleus Collisions: The Central Rapidity Region. *Phys. Rev. D*, 27:140–151, 1983.

[42] Miklos Gyulassy and Michael Plumer. Jet Quenching in Dense Matter. *Phys. Lett. B*, 243:432–438, 1990.

[43] Miklos Gyulassy and Xin-nian Wang. Multiple collisions and induced gluon Bremsstrahlung in QCD. *Nucl. Phys. B*, 420:583–614, 1994.

[44] G. Abbiendi et al. Dijet production in photon-photon collisions at s(ee)**(1/2) from 189-GeV to 209-GeV. *Eur. Phys. J. C*, 31:307–325, 2003.

[45] K. Aamodt et al. Particle-yield modification in jet-like azimuthal di-hadron correlations in Pb-Pb collisions at $\sqrt{s_{NN}} = 2.76$ TeV. *Phys. Rev. Lett.*, 108:092301, 2012.

[46] Betty Bezverkhny Abelev et al. Transverse momentum dependence of inclusive primary charged-particle production in p-Pb collisions at $\sqrt{s_{\rm NN}} = 5.02$ TeV. *Eur. Phys. J. C*, 74(9):3054, 2014.

[47] Shreyasi Acharya et al. Measurement of inclusive charged-particle jet production in pp and p-Pb collisions at $\sqrt{s_{\rm NN}} = 5.02$ TeV. *JHEP*, 05:041, 2024.

[48] Shreyasi Acharya et al. ψ(2S) Suppression in Pb-Pb Collisions at the LHC. *Phys. Rev. Lett.*, 132(4):042301, 2024.

[49] Xiaojian Du and Ralf Rapp. Sequential Regeneration of Charmonia in Heavy-Ion Collisions. *Nucl. Phys. A*, 943:147–158, 2015.

[50] Anton Andronic, Peter Braun-Munzinger, Markus K. Köhler, Krzysztof Redlich, and Johanna Stachel. Transverse momentum distributions of charmonium states with the statistical hadronization model. *Phys. Lett. B*, 797:134836, 2019.

[51] Shreyasi Acharya et al. Dielectron production in central Pb−Pb collisions at $\sqrt{s_{\rm NN}}$ = 5.02 TeV. 8 2023.

[52] Betty Bezverkhny Abelev et al. $K^*(892)^0$ and $\phi(1020)$ production in Pb-Pb collisions at $\sqrt{sNN} = 2.76$ TeV. *Phys. Rev. C*, 91:024609, 2015.

[53] Jaroslav Adam et al. Production of K* $(892)^0$ and ϕ (1020) in p–Pb collisions at $\sqrt{s_{\rm NN}}$ = 5.02 TeV. *Eur. Phys. J. C*, 76(5):245, 2016.

[54] Jaroslav Adam et al. K$^*(892)^0$ and $\phi(1020)$ meson production at high transverse momentum in pp and Pb-Pb collisions at $\sqrt{s_{\rm NN}} = 2.76$ TeV. *Phys. Rev. C*, 95(6):064606, 2017.

[55] A. G. Knospe, C. Markert, K. Werner, J. Steinheimer, and M. Bleicher. Hadronic resonance production and interaction in partonic and hadronic matter in the EPOS3 model with and without the hadronic afterburner UrQMD. *Phys. Rev. C*, 93(1):014911, 2016.

[56] Shreyasi Acharya et al. Evidence of rescattering effect in Pb-Pb collisions at the LHC through production of K$^*(892)^0$ and $\phi(1020)$ mesons. *Phys. Lett. B*, 802:135225, 2020.

[57] M. M. Aggarwal et al. K^{*0} production in Cu+Cu and Au+Au collisions at $\sqrt{s_N N}$ = 62.4 GeV and 200 GeV. *Phys. Rev. C*, 84:034909, 2011.

[58] B. I. Abelev et al. Hadronic resonance production in d+Au collisions at s(NN)**(1/2) = 200-GeV at RHIC. *Phys. Rev. C*, 78:044906, 2008.

[59] Shreyasi Acharya et al. Long- and short-range correlations and their event-scale dependence in high-multiplicity pp collisions at $\sqrt{s} = 13$ TeV. *JHEP*, 05:290, 2021.

[60] Shreyasi Acharya et al. Emergence of long-range angular correlations in low-multiplicity proton-proton collisions. 11 2023.

[61] Anju Bhasin and Meenakshi Sharma. Strangeness production in small-collision systems with ALICE. In *51st International Symposium on Multiparticle Dynamics*, 10 2022.

[62] Jaroslav Adam et al. Multiplicity dependence of charged pion, kaon, and (anti)proton production at large transverse momentum in p-Pb collisions at $\sqrt{s_{\rm NN}}$ = 5.02 TeV. *Phys. Lett. B*, 760:720–735, 2016.

[63] R. L. Workman et al. Review of Particle Physics. *PTEP*, 2022:083C01, 2022.

[64] Shreyasi Acharya et al. Suppression of $\Lambda(1520)$ resonance production in central Pb-Pb collisions at $\sqrt{s_{\rm NN}} = 2.76$ TeV. *Phys. Rev. C*, 99:024905, 2019.

[65] Shreyasi Acharya et al. Multiplicity dependence of K*(892)0 and $\phi(1020)$ production in pp collisions at s=13 TeV. *Phys. Lett. B*, 807:135501, 2020.

[66] S. Acharya et al. Measurement of $\Lambda(1520)$ production in pp collisions at $\sqrt{s} = 7$ TeV and p-Pb collisions at $\sqrt{s_{\rm NN}} = 5.02$ TeV. *Eur. Phys. J. C*, 80(2):160, 2020.

[67] Sonali Padhan. Understanding the rescattering effect on $\Lambda(1520)$ resonance production in different systems and collision energies with ALICE at LHC. *PoS*, LHCP2023:269, 2024.

[68] E. Lopienska. The cern accelerator complex, layout in 2022. CERN Document Server, 2022. General Photo.

[69] LHC Machine. *JINST*, 3:S08001, 2008.

[70] K. Aamodt et al. The ALICE experiment at the CERN LHC. *JINST*, 3:S08002, 2008.

[71] Betty Abelev et al. Performance of the ALICE Experiment at the CERN LHC. *Int. J. Mod. Phys.*, A29:1430044, 2014.

[72] G. Dellacasa et al. ALICE technical design report of the inner tracking system (ITS). 6 1999.

[73] G. Dellacasa et al. ALICE: Technical design report of the time projection chamber. 1 2000.

[74] David Rohr, Sergey Gorbunov, Artur Szostak, Matthias Kretz, Thorsten Kollegger, Timo Breitner, and Torsten Alt. ALICE HLT TPC tracking of Pb-Pb Events on GPUs. *J. Phys. Conf. Ser.*, 396:012044, 2012.

[75] G. Dellacasa et al. ALICE technical design report of the time-of-flight system (TOF). 2 2000.

[76] The alice transition radiation detector: Construction, operation, and performance. *Nuclear Instruments and Methods in Physics Research Section A: Accelerators, Spectrometers, Detectors and Associated Equipment*, 881:88–127, 2018.

[77] S. Beole et al. ALICE technical design report: Detector for high momentum PID. 8 1998.

[78] E. Abbas et al. Performance of the ALICE VZERO system. *JINST*, 8:P10016, 2013.

[79] P Cortese et al. ALICE technical design report on forward detectors: FMD, T0 and V0. 9 2004.

[80] G. Dellacasa et al. ALICE technical design report: Photon multiplicity detector (PMD). 9 1999.

[81] G. Dellacasa et al. ALICE technical design report of the zero degree calorimeter (ZDC). 3 1999.

[82] A. Bruna, A. Dainese, M. Masera, and F. Prino. Vertex reconstruction for proton-proton collisions in alice. 2012.

[83] Antonin Maire. Track reconstruction principle in ALICE for LHC run I and run II. Principes de reconstruction de traces dans ALICE pour les runs I et II du LHC. General Photo, 2011.

[84] Giuseppe Cerati, Peter Elmer, Steven Lantz, Ian MacNeill, Kevin McDermott, Dan Riley, Matevž Tadel, Peter Wittich, Frank Würthwein, and Avi Yagil. Traditional Tracking with Kalman Filter on Parallel Architectures. *J. Phys. Conf. Ser.*, 608(1):012057, 2015.

[85] M. Ivanov, I. Belikov, P. Hristov, and K. Safarik. Track reconstruction in high density environment. *Nucl. Instrum. Meth. A*, 566:70–74, 2006.

[86] Y. Belikov, M. Ivanov, K. Safarik, and J. Bracinik. TPC tracking and particle identification in high density environment. *eConf*, C0303241:TULT011, 2003.

[87] Raimond Snellings. Collective Expansion at the LHC: selected ALICE anisotropic flow measurements. *J. Phys. G*, 41(12):124007, 2014.

[88] Betty Abelev et al. Centrality determination of Pb-Pb collisions at $\sqrt{s_{NN}} = 2.76$ TeV with ALICE. *Phys. Rev. C*, 88(4):044909, 2013.

[89] Michael L. Miller, Klaus Reygers, Stephen J. Sanders, and Peter Steinberg. Glauber modeling in high energy nuclear collisions. *Ann. Rev. Nucl. Part. Sci.*, 57:205–243, 2007.

[90] Shreyasi Acharya et al. Multiplicity dependence of light-flavor hadron production in pp collisions at $\sqrt{s} = 7$ TeV. *Phys. Rev. C*, 99(2):024906, 2019.

[91] Shreyasi Acharya et al. Multiplicity dependence of (multi-)strange hadron production in proton-proton collisions at $\sqrt{s} = 13$ TeV. *Eur. Phys. J. C*, 80(2):167, 2020.

[92] Jaroslav Adam et al. Pseudorapidity and transverse-momentum distributions of charged particles in proton–proton collisions at $\sqrt{s} = 13$ TeV. *Phys. Lett. B*, 753:319–329, 2016.

[93] M. Tanabashi et al. Review of Particle Physics. *Phys. Rev. D*, 98(3):030001, 2018.

[94] Peter Skands, Stefano Carrazza, and Juan Rojo. Tuning PYTHIA 8.1: the Monash 2013 Tune. *Eur. Phys. J. C*, 74(8):3024, 2014.

[95] T. Ullrich and Z. Xu. Treatment of errors in efficiency calculations. *arXiv:physics/0701199 [physics.data-an]*, 2007. Available at: `https://arxiv.org/abs/physics/0701199`.

[96] Roger Barlow. Systematic errors: Facts and fictions. In *Conference on Advanced Statistical Techniques in Particle Physics*, pages 134–144, 7 2002.